Synthesis and processing of sub-micron hafnium diboride powders and carbon fibre-hafnium diboride composites

by

Saranya Venugopal

A doctoral thesis
submitted in partial fulfilment of the requirements
for the award of

Doctor of Philosophy of Loughborough University
April 2013

To:

My Family and Myself ;)

Acknowledgement

I would like to express my sincere gratitude to Prof. Jon Binner and Dr. Bala Vaidhyanathan for giving me the opportunity to conduct my PhD on the most interesting and niche area of ultra high temperature ceramics. I like to thank them for inspiring me, supporting me with their valuable ideas and guidance, and most importantly for believing in me even after I broke a couple of expensive platinum sensors. I admire their patience, and support which helped me groom myself as a researcher. I would also like to thank my sponsors Defence Science and Technology Laboratories (DSTL), UK and Science Faculty Fellowship, Loughborough University, for without them all this wouldn't have been possible.

My special appreciation and thanks to Mr. Andrew Lau, Dr. Geoff West, Dr. Keith Yendall, Dr. John Bates, Dr. Scott Doak, Mr. Dave Insley, Mr. Mac Callender and Mr. Mike Kemp for their continual support with day-to-day lab requirements, characterization techniques and workshop facilities. I would like to acknowledge the help from Dr. Luc Vandeperre and Dr. Doni Jayasheelan, Imperial College, London for conducting high temperature TGA/DTA experiments and for valuable discussions.

With great appreciation I shall acknowledge all my colleagues and ex-colleagues at the advanced ceramic research group, Loughborough University, who constantly supported me throughout my Ph.D. In particular, I would like to thank Ms. Juliane Fehlhauer, Dr. Anish Paul, Mrs. Shaghayegh Ghani-Zadeh, Dr. Minnah Tong, Dr. Sina Saremi, Mr. Siyuan Qi, Mr. Yifei Zhang and Mr. Prabhu Ramanujam for all their scientific and emotional support, encouragement and most importantly for putting up with me during my Ph.D.

Last but not the least, I thank my parents, my brother, my family and all my friends residing in Loughborough and Birmingham for not letting the stress from the PhD get to me and for the most valuable and enjoyable three and half years of my life.

Abstract

A vehicle flying at hypersonic speeds, i.e. at speeds greater than Mach 4, needs to be able to withstand the heat arising from friction and shock waves, which can reach temperatures of up to 3000^{o}C. The current project focuses on producing thermal protection systems based on ultra high temperature ceramic (UHTC) impregnated carbon-carbon composites. The carbon fibres offer low mass and excellent resistance to thermal shock; their vulnerability is to oxidation above 500^{o}C. The aim of introducing HfB_2, a UHTC, as a coating on the fibre tows or as particulate reinforcement into the carbon fibre preform, was to improve this property.

The objectives of this project were to:

i) identify a low temperature synthesis route for group IV diborides,

ii) produce a powder fine enough to reduce the difficulties associated with sintering the refractory diborides,

iii) develop sol-gel coating of HfB_2 onto carbon fibre tows

iv) improve the solid loading of the particulate reinforcement into the carbon fibre preform, which should, in turn, increase the oxidation protection.

In order to achieve the above set objectives, fine HfB_2 powder was synthesized through a low temperature sol gel and boro/carbothermal reduction process, using a range of different carbon sources. Study of the formation mechanism of HfB_2 revealed an intermediate boron sub-oxide and/or active boron formation that yielded HfB_2 formation at 1300^{o}C. At higher temperatures the formation of HfB_2 could be via intermediate HfC formation and/or B_4C formation. Growth mechanism analysis showed that the nucleated particles possessed screw dislocations which indicated that the formation of HfB_2 was not only through a substitution reaction, but there could have been an element of a precipitation nucleation mechanism that lead to anisotropic growth under certain conditions. The effect of carbon sources during the boro/carbothermal reduction reaction on the size of the final HfB_2 powders was analysed and it was found that a direct relation existed between the size and

level of agglomeration of the carbon sources and the resulting HfB_2 powders. A powder phenolic resin source led to the finest powder, with particle sizes in the range 30 to 150 nm. SPS sintering of the powder revealed that 99% theoretical density could be achieved without the need for sintering aids at 2200^{o}C.

Sol-gel coatings and slurry impregnation of HfB_2 on carbon fibres tows was performed using dip coating and a 'squeeze–tube' method respectively. Crack free coatings and non-porous matrix infiltration were successfully achieved. The solid loading of the fine HfB_2 into the carbon fibre preform was carried out through impregnation of a HfB_2 / phenolic resin / acetone slurry using vacuum impregnation. Although the sub-micron Loughborough (LU) powders were expected to improve the solid loading, compared to the commercially available micron sized powders, due to the slurry made from them having a higher viscosity because of the fine particle size, the solids loading achieved was consequently decreased. Optimisation of the rheology of the slurry with LU HfB_2 still requires more work.

A comparison of the oxidation and ablation resistance of the Cf-HfB_2 composites prepared with both commercial micron sized HfB_2 powder and Loughborough sub-micron sized HfB_2 powder, each with similar level of solid loading, was carried out using oxyacetylene torch testing. It was found that the composite containing the finer, Loughborough powders suffered a larger erosion volume than the composite with the coarser commercial powders indicating that the former offered worse ablation and oxidation resistance than the latter. A full investigation of the effect of solids loading and particle size, including the option of using mixtures of fine and coarse powders, is still required.

Keywords: UHTC, HfB_2, sol-gel, formation mechanism, slurry impregnation, oxidation resistance, oxyacetylene torch test.

Table of Contents

List of Tables

List of Figures

Chapter 1

1 Introduction

1.1 Need for speed

Since the first, successful, controlled and heavier than air, human flight by the Wright Brothers, there has always been a drive and desire to fly higher and faster. Hypersonic vehicles which could provide quick and on-demand access to space, rapid access to distant points on earth, good manuverability and horizontal take-off was hypothesized by many during World War I [1]. The earliest of the experiments were conducted during World War II in Germany and subsequently launches were carried out in USA. The first successful hypersonic flight was Bumper 5, which was a large two-stage rocket composed of a German V-2 and an American WAC Corporal Research missile, the former being the second stage, and was launched from White Sands, New Mexico on 24 February, 1949 [2].

Since then, numerous vehicles have flown at hypersonic speeds including the nose cones of intercontinental ballistic missiles, manned vehicles such as Mercury, Gemini, and Apollo space capsules, and the X-15 hypersonic research vehicle, all of which share the same feature with the Bumper, i.e. following the initial boost to altitude, subsequent re-entry is propelled by only gravitational force. The Mach number for hypersonic flights ranges from Mach 7 for the X-15 to Mach 36 for the Apollo capsule [1].

Although, the hypersonic flight is defined as flight at Mach 5 or higher, there is very little change in air flow as the vehicle crosses the Mach 5 boundary, unlike when it passes through Mach 1 and enters the supersonic flight regime from the subsonic, causing a sonic boom. In short, hypersonic flight is the high-speed part of the flight spectrum where aero-thermal dynamics are very important. The aerodynamic heating of the surface due to friction and shock wave heating causes temperatures to exceed 1800^{o}C very rapidly. When combined with the fact that the environment is very oxidising, these are the

dominant features that drive the design of hypersonic vehicles and are one of the major obstacles between us and our dream of hypersonic flight [1].

One example of the aerodynamic heating occurring on a hypersonic test vehicle is Hypersonic Technology Vehicle 2 (HTV-2), launched by the Defence Advanced Research Projects Agency (DARPA). This unmanned vehicle which was powered by rockets to Mach 20, spent about 200 seconds flying within the atmosphere prior to the intense aerodynamic heating which resulted in stripping of the skin from the internal structure.

The development of structural materials for use in extreme temperature and oxidizing environments is of great interest to the defence and aerospace sectors and is the aim of this project. Materials for these environments are currently largely limited to silicon-based ceramics due to the beneficial formation of a protective SiO_2 surface film in a suitably oxygen-rich atmosphere [3,4]. Although SiO_2 is an excellent oxidation barrier at temperatures below 1600°C, above this temperature it softens dramatically and in low oxygen atmosphere develops a substantial vapour pressure, which restricts its use. Relatively few refractory oxides are stable in an oxidizing environment at or above 2000°C, but among those, zirconia (ZrO_2) and hafnia (HfO_2) have the highest melting points, ~2700°C and ~2800°C, [5] respectively. Despite being stable and chemically inert, these are susceptible to thermal shock, will undergo phase transformation and exhibit high creep rates at higher temperatures [3, 5].

1.2 Ultra high temperature ceramics (UHTCs)

UHTCs are a class of refractory materials that includes transition metal borides, carbides and nitrides. These display extremely high melting temperatures i.e. over 3000ºC, high thermal conductivities, high hardness, good strength retention and chemical stability at elevated temperatures [6-8]. Examples include TaC, ZrC, HfC, ZrB_2 and HfB_2. In recent years, UHTCs have been extensively investigated for innovative thermal protection systems (TPS) [9-15] and sharp leading edge components [16,17] for aerospace vehicles and

for other applications where oxidation and/or erosion resistance at high temperature (up to 2000°C) are required. The ‘‘sharp’’ configuration of the leading edges and of the nose of re-entry vehicles increases aerodynamic efficiency and vehicle manoeuvrability [18], and so improves the safety of manned space flight and decreases the cost of such missions. However, the sharper the configuration the higher will be the thermal loads experienced by these materials compared to a blunt configuration. UHTC compounds, with their thermal and chemical stability, qualify as potential candidates for use in extreme environments, including hypersonic flight (1400°C and above in air) and rocket propulsion (3000°C and above in reactive chemical vapours) [19].

More than 300 materials have melting points over 2000°C. Although carbides typically have the highest melting points (>3500°C), ZrB_2 and HfB_2 - based ceramics are the most widely studied due to their unique combination of mechanical and physical properties, including high melting points (>3000°C), high thermal and electrical conductivities and chemical inertness against molten metals, [3-11]. However, the poor oxidation and ablation resistance, and poor damage tolerance limits the use of bulk, single-phase materials for high-temperature structural applications.

A composite model has been incorporated successfully to improve the densification [20-25], mechanical and physical properties [26,27], as well as the oxidation and ablation resistance of ZrB_2 and HfB_2 ceramics. The mechanical and physical properties of these are closely linked with the densification processes, compositions, starting powders, microstructures and intergranular second phases.

Despite having several advantages, the intrinsic characteristics of these materials such as low fracture toughness, poor thermal shock resistance and poor sinterability limit their usage. One approach to enhance their mechanical properties is by introducing carbon fibres (Cf) as a toughening and strengthening phase; however their poor oxidation resistance above 500°C potentially limits their high temperature applications [28, 29]. It has been demonstrated, however, that it is possible to prepare Cf-UHTC hybrid powder

composites where the Cf improve the toughness while the UHTC phase provides oxidative resistance [29]. A variety of UHTC compositions have been studied and their potential for high temperature oxidation resistance demonstrated [28].

The carbon-fibre based reinforcement can be protected by UHTCs in the following different ways, fig. 1.1:

i. Impregnating UHTC powders into the voids between the tows in carbon fibre-based composites;

ii. Coating the carbon fibre tows with thin layers of a low oxygen diffusivity UHTC;

iii. Joining a thin piece of monolith UHTC to the surface of the Cf-UHTC composite.

This research work forms part of a larger research programme that will examine the first 2 options above.

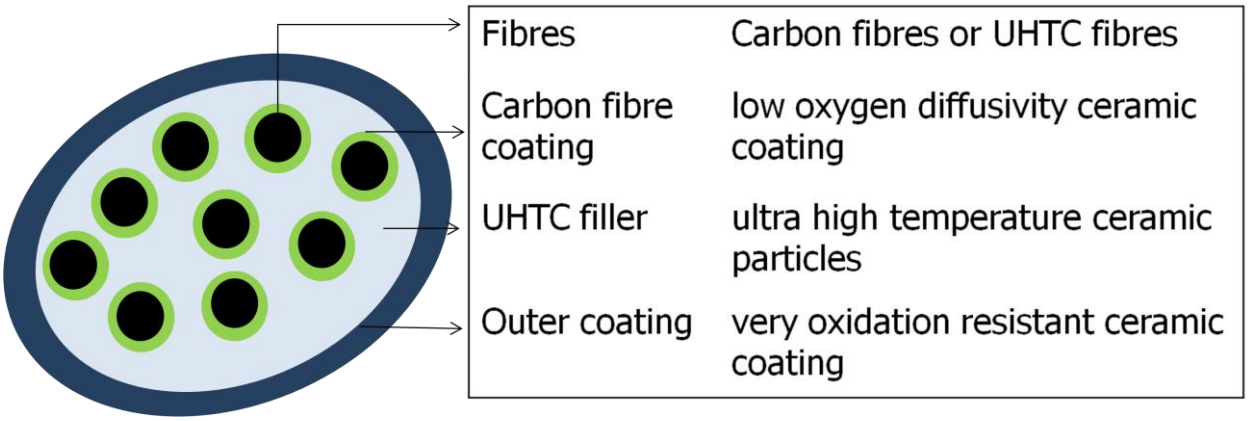

Figure 1.1: Schematic representation of a carbon fibre-based composite protected as outlined in the text.

Impregnation of the UHTC powders in the carbon preforms was carried out by synthesis of sub-micron sized powders followed by squeeze and vacuum impregnation into the carbon preform. Previous experiments conducted in this overall project concluded that HfB_2 offers better protection to the carbon fibre

preforms upon impregnation compared to other group V borides and carbide, when tested using an oxyacetylene torch. Hence the current thesis is focused on synthesis and formation and growth mechanism of HfB_2 and the effect on its oxidation resistance of impregnating the same into carbon fibre preform.

The report is divided into six chapters. The current chapter, the Introduction, outlines the overall objective of the project. Chapter 2 provides an overview of UHTC materials, including their synthesis methods, and the use of UHTCs for ultra high temperature thermal resistance. It also reviews the various methods employed for sintering the UHTCS and for evaluating the oxidation performance of both the monolithic UHTCS and C-UHTC composites. Chapter 3 presents the experimental work performed, including the different synthesis routes and characterization techniques used. The first part of Chapter 4 discusses the synthesis and sintering of monolithic UHTC whilst the second part focusses on the coating and impregnation of UHTC coating and powders on and into carbon fibre tows and carbon preforms respectively. The conclusions are drawn in chapter 5 and possible future experimentation to be undertaken is outlined chapter 6.

Chapter 2

2 Literature Review

2.1 Thermal Protection Systems (TPS) for hypersonic applications

The growth in aerospace science and technology sector can be attributed to the demand for hypersonic vehicles. With this demand, rises a responsibility to protect the vehicles against ultra high temperatures and oxidizing environments.

Modern aircraft vehicles such as, DARPA's hypersonic test vehicle HTV-2 Falcon [30] and the X43-A by NASA (National Aeronautics and Space Administration, USA) [31] (Figure 2.1) have slender body design with UHTC materials that gives not only great maneuverability and flight speeds above Mach 7 but also allows the reusability of these vehicles. Small radii of curvature (in the order of millimetres) of the leading edges and nose cone tips enhance the maneuverability of these vehicles. The radii of curvature being inversely proportional to surface temperatures, the sharp edges result in temperatures of 2000-2700^{o}C in the aero thermodynamic environment. Thus, with the increase in speed comes a need to develop an advanced thermal protection system that can retain its strength at these ultra high temperatures [32-34].

Figure 2.1: a) DARPA's Falcon HTV-2 hypersonic aircraft and b) X43-A, a design of reusable space vehicle by NASA [31]

For years people have been taking advantage of refractory ceramics due their high melting points resulting from strong covalent/ionic bonds. The ceramic materials can be classified into i) high temperature ceramics that offer thermal protection up to 1700^{o}C, such as Al_2O_3, SiC etc, and ii) ultra high temperature ceramics that are required in the current scenario as they offer protection for temperatures over 2000^{o}C.

2.2 Ultra high temperature ceramics (UHTCs)

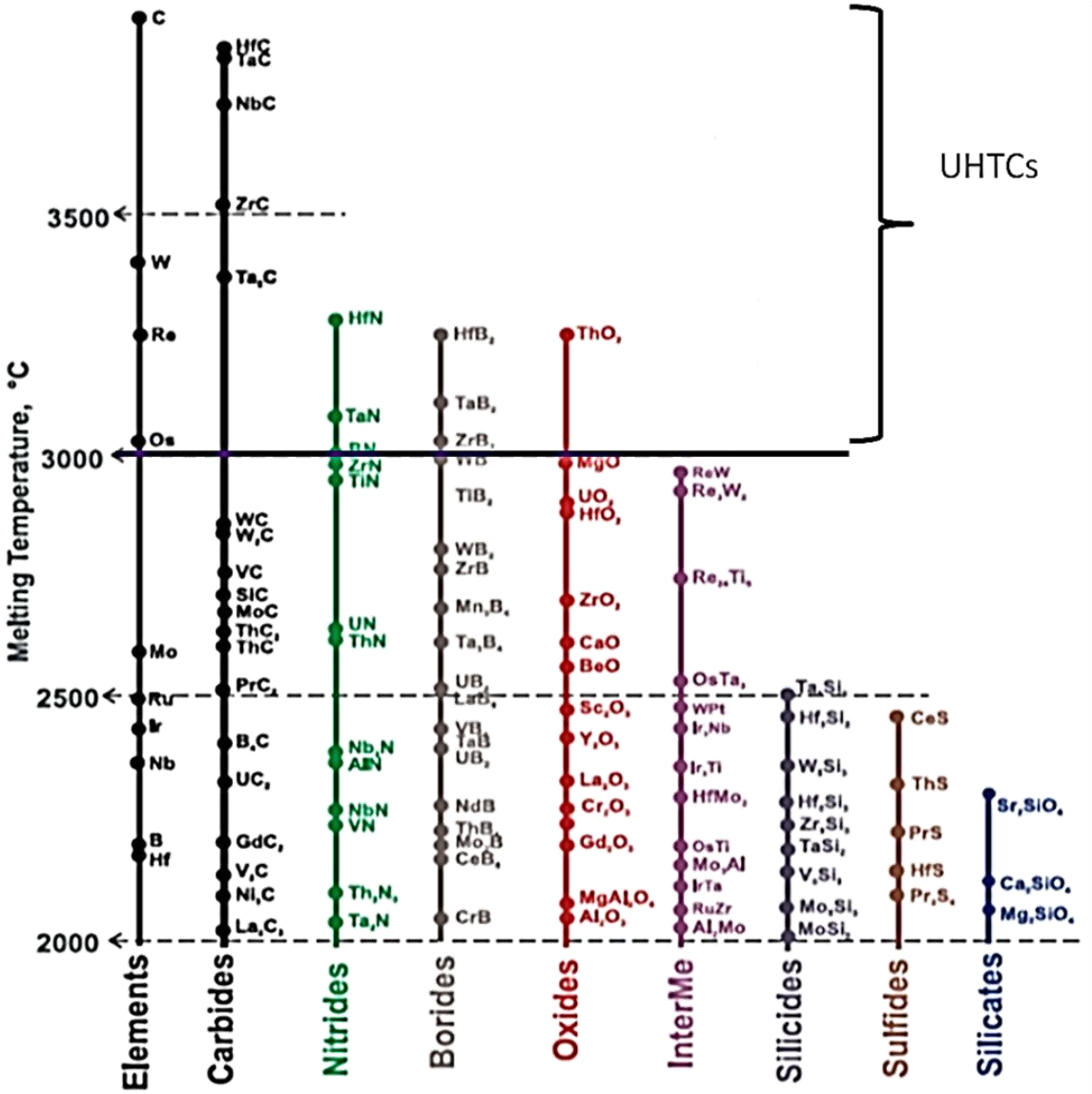

Figure 2.2: Melting temperatures of UHTC materials [35]

UHTCs are a group of materials that includes nitrides, borides and carbides of hafnium, zirconium and tantalum based systems. They possess some of the highest melting points of known materials. Figure 2.2 gives an idea of materials whose melting temperature is higher than 2000^{o}C; materials with melting temperatures higher than 3000^{o}C are generally classified as UHTCs [35]. In addition to a high melting point, they have high hardness along with good mechanical strength and wear resistance, and have relatively higher thermal conductivity compared to other ceramic materials. Based on these properties, UHTCs seem to be promising materials for thermal protection systems, especially for those requiring chemical and structural stability at extremely high operating temperatures. They have the potential to revolutionize the aerospace industry by enabling the development of sharp leading edges for re-entry and hypersonic vehicles.

A UHTC is required to possess some important properties, including:

i. High oxidation/ablation resistance: The re-entry atmosphere contains oxygen and nitrogen molecules in extremely reactive ionic/atomic states. This facilitates aggressive oxidation of the protecting materials which is enhanced by the increase in the surface temperature of these vehicles resulting from high flow rates generated by their high speed and large quantities of exothermic heat generated from the recombination of the oxygen atoms/ions at the surface of the TPS. In such environments, the UHTCs are oxidized well below their melting points and lose their function. Therefore, in the aero-thermodynamic environment with ultra high temperatures, high oxidation, high heat flux and high gas flow rates, oxidation/ablation resistance becomes the dominant criteria [32].

ii. Thermal conductivity: The nose tips and the leading edges of the hypersonic vehicles need to be made of materials with high thermal conductivity, i.e. those that are capable of effectively transferring the heat from the tip to the other lower temperature parts of the leading edge, thus reducing the temperature concentration in these regions and providing additional

thermal protection. Ceramics generally have low thermal conductivities and hence are good thermal insulators, but some exceptions like diborides have a relatively high thermal conductivity, which is beneficial for extracting heat [4]. The thermal conductivity of UHTCs usually depends on the operating temperature, material and processing conditions, thus making it difficult for any performance predictions [32].

Thermal conductivity, k, can be calculated using the specific heat capacity of the material, as given by the equation,

$$k=\alpha \rho c_p \quad (2.1)$$

where ρ is the density, α is the thermal diffusivity and c_p is the specific heat, of the material [32].

iii. Coefficient of thermal expansion (CTE): The different components of UHTCs in a structure should have similar CTE values to prevent any internal stresses and strains arising from temperature changes. These internal stresses and strains can cause the structure to crack and hence fail. The shape and size of UHTC components are often restricted by this CTE effect [32].

iv. Thermal shock resistance: UHTC materials should be able to withstand high heating and cooling rates, thus protecting the vehicles during their flight. The thermal shock parameter, R, which is a measure of the thermal shock resistance, can be calculated using equation 2. It is measured in ^{o}C.

$$R = \Delta T_{max} = \sigma((1-\nu)/\alpha E) \quad (2.2)$$

where ΔT_{max} is the maximum allowable temperature change in transient heating or cooling without failure; σ is flexural strength; ν is Poisson's ratio; α is CTE; E is Young's modulus. As shown by the equation, R is dependent on both the mechanical and thermal properties of the material [36].

v. Mechanical properties: At very high temperatures the mechanical properties of UHTCs tend to degrade resulting in a non-linear and plastic behaviour, leading to the failure of the structure. Hence the material is required to possess sufficient flexural strength and fracture toughness to withstand the ultra high temperatures. Testing and predicting the high temperature mechanical performance of UHTCs still remains a challenge [32].

vi. Surface properties: Surface temperatures of the UHTCs are also influenced by their surface properties, including emissivity and surface roughness which alter the surface energy balance. Emissivity is the ability of the material to radiate the absorbed heat, and is dependent on the temperature, wavelength and emission angle [32; 34; 35]. The higher the emissivity, the lower the surface temperature. The surface roughness on the other hand, plays a destructive role in introducing turbulence in gas flows, which is unfavourable both to the heating conditions and performance [3].

In summary, materials which fulfill all the mechanical, thermal and surface properties, or at least most of them, are classified as UHTCs. This project focuses mainly on the oxidation/ablation resistance of the UHTCs and other properties are mentioned where necessary.

2.2.1 UHTC MONOLITHICS

UHTCs are a family of materials composed of transition metals (Group IVB, VB and VIB) combined with non-metallic atoms such as boron and carbon. The resulting ceramics such as zirconium diboride (ZrB_2), hafnium diboride (HfB_2), tantalum carbide (TaC), zirconium carbide (ZrC) and hafnium carbide (HfC) are distinguished by their very high melting points and good oxidation resistance.

2.2.1.1 Oxides

Oxides such as ZrO_2 and HfO_2 are intrinsically oxidation resistant with very high melting points of about 2700^{o}C [37] and 2900^{o}C [38] respectively. Yet they are not classified as UHTCs for the following reasons:

- Low thermal shock resistance and fracture toughness, that can cause the material to crack whilst cooling from high temperatures,
- Low thermal conductivity, hence cannot be used as refractory oxide components [8],
- Undesirable phase transformations at high temperatures, leading to undesirable volume changes causing cracks that result in component failure. For instance, HfO_2 and ZrO_2 experience solid phase transformations, from monoclinic to tetragonal at 1650^oC and 1150^oC respectively, and from tetragonal to cubic at 2700^oC and 2370^oC respectively. Stabilizing additives or compositional reinforcement can solve some of the drawbacks but at the expense of increased cost [8].

Carbides and borides are usually preferred for high temperature applications because they [39];

- Have strong covalent bonding that leads to high strength;
- Have strength retention at high temperature;
- Have metallic character in their bonding;
- Have high thermal shock and creep resistance.

2.2.1.2 Carbides

Carbide (and boride) synthesis goes as far back as the mid 1800s, when Henri Moisson, a pioneer, developed a specialized electric arc furnace to synthesize SiC.

i. <u>Synthesis and particle size</u>

Carbides can be synthesized via three routes, viz. reduction reactions that use metal oxides as the metallic source; reactive processes, that employ elemental metals and chemical routes, that use metal hydrides (ZrH_2 and HfH_2). Various carbon sources including pitch, graphite, carbon black and phenolic resin have

all been used in these processes. ZrC and HfC are mainly produced through carbothermal reduction reactions using metal oxides, as described by equations 3 and 4 [40,41], due to the more expensive precursors involved in the other methods. Commercially available ZrC and HfC powders with particle sizes from 2 μm to about 30 μm and crystallite sizes in the micron range, contain impurities like oxygen, free carbon, metal oxides etc, [42,43].

$$\mathrm{ZrO_2(s) + 3C(s) \rightarrow ZrC(s) + 2CO(g)} \quad (2.3)$$

$$\mathrm{HfO_2(s) + 3C(s) \rightarrow HfC(s) + 2CO(g)} \quad (2.4)$$

Smaller particle sizes can be obtained via the sol-gel method that uses metal chloride or alkoxide as the metal sources. For example, precursors like hydrated zirconium chloride and pentanedione yield crystals of less than 200 nm in size. Partially hydrated hafnium tetrachloride, magnesium and carbon were used to produce ~100 nm HfC crystals [44]. Liu et al. [11] used two different carbon sources, viz, graphite and carbon black and obtained HfC powders with two different particle sizes. The smaller particle size, ~225 nm, obtained via carbon black was attributed to the smaller particle size of the carbon source, ~42 nm, than when graphite was used.

ii. Mechanical and thermal properties

The face centered cubic crystal structure with strong ionic and metallic bonds is responsible for their high melting points of the carbides; 3445^{o}C for ZrC, 3928^{o}C for HfC and 3997^{o}C for TaC [39]. In the case of vacancies of carbon atoms from the lattice, the carbides can be described as MC_x, where x can vary from 0.5 to 0.98. Upon oxygen contamination of the lattice, the material is modified to what is called an oxycarbide MC_xO_y. This stoichiometric difference leads to some property changes, as listed in Table 2.3. The carbides distinguish themselves from the other UHTCS with a unique brittle to ductile transition (BDT) behaviour which varies with the vacancy concentration [45]. This is due to the presence of carbon, which increases the strength of metal covalent bonds, which in turn increase the lattice resistance to dislocations

and hence the thermal activation of the dislocations occur at relatively higher temperatures, shifting the BDT temperature [46, 47, 48].

Table 2.1: Properties of HfC_x at room temperature [45]

	Young's modulus / GPa	Flexural strength / MPa	CTE at 2000 / $^oC^{-1}$	Thermal conductivity / W/(mK)	BDT temperature / ^oC
$HfC_{0.98}$	450	340	13	22	2200
$HfC_{0.67}$	320	260	13	7	1090

iii. Oxidation mechanism

The oxidation studies on ZrC and HfC were carried out from 400^{o}C to over 2000^{o}C. The oxidation mechanism can be described by reactions 2.5 and 2.6:

$$ZrC(s) + 2O_2(g) \rightarrow ZrO_2(s) + CO_2(g) \quad (2.5)$$

$$HfC(s) + 2O_2(g) \rightarrow HfO_2(s) + CO_2(g) \quad (2.6)$$

Early studies showed that the oxidation rate was linear with temperature and oxygen pressure below 600^{o}C [**Error! Bookmark not defined.**], further ompositional analysis showed that whilst at 400^{o}C the oxidation rate was linear and was mainly due to the oxygen diffusion into the lattice, between 400-600^{o}C, both oxygen diffusion and surface reactions occurred. This resulted in parabolic oxidation rates. Free carbon production is favoured in this step due the low oxygen partial pressure, as shown below:

$$ZrC(s) + O_2(g) \rightarrow ZrO_2(s) + C(s) \quad (2.7)$$

Above 600^{o}C, two different oxide layers were observed: an inner dense oxide layer and an outer porous oxide layer with free carbon. Above 1400^{o}C, a third layer, made up of oxycarbide, was formed at the interface between the carbide and oxide layer. The former was passive and prevented further oxidation, thus protecting the underlying carbide. At these temperatures oxidation was

controlled by the oxygen diffusion through the grain boundary and hence was affected by the grain size and stoichiometry of the starting material. The oxidation resistance increased with a decrease in the residual carbon content. Above 2000^{o}C, the interlayer remained (Figure 2.3) but the oxidation was controlled by the bulk oxygen transportation. Despite being inferior to their diboride counterparts in oxidation resistance, ZrC and HfC still resist ultra high temperatures of over 2000^{o}C [49-54].

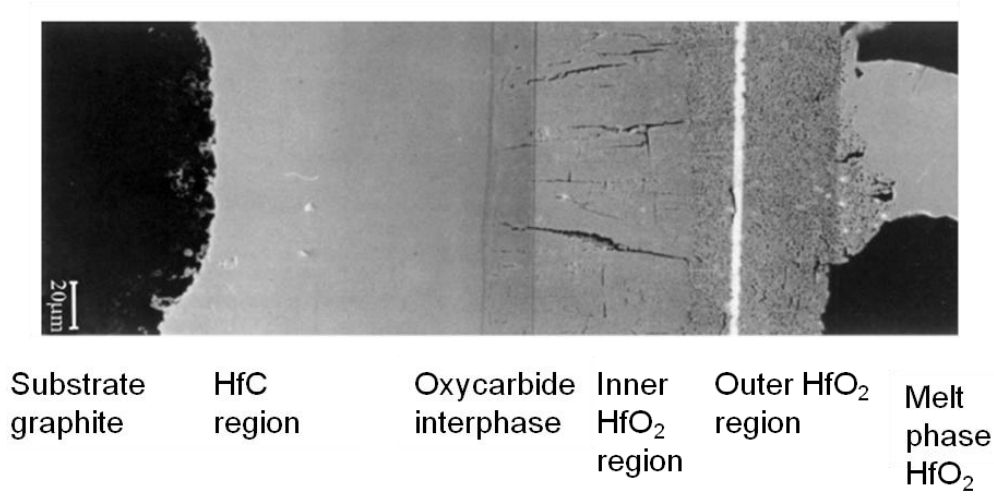

Figure 2.3: Cross-section of HfC (arc-heater) oxidized at 2700 ^{o}C for 30 s [48]

Li et al. [55] summarized the oxidation of TaC over the temperature range room temperature to 2000^{o}C. Oxidation was initiated around 500^{o}C, leading to the formation of a hexagonal Ta_2O_3 layer on the surface, see equation (2.8). This was followed by a phase transformation to orthorhombic Ta_2O_5 at 900 to 1500^{o}C and subsequent state transformation to liquid Ta_2O_5, equation (2.9). The latter wetted the surface, offering protection to over 2000^{o}C.

$$4TaC(s) + 7O_2(g) \rightarrow 2Ta_2O_3(s) + 4CO_2(g) \quad (2.8)$$

$$4TaC(s) + 9O_2(g) \rightarrow 2Ta_2O_5(l) + 4CO_2(g) \quad (2.9)$$

Carbides generally show linear oxidation kinetics over a wide range of temperatures, whilst the borides have parabolic kinetics at some temperatures and are often deemed promising [56].

2.2.1.3 Borides

Reactive processing of ZrB_2, from Zr and B_4C, was first demonstrated by Tucker et al. in 1901. NASA started its research on high melting point diborides, ZrB_2 and HfB_2 in the 1960s and since then these have been referred to by different terms, such as refractory transition metal borides, oxidation resistant diboride materials, hard metal and ceramals.

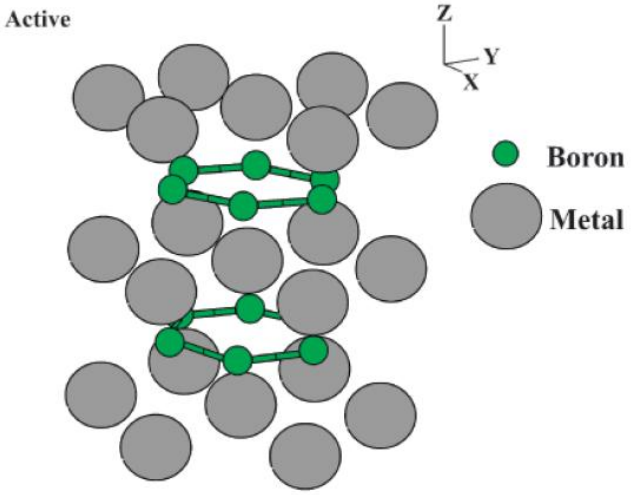

Figure 2.4: Hexagonal crystal structure of diborides like ZrB_2 and HfB_2 [56]

The crystal structure of the diborides is hexagonal, as shown in Figure 2.4 [57]. The covalent/ionic bonds render the diborides oxidation resistance, whilst the B-B and M-B bonds control their thermal properties. Compared to other transition metal diborides, group IVB diborides, including TiB_2, ZrB_2 and HfB_2 have very high melting points, viz 3230^{o}C, 3245^{o}C and 3380^{o}C respectively, higher oxidation resistance, higher Young's modulus, higher thermal conductivity and lower CTE. They also show superior strength retention at high temperatures and better thermal shock resistance, thus making them potential UHTC candidates suitable for manufacturing advanced thermal protection systems [15, 27].

Initial studies by L. Kaufman et al. [58] at the Air Force Research Laboratories (AFRL), focused on comparing borides with other materials and found that borides had superior oxidation resistance compared to the carbides, due to their parabolic oxidation kinetics at high temperatures. L. Kaufman's phase II study, compared the oxidation behaviour of different borides and concluded that HfB_2 and ZrB_2 performed better than diborides of Ta, Ti or Nb, i.e. they had lower oxidation rates. Hence further discussion here will be narrowed down to HfB_2 and ZrB_2. The general properties of these two ceramics are given in Table 2.2.

Table 2.2: Summary of some properties of ZrB_2 and HfB_2 [8]

Property	ZrB_2	HfB_2
Crystal system space group prototype structure	Hexagonal *P6/mmm AlB₂*	Hexagonal *P6/mmm AlB₂*
a (Å)	3.17	3.139
c (Å)	3.53	3.473
Density (g/cm³)	6.1	11.2
Melting température (°C)	3245	3380
Young's modulus (GPa)	489	480
Hardness (GPa)	23	28
Coefficient of Thermal Expansion ($°C^{-1}$)	5.9×10^{-6}	6.3×10^{-6}
Heat capacity at 25°C ($J.mol^{-1}.°C^{-1}$)	48.2	49.5
Thermal conductivity ($W.m^{-1}.°C^{-1}$)	60	104
Electrical conductivity (S/m)	1.0×10^{7}	9.1×10^{6}

i. Synthesis

Three routes are usually used for the synthesis of ZrB_2 and HfB_2 similar to the situation for carbides, viz. reduction reactions, chemical routes and reactive processes. Each route has its own advantages and disadvantages.

Chemical routes use boron and transition metal containing precursors to make the corresponding metal diborides. Chen et al. [59] synthesized nano sized hafnium diboride from $HfCl_4$ and $NaBH_4$ at 600^oC using a hydrothermal reaction method. This is the lowest temperature reported for the synthesis of HfB_2 in the literature. The reaction for HfB_2 formation at 600^oC (also applicable to ZrB_2) is:

$$\mathrm{HfCl_4(g) + NaBH_4(g) \rightarrow HfB_2(s) + 2NaCl(s) + 2HCl(g) + 3H_2(g)} \qquad (2.10)$$

The synthesized powders had crystallite sizes of about 20 to 25 nm. Yan et al. [60] synthesized spherical ZrB_2 with particle sizes of 100 to 200 nm, from a novel hybrid precursor system of inorganic $ZrOCl_2{\cdot}8H_2O$, H_3BO_3, and phenolic resin. The powders, however, contained impurities like ZrC, carbon, and Cl, which could not be removed.

Reactive processes use elemental Hf, Zr and B powders to produce diborides. The powder, pressed to a pellet, was ignited using an electrical heated tungsten coil. The resulting exothermic reaction generated large amounts of heat, sufficient enough to melt the metal and to yield diborides. This route, called self-propagation high temperature synthesis (SHS) or combustion synthesis, was adopted by Mishra et al. [61] to synthesize ZrB_2 powder with particle sizes of ~3 microns and crystallite sizes in the sub-micron range. The high heating and cooling rates involved in SHS are thought to introduce planar defects, such as linear defects i.e. dislocations, and stacking faults whose associated strain fields increase the sinterability of the powders by providing a driving force for rearrangement of atoms. Double SHS reactions using NaCl as diluents, can yield smaller particles of 200 nm, with the primary particle size being only 30 nm [62, 63]. Hafnium diboride has been prepared by the self-propagating high temperature synthesis (SHS) route by Munir et al. [64], Blum et al. [65] used a Hf and B powder mixture in a non self-propagating high temperature synthesis process to produce HfB_2 at 1500^oC. They also reported a synthesis route employing metallic Hf strips and elemental boron powders. Despite the use of elements, the authors reported the presence of a

significant level of unaccounted impurities, which may or may not have been core shell structures of Hf and B.

Reduction reactions usually occur at relatively high temperatures from 1500 to 2000^{o}C. There are two types, viz. boro/carbothermal and borothermal reduction. The former uses a carbon source to create a reducing atmosphere to facilitate the reaction between the Hf and B sources, which are typically oxide sources whilst the latter uses a Hf source and reactive metal boron powder. The powders produced inevitably contain impurities like boria, free carbon, metal carbide and oxides, which is a drawback of this process [66]. Despite this, carbothermal/borothermal reduction is reported as the commercial synthesis route for the diborides, due to the simplicity of the process involved [67]. Fine ZrB_2 powders with particle sizes from 0.5 to 1.5 μm can be obtained from boro/carbothermal synthesis. The finer particles had a spherical shape, whilst the coarser particles had a columnar shape, due to the higher synthesis temperatures (1750^{o}C) involved [66]. Zhang et al. [68] and Guo et al. [69] synthesized equiaxed HfB_2 particles through borothermal reduction reactions at 1600^{o}C. The former obtained particle sizes ranging between 1 to 1.5 μm, whilst the latter used an additional washing step at 1100^{o}C to remove any B_2O_3 formed and achieved a HfB_2 particle size of ~0.8 μm. Guo et al. [39] believed that B_2O_3 was the reason for coarsening of the HfB_2 particles, and despite the washing step, they reported that the oxygen content in their powders was as low as 2.5%. A modified boro/carbothermal reduction reaction with excess B_4C and carbon to yield high purity HfB_2 with particle sizes less than 1 μm was reported by Ni et al. [37]. One of the issues faced with this method of synthesis, was that the boron loss occurring at high temperatures was due to the formation of volatile B_2O_3. Both Ni et al. [37] and Guo et al. [39] reported a 10 to 15% boron loss and hence the need to add excess boron precursor to compensate for this loss.

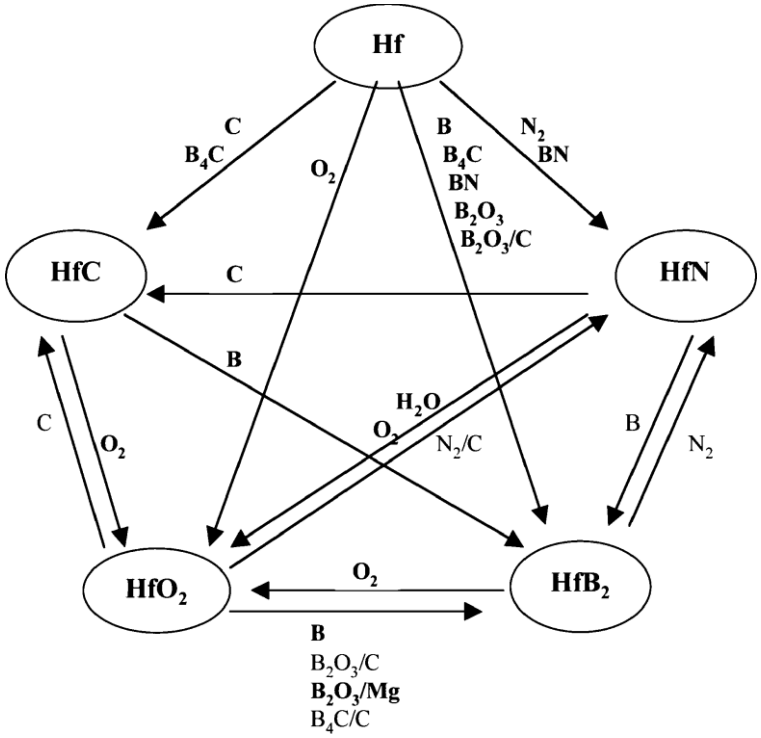

Figure 2.5: Reactions within the system of Hf-B-C-N-O. Additional reaction products within each of the reactions (if present) are omitted [69].

Blum et al. [70] studied the reduction reactions in the Hf-B-C-N system and summarized a broad range of reactions that occurred at 1500^{o}C and below for the Hf-B-C-N-O system. They reported that reactions with either elemental Hf or all of its derivatives lead to the formation of HfB_2. Of them, only the carbothermal and borothermic reactions required temperatures higher than 1500^{o}C to take place. The incorporation of additives such as silicon or magnesium could aid the Hf reactivity and yield HfB_2 at lower temperatures. The enthalpies of all the reactions that lead to HfB_2 formation, are summarized in Table 2.3, and Figure 2.5 gives the reactions within the system of Hf-B-C-N-O. Reactions with reagents marked in bold letters proceed (at least partially) at 1500^{o}C or below, the rest require higher temperatures.

Table 2.3: Calculated thermodynamic values for reactions in which HfB_2 is formed [69]

Reaction	$\Delta G_{1000°C}$ (kJ/mol)	$\Delta H_{1000°C}$ (kJ/mol)	$\Delta G_{1500°C}$ (kJ/mol) (temp of $\Delta G = 0$)	$\Delta H_{1500°C}$ (kJ/mol)
$Hf + 2B \rightarrow HfB_2$	-315	-328	-308	-332
$Hf + B_2O_3 \rightarrow HfB_2 + 3/2O_2$	647	901	549	889
$Hf + 2/3B_2O_3 \rightarrow HfO_2 + 4/3B$	-243	-282	-228	-281
$Hf + 2/5B_2O_3 \rightarrow 2/5HfB_2 + 3/5HfO_2$	-272	-301	-260	-301
$Hf + B_2O_3 + 3C \rightarrow HfB_2 + 3CO$	-25	561	-252	538
$Hf + 2BN \rightarrow HfB_2 + N_2$	-38	171	-119	166
$Hf + BN \rightarrow HfN + B$	-115	-113	-116	-112
$Hf + 2/3BN \rightarrow 1/3HfB_2 + 2/3HfN$	-181	-185	-180	-185
$Hf + 1/3B_4C \rightarrow 2/3HfB_2 + 1/3HfC$	-252	-265	-247	-268
$Hf + 1/2B_4C \rightarrow HfB_2 + 1/2C$	-278	-296	-270	-298
$Hf + 1/3HfO_2\ 2/3B_4C \rightarrow 4/3HfB_2 + 2/3CO$	-215	-93	-262	-102
$HfO_2 + 2B \rightarrow HfB_2 + O_2$	569	774	491	763
$HfO_2 + B_2O_3 + 5C \rightarrow HfB_2 + 3CO$	410	1435	14 (1518°C)	1398
$HfO_2 + 2B + 2\ C \rightarrow HfB_2 + 2CO$	121	546	-43	529
$HfO_2 + 1/2B_4C + 3/2C \rightarrow HfB_2 + 2CO$	330	608	25 (1580°C)	591
$HfO_2 + 10/3B \rightarrow HfB_2 + 2/3B_2O_3$	-13	-21	-9	-27
$HfC + 2B \rightarrow HfB_2 + C$	-113	-124	-108	-126
$HfC + 2B + 2H_2 \rightarrow HfB_2 + CH_4$	-64	-214	-5	-215
$HfC + 6B \rightarrow HfB_2 + B_4C$	-171	-191	-163	-196
$HfC + 4/3B + 1/3B_2O_3 \rightarrow HfB_2 + CO$	-17	172	-89	163
$HfC + 2C + B_2O_3 \rightarrow HfB_2 + 3CO$	176	765	-51	743
$HfN + 2B \rightarrow HfB_2 + 1/2N_2$	-61	34	-98	28

ii. Densification

Hot pressing:

The densification of diborides is a diffusion controlled process [71, 72] and usually requires very high temperatures [73] due to their strong covalent bonds and low volume and grain boundary diffusion rates. Hot pressing (HP) of ZrB_2 typically requires a temperature of 2100°C or above and moderate pressure (20 to 30 MPa) [74], or relatively lower temperatures (~1800°C) and extremely high pressures (>800 MPa) [75, 76]. HP of coarse ZrB_2 powder ($d \approx 20$ µm) at 2000°C with a pressure of 20 MPa, resulted in a relative density of ~73% [101], whilst a finer powder ($d \approx 2.1$µm) gave ~91% relative density under the same HP conditions [74]. However, an attrition-milled ZrB_2 powder, with an average particle size of $d \leq 0.5$ µm, sintered to full density at 1900°C and 32

MPa for 45 min [131]. The lower HP temperature was attributed to the reduction of the starting particle size from micron ($d \approx 2.1$ µm) to submicron ($d \leq 0.5$ µm) by attrition-milling. However, oxygen impurities (B_2O_3 and ZrO_2) may be introduced into the starting powder due to milling, which will inhibit densification and promote grain growth in these non-oxide ceramic systems.

Reactive Hot Pressing (RHP):

RHP is an alternate potential route to produce ZrB_2 and HfB_2 ceramics with low impurity content and high density at temperatures lower than that required for HP. In situ reaction of precursor powders and densification, are the two processes that are completed simultaneously during heating and subsequent holding in RHP. ZrB_2 and HfB_2 dense compacts have been produced through RHP by using Zr and/or Hf and B precursors. ZrB_2-based composites with SiC or ZrC have also been fabricated through this route using Zr, Si and B_4C precursors. Table 2.4 summarizes RHP sintering conditions, precursors, grain size and final density of the fabricated ceramics. Chamberlain et al. [157] used two step heating to produce a nearly fully dense nano-sized ZrB_2 ceramic from Zr and B powders. The first step was at 600^{o}C with a 6 h hold to enable the fine Zr and B powders to react and the second step was at 1650^{o}C and 40 MPa pressure. Increasing the temperature to 1700°C increased the density to 99%, however, the ZrB_2 grains coarsened significantly. A sample sintered at 1800°C had a grain size of ~1.5 µm, which was 3 times larger than for the sample sintered at 1650°C. On the other hand, HP of commercially available micron-sized ZrB_2 powders ($d \approx 2.1$ µm) resulted in only 91% relative density even after 60 min at 2000°C and 20 MPa pressure and had an average grain size of 6.1 µm [75]. The significant improvement of densification by RHP was attributed to the formation of nano-sized ZrB_2 particles during the reactive process resulting in large surface areas and surface reactivity.

Table 2.4: Reactive hot-pressing conditions, precursors, grain size and final density of ZrB_2 or HfB_2 ceramics fabricated by a RHP method [61]

Materials	Precursors	Remarks	HP or SPS Processing Conditions	Final density / %	Grain Size / µm	
					ZrB_2	SiC
ZrB_2	Zr, B	Attrition-milled	1650°C/30 min/ 40 MPa/ Ar (HP)	>95	0.5	-
HfB_2	Hf, B	None	1700°C/10 min/95 MPa/ vacuum (SPS)	~98	-	-
HfB_2	HfB_2	None	1900°C/10 min/95 MPa/ vacuum (SPS)	~97	-	-

Spark Plasma Sintering (SPS):

SPS of ZrB_2 ceramics required a temperature of 1900°C, 40 MPa pressure and a holding time of 3 min, with 200°C/min heating rates to achieve full density as opposed to the 2100°C, 0.5 h and 40 MPa pressure required in HP [77]. HfB_2 ceramic was also produced by the reaction between Hf and B powders at a low temperature, by using SPS; a nearly dense HfB_2 compact was produced by subjecting the powder mixture to 1700°C and 95 MPa for 10 min *in vacuo* using SPS [78].The reaction between Hf and B occurred at 1100°C, whilst the completion of the reaction extended over a relatively wide temperature range. However, commercially available micron sized HfB_2 powder attained only ~62% and ~87% densities at 1800°C with 30 to 85 MPa for 10 min, and at 1900°C with 80 to 95 MPa for 10 min [78], respectively in SPS.

iii. Mechanical and thermal properties

Refractory metal borides of Ti, Zr, Hf and Ta have attractive properties that render them of potential value for ultra-high temperature structural applications. The properties include high melting temperature and high hardness as a result of strong covalent bonding characteristics, high thermal and electrical conductivity and low volatility. Borides exhibit good thermal shock resistance when compared to other ceramics due to their high thermal

conductivity and high elastic modulus [39]. The bend strengths of TiB_2, ZrB_2 and HfB_2 as a function of temperature, (in an inert environment), are shown in Figure 2.6 [8]. As expected, the strengths of the refractory borides are widely scattered.

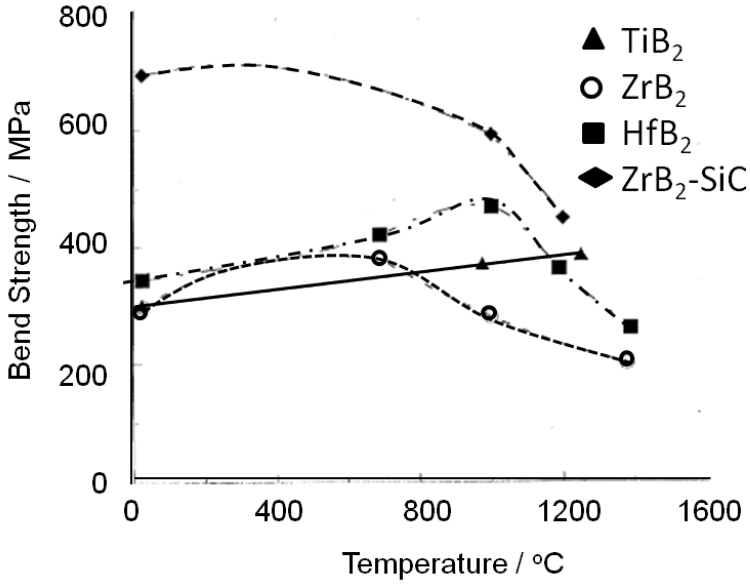

Figure 2.6: Bend strength of borides in inert atmosphere [8]

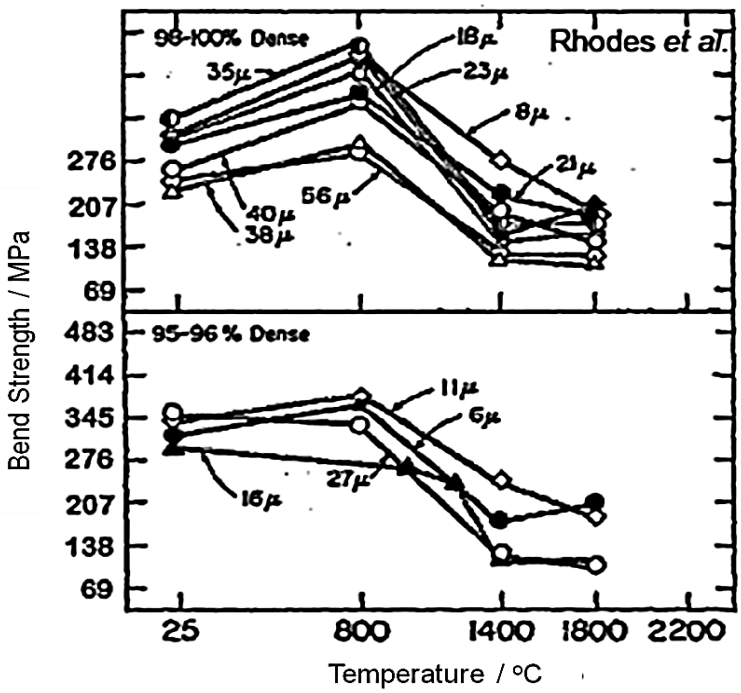

Figure 2.7: Bend strength for ZrB_2 ceramics with various grain sizes [78]

Rhodes et al. [79] measured the bend strength of ZrB_2 pellets with varying densities and grain sizes, Figure 2.7. In all cases the strength decreased with an increase in the grain size due to grain boundary strengthening.

Clougherty et al. [80] built a unique furnace to measure the thermal properties of ZrB_2. They measured the thermal conductivity from 100^{o}C to 1000^{o}C by the comparative cut bar method (ASTM E1225 Test Method), wherein heat flux is passed through a known sample and an unknown sample and the respective thermal gradients, which will be inversely proportional to their thermal conductivities, are compared. Generally, the unknown sample is sandwiched between two known samples, the references, to further account for minor heat losses that are difficult to eliminate, Figure 2.8 [81].

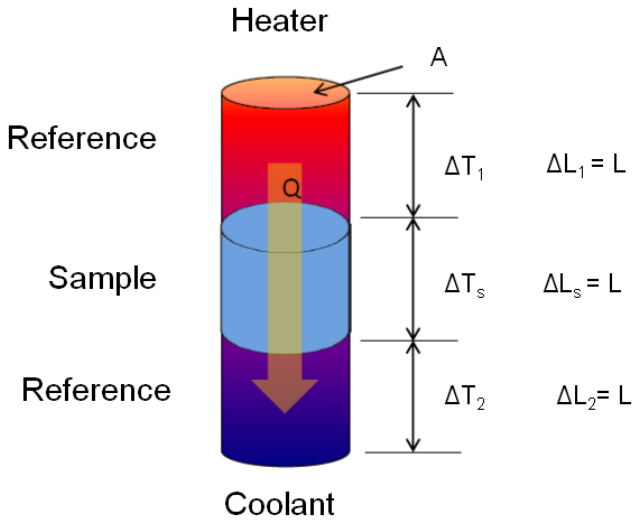

Figure 2.8: Cut bar method to measure thermal conductivity [80]

The thermal diffusivity was measured from 1000^{o}C to 2000^{o}C by using a laser flash (ASTM E1461-11 test method), i.e. passing an energy pulse that heats one side of a plane-parallel sample and detecting the temperature rise on the back side, which is time-dependent. The higher the thermal diffusivity of the sample, the faster the energy reaches the back side. Clougherty et al. [42] also measured the CTE, total emittance, heat capacity, entropy and enthalpy. Table 2.5 provides a list of references reporting high temperature thermal

conductivity values for ZrB_2, and Figure 2.9 gives the corresponding data. A broad range of values have been reported since 1970.

The thermal conductivity for a fully dense and pure material as reported by Tye et al. [82], should have a slope value equal to zero demonstrating the metallic nature i.e. thermal conductivity occurring through electron conduction. The highest conductivity values measured by Branscomb et al. [83] and Zhang et al. [84] had negative slopes indicating that the electron conduction was dominating the phonon conduction at high temperatures whilst the ones with the negative slope [85-88], indicating phonon conduction domination was due to low density or the presence impurities such as WC introduced through milling.

Table 2.5: Reported high temperature thermal conductivity values for ZrB_2 [84-87]

Reference	Year	Relative Density / %	Test Temperature / ^oC	Special Consideration
Tye and Clougherty [44]	1970	100	100-1000	-
Tye and Clougherty[44]	1970	90	100-1000	Fluid energy milled
Branscomb and Hunter[45]	1971	97.4	200-1300	0.92% impurity content
Zhang et al.[46]	2011	92.5	25-427	Reaction processed (Zr+B)
Fridlender et al.[47]	1980	92	1000-2200	Vibrogrinding (60 h)
Andrievskii et al.[48]	1980	95	100-900	-
Zimmermann et al.[49]	2008	100	25-1327	Attrition milled with WC
Thompson et al.[50]	2012	100	400-2000	Attrition milled with WC

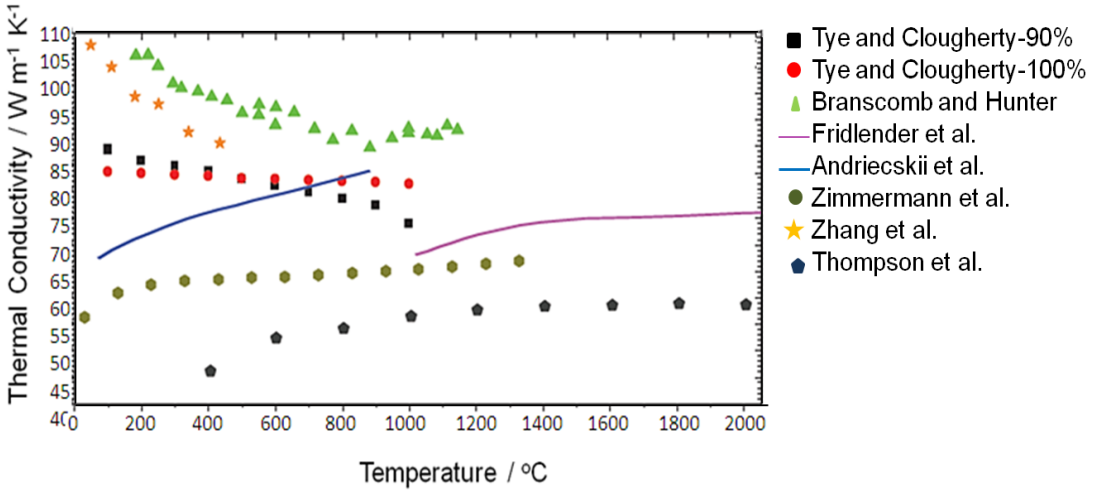

Figure 2.9: High temperature thermal conductivity values for ZrB_2 ceramics of different density [84-87]

iv. Oxidation mechanisms

A series of physical and chemical reactions occur during the oxidation of diborides that produce scales and glassy phases. The latter help prevent further oxygen diffusion and hence further oxidation. ZrB_2 and HfB_2 are thermodynamically unstable at temperatures above 600°C in the presence of oxygen and tend to form oxides as shown below:

$$ZrB_2\,(s) + \frac{5}{2}O_2(g) \rightarrow ZrO_2(s) + B_2O_3; \qquad \Delta G^0_{rxn} = -1977 + 0.361T\ (kJ) \tag{2.11}$$

$$HfB_2\,(s) + \frac{5}{2}O_2(g) \rightarrow HfO_2(s) + B_2O_3; \qquad \Delta G^0_{rxn} = -2003 + 0.374T\ (kJ) \tag{2.12}$$

According to TGA results the sample mass begins to increase in the temperature range 600 to 700°C, indicating the initiation of the oxidation reactions [89, 90]. Oxides like ZrO_2, HfO_2 and liquid boria (B_2O_3), the latter having a very low vapour pressure, are formed on the surface as a continuous protective layer composed of the porous metal oxide and liquid boria filling in

the pores, through which oxygen diffuses. At temperatures below 1100^{o}C, the oxidation rate is parabolic (passive oxidation) and is proportional to the oxygen partial pressure. Further increase in the temperature causes the boria to evaporate, disrupting the oxide scale and increasing the oxidation rate. At 1400^{o}C, only 10% of boria is left and any mass change in the TGA is directly proportional to the formation of metal oxides. Above 1400^{o}C, the liquid boria evaporates quickly as it is formed and the rate of oxidation increases as the oxygen permeation increases through the pores in the metal oxides. At even higher temperatures, the metal oxides, ZrO_2 and HfO_2 begin to evaporate reducing the scale thickness and the weight of the sample. A sharp increase in oxidation rate, observed around 1130^{o}C for ZrB_2 and 1730^{o}C for HfB_2, is called an “abrupt transition” [91]. This occurs due to the phase transitions of the metal oxides from monoclinic to tetragonal. It causes volumetric grain shrinkage, leading to the enlargement of pores and creating additional porosity. HfO_2 having the higher phase transition temperature, is more oxidation resistant than ZrO_2. Above 1800^{o}C, the oxidation also takes place via oxygen ion permeation through the metal oxide, thus further increasing the oxidation and recession rates [92]. Figure 2.10 schematically represents the oxidation process of ZrB_2.

Kaufman et al. [93] reported that HfB_2 pellets made from powder having a B/Hf ratio of 1.88 exhibited a parabolic rate constant which was 50 times smaller than for HfB_2 prepared from a powder having a B/Hf ratio of 2.12. Moreover, it was shown that hafnium additions to the B/Hf = 2.12 powder in quantities sufficient to reduce the B/Hf ratio to 1.70 reduced the rate constant to a level comparable with the B/Hf = 1.88 powder. Similarly, in the case of ZrB_2 at 1627^{o}C it was found that the rate constant for ‘B/Zr = 1.89’ was ten times smaller than ‘B/Zr = 2.1’. Their work indicated that the rate constants for HfB_2 were approximately one order of magnitude lower than for ZrB_2, which in turn was five to ten times better than that for TiB_2 and TaB_2. Usually, the oxidation mechanism is studied using a TGA or a furnace under isothermal will be a large temperature

gradient between the surface and the core of the sample due to surface heating. At higher temperatures, though the protective boria scale evaporates from the top surface, the temperature gradient helps to retain this scale within the sample, thus reducing the oxidation rate to 10% at 2200^{o}C [94, 95].

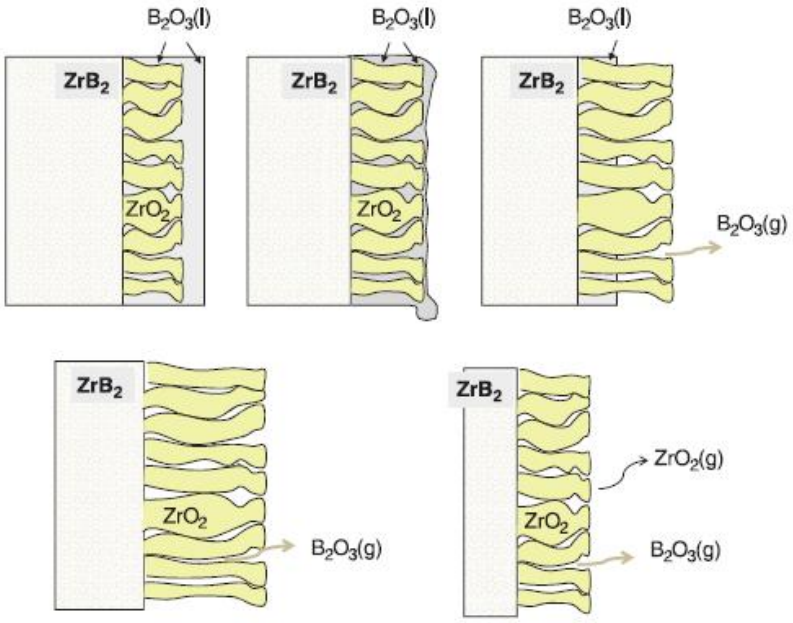

Figure 2.10: Schematic representations of ZrB_2 oxidation products and morphology [91]

Although the monolithic ceramics like zirconium and hafnium diborides and carbides have better intrinsic oxidation resistance compared to other group IV and V carbides and borides, they require high sintering temperatures and have low thermal shock resistance that limits their performance. Thus intensive research has turned to UHTC based composites since last 20 years.

2.2.2 UHTC Composites

2.2.2.1 Synthesis

In order to improve the sinterability and inhibit the grain growth, additives such as SiC can be added to the diboride. The additives, usually ceramic powders, when added over 10 wt% yield UHTC composites.

UHTC composites are usually made through solid state mixing of the different powders followed by densification. Homogenous mixing is usually achieved through milling. The critical part of the processing is densification and different routes have been investigated to optimize the fabrication procedures and the performance of these ceramics. The conventional method to sinter UHTCs is hot pressing [96-103] which is performed either with or without sintering additives. Extensive research has examined alternative processing routes for UHTCs, with an aim to reduce processing times, temperatures and cost. Pressure-less sintering [104-115], spark-plasma sintering (SPS) [116-121], self-propagating high-temperature synthesis (SHS) [122-127] and reactive hot pressing (RHP) [128-136] are other alternative routes that help reduce time and temperature involved in the densification process.

i. Hot pressing (HP)

Monteverde et al. [137] showed that ZrB_2 with 10 vol% ultra-fine SiC (d_{90} = 0.8 µm) on HP at 1900°C and 40 MPa for 20 min *in vacuo* yielded full density. The attrition-milled ZrB_2–30 vol% SiC mixture powders ($d \approx 0.5$ µm) could be HPed at 1900°C to a relative density exceeding 97%. The HP temperature significantly decreased to 1650°C, (pressed for 120 min at 60 MPa) [138], upon addition of 22.4 vol% SiC, with average particles sizes ranging from ~40 nm to 0.6 µm, due to the formation of inter-granular liquid phases during hot-pressing, which in turn assisted in densification at lower temperatures [102,137]. Addition of polycarbosilane (PCS), a precursor to SiC, instead of SiC to ZrB_2 allowed lowering of the hot-pressing temperature to 1800°C (pressed for 60 min at 20 MPa) and resulted in a fully dense ceramic, as opposed to only 78% dense ceramic without any addition, i.e. pure ZrB_2 powder [100].

Nitrides are other potential additives for improving the sinterability of ZrB_2. The nitrides with their unique property of consuming the oxygen-bearing species from the surface of the diboride powder, actually increases the boron activity thus favouring lattice diffusion and, consequently, densification [139]. The

addition of ≥2.5 wt% Si_3N_4 results in almost fully dense ZrB_2 (RD: 98%) after compaction at 1700°C [140] and fully dense HfB_2 at 1900°C [141].

Transition metal disilicides are other alternative and effective sintering additive as they not only enhance sinterability but also improve the oxidation resistance of the diborides. In the early 1970s, Kinoshita et al. [101], investigated the densification behaviour of ZrB_2- $MoSi_2$ composites. They achieved a 95% dense ZrB_2 with ≥ 20 vol% $MoSi_2$. The ZrB_2 powder had a particle size of 20 µm whilst that of the $MoSi_2$ powder was 5 µm. Later studies showed that the finer the particle size of the starting powders, the lower was the sintering temperature [103, 142, 143]. Guo et al. [144] found that an addition of 10 to 40 vol% $ZrSi_2$ could further lower the densification temperature of ZrB_2 to 1550°C. Furthermore, a fully dense ZrB_2–$ZrSi_2$ composite with a fine and homogeneous microstructure was obtained, using a two step HP process, which consisted of a first stage at 1400°C for 30 min and a second stage at 1550°C for 15 min at a pressure of 30 MPa. Thus, disilicides of the transition metals are potential additives for lowering the sintering temperature of ZrB_2-based ceramics.

ii. Pressureless sintering (PS)

Diborides usually require high pressure for densification and it was not until the late 1980's that pressureless sintering seemed promising to densify them. Unlike HP, PS also enabled densification of complex shapes using standard powder processing routes. Various additives that have been used to improve densification of diborides, can be divided into main two groups, viz. liquid phase formers and reactive agents. The former is a group of refractory metals, such as Ni, Fe, Co, and Mo [145-147], and disilicides of transition metals, such as $MoSi_2$ [148] and $ZrSi_2$ [112] that form liquid phase at sintering temperatures thus enabling densification of diborides by improving diffusion. Cech et al. [145] used Ni, Co, Fe and Re to produce nearly fully dense ZrB_2 at 2000°C *in vacuo* and 2200°C in an argon atmosphere. They reported that a minimum of 2 wt% of metals was required for continuous formation of liquid phase and to

bring about adequate sintering. The additions were found to be more efficient to produce adequate sintering in an argon atmosphere than in vacuum as the latter favoured volatilization and hence loss of metals. Kislui et al. [146] studied the effect of addition of Mo on the sinterability of ZrB_2 whilst Yan et al. [149] studied its effect on the sinterability of ZrB_2–20 wt% SiC. Addition of 20 vol% $MoSi_2$ produced the almost fully dense ZrB_2 at 1850°C for 30 min without external pressure [150, 151]. It was found that the densification temperature could be further reduced to 1650°C with the addition of ≥20 vol% $ZrSi_2$ [152].

In contrast to the liquid phase formers, reactive agents improve the densification of the diborides by reacting with and removing the oxide impurities (such as ZrO_2 and B_2O_3), from the surface, which inhibit their densification. The main reactive agents include B_4C [104,110], C [153, 154], and/or WC [155, 156]. Attrition milled ZrB_2 and 4 wt% B_4C on pressureless sintering at 1850°C for 60 min in vacuum yielded nearly fully dense ceramics [150]. On the other hand replacing 4 wt% B_4C with 4 wt% WC, resulted in only 95% relative density even after 240 min at 2050°C. Chamberlain et al. [99] achieved fully dense ZrB_2 with WC (~2 vol%) after 180 mins. at 2150°C. They reported that the elimination of oxide impurities from the ZrB_2 particle surfaces with B_4C or WC, was the key to densification.

iii. Reactive hot pressing (RHP)

The use of metallic and ceramic additives during HP, has been reported to reduce the densification temperature and also inhibit grain growth in diboride ceramics. However, the softening of inter-granular amorphous phase at temperatures above 1200°C caused a drastic reduction in strength, as reported for ZrB_2-based composites with SiC additions [130-135, 157-160]. Table 2.6 summarizes RHP sintering conditions, precursors, grain size and final density of the fabricated ceramics.

Table 2.6: Reactive hot-pressing conditions, precursors, grain size and final density of ZrB_2 or HfB_2 based composites fabricated by a RHP method [31]

Materials	Precursors	Remarks	HP or SPS Processing Conditions	Final density / %	Grain Size / µm	
					ZrB_2	SiC
ZrB_2-SiC	Zr, Si, B_4C	Ball-milled	1900°C/60 min/ 30 MPa/ Ar (HP)	96.7	3-10	<3
ZrB_2-SiC-ZrC	Zr, Si, B_4C	None	1800°C/60 min/ 20 MPa/ Ar (HP)	96.8	-	-
ZrB_2-SiC	Zr, Si, B_4C	Ball-milled	1450°C/3 min/30 MPa/ vacuum (SPS)	~98.5	<5	<1
ZrB_2-SiC	Zr, Si, B_4C	Ball-milled	1890°C/10 min/30 MPa/ vacuum (HP)	100	2	1
HfB_2-SiC	Hf, Si, B_4C	Ball-milled	1900°C/60 min/50 MPa/ vacuum (HP)	100	3	1

Zhang et al. [141] used RHP to fabricate ZrB_2-SiC composites by reacting Zr, Si and B_4C at 1800^{o}C, equation 2.13.

$$2Zr + Si + B_4C \rightarrow 2ZrB_2 + SiC \quad (2.13)$$

A relative density (RD) of ~98% was obtained when Zr, B and B_4C powder mixtures were reactive hot pressed at 1900°C with 30 MPa pressure for 60 min. Later, Wu et al. [132] successfully consolidated ZrB_2–SiC–ZrC composites (RD: ~97%) by RHP of Zr, Si and B_4C powders at 1800^{o}C and 20 MPa pressure for 60 min in an argon atmosphere. In addition, Zimmermann et al. [161] found that excess B_4C and Si were required in the ZrH_2–B_4C–Si system to obtain ZrB_2–SiC composites without oxide impurity and also to avoid grain coarsening during sintering. They reported the synthesis of ZrB_2-27 vol% SiC in the presence of excess B_4C and Si. The resultant ceramic had an average ZrB_2 grain size of ~2 µm and a SiC particle size of ~1 µm. Similarly, RHP has also been used to produce HfB_2-based composites. Monteverde [58] obtained a fully sintered HfB_2–22 vol% SiC–6 vol% HfC at 1900^{o}C and 50 MPa for 60 min from Hf, B_4C and Si powders.

iv. Spark plasma sintering (SPS)

SPS is one of the most recent advanced processing techniques developed for producing dense ceramic bodies [162-165]. SPS is similar to HP in that densification occurs through applied heat and pressure, except that in SPS the heating is indirect through applied electrical fields. The applied direct or pulsed current causes very fast heating and cooling, this in turn restricts grain growth. Previous investigations on SPS compaction of oxide, nitride, and carbide ceramics have shown that the sintering time, heating rate and sintering temperature are critical for maintaining a balance between grain size and density; in particular, the sintering temperature dictates the microstructure [166-168].

Recent studies have shown that SPS enhanced the densification and refined the microstructures of ZrB_2-based ceramics, using very short processing cycles. Medri et al. [169] reported the synthesis of 60 ZrB_2–30 ZrC–10 SiC (vol%) composite with RD of ~96% using SPS at 2100°C and 30 MPa for 2 min. Grain size measurement indicated that the grain growth (maximum grain size: ~3 μm) was inhibited during SPS. Various ZrB_2–ZrC–SiC composites have been reported to have been sintered to full density with fine and homogeneous microstructure at 1950°C and 30 MPa for 2 min, using SPS[118]. This difference in the sintering temperature attributed to the starting powder size and SPS conditions. Minor difference like extending the soaking time by 2 min, e.g. from 3 min to 5 min, can produce fully dense ZrB_2–ZrC–SiC composites at 1900°C instead of 1950°C [170]. To further reduce the sintering temperature of this composite 5 wt% AlN was added, which resulted in complete densification at 1850°C and 30 MPa for 5 min. However, addition of 5 wt% Si_3N_4 did not have the same effect as the AlN on the ZrB_2–ZrC–SiC system. Guo et al. [170] hypothesized that the AlN addition might have lowered the onset temperature of densification and increased the shrinkage rate. They also reported the dependence of percentage densification and grain growth of ZrB_2 ceramics on the SPS sintering temperature and holding time.

SPS has been used for fabricating dense HfB_2–SiC [171], TiB_2–WB_2–CrB_2 [172], HfB_2–$MoSi_2$ [173], and HfC and HfB_2-based composites with $MoSi_2$ additives [174, 175]. The enhanced densification in SPS was due to the significant increase in mass transfer processes, which in turn promoted effective densification. How the electric field increased the mass transfer process is still subject to debate. It is believed that it is most probably due to

(i) the high applied pressure;

(ii) an efficient heat transfer through graphite dies;

(iii) the presence of an electrical field (use of DC pulses); and

(iv) the generation of local spark discharges within the powder mixtures under high-energy electrical pulses.

2.2.2.2 Thermal and Mechanical Properties

The proportion of ceramic additives and their grain sizes, play a crucial role in the thermal and mechanical properties UHTC materials. The presence of additives decreases the grain size of the UHTCs, thus increasing some of their room temperature mechanical properties, like flexural strength and thermal shock resistance. So the mechanical properties can further be tailored by altering the particle size of the additives [36].

Rhodes et al. [79] tested the bend strength of HfB_2 with varying SiC and C content, up to 1800^{o}C, Figure 2.12. His study showed that:

i. SiC addition increased the strength by reducing the grain growth;
ii. Despite having a small grain size any porosity in the sintered body only reduced the strength; and
iii. Carbon addition improved resistance to crack propagation and reduced elastic modulus, i.e. making the material less brittle.

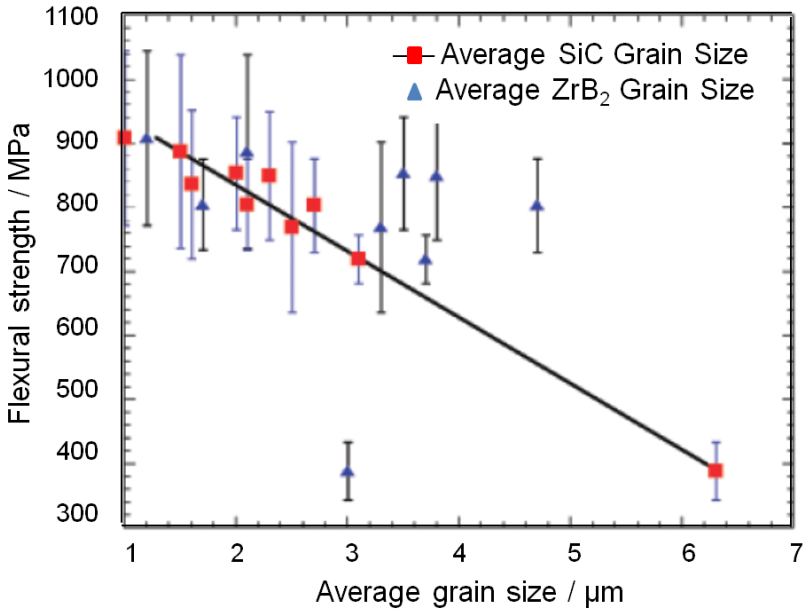

Figure 2.11: Flexure strength as a function of the average ZrB_2 grain and SiC particulate size in ZrB_2–30 vol% SiC ceramics [36]

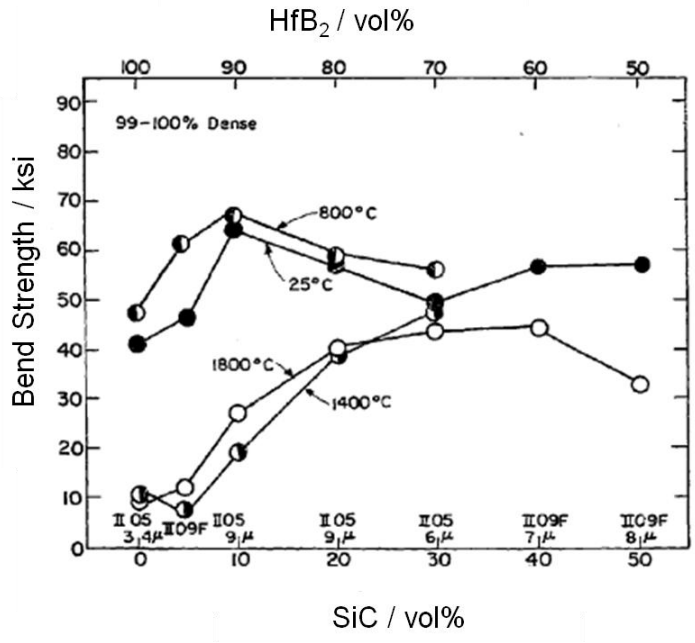

*50 ksi = 350 MPa

Figure 2.12: High temperature bend strength of HfB_2-SiC composite [78]

2.2.2.3 Oxidation behaviour

Many studies have been written on improving the oxidation resistance of ZrB_2 and HfB_2 based composites, with the addition of 20-30 vol% SiC [176-181]. Compared to B_2O_3, liquid borosilicate (BS) glass, which is formed when MB_2-SiC composite oxidises (M: Hf or Zr), has a higher melting temperature, better but still low viscosity, and lower oxygen diffusivity, thus providing more effective oxidation protection up to 1500^{o}C [182]. To further improve the oxidation resistance of ZrB_2-SiC composite, transition metal borides such as CrB_2, TiB_2, TaB_2, NbB_2 and VB_2, have been added [183]. Any improvement in the oxidation resistance was attributed to the presence of transition metal oxides in the borosilicate glass, which induced phase separation (immiscibility) leading to increased liquidus temperatures and viscosities, and subsequently decreasing oxygen diffusivity and suppressing boria evaporation from the glass [184].

The effect of different silicides addition on the oxidation behaviour of ZrB_2, has been discussed by Talmy et al. [185], whilst Opila et al. [186] reported that the enhanced oxidation resistance of ZrB_2-20 vol% SiC upon addition of 20 vol% $TaSi_2$ at 1627°C in air, was due to the presence of Ta and not due to the increased Si content arising from the additional Si-containing component. In general, the oxidation kinetics of non-oxide ceramics are dictated largely by the physical and chemical processes taking place on the surface exposed to the oxidising environment, and the chemical composition and properties of the oxidation products formed on the surface [187]. Modification of the chemical composition of the oxidised layer can lead to alteration of the diffusion rate of oxygen, which in turn alters the oxidation resistance. Zhang et al. [188] reported liquid phase sintering (LPS) at 2050°C for 4 h, when WC was added to SiC-reinforced ZrB_2 composites, which lead to the formation of a two layer dense, protective, oxide scale; the outer layer comprising ZrO_2, B_2O_3 and WO_3 and the inner layer ZrO_2 and WO_3.

The addition of Si containing additives improved the oxidation resistance and mechanical properties of the composite, only in the temperature regime up to 1800^{o}C. SiC oxidizes to form a SiO_2 scale that protected the composites until they decompose at 1800^{o}C, above which it left the structure porous and prone to oxidation. Thus SiC is not suitable for ultra-high temperature oxidation protection [189].

The oxidation behaviour of HfC-TaC and HfC-PrC_2 between 1200 to 2200^{o}C, was reported by Courtright [190]. Below 1800^{o}C, the scale structure of HfC-TaC was the same as monolithic HfC; above 1800^{o}C, the scale was composed of $Ta_2Hf_6O_{19}$ in addition to HfO_2 and the oxidation rate was parabolic. Neither the TaC nor the PrC_2 improved the oxidation resistance of HfC [190]. Further studies on the oxidation behaviour and mechanical performance at ultra high temperatures over 2000^{o}C, are still required for better understanding. The critical thermal shock temperature of ZrB_2 - 30 vol% SiC cells, increased from 1000^{o}C to 1400^{o}C when 85% graphite was introduced at the cell boundary [191].

Even though these UHTC composites are chemically stable at high temperatures, they require fibre reinforcement to improve damage tolerance, (fracture toughness), and high temperature strength. An obvious choice is to use high strength carbon fibres as they can be readily formed into a construct or preform of desired configuration by winding, weaving, knitting, braiding or wrapping over a suitably formed mandrel [192].

2.3 Carbon-based UHTC composites

Carbon-carbon (C-C) composites possess a distinct combination of desirable properties, such as resistance to extreme thermal shock, very low coefficient of thermal expansion, high strength to weight ratio, as well as excellent strength retention and creep resistance over a wide temperature range. Table 2.7 compares the properties of C-C composite to two metallic alloys [193].

Table 2.7: Range of properties for carbon-carbon composites compared to two metallic alloys [75]

Property	Carbon-carbon	Ferritic steel	Titanium alloys
Compressive strength / MPa	100 to 150	240 to 400	130 to 1400
Density / g cm^{-3}	1.3 to 2.5	7.5 to 7.7	4.38 to 4.82
Tensile strength / MPa	Up to 900	500 to 800	241 to 1280
Thermal expansion / K^{-1}	-2 to +2 * 10^{-6}	12 to 5 * 10^{-6}	7.9 to 9.8 *10^{-6}
Thermal conductivity / Wm^{-1} K^{-1}	20 to 150	23 to 27	4 to 21.9
Thermal shock resistance / Wmm^{-1}	150 to 170	5.5	N/A
Young's modulus / GPa	Up to 300	200 to 205	95 to 125

As shown in Figure 2.13, C-C composite exhibits the highest specific strength when compared to several metallic alloys and ceramic matrix composites from room temperature to over 2000^{o}C [46].

Despite the above mentioned properties, the use of C-C composite as high temperature structural materials is very limited because of their extremely poor ablation resistance, especially above 350^{o}C. This raises a need to develop reliable oxidation protection in order to be able to utilize the full potential of C-C composites.

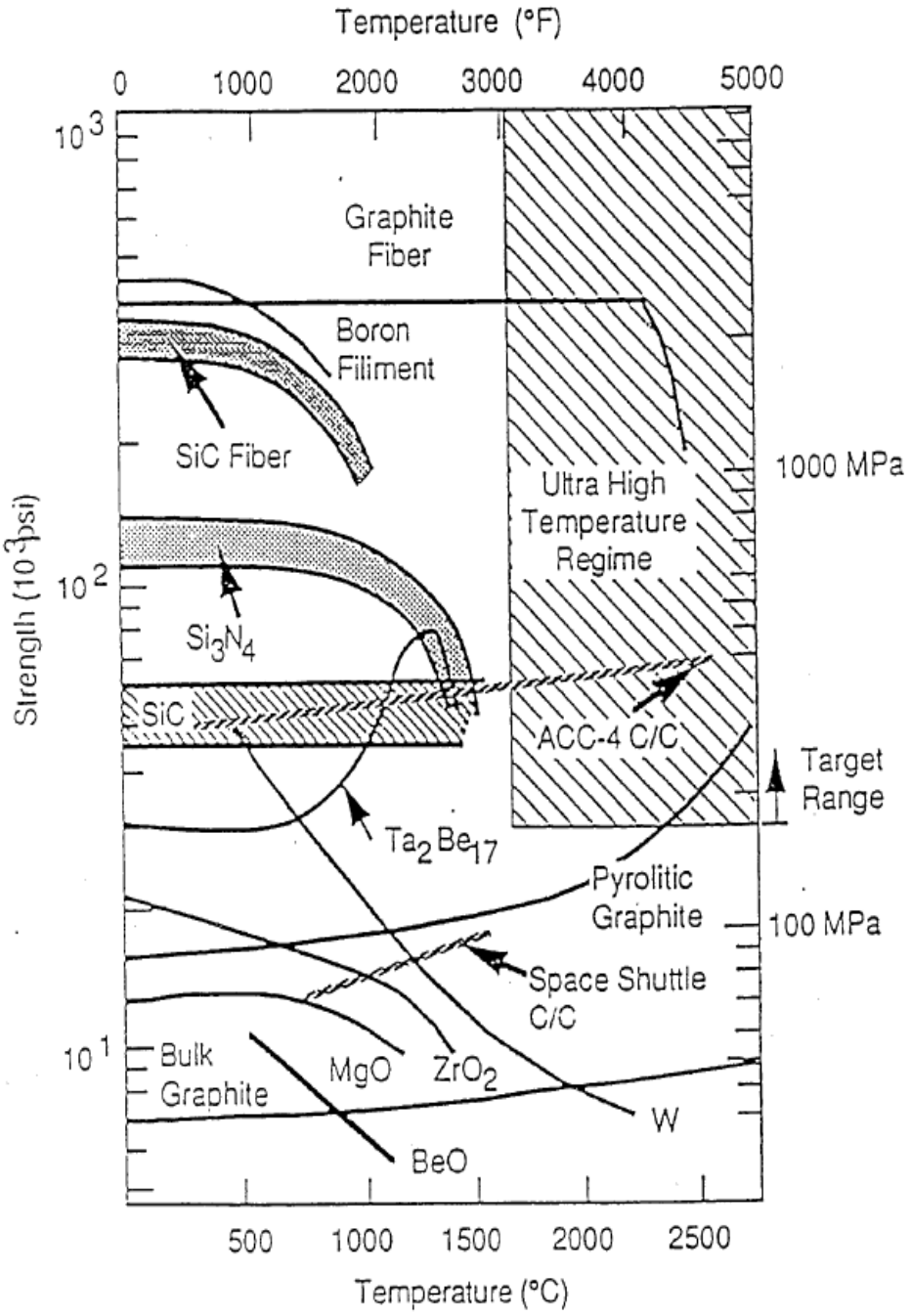

Figure 2.13: Strength of C-C composites compared to other high temperature materials [44].

2.3.1 Fabrication of carbon based UHTC composites

Coatings based on metal carbides and metal oxides, coupled with internal inhibitors, are currently being used to provide reasonable oxidation resistance up to 1600^{o}C [46]. However, the currently available coating systems have not

proven adequate at temperatures over 1700°C. Strife et al. [194] proposed that a potential high temperature oxidation protection system would involve a multi-layer coating system, consisting of a refractory carbide inner layer around the carbon fibre as a carbon diffusion barrier, a silica glass layer sandwiched between two refractory oxide layers, i.e. the outer most refractory oxide layer for erosion protection and the inner layer as an isolation from carbon surface, whilst the silica glass layer would act as an oxygen diffusion barrier and crack sealant. Although the multi-layer coating possesses the necessary chemical stability, depositing a coating of this nature is certainly a problem especially given the high thermal expansion coefficient of the coating relative to C-C composites, which will result in severe mechanical compatibility problems with thermal shock. It is clear that basic research is needed to identify new materials and material combinations for long term oxidation protection at very high temperatures. These UHTCs can be introduced into a carbon preform in several different ways, of which a few that are related to this project, are discussed in this section.

2.3.1.1 Solution Infiltration

In this method either a precursor solution or a sol is infiltrated into the carbon preform and the precursor is later converted into its respective ceramic by in-situ reactions. Zirconium oxychloride octahydrate ($ZrOCl_2.8H_2O$) has been used as a precursor for zirconium [195]. The pores in the carbon preform were evacuated under vacuum and an aqueous solution of the $ZrOCl_2.8H_2O$ precursor was infiltrated into the carbon preform by capillary action. The latter was dried at 150^oC in an oven. After complete drying the preform was placed in an electric furnace maintained at 600ºC under a nitrogen atmosphere for an hour where the precursor decomposed and formed ZrO_2. The densities of the resulting preforms were then increased through a thermal gradient chemical vapour infiltration (TCVI) process, after which the composites were graphitized at 2500^oC where the ZrO_2 reacted with the deposited carbon to form ZrC.

$$ZrO_2\,(s) + C(s) \rightarrow ZrC(s) + 2CO(g) \qquad (2.14)$$

The schematic preparation procedure for ZrC impregnated C/C composites made by solution infiltration, is shown in Figure 2.14.

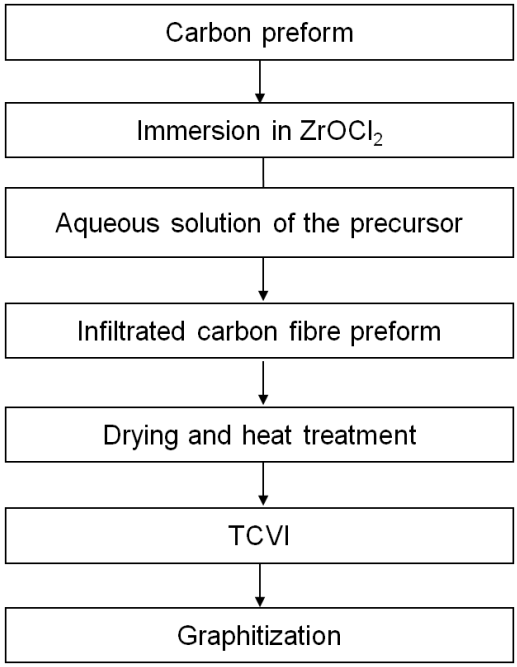

Figure 2.14: Schematic preparation procedures of ZrC doped C/C composites [194]

2.3.1.2 Chemical vapour infiltration/deposition (CVI/CVD)

This is a familiar technique to prepare coatings of refractory carbides, far below their melting point. Adhesion and stability, which are the fundamental prerequisites for protective coatings for high temperature applications, are also offered by this method. The process relies on infiltrating a gaseous species into the preform at a temperature where the gas subsequently decomposes to yield an in-situ matrix. However, one of the critical problems of CVI is the stress generation between the layers, while cooling from the deposition temperature to room temperature. The stress is caused due to the mismatch in the coefficient of thermal expansion between the deposited material and the carbon preform. Therefore, a multi-component layer system with as small as

possible CTE mismatch between the layers is usually used, to minimize stress and to achieve effective oxidation protection [196].

Before the CVI process the carbon preforms are pre-heated at 1600^{o}C for 4 h under vacuum, to modify the adhesion between the composite and the material to be deposited. The heat treatment partially removes the surface chemical groups, including any amorphous carbon, and cleans the carbon fibre surfaces by defunctionalizing them, thus enhancing their crystallinity. This resulting surface is uniform, with a higher degree of graphitization, which will allow better wetting and infiltration of the chemical species. The graphitization results in more ordered and tightly packed fibres that create larger void spaces between them, giving rise to larger channels for UHTC precursor infiltration [197].

Hafnium carbide can be infiltrated into a carbon fibre preform using the reaction between hafnium (IV) - chloride and methane gas, which occurs between 850^{o}C and 1025^{o}C under reduced pressure (15 kPa) and a hydrogen atmosphere.

$$HfCl_4 + CH_4 \rightarrow HfC + 4HCl + H_2 \quad (2.15)$$

Hafnium (IV) - chloride deposits can be formed either in-situ as a result of the reaction between hafnium powders and HCl at 450^{o}C under reduced pressure, or by the sublimation of $HfCl_4$ powders.

$$Hf + 4HCl \rightarrow HfCl_4 + 2H_2 \quad (2.16)$$

In-situ chlorination of the hafnium powders is found to increase the deposition of $HfCl_4$ by 30 times, than when sublimation of $HfCl_4$ powders is used [198]. This deposit is then reacted with methane gas to form HfC.

Deposition of SiC on carbon preforms can be carried out by using an isothermal CVI method [199]. Several precursors like hexamethyldisilane [200] and methyltrichlorosilane (CH_4SiCl_3) [199] can be used for CVI synthesis of SiC. Hydrogen is usually used as the carrier gas. The hydrogen is passed over

an evaporator containing the liquid precursor, which is carried as vapour into a reactor containing the preform, where the thermal decomposition of precursor occurs resulting in SiC deposits within the preform. The molar ratio of H_2/precursor has been found to affect the SiC deposition. Whilst a large molar ratio, caused the SiC to hinder the thermal decomposition of the methyl groups to free carbon resulting in a coating with high free silicon content, a lower molar ratio and/or very high deposition temperature favoured carbon deposition and resulting in an SiC coating with high carbon content [200].

2.3.1.3 Self propagating high temperature synthesis (SHS)

Self-propagating high temperature synthesis is an approach in which the thermal energy from an exothermic reaction is used to initiate a different endothermic reaction, as described in section 2.2.1.3. In order to initiate the reaction between silicon and a graphite block, to form a silicon carbide coating on the graphite, Ohyanagi et.al. [201] utilized the energy from a strong exothermic reaction between titanium (Ti) and carbon. The experimental set-up used by them is shown in Figure 2.15. An electric current passed through a carbon ribbon ignited a pellet of titanium and carbon mixed powders, which generated 2700^{o}C. This was sufficient to initiate the reaction between the Si and the graphite.

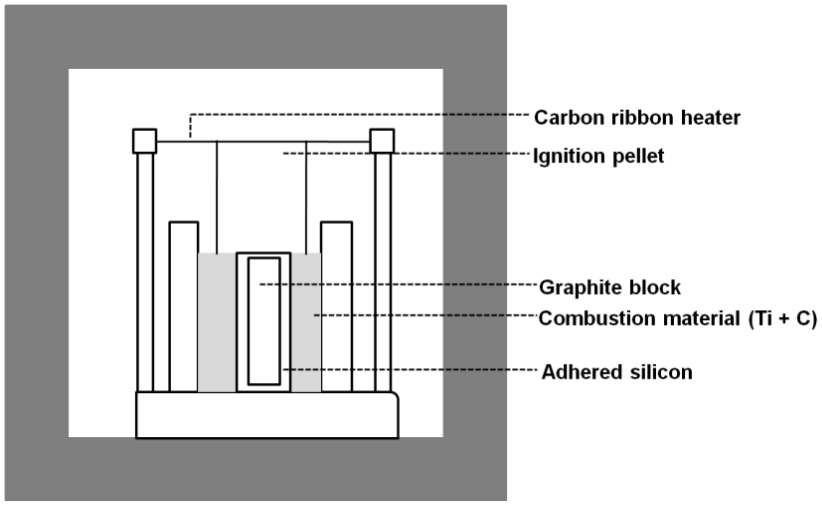

Figure 2.15: Schematic diagram for the formation of SiC coating on a graphite block using SHS [200]

2.3.1.4 Electrophoretic deposition/infiltration (EPD/EPI)

EPD is a method that involves deposition of charged particles from an electrolyte suspension on to an electrode [202]. A schematic of this method is shown in Figure 2.16. The desired particles are suspended in a suitable liquid medium with the help of surfactants and two electrodes are immersed into the well dispersed suspension. On the application of a voltage across the electrodes, the charged particles migrate to one of the electrode surfaces where they are deposited. The thickness of the deposited layer can be controlled by adjusting the voltage across the electrodes and the time of deposition [202].

EPI is a related process that involves infiltration of charged particles into a fibrous preform that is positioned adjacent to the deposition electrode. The potential difference across the electrodes causes the charged particles to be pulled into the pores of the preform, where they become trapped. The rate of movement of the charged particles depends on the pH of the suspension and its ionic strength. The use of the EPI technique used to synthesize various UHTC-carbon composites is shown in table 2.8 [203, 204, 205].

Table 2.8: Parameters involved in EPI of SiC and TiC

Suspension	Medium	Surfactant	pH	Voltage / V	Time / mins	Reference
25 wt% SiC	Water	CTAB, TMAH, PEI	4-9	60	5	203
5 wt% SiC	Isoproponol	Iodine (I_2/SiC=10%)	-	210	15	204
50 wt% TiC	Alcohol	Nitromethane and 1% protein	-	100	-	205

CTAB: Cetyl trimethylammonium bromide

TMAH: Tetramethylammonium hydroxide

PEI: Polyethyleneimine

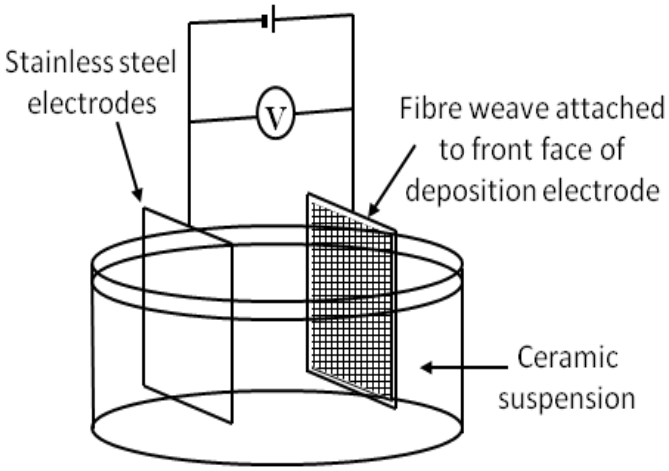

Figure 2.16: Schematic of electrophoretic infiltration equipment [201]

2.3.1.5 Slurry Infiltration

Tang et al. [206] infiltrated a range of UHTC powders including ZrB_2 (size 2.5 µm, purity >90.0%), SiC (7µm, >99.5%), HfC (<1.2µm, >99.9%), and TaC (<2.6 µm, >99.0%), as oxidation inhibitors into carbon preforms through a slurry infiltration route. Each of these powders was mixed with deionised water to form a slurry that was spread on the surface of the preform. On application of pressure, the slurry infiltrated through the preform and the powders in the slurry were trapped in the pores, whilst the excess water was squeezed out. The work involved using 2D carbon fibre preforms, mounted on filters within a die cavity and impregnating them with the powders to produce five different composites: C/C–ZrB_2, C/C–4ZrB_2–1SiC, C/C–1ZrB_2–2SiC, C/C–1ZrB_2–2SiC–2HfC and C/C–1ZrB_2–2SiC–2TaC (the numbers denote the volume ratios of the UHTC powders). After the infiltration process, the green composites were dried in an oven and were later densified using an ICVI (isothermal chemical vapour deposition) process at 1000 to 1100^{o}C. The UHTC powders were mainly concentrated in a layer from the surface to a depth of 2 mm. High temperature oxidation performance of the composites were evaluated using an oxyacetylene flame and the details are discussed in section 2.4.2.6. The C/C-ZrB_2 showed the best protection after 30 s at 3920 kW m^{-2} and 2700°C. The

addition of SiC was found to improve the oxidation resistance after 300 s but only at 2380 kW m^{-2} and 1800°C. Levine et al. [188] undertook one of the earliest studies of Cf-based composites for high temperature applications. The composites were prepared using Zoltek Panex® 30 carbon fabric, allylhydridopolycarbosilane preceramic polymer, HfB_2 powder and SiC powder. The composites formed had a gradient structure with one side rich in SiC and the other side rich in HfB_2 with Si-O-C preceramic polymer on both sides. Microcracks were present in the final composites. They also synthesized SiC fibre reinforced ZrB_2-20 vol% SiC composites (ZSS) through a filament winding and slurry impregnation technique followed by hot pressing.

Compounds of Hf, Zr and Th have also been impregnated into the surface of C/C composites for oxidation protection [46]. For example, powders of HfC, HfC/SiC, HfC/HfB_2, HfB_2, $HfTaB_2$ and Ir/Re have been evaluated to protect carbon-based materials for very short time periods at temperatures where SiC and SiN_4 cannot be used. Newman et al. [207] reported that the HfC-infiltrated C-C composites could survive exposure to 2760^{o}C in oxidizing flow for periods exceeding 10 minutes. HfC/TaC has also been infiltrated into a carbon fibre preform for rocket thruster applications [208]. Most recently Paul et al. [209] reported slurry impregnation of 5 different UHTC powders/compositions namely, ZrB_2, ZrB_2–20 vol% SiC (ZS20), ZrB_2–20 vol% SiC–10 vol%, LaB_6 (ZS20–1La), HfB_2 and HfC into the carbon preforms. The slurry composition consisted of UHTC powder (40 g), phenolic resin (20 g) and acetone (12.5 g). Two routes were used to impregnate the carbon preform with UHTC slurry, namely squeeze and vacuum impregnation. Squeeze impregnation involved fully immersing the carbon preform in a beaker containing the slurry with subsequent manual squeezing so as to get maximum amount of slurry inside the preforms whilst vacuum impregnation involved application of vacuum using rotary pump to suck the slurry inside the preform. The composites were also subjected to multiple pyrolysis cycles to remove maximum amount of volatiles and hence to increase the powder loading. Special attention was also given to avoiding the formation of any crust layer on the surface of the composite, by

wiping it with a tissue dipped in acetone. The differences in weight gain achieved after squeeze and vacuum impregnation are summarised in Table 2.9 and the changes in their weight after each processing step is shown in Figure 2.17.

Table 2.9: Comparison of weight increase after squeeze and vacuum impregnation [208]

Composite	Cf-HfB_2 Squeeze Impregnation	Cf-HfB_2 Off cut Vacuum Impregnation	Cf-HfC Squeeze Impregnation	Cf-HfC Off cut Vacuum Impregnation
% weight increase	250	540	370	620

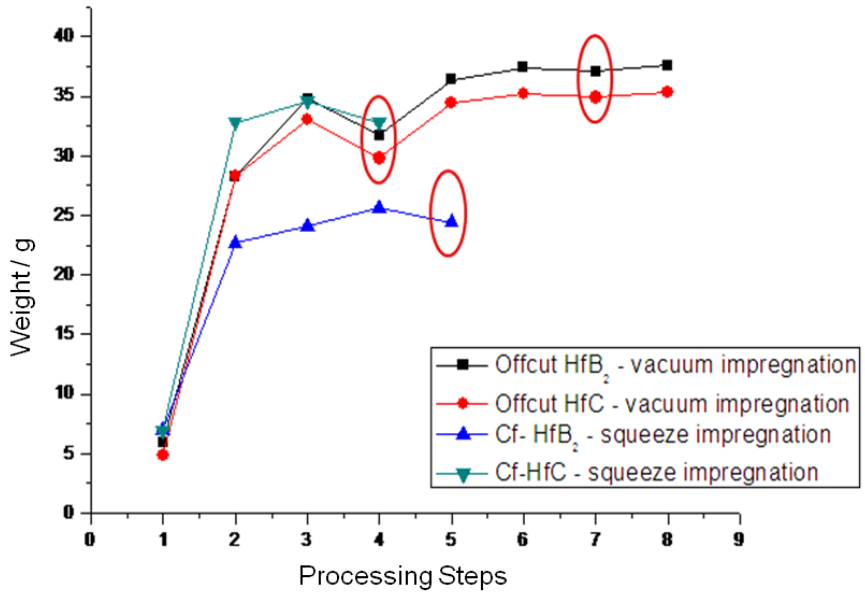

Figure 2.17: Weight change after different stages of processing during vacuum and squeeze impregnation. Pyrolysis steps are indicated with the ellipses [208]

It is to be noted that the weight increase achieved after vacuum impregnation was more than double of that achieved after squeeze impregnation for Cf-HfB_2 composite, and considerably higher in the case of Cf-HfC composite.

Oxyacetylene testing of these composites is discussed in section 2.4.2.6. Long term oxidation protection of carbon-based materials at very high temperature, remains a very challenging problem.

2.4 Evaluation of UHTC materials for high temperature applications

2.4.1 Mechanical properties

The flexural strength of carbon-UHTC composites can be determined using a three point bend test [210, 211] and the fracture toughness using the single edge notched beam test [210] similar to that used for monolithic ceramics. Results had shown that the flexural strength and fracture toughness of the composites increased with an increase in the carbon fibre content [211]. The presence of carbon fibres bridged the cracks and also deflected them. Since this consumes more energy than a crack propagating directly, it increased the fracture surface energy which in turn improved toughness.

Table 2.10: Effect of carbon fibre content on the properties of UHTC composites [209]

Composition / vol %	Elastic Modulas / GPa	Flexural strength / MPa
SiC-20%ZrB_2–36%Csf*	91±12	81±24
SiC-14%ZrB_2–39%Csf*	106 ±13	178 ±77

Csf*: Short carbon fibres

2.4.2 Oxidation tests

A large number of testing techniques are available for evaluating the high temperature oxidation performance of UHTC materials. These include static furnace oxidation testing, laser ablation testing, oxyacetylene torch testing, plasma wind tunnel testing, strip heater, arc jet testing and scramjet testing.

There is no one test method that can reproduce all the conditions experienced during hypersonic flight. Furnace oxidation testing and oxyacetylene torch testing are relatively cheap, less time consuming and require minimal sample preparation and can be used as screening tests. Arc jet is the only test whose testing conditions bear close resemblance to the real time re-entry conditions.

2.4.2.1 Furnace heating

This approach gives an idea of the oxidation resistance of carbon-based UHTC composites at low temperatures and in a static environment. It involves heating the composites in a disilicide furnace either in static air or under very low flow rates and then calculating the weight change, which is proportional to the oxidation rates [212]. The maximum temperature that can be attained using this test is typically around 1700^{o}C whilst the duration can be for as long as desired. Clearly such tests do little to simulate actual ultra-high temperature applications but they can yield important information on the mechanisms and stages underlying the oxidation process. Levine et al. [213] carried out furnace oxidation tests on their carbon composites with one side rich in SiC and the other rich in HfB_2 for 1, 5 or 10 ten minute cycles at 1617°C. They reported the formation of a non-uniform glassy layer consisting of SiO_2 on the SiC rich side and $HfSiO_4$ and monoclinic HfO_2 on the HfB_2 rich side. Attack on the Cf was found to be less on the UHTC side compared to the SiC side. They also studied the high temperature performance of SiC fibre reinforced ZrB_2-20 vol% SiC composites (ZSS) at temperatures up to 1927°C for a period of up to 100 min, and results were compared with ZrB_2-20 vol% SiC (ZS) and ZrB_2-14 vol% SiC-30 vol% carbon (ZSC) compositions containing no fibre reinforcement. At lower temperatures of 1327 and 1627°C, the ZS composite showed the best performance. At 1927°C all the compositions underwent severe degradation and bloating. The authors indicated the importance of thermal shock resistance of ZS and ZSC materials in high heat flux aero-convective environments, which might be encountered in propulsion applications, which was not considered in furnace oxidation tests.

2.4.2.2 Laser testing

Laser heating / melting has been used extensively to study UHTCs and other ceramics used at extreme temperatures including refractories and nuclear fuels [214, 215]. The approach offers several benefits over traditional methods, including rapid heating rates, and small sample size [216, 217]. The Institute for TransUranium Elements (ITU) in Karlsruhe, Germany, developed a technique with a 4.5 kW Nd:YAG laser for melting and a second low power Ar laser to detect oscillations from surface liquid to reveal the onset of melting for studying the oxidation behaviour of materials [218]. The laser facility at The Welding Institute (TWI), uses a 4 kW collimated (parallel sided) laser beam (CLB). A high brightness ytterbium (Yb) fibre laser beam generates heat flux of 44 MW m^{-2}, and enables testing temperatures as high as 4000°C. Another key feature of CLB testing is its speed, allowing over twenty specimens to be evaluated in a day. The heat flux/duration of each test can be adjusted easily to simulate a range of environments. The laser beam can be applied for one second or, potentially, an hour and the heat flux within that beam can be controllable to within a few watts. Micro-structural changes in the UHTC specimens (determined by post-test micro-structural characterization), along with in-test pyrometry can then be used to infer the maximum temperatures (±100°C) reached during testing. The depth to which UHTC specimens are oxidized during CLB testing can be measured during subsequent microstructural characterization. However, an immediate qualitative assessment of their high temperature oxidation resistance can usually be obtained by post-test visual inspection.

2.4.2.3 Arc-jet testing

Arc-jet testing represents the best ground based simulation of a re-entry environment. It provides the opportunity to explore the oxidation behaviour of UHTC materials under extreme conditions and help evaluate the materials response to large heat fluxes through the determination of two important parameters, emissivity and catalytic efficiency. High emissivity and low surface catalytic efficiency are desirable for hypervelocity applications in order to keep

the temperature gradients and thermal stresses in the structure to a minimum, and to enable the vehicle to operate under relatively high enthalpy flow conditions.

Arc jet testing is performed on machined flat face models, to evaluate the oxidation/ablation behaviour of the material. Figure 2.18 shows a schematic of the types of arc heaters in use at Ames Research Center. The arc heater produces a high temperature gas stream by combined radiative, conductive and convective heat transfer from a high voltage DC electric arc discharge to a gas flowing through a cooled column. The facilities at Ames are capable of input power levels of 20 to 60 MW for up to 30 min durations [219].

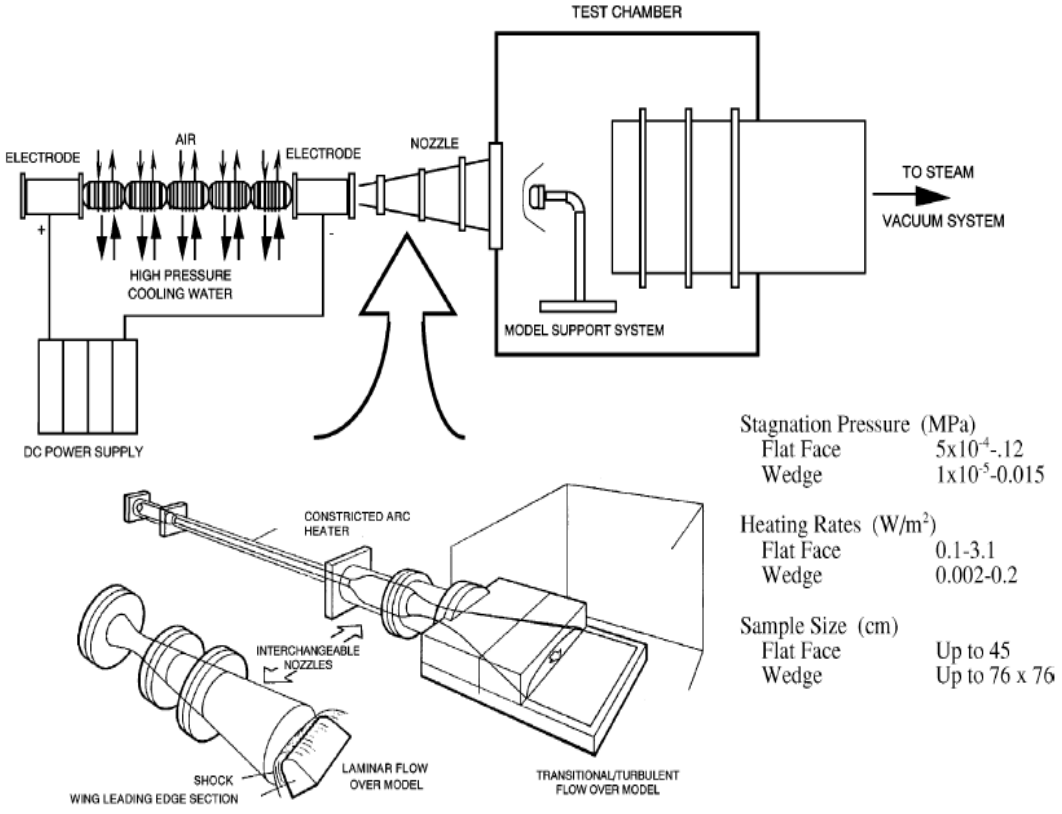

Figure 2.18: A schematic of arc-jet facility based in Ames Research Center, USA with illustrations of the different nozzle types for flow simulations [218]

Examples of various HfB_2 UHTC based models that have recently been tested at Ames are shown in Figure 2.19 a. A photograph of an as-machined flat face

arc-jet model is shown in Figure 2.19 b. The model is 25.4 mm in diameter and the overall height is 8 mm. Models were placed in SiC-coated graphite holders which enabled test durations in excess of 10 min; in comparison an uncoated graphite holder would have allowed only a few minutes of testing. A variety of instrumentation is used to calibrate the arc jet conditions and to measure the thermal response of the materials. Two 1-colour and one 2-colour optical pyrometers are used to make surface temperature measurements during the tests.

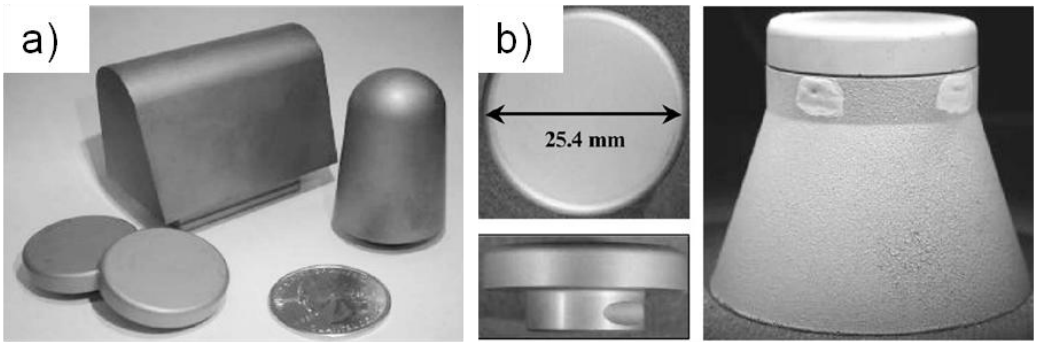

Figure 2.19: The family of arc jet models fabricated and tested at NASA Ames [218]

2.4.2.4 Plasma wind tunnel

A plasma wind tunnel is nothing but a wind tunnel that uses plasma to simulate aerodynamic heating. Monteverde et al. [220] used the Small Planetary Entry Simulator (SPES) – an arc-jet plasma wind tunnel to reproduce the thermal conditions of the re-entry. An 80 kW plasma torch that operates with inert gases (He, N_2, Ar and their mixtures) at mass flow rates up to 5 g s^{-1}, with a torch nozzle diameter of 11 mm was used to mimic mach 3 conditions. The UHTC sample was placed at a distance of 10 mm from the nozzle exit. The test chamber was equipped with portholes and windows for optical diagnostics. A two-colour pyrometer (Infrather ISQ5, Impac Electronic GmbH, Germany) was used to measure the sample surface temperature at an acquisition rate of 100 Hz. The pyrometer had a measuring spot of 3 mm, used two overlapping infrared wavelength bands at 0.8 to 1.1 and 1 to 1.1 μm and measured temperatures from 1300 to 3300 K with a 1% measurement

accuracy in the range 1720 to 3300 K. The two colour mode measured the surface temperature, whilst the single colour mode helped in determining the emissivity once the temperature is known. For conical and hemispherical samples the pyrometer pointed, respectively, at 50% and 80% of the radius distances from the tip. The plasma wind tunnel, when used in the supersonic flow regimes, feeds a non-equilibrium flow to the shock edge i.e. at the sample's location, thereby introducing some uncertainties in estimation of the actual gas chemical composition at the sample surface.

2.4.2.5 Strip heater

A desktop strip heater uses the fact that the UHTC materials are metallic conductors to resistively heat them to ultra high temperatures. The sample to be tested was fabricated by reducing the thickness at the centre to make a ribbon of about 4 to 5 mm thick, Figure 2.20. Current was passed through the thicker ends of the specimen thus heating up the ribbon resistively, and forming a hot zone. The hot zone would reach very high temperatures whilst the thicker ends of the specimen remained relatively cool. This geometry allowed the specimen to be self-supportive and isolated the hot zone from any foreign material thus preventing it to react with unwanted materials at the high temperatures. The specimen was in open air during testing and had a small heat load, thus enabling easy use of optical diagnostics during oxidation.

The control unit of the apparatus consists of a control panel and a programmable temperature controller. The power input used to heat the ribbon specimen to temperatures from 900 to 2000°C was around only 90 to 125 W, with the voltage across the specimen being of the order of 1 V and the current ranged from 90 to 125 A.

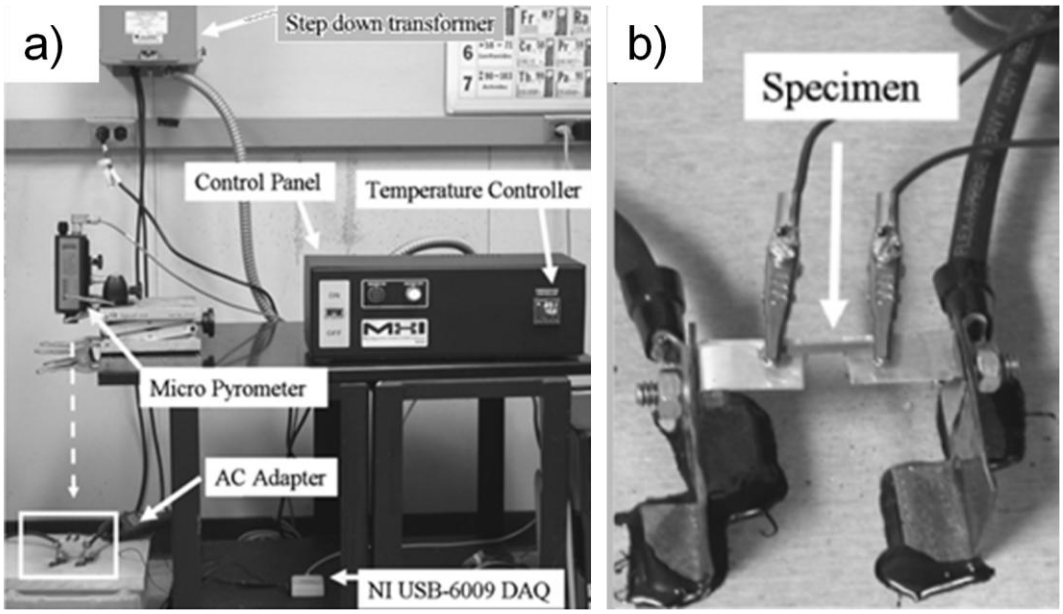

Figure 2.20: (a) The self-supported ribbon specimen (white box) and its table-top apparatus, and (b) the specimen sitting on a Cu/Ag holder (magnification of the white box in the lower left corner of (a)) [218]

2.4.2.6 Oxyacetylene testing / ablation property

An oxyacetylene flame can be used as a screening technique to characterise the high temperature performance of materials using a steady flow of hot gas, provided by an oxyacetylene burner. This technique is much cheaper compared to other techniques, such as arc jet testing and a plasma wind tunnel. ASTM standard E285-08 [221] describes the test method in detail. The general characteristics of a neutral oxyacetylene heat source are:

heat flux: 835 W cm^{-2} (cold-wall calorimeter)

velocity: 210 m s^{-1} (mach 0.62, cold unreacted gases)

An oxygen to acetylene volume flow ratio of 1.20 corresponds to a neutral flame. A schematic diagram of the gas system is shown in Figure 2.21.

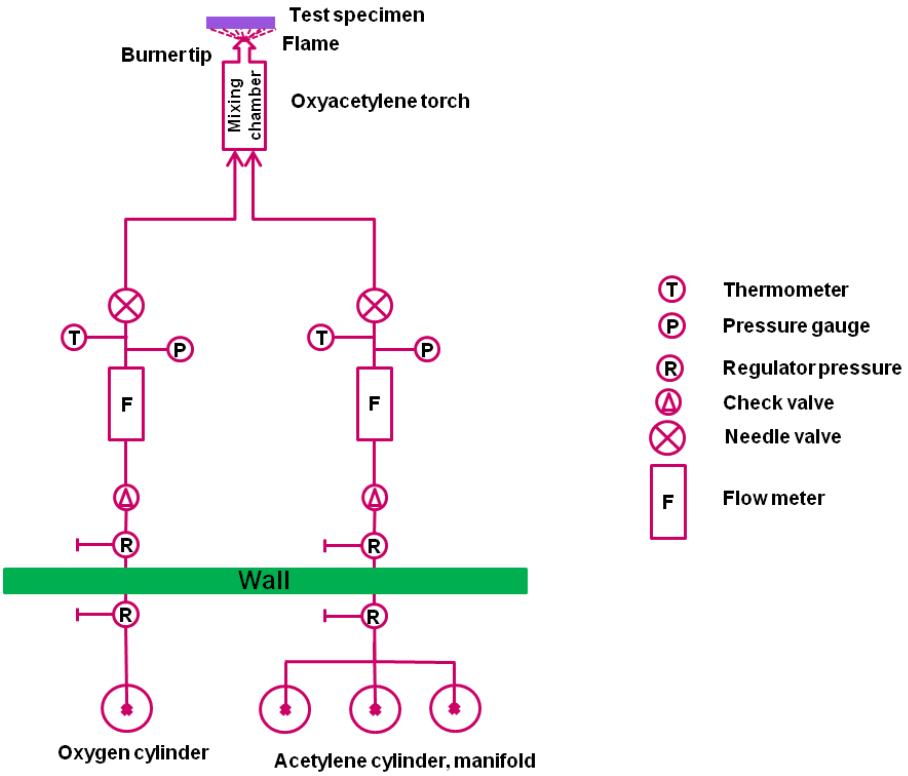

Figure 2.21: Schematic diagram of oxyacetylene torch test set up [220]

There are a number of reports in the literature about the use of this technique for the testing of monolithic and composite materials. NASA researchers used it to measure the performance of HfC-TaC coatings on graphite substrates intended for rocket thruster applications [222]. The O_2/C_2H_2 ratio was 4:1 and the test duration was 5 minutes. The reported temperatures measured using an optical pyrometer ranged from 1370 to 1650°C.

The oxidation performance of ZrC containing W matrix composites were compared with pure W and Cu/W using an oxyacetylene flame [223]. The technique has also been used to compare the high temperature ablation behaviour of W composites with the addition of ZrC and TiC [224]. Zhang et al. [225] used an oxyacetylene torch facility to compare the oxidation performance of ZrB_2-20 vol% SiC with ZrB_2-20 vol% SiC-10 vol% LaB_6 for up to 600 s. The gas flow rates were 1.15 $m^3\ h^{-1}$ and 2.30 $m^3\ h^{-1}$ respectively for oxygen and acetylene and the temperature was measured using a one colour pyrometer. The temperature increased to 2000°C within a short period of time

and then increased slowly to reach a peak value of ~2400°C. The authors reported that the oxidation performance increased with the addition of LaB_6. Han et al. [226] also reported the testing of ZrB_2-SiC using a similar technique, though the acetylene and oxygen flow rates were lower (0.95 and 1.90 m^3 h^{-1} respectively) and the peak temperature was only 2200°C.

Chen et al. [227] ablated 3D orthogonal C/SiC composites using an oxyacetylene flame and the surface temperature measured using an optical pyrometer was 2900°C. The reported heat flux was 4280 kW m^{-2}. For unknown reasons they used a highly reducing flame (0.72 oxygen/acetylene), which resulted in the formation of C and the decomposition of SiC into Si and C and the subsequent oxidation of Si into SiO_2. In another paper [228] the same group claimed that the temperature of the oxyacetylene flame reached as high as 3550°C during the testing of C-SiC composites using a reducing flame. At 3550°C, the main oxidation mechanisms were reported to be the sublimation of the SiC matrix and C fibre.

NASA, again, used the technique to compare the oxidation performance of UHTC composites prepared using carbon fabric, allylhydridopolycarbosilane preceramic polymer, HfB_2 powder and SiC powder [221]. Two test coupons were subjected to oxyacetylene flame testing. One specimen was exposed to one 4 minute exposure, reaching a maximum temperature of 1805^oC, and the second to three 4 minute cycles attaining temperatures of 1815, 1915 and 2015^oC on the first, second and third cycles. Temperature measurements were made using a 2 colour pyrometer. No information is given on the gas flow rates or gas flow ratios. The C/SiC side showed consumption of the carbon fibre to more than 1 ply after 4 minutes and 2 plies after 12 minutes. The HfB_2 plus Si-O-C coating was nearly fully consumed after 4 min and totally consumed after 12 min. But the material withstood ~2000°C, severe heat ups and thermal gradients.

Tang et al. [206] used an oxyacetylene flame to evaluate the oxidation performance of 2.5D Cf-UHTC powder composites prepared using a pressure

assisted slurry impregnation followed by a CVI carbon densification process. Three ablation test parameters were used as summarised in Table 2.11.

Table 2.11: Ablation parameters used by Tang et al. [206]

Flow rate / $m^3 h^{-1}$		Heat flux /	Temperature /
Oxygen	Acetylene	kW m^{-2}	^oC
1.36	1.04	3920	2700 ± 300
1.12	0.83	3200	2200 ± 200
0.88	0.65	2380	1800 ± 100

The water flowing through a calorimeter during the ablation process enabled the calculation of heat flux whilst the temperature was measured using an optical pyrometer. A water cooled steel sample holder was used to hold the samples during the test and the total test duration varied from 30 s up to 300 s. They exposed 5 different composites, viz: C/C-ZrB_2, C/C-4ZrB_2-1SiC, C/C-1ZrB_2-2SiC, C/C-1ZrB_2-2SiC-2HfC and C/C-1ZrB_2-2SiC-2TaC, at three different heat fluxes for 30 seconds and the composites were ablated causing mass erosion. The outcome of the test at a heat flux of 3920 kWm^{-2} (2700±300^oC) is indicated in Figure 2.23. All samples except the C-C composite were covered with a white oxide layer and the C/C-ZrB_2 showed the best ablation resistance at all heat fluxes.

The superior oxidation resistance of C/C-ZrB_2 was explained by the evaporation of boria, which caused a thermal barrier effect due to the gas escape and low oxygen diffusion rate through a ZrO_2 porous layer that formed. The addition of SiC to the composite worsened its ablation resistance due to the formation of several low melting point liquids that peeled off under the impact of the combustion gas.

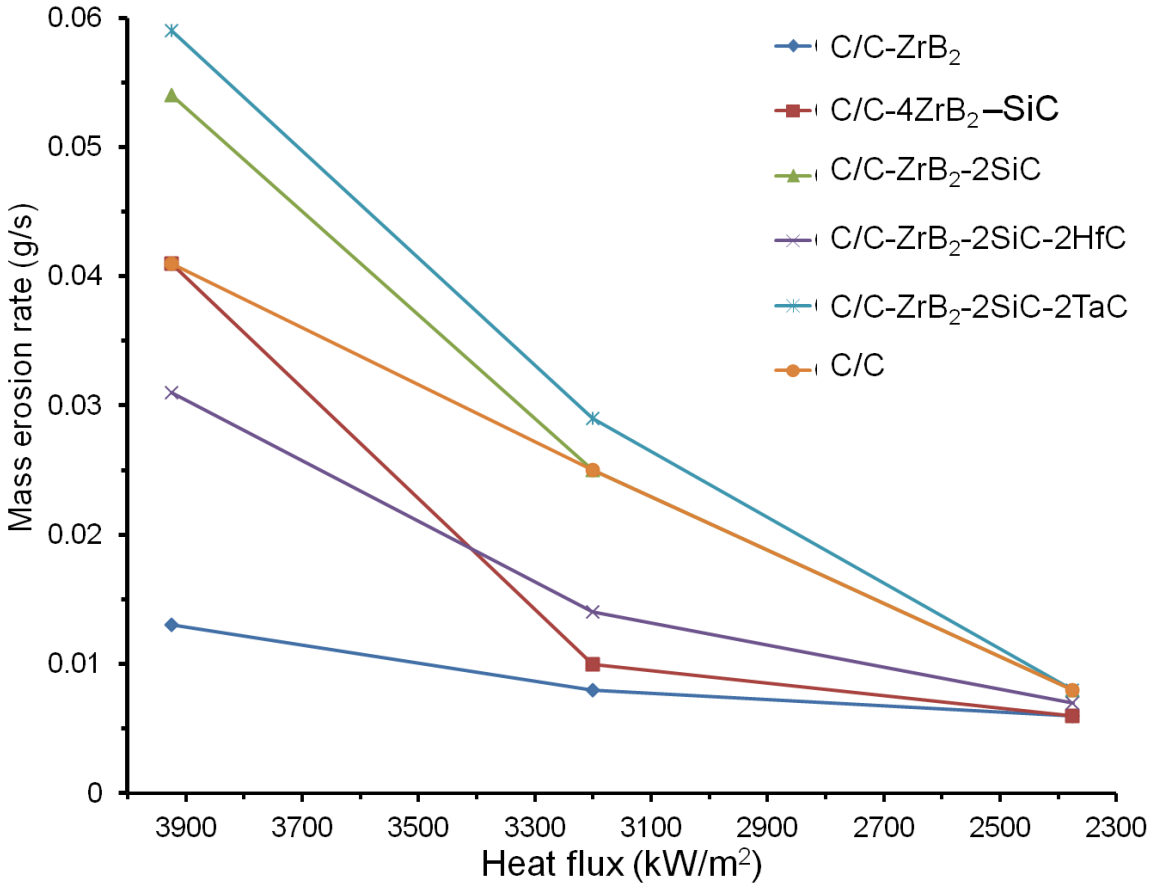

Figure 2.22: Mass erosion rate of UHTC-C/C composite and C/C composites [205]

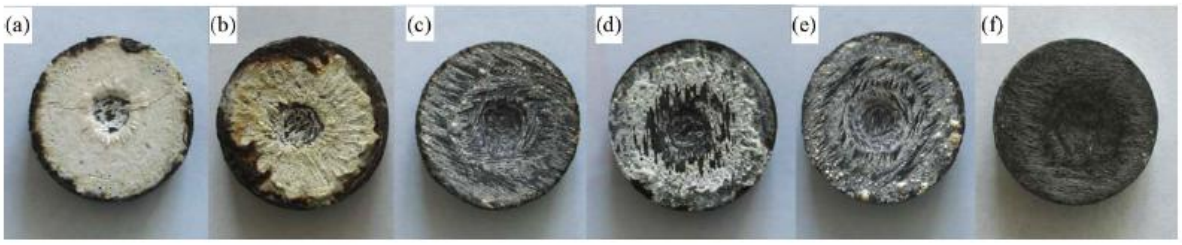

Figure 2.23: C/C-UHTC composites tested at 3920 kW/m^2 heat flux for 30 s: (a) C/C-ZrB_2 (b) C/C-4ZrB_2-1SiC (c) C/C-1ZrB-2SiC (d) C/C-2SiC-1ZrB_2-2HfC (e) C/C-2SiC-1ZrB_2-2TaC and (f) C/C [205]

The effect of HfC and TaC on the ablation behaviour of the C/C–1ZrB_2–2SiC was attributed to the formation of the high melting point solid HfO_2 phase which offered better protection than the liquid Ta_2O_5 phase formed.

A similar study was carried out by Paul et al [209] to test the 30 mm diameter C fibres preforms, slurry impregnated with UHTC powders/compositions such as, ZrB_2, ZrB_2–20 vol% SiC (ZS20), ZrB_2–20 vol% SiC–10 vol%, LaB_6 (ZS20–1La), HfB_2 and HfC. The testing employed an oxygen rich oxyacetylene flame (1:1.35 acetylene: oxygen) to ablate the sample surface at temperature higher than 2500^{o}C and C-C composite was used as the benchmark.

Photographic images of the various composites after 30 s oxyacetylene torch testing are shown in Figure 2.24. Although the effects of oxidation are clear, there was little or no erosion for any of the UHTC-based samples, except for the C-C preform, in spite of cracking on the front face. An unusual detail observed for the Cf-HfC composite is the lack of adhesion of the formed oxide layer to the base composite, the layer detached during cooling. This is thought to be due to the pressure build-up below the oxide layer resulting from CO/CO_2 gas formation and the absence of formation of any glassy phases such as B_2O_3, during the test.

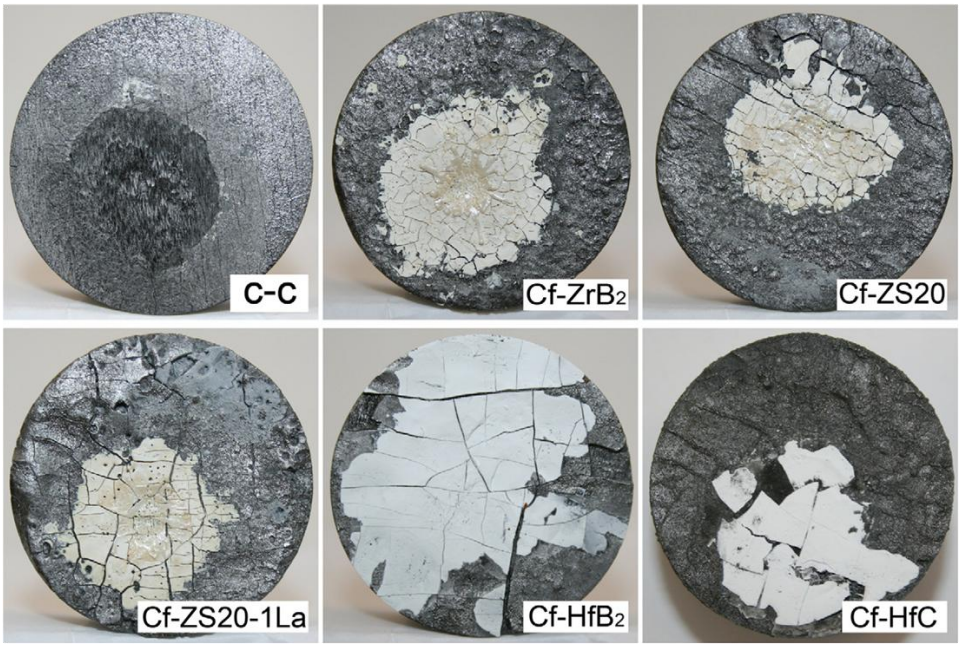

Figure 2.24: CC and Cf-UHTC composites after 30 s oxyacetylene testing (Work done by Dr. Paul) [208]

Figure 2.25 shows the images of the composites after 60 s of oxyacetylene torch testing and the corresponding 2D micro-CT images highlighting the depth of erosion are shown in Figure 2.26. The peak front and back face temperatures, mass loss data and erosion depth after the 30 and 60 seconds oxyacetylene torch tests are summarised in Table 2.12; note that the analyses on Cf–HfC sample reported was done after the surface oxide layer had dropped off. The depth of erosion was found to be the lowest for the Cf–HfB_2 system. From Figure 2.25, it can be observed that the C–C sample eroded over the entire 20 mm diameter area on the front face of the sample and the depth of erosion reported was ~4 mm. The surface erosion of the Cf–ZrB_2 and Cf–ZS20 composites were reported to be similar to each other, with the damage centred over an area of ~5 mm in diameter and the depth of erosion being 4.8 mm and 5.3 mm respectively. In the case of Cf–ZS20–1La composite, erosion depth of ~6.2 mm was observed due to the penetration of the high temperature flame through the dense UHTC powder rich layer attacking the C–C layer below. The extent of damage was reported to be much lower for the preforms impregnated with either HfB_2 or HfC.

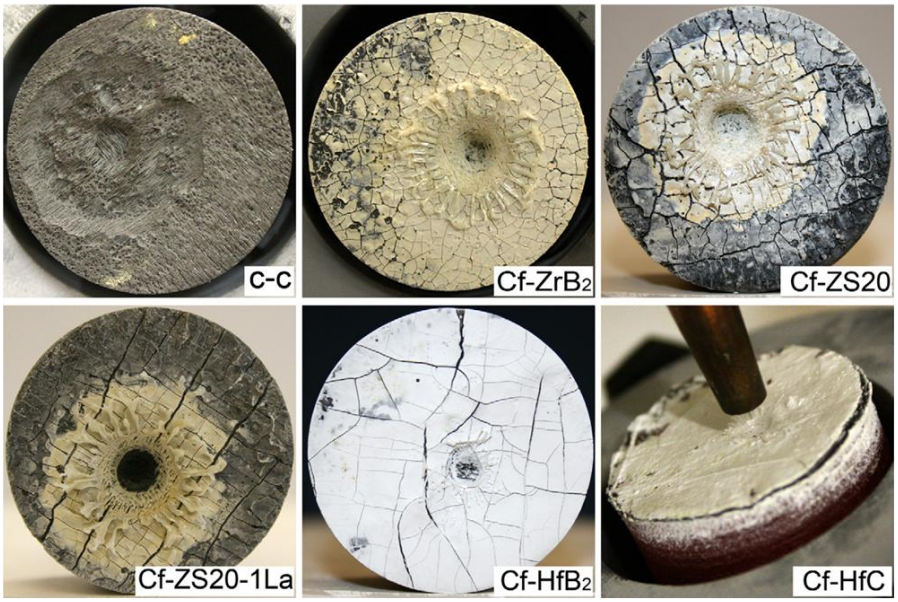

Figure 2.25: CC and Cf-UHTC composites after 60 s oxyacetylene testing [208]

Table 2.12: Summary of the results after 30 and 60 s oxyacetylene torch test [208]

Composite	Test duration / s	Peak temperature / °C		Weight loss / g	Erosion Depth / mm
		Front (±150°C)	Back (±10°C)		
CC	30	2208	573	0.38	1.0
Cf-ZrB_2	30	2563	634*	0.22	Negligible
Cf-ZrB_2-2SiC	30	2522	614*	0.18	Negligible
Cf-ZrB_2-2SiC-1LaB_6	30	2577	761*	0.17	Negligible
Cf-HfB_2	30	2624	713*	0.77[#]	Negligible
Cf-HfC	30	2680	688*	0.55[#]	Negligible
CC	60	2315	763	1.63	4.0
Cf-ZrB_2	60	2592	857*	0.67	4.8
Cf-ZrB_2-2SiC	60	2551	723*	0.63	5.3
Cf-ZrB_2-2SiC-1LaB_6	60	2523	877*	0.74	6.2
Cf-HfB_2	60	2638	918*	0.57	<2.0
Cf-HfC	60	2528	847*	1.69[#]	NM

* Thermocouple in the drilled cavity

[#] Includes weight of the lost surface layer

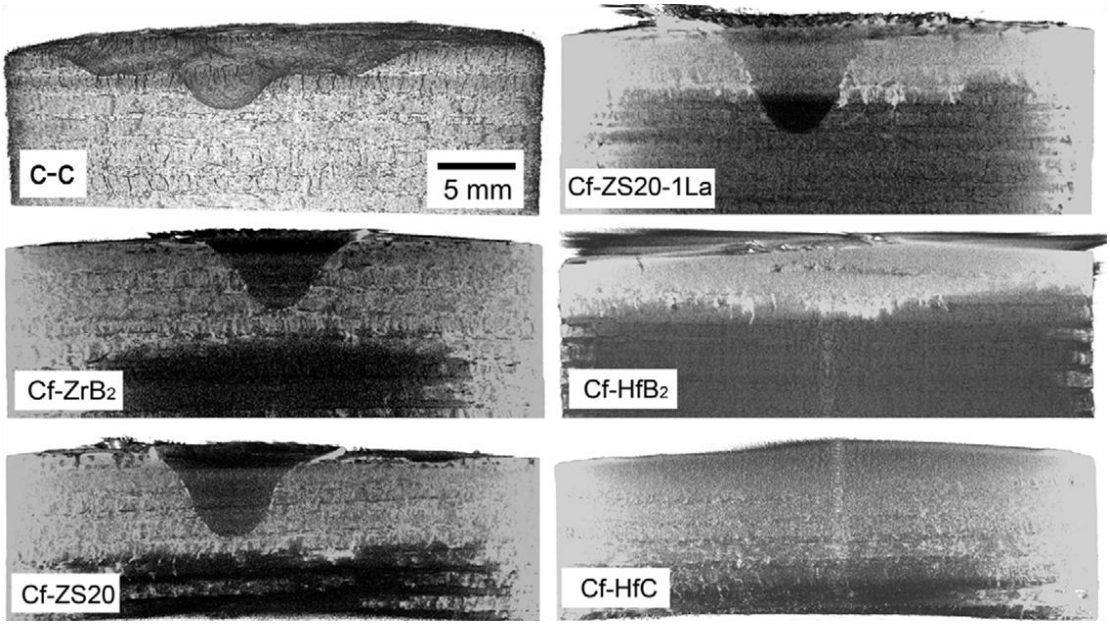

Figure 2.26: Depth of erosion measured using micro-CT after 60 s oxyacetylene torch testing of CC and Cf-UHTC composites [208]

Summarising all the oxyacetylene torch testing papers discussed so far, it was observed that most of the tests were carried out by groups in America or China. There was not much information available on the gas flow rates and ratios used by the American groups. Also there was no mention about the nozzle type, size or the distance between the tip of the nozzle and the sample. The test methods used by the Chinese groups are all derived from the Chinese military standard GJB323A – 96, (test method for the ablation of ablators). However, there is considerable variation between the test parameters used by the various groups in terms of gas flow rates, gas flow ratios, temperature measurements and test durations.

Very recently, researchers in Italy [229] modelled the heat flux and temperature distribution during oxyacetylene testing. An ablative composite material was used to perform actual tests and compare the results with modelling; some of their results are shown in Figure 2.27.

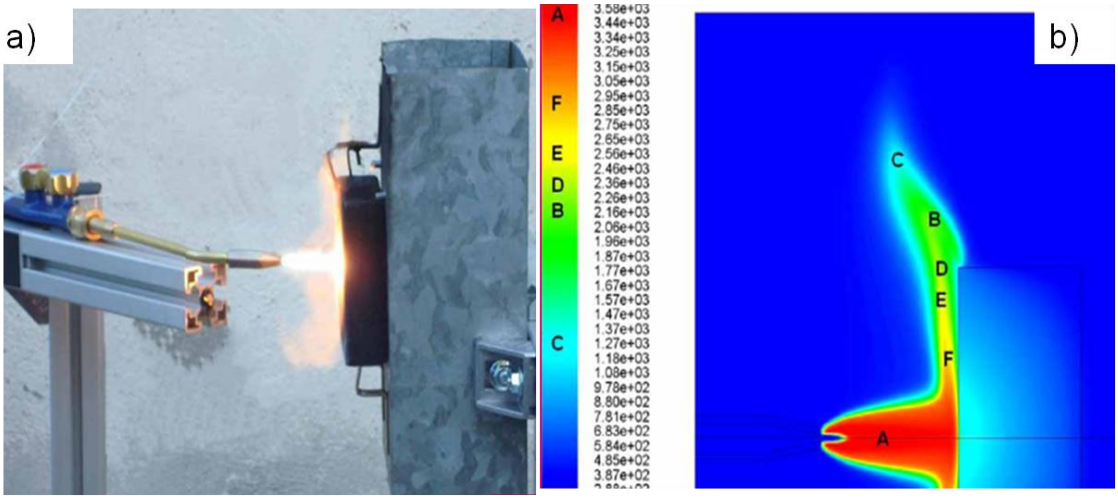

Figure 2.27: a) Testing of an ablative sample using an oxyacetylene flame and b) simulated temperature field during the test [227]

The results of their measurements are summarised in Table 2.13 [229] and they were able to achieve reasonable agreement between the measured and calculated heat flux and temperature.

Table 2.13: Percent variation between numerical simulation and experimental measurements

Quantity	Numerical simulation	Experimental measurement	Variation / %
Heat flux/ MW m^{-2}	1.58	1.5 to 1.6	-1.2 to +5
Exposed face sample temperature / K	1900	1970 / 2070	-8.2 to -3.5
Back face sample temperature / K	850	630	+34.9

Researchers from Ohio State University developed a computer controlled oxyacetylene test rig which can be used for cyclic testing of thermal barrier coatings. The test rig creates thermal gradients on test samples (25°C on one side and 1200°C on the other) while bombarding the coated surface with sand or volcanic ash particles. The rig can automatically subject samples to

repeated 7 minute heating–cooling cycles, (while measuring and recording data), until the coatings fail [230].

Chapter 3

3 Experimental

This chapter explains the experimental procedure involved in this project. The overall work done, including the characterisation, is depicted in Figure 3.1.

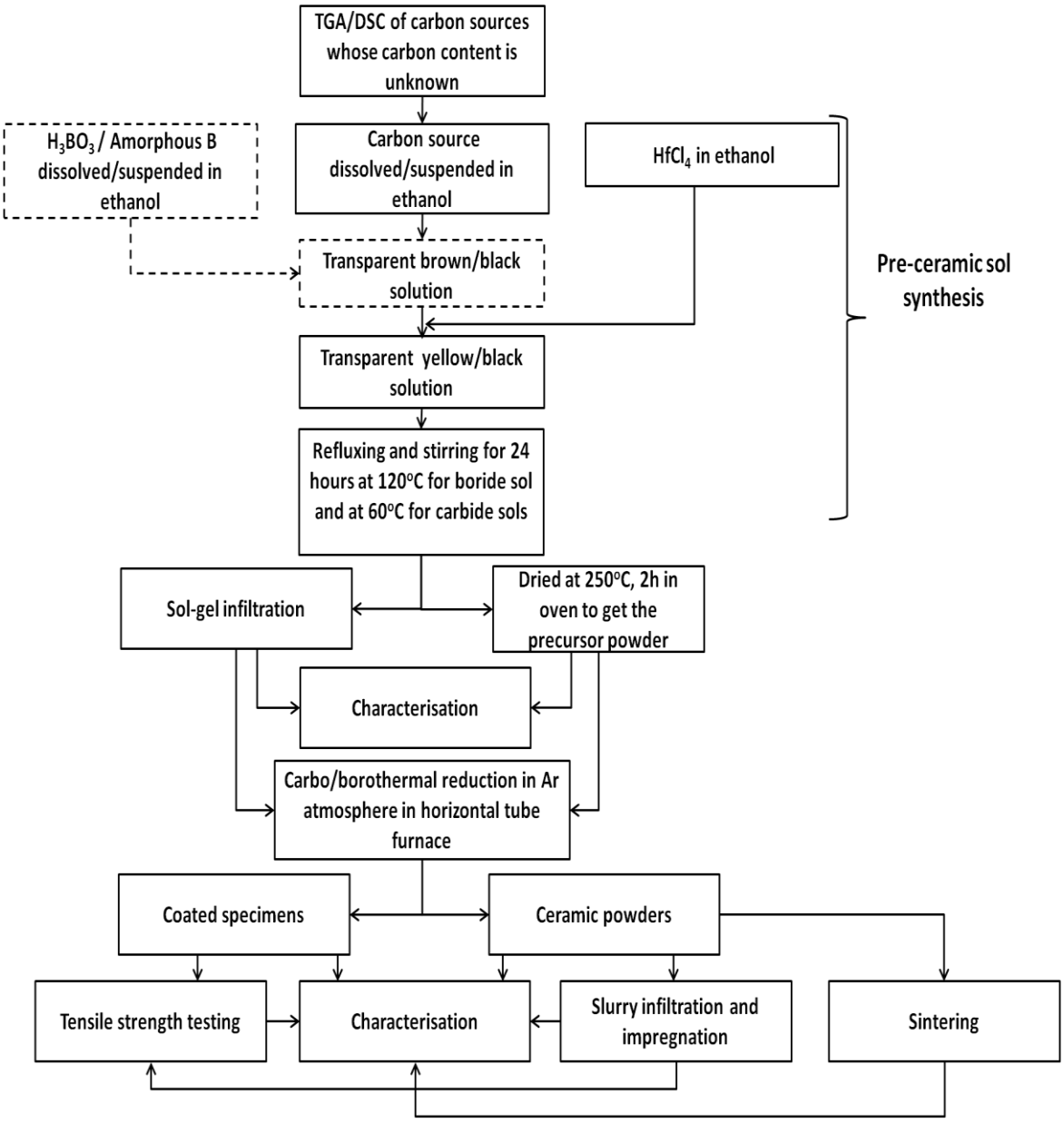

Figure 3.1: Flow chart of the experimental work carried out in this project

3.1 Raw materials

The purity and the source of the starting materials used are listed in Table 3.1.

Table 3.1: Starting materials used in this project

Chemical	Molecular formula	Source	Purity/ Carbon content/ Surface treatments
Tetraethylorthosilicate (TEOS)	$Si(OC_2H5)_4$	Sigma Aldrich	99.999%
Hafnium chloride	$HfCl_4$	Sigma Aldrich	98%
Boric acid	H_3BO_3	Fischer Scientific, Loughborough, UK	99.5%
Amorphous boron powder	B	Sigma Aldrich, Dorset, UK	95-97%
Liquid phenolic resin (LPR)	$[(HOC_6H_4)_2CH_2]_n$	Cellobond J2027L, Momentive Speciality Chemicals, Louisville, USA	51% carbon content
Powder phenolic resin (PPR)	$[(HOC_6H_4)_2CH_2]_n$	Crios resins, SI group, Inc, So Paulo, Brazil	41.7% carbon content
Sucrose	$C_{12}H_{22}O_{11}$	Fischer Scientific, Loughborough, UK	21.8% carbon content
Pitch	Carbores® P	Rutgers chemicals, Zelzate, Belgium	65.6% carbon content
Graphite	C; 325 mesh	Fischer Scientific, Loughborough, UK	99% purity
Multi-walled carbon nano tube (MWCNT)	C; 10 – 20 nm diameter	NTP, Shenzhen, China	>97% purity
Carbon black N115	C; 20 – 40 nm, oil absorption coefficient* 1.1 ml/g	Columbian Chemicals UK, Bristol, UK	>99% purity
Carbon black N772	C; 100 – 150 nm, oil absorption coefficient* 0.65 ml g^{-1}	Columbian Chemicals UK, Bristol, UK	>99% purity
Ethanol	C_2H_5OH	Fischer Scientific, Loughborough, UK	96% purity
SiC fibres (Hi- nicalon grade)	SiC	Sigma Tech, Alabama, USA	Surface treated; Fibre diameter: 7 µm
Carbon fibres	C	Easy composites, Stoke-on-trent, UK	Surface treated; Fibre diameter: 7 µm
Carbon fibre performs*	C	Surface transforms, UK	No surface treatments; 30 mm dia x 20 mm thick; 2.5 D

3.2 Synthesis of pre-ceramic sols

Those carbon sources with unknown carbon content such as pitch, sucrose, LPR and PPR were subjected to thermo gravimetric analysis (SDT 2960, TA Instruments, Newcastle, UK) to obtain the weight loss curves. The samples were heated in an alumina crucible up to 1000^{o}C in an Ar atmosphere at a rate of 5^{o}C min^{-1}. An empty alumina crucible was used as the reference. The residual weight was taken as the percentage of carbon present in the samples, see Table 3.1.

3.2.1 Carbide sols

The carbide sols SiC and HfC were prepared using liquid phenolic resin as the carbon source and TEOS and $HfCl_4$ as the respective metal sources. The reactions employed for carbide sol synthesis are given in equations 3.1 and 3.2.

$$SiO_2 + 3C \rightarrow SiC + 2CO\uparrow \quad (3.1)$$

$$HfO_2 + 3C \rightarrow HfC + 2CO\uparrow \quad (3.2)$$

The stoichiometric calculations for obtaining 5 g of the ceramic powders are as follows:

For SiC pre-ceramic sol:

$$\text{weight of TEOS} = \frac{5\text{g} \times \text{molecular weight (MW) of TEOS}}{\text{MW of SiC} \times \text{purity of TEOS}}$$

$$= \frac{5\text{g} \times 208.33}{40.10 \times 99.99\%}$$

$$= 25\ \text{g}$$

$$\text{volume of TEOS} = 27.8\ \text{ml}\ ; (\text{density} = 0.933\ \text{g ml}^{-1})$$

$$\text{weight of LPR} = \frac{5\text{g} \times \text{MW of C}}{\text{MW of SiC} \times \text{carbon content in LPR}} \times \text{C: Si ratio}$$

$$= \frac{5\text{g} \times 12}{40.10 \times 51\%} \times \text{y} = 0.97\text{y g}$$

Similarly for HfC pre-ceramic sol:

$$\text{weight of } HfCl_4 = \frac{5\text{g} \times \text{MW of } HfCl_4}{\text{MW of HfC} \times \text{purity of } HfCl_4}$$

$$= \frac{5\text{g} \times 320.30}{190.50 \times 98\%} = 8.58\text{g}$$

$$\text{weight of LPR} = \frac{5\text{g} \times \text{MW of C}}{\text{MW of HfC} \times \text{carbon content in LPR}} \times \text{C: Hf ratio}$$

$$= \frac{5\text{g} \times 12}{190.50 \times 51\%} \times \text{y} = 0.62\text{y g}$$

The carbon to metal ratio 'y' was kept as 3 and 10 for the carbide pre-ceramic sols and were identified as, MC and MC_e (M= Si or Hf) respectively; e representing excess carbon present in the system. The metal precursor and LPR were individually dissolved in ethanol and then mixed with each other at 60^{o}C for 24 h under reflux, to obtain the carbide pre-ceramic sol. 20 ml of ethanol was used to dissolve each precursor, however, TEOS being a liquid precursor, the SiC pre-ceramic sol had slightly more solvent than the HfC pre-ceramic sol.

3.2.2 Diboride sols

For the diboride sol, several ratios of metal to boron to carbon were synthesized in order to study the diboride formation mechanism. The basic reactions employed in this synthesis are given in equations 3.3, 3.4 and 3.5.

$$HfO_2 + B_2O_3 + 5C \rightarrow HfB_2 + 5CO\uparrow \quad (3.3)$$

$$HfO_2 + 2B + 2C \rightarrow HfB_2 + 2CO\uparrow \quad (3.4)$$

$$HfO_2 + 4B \rightarrow HfB_2 + B_2O_2\uparrow \quad (3.5)$$

The stoichiometric calculations, similar to the carbide sols are as follows,

$$\text{weight of } HfCl_4 = \frac{5\text{g} \times \text{MW of } HfCl_4}{\text{MW of HfB2} \times \text{purity of } HfCl_4}$$

$$= \frac{5\text{g} \times 320.30}{200.1 \times 98\%} = 8.17 \text{ g}$$

$$\text{weight of } H_3BO_3 = \frac{5\text{g} \times \text{MW of } H_3BO_3}{\text{MW of } HfB_2 \times \text{purity of } H_3BO_3} \times \text{B: Hf ratio}$$

$$= \frac{5\text{g} \times 62}{200.1 \times 99.5\%} \times x = 1.56x \text{ g}$$

$$\text{weight of B} = \frac{5\text{g} \times \text{MW of B}}{\text{MW of } HfB_2 \times \text{purity of B}} \times \text{B: Hf ratio}$$

$$= \frac{5\text{g} \times 10.21}{200.1 \times 95\%} \times x = 0.27x \text{ g}$$

$$\text{weight of LPR} = \frac{5\text{g} \times \text{MW of C}}{\text{MW of HfB}_2 \times \text{carbon content in LPR}} \times \text{C: Hf ratio}$$

$$= \frac{5\text{g} \times 12}{200.1 \times 51\%} \times \text{y} = 0.588\text{y g}$$

The different compositions, i.e. different x and y values investigated for HfB_2 pre-ceramic sol synthesis are given in Table 3.2.

LPR dissolved in 20 ml of ethanol was added to a boric acid ethanol solution, contained in a round bottomed flask held which was held in an oil bath maintained at 120^{o}C. $HfCl_4$ dissolved in 20 ml of ethanol, was then added and the mixture was allowed to stir for 24 h in an oil bath maintained at 120^{o}C under reflux conditions. When boron powder was used as the boron source, it was suspended in 20 ml of ethanol contained in a round bottomed flask, kept in a oil bath held at 120^{o}C to which LPR-ethanol and $HfCl_4$-ethanol solution were then added, in that order.

For those precursor sols containing B:Hf molar ration ≤ 4, 20 ml ethanol was used to dissolve the boric acid. For higher concentration of B_2O_3 the amount of ethanol used to dissolve the former was increased to allow complete dissolution and to prevent super saturation and hence precipitation. In order to study the effect of different carbon sources on the final HfB_2 powder, HB_eC was synthesized using sources such as PPR, sucrose[i], graphite, pitch, C black (N115, N772) and MWCNT[ii].

$$\text{weight of carbon source} = \frac{5\text{g} \times \text{MW of C}}{\text{MW of HfB}_2 \times \text{carbon content}} \times \text{C: Hf ratio}$$

$$= \frac{5\text{g} \times 12}{200.1 \times z\%} \times 3 = 0.9/z\%\ \text{g}$$

[i] Being immiscible in ethanol, the sucrose was dissolved in water and hence the $HfCl_4$ and boric acid were also dissolved in water.
[ii] Graphite, pitch, C black and MWCNT were dispersed in ethanol, unlike the LPR and PPR which were dissolved in ethanol.

where z is the percentage of carbon content in the different carbon sources, as obtained from TGA, Table 3.1.

Table 3.2: Compositions investigated for HfB_2

Sample	Elemental stoichiometry			Remarks
	Hf	B *x*	C y	
HBC	1	2	5	Exact stoichiometry, as equation 1a
HB_eC	1	3 to 3.8	5	Equation 3.3 with slight excess B to compensate for losses
HB_eC_e	1	3	20	Equation 3.3 with slight excess B to compensate for losses excess C
$HB_{e1}C$	1	6	5	Equation 3.3 with excess B
$HB_{e2}C$	1	8	5	Equation 3.3 with excess B
$HB_{e2}C_e$	1	8	20	Equation 3.3 with excess B and C
HB	1	3	0	Equation 3.3 without C
$B_{e2}C_e$	0	8	20	Equation 3.3 without Hf; attempt to synthesize B_4C
HB_aC	1	2	2	Equation 3.4 using amorphous B powder
$HB_{ae}C$	1	2	2	Equation 3.4 using excess amorphous B powder
HB_a	1	4	0	Equation 3.5
HB_{ae}	1	5	0	Equation 3.5 using excess amorphous B powder

3.3 HTC and UHTC powder synthesis

Following the sol synthesis, the solvent from the sols was completely evaporated by removing the reflux whilst still stirring at 60^{o}C and/or 120^{o}C, i.e. the mixing temperature for the carbide and boride sols respectively. The resulting aerogels were dried at 250^{o}C in a conventional air oven for 2 h and subsequently ground using a mortar and pestle to obtain the precursor powders.

The high temperature ceramic (HTC) powder, i.e. SiC, and the ultra high temperature ceramic (UHTC) powders, i.e. HfC and HfB_2, were achieved through carbothermal or boro/carbothermal reduction of the precursor powders. The heat treatments were carried out in an argon atmosphere in a high temperature horizontal tube furnace (TSH17/75/450, Elite Thermal Systems Ltd, UK) fitted with a 99.7% pure alumina tube. The heating and cooling rates were maintained at 5^{o}C min^{-1} up to 1000^{o}C and 3^{o}C min^{-1} above 1000^{o}C in all cases. A heat treatment temperature of 1500^{o}C and a dwell time of 4 h were required to produce SiC powder from its precursor powder, whilst HfC and HfB_2 required a 2 h dwell at 1600^{o}C.

The furnace set up is shown in Figure 3.2. The samples were placed on an alumina crucible at the centre of the high purity alumina tube fitted with stainless steel end caps. Porous alumina plugs were placed inside the tube near the inlet and outlet ends to protect the tube from thermal shock and also to prevent heat dissipation to the end caps. The outlet was connected in series to a pressure gauge and an air tight silicone oil container to trap the heat and small solid particles from the outlet gas and exhaust respectively.

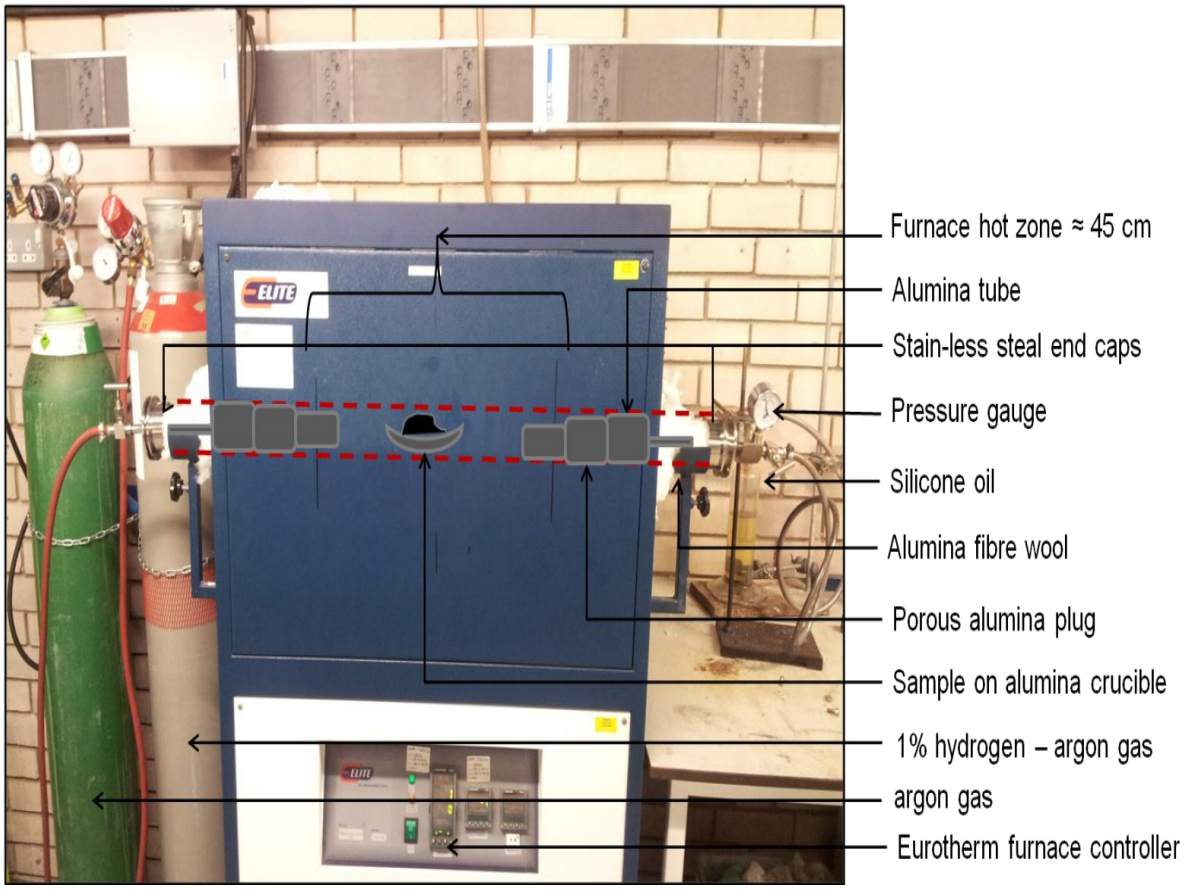

Figure 3.2: Furnace set-up

Prior to the heat treatment, the tube was completely evacuated using a rotary vacuum pump and purged using argon – 1% hydrogen gas. This process was repeated twice and before starting the heating cycle. The argon – 1% hydrogen mixture was passed through the tube for the first 500^{o}C step increase for all of the runs. This helped to remove both the Cl^- ions [231] trapped in the system as HCl vapours[iii] in the case of the HfC and HfB_2 precursor powders, and also the oxygen from the tube.

In order to study the structure of the carbon resulting from the pyrolysis of the different carbon sources, the latter were dissolved/suspended in ethanol

[iii] $HfCl_4$ being highly hygroscopic and oxygen sensitive reacts with moisture in both the air and the ethanol during the synthesis stage to release HCl vapours. Any reaction with H_2 gas only triggers this reaction and helps remove Cl^- ions from the precursor powder.

(water for sucrose) and refluxed at 120^{o}C for 24 h with subsequent drying and grinding using a motor and pestle. The product was then heated to 1000^{o}C in an argon atmosphere in the aforementioned horizontal tube furnace.

3.3.1 Sintering

The finest of all the synthesized HfB_2 powders, which was obtained when using Hf:B:C stoichiometric ratio of 1:3.8:5 and PPR as the carbon source, was sintered using spark plasma sintering (SPS) apparatus in vacuum at 2000, 2100 and 2200^{o}C for 10 min. 10 grams of the powder was cold pressed at 1 tonne pressure and placed in graphite foil-lined, 20 mm diameter graphite dies, the latter being covered with graphite felt to reduce heat loss. The heating rate and the cooling rates were 100°C min^{-1} and 50°C min^{-1} respectively. A load of 16 kN was applied during sintering. The linear change in shrinkage was recorded, during sintering, by monitoring the displacement of the sample along the pressing direction. It should be noted that the optical pyrometer was focused on the surface of the graphite die and not directly on the specimen which may in turn give rise to a difference between the temperature of the die and that of the specimen especially, at the faster heating rates and shorter hold times. Similar runs were carried out for 99% pure HfB_2 powder with d_{50} = 2 µm, procured from Treibacher, Austria. After densification, the resulting 20x3 mm billets were polished to a surface finish of 1 µm using a 1200 grit diamond platen.

3.3.1.1 Sintering density

The density of the sintered samples was measured using the Archimedes principle using deionised water as the displacing medium and utilizing the proper density correction for the temperature of the medium. Equation 3.6 gives the relative density of the sample.

$$\rho = \frac{M_s . \rho_l}{M_s - M_l} \tag{3.6}$$

Where, *Ms,* mass of sample in air, M_l, mass of sample in water, and ρ_l is the density of the liquid at measuring temperature. The percentage of densification (%ρ) is given by Equation 3.7.

$$\% \rho = \frac{\rho}{Theoretical \quad density \quad of \quad HfB_2} \tag{3.7}$$

Theoretical density of HfB_2 = 10.5 g cm^{-3} [232]

3.4 Sol-gel coatings and infiltration

Following the sol synthesis, the viscosity values of the sols were varied by evaporating the solvent from the sols, by removing the reflux whilst still stirring at 60^{o}C or 120^{o}C, for the carbide and boride sols respectively. The time for which the sols were stirred after removing the reflux, dictated their viscosity values. For the sake of consistency and direct comparison, all the sols were synthesized to the same viscosity by varying the stirring time, (refer to section 3.6.12).

UHTC coating and infiltrations were performed on the carbon fibre tows and on the carbon fibre preforms to protect the latter from high temperature oxidation. The coatings of the pre-ceramic sols onto fibre tows of carbon and SiC was carried out using manual dip coating and automatic dip coating whilst the infiltration was carried out using either the automatic dip coating or a combination of manual dip coating and a squeeze-tube method. Heat treatment of the infiltrated samples led to the boro/carbothermal reduction reaction occurring and resulted in mini-composites, (UHTC matrix infiltrated into a single tow of carbon or SiC fibre filaments), which were used for the

basic strength measurements as they were easier to prepare and test compared to a large Cf preform-UHTC composites. Prior to the dip coating, the surface treatments on the SiC and C fibre tows were removed by immersing them into acetone and a water bath maintained at 100^{o}C, respectively.

Initial experiments involved dipping the fibres into the sol using a pair of tweezers and drawing them out manually. This gave no control over the coating thickness, the infiltration level or the porosity of the resultant matrix. Later, an automatic dip coater was used to dip the fibres into and draw them out of the sol at a fixed speed. The variation of the coating thickness was plotted against the withdrawal speed and a linear relation existed between the two, as per equation 3.8 [233]. The lowest withdrawal speed (1 mm min^{-1}) was used to obtain thin coatings of HfC and HfB_2 around individual carbon fibres, in the tow whilst the highest speed (200 mm min^{-1}) was used to infiltrate the HfC and HfB_2 pre-ceramic sols into the carbon and SiC fibre tows.

$$h_o = 0.94(\eta U_o)^{2/3} / v_{LV}^{1/6} (\rho g)^{1/2} \quad (3.8)$$

where: h_o = thickness

η = viscosity

Uo = withdrawal speed

v_{LV} = surface tension

ρ = density

g = acceleration due to gravity

Very thin coatings around the fibres were achievable through this method, however, infiltration remained a problem due to the lack of control over trapped air bubbles which resulted in porosity in the matrix. Later experiments involved infiltrating the pre-ceramic sols into the fibre tows using a squeeze-tube technique to obtain a mini-composite. The carbon fibre tows of fixed

length and folds were dipped into the pre-ceramic sol as shown in Figure 3.3. The dip coated tows were pulled into a shrink tube (polyolefin tube with 3.2 mm inner diameter and shrink diameter of 1.6 mm, ShrinkTek Polymers International, Cheltenham, UK). While the tows were still inside the tube, a hot air gun was used to heat the tube from the centre to the end. The heat helped the tube to shrink and forced out any excess sol and trapped air bubbles. During heat treatment the shrink tube evaporated cleanly at around 350^{o}C.

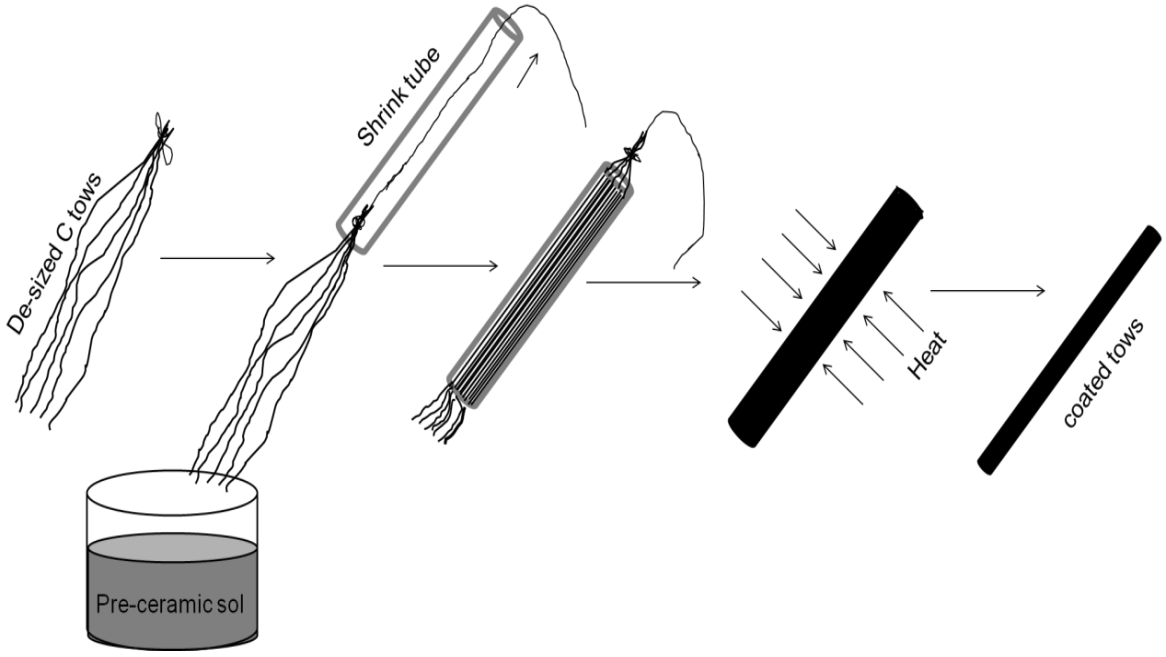

Figure 3.3: Dip coating and squeeze tube method

All the coated and infiltrated samples were then dried in an air oven at 80^{o}C for 24 h. This was followed by boro/carbothermal reduction reactions at high temperature, i.e. 1500^{o}C, 5 h for SiC matrix and 1600^{o}C, 2 h for HfC and HfB_2 matrix, in the aforementioned horizontal tube furnace. The heating and cooling rates were kept as 1^{o}C min^{-1}. Thin coatings were obtained using automatic dip coating whilst the best infiltration, i.e. a dense ceramic matrix, was achieved when using the squeeze-tube method. The coatings and matrix infiltration were characterized using a FEGSEM (Leo 1530VP FEGSEM, LEO Elektronenskopie GmbH, Oberkochen, Germany).

3.5 Slurry infiltration and impregnation

Slurry infiltration was used to prepare mini-composites using the aforementioned squeeze-tube technique. The process was the same as shown in Figure 3.3, but instead of a pre-ceramic sol, a HfB_2 powder – phenolic resin – acetone slurry, prepared by ball milling in a plastic container using alumina milling media for 48 h, was used. The weight ratio of the 3 ingredients was 80:40:25 respectively. Finest HfB_2 powder obtained when using powder phenolic resin as the carbon source was used for this experiments. The purpose was to see if the impregnation altered the strength of the carbon fibre tows and to compare the mini-composite strength against those prepared by the sol-gel infiltration route.

The slurry was also impregnated into a 30 mm dia x 20 mm thick, 2.5 D carbon fibre (Cf) preform with 23 vol% fibres. Slurry impregnation was carried out using a vacuum impregnation technique where the preforms were fully immersed in a beaker containing the slurry, which was then placed in a low pressure vessel and a rotary pump used to create the low pressure. The slurry infiltrated through the pores of the preform to fill the interior porosity. The finest in-house synthesized HfB_2 powder was used for these experiments.

Both the slurry-impregnated preforms and the slurry-infiltrated tows were dried in an air oven at 75°C for 4 h followed by curing at 125 to 150°C for 2 h. The whole cycle of impregnation, drying and curing was repeated 3 times for the Cf-preforms to maximise the amount of UHTC powder within the composite. At the end of the drying and curing process both the infiltrated tows and impregnated tows were pyrolysed at 800°C for 2 h under a flowing argon (99.998% pure, flow rate 60 cm^3 min^{-1}) atmosphere at a heating/cooling rate of 1.5°C min^{-1} using a horizontal tube furnace. A schematic of the process is shown in Figure 3.4.

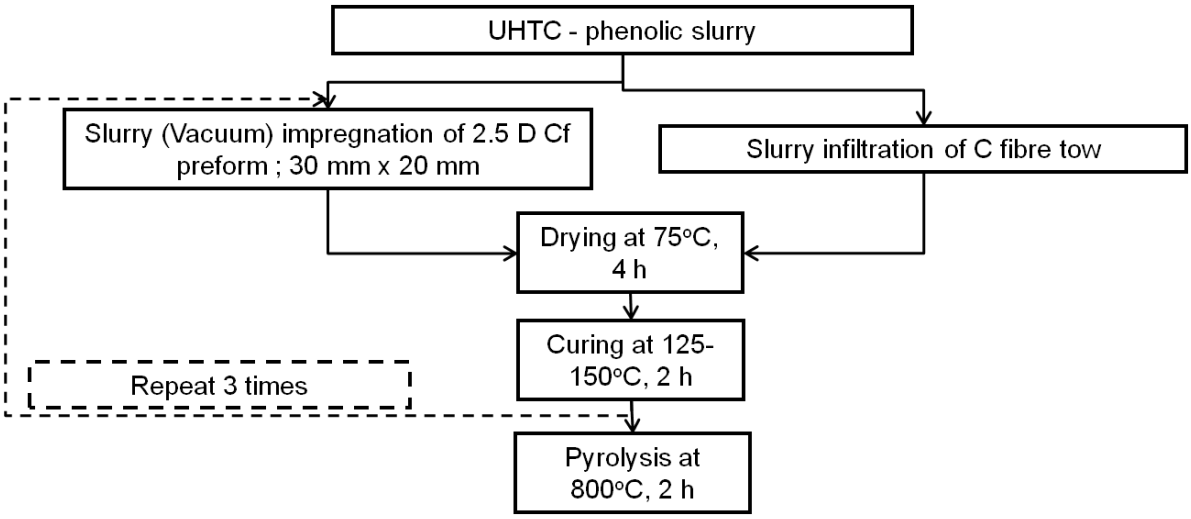

Figure 3.4: Slurry infiltration and impregnation into C, SiC tows and Cf-preform respectively

3.6 Characterisation

3.6.1 Oxidation testing

3.6.1.1 Furnace testing

Oxidation studies of the SiC and carbon tows with HfC and HfB_2 coatings produced through manual dip coating were carried out in the horizontal tube furnace for 1 h at 1000, 1250 and 1400°C using a heating and cooling rate of 1°C min^{-1}. The weights of the resulting oxidised samples were measured and the latter cut and carefully mounted on a vertical copper tape on a copper stub for surface analysis using FEGSEM.

3.6.1.2 Oxyacetylene testing

An oxyacetylene torch test facility had been constructed at Loughborough University to perform high temperature oxidation testing [208]. A schematic of the set up is shown in Figure 3.5. The HfB_2-phenolic-acetone slurry impregnated Cf preforms using vacuum impregnation, were tested for their oxidation resistance using this set up. Prior to this, Cf preforms impregnated with commercially available HfC and HfB_2 powders were tested each for 140 and 180 s. The sample to be tested was mounted in a graphite sample holder and an oxygen-rich oxyacetylene flame with acetylene to oxygen ratio of

1:1.35 focused onto the sample and the temperature and temperature distribution experienced by the sample were recorded by using a 2 colour pyrometer (Marathon MR1SCSF, Raytek GmbH, Berlin, Germany) and a modified infrared thermal imaging camera (Thermovision A40, FLIR Systems AB, Danderyd, Sweden). The thermal imaging camera was only capable of measuring temperature up to 1700^{o}C and so was fitted with a neutral density filter to extend the maximum temperature rage to 2700^{o}C. The back face temperature of the samples was recorded using a K-type thermocouple with a data logger. The weight loss of the samples after oxyacetylene testing was recorded.

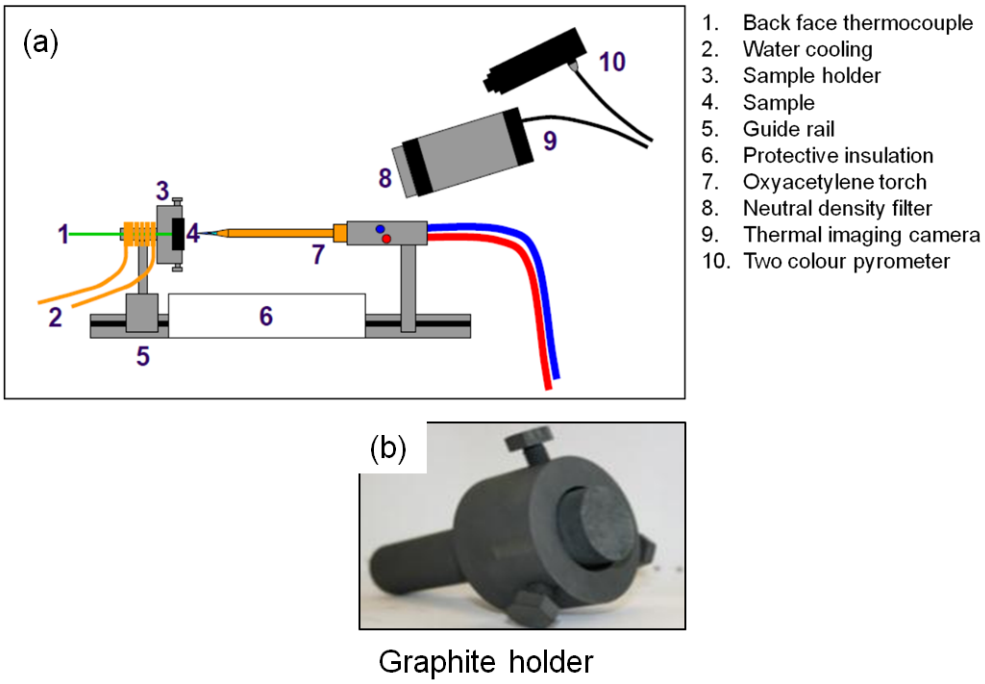

Figure 3.5: a) Oxyacetylene torch test setup and b) graphite sample holder

3.6.2 Tensile testing

C tows – HfB_2 mini-composites prepared by the squeeze-tube method using sol-gel and slurry infiltration of HfB_2 pre-ceramic sol and HfB_2-phenolic-acetone slurry respectively, were compared for their tensile strength using a bench top computer controlled, dual column tensometer (LR50K plus, Lloyd Instruments, West Sussex, UK). The samples for analysis were prepared by

attaching the ends of the mini-composite to a piece of cardboard using Araldite adhesive as shown in Figure 3.5, and left to dry overnight. The distance between the glued ends was kept constant at 5 cm. Before testing the sides of the cardboard were cut along the dotted lines as shown in the Figure.

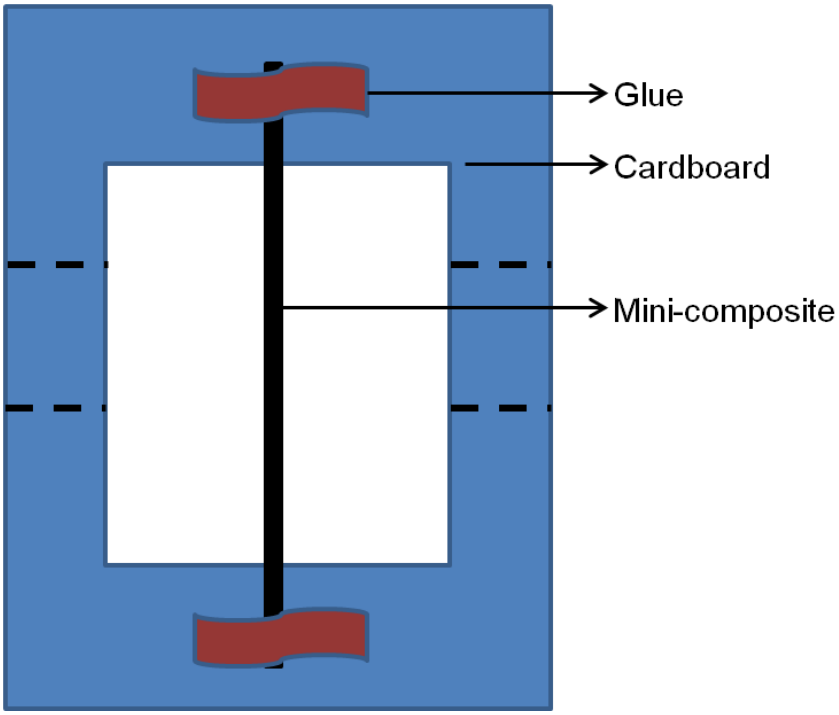

Figure 3.6: Sample for tensile testing

A wedge grip with teeth was used to hold the sample and a 1 kN load cell and 10 mm min^{-1} withdrawal speed, were used to stretch the samples to failure. The LR50KPlus microprocessor controlling the tensometer generated a stress-strain curve for each test and calculated the Young's modulus and ultimate tensile strength values.

3.6.3 Thermal analysis

High temperature thermogravimetric analysis coupled with differential scanning calorimetry (Netzch TGA/DSC, Germany) was performed on HfB_2, HfC and SiC precursor powders to investigate the onset temperature of the carbothermal and borothermal reduction reactions. The sensitivity of the equipment used was 0.1 µg and the weight accuracy was ± 0.1%. The heating

rate of the chamber could be selected from 0.1 to 500^{o}C/min up to 1600^{o}C from ambient temperature under an air or argon atmosphere. About 30 to 40 mg of the precursor powder was placed in an alumina crucible and heated at a rate of 5°C per minute up to 1000°C and then at 3^{o}C min^{-1} up to 1600^{o}C and cooled down to room temperature under a constant flow of argon gas. An empty alumina crucible was used as the reference material. The difference in heat flow was monitored to identify any transition in the material under investigation.

Isothermal TGA (Q5000IR TGA, TA instruments, Zellik, Belgium) was used to study the weight loss of the precursor powders due to the presence of Cl^- ions. The precursor powders were heated to 350^{o}C or 450^{o}C for 6 h in air; a heating rate of 10^{o}C min^{-1} was used.

3.6.4 Fourier Transform Infra-Red (FTIR) analysis

The nature and characteristics of the bonding of the HfC and HfB_2 precursor powders and the UHTC powders was analysed using FTIR (FTIR 8400S, Shimadzu, Maryland, USA). The sample for analysis was prepared by mixing 1 g of potassium bromide (KBr) with a pinch (< 1 mg) of the powder of interest using a motor and pestle. This powder mixture was then pressed into a pellet using a 12 mm diameter stainless steel die and a pressure of 100 MPa for a minute. A KBr pellet pressed using the same conditions was used to obtain a background scan first, which was then automatically subtracted from any further scans obtained from the samples.

3.6.5 Phase analysis (XRD)

Phase analysis of the synthesized SiC, HfC and HfB_2 powders, sintered and oxidised composites was carried out by X-ray diffraction (XRD) using a Philips PW7100 diffractometer (UK) and a Bruker D8 diffractometer (Bruker AXS GmbH, Karlsruhe, Germany) with Cu-K α radiation and a quarter-circle eulerian cradle. The testing conditions were identical for all samples used and were CuKα radiation with a wave length of 1.5406 Å, and a step size of 0.02°

increment in 2θ, with a step time of 1 s, XRD patterns were recorded from 20° to 80° 2θ range

The crystallite size (t) was obtained using the Scherer equation (Equation 3.9),

$$t = k \lambda / \beta \cos\theta \quad (3.9)$$

Where:
λ is the wavelength of the incident X-ray (in nm),

k is the dimensionless shape factor which varies from 0.89 to 0.94 for spherical shape to cubic shaped particles, (here assumed to be 0.9 as the particles are nearly spherical),

β is the full-width-half-maximum (FWHM) value of the specific diffraction peak (in radians), and,

θ is the angle at which the peak is observed.

The width of the peak is strongly affected by instrumental effects and stress in the film. As shown in Equation 3.9, in highly crystalline materials where crystallite size is large, β must be small thus sharp peaks are observed, i.e. the less crystalline the material the broader the peaks.

High temperature XRD patterns were recorded for the HfB_2 and HfC precursor powders to determine the temperature at which the HfB_2 and HfC peaks were formed. The quarter circle cradle was replaced by a high temperature furnace that used a Pt band type heater and could be operated in the range 400 to 1400ºC. X-ray patterns were recorded from 20° to 80° 2θ at room temperature and then at every 100^{o}C from 500^{o}C to 1600^{o}C and after cooling down to 25^{o}C.

The International Centre for Diffraction Data (ICDD) cards used to identify phases were HfB_2 (00-038-1398), HfC (00-039-1491), 3C-SiC (00-029-1129), 6H-SiC (00-029-1131) HfO_2 (00-034-0104), B_4C (00-035-0798), B (00-031-0206), and $B_{13.34}C_{1.66}$ (01-083-0861).

3.6.6 Raman spectroscopy

Raman spectroscopy was undertaken using a Horiba Yvon Raman Labram HR spectrometer (Horiba Jobin Yvon SAS, Villeneuve d´Ascq, France). The spectrometer was equipped with a liquid nitrogen cooled CCD detector, two objective lenses, x10 and x50 magnification, argon (wavelength 514 nm) and helium-neon (wavelength 632.8 nm) lasers and an automated stage. The optical microscope connected to a video monitor allowed the selection of specific areas on the sample to record the Raman spectrum.

Micro-Raman spectra were recorded for the UHTC powder samples especially HfB_2, to check for the presence of free carbon impurity. The powders were pressed between two glass slides to obtain a visibly flat surface. Since the Raman peaks for carbon occur over a broad range, the spectra were obtained from 400 to 4000 cm^{-1} over an average of 128 scans and exposure of 2 s using the He-Ne laser with a power of 20 mW.

3.6.7 CHN (Carbon Hydrogen Nitrogen) analyser

A bench-top, fully automated CHN elemental analyzer (CE-440 Elemental Analyser, Exeter Analytical Inc., Coventry, UK) with an accuracy of +/- 0.15% was used to analyse the carbon content of the HfC and HfB_2 powder samples. The test duration per sample was only 5 min. The samples were subjected to combustion in an excess of oxygen at 975^{o}C and the combustion gases were carried by helium through the analytical system to the atmosphere; the combustion train is shown in Figure 3.7. The water, CO_2, and nitrogen concentrations of the sample were measured by displacing the sample gas through the detectors to atmosphere.

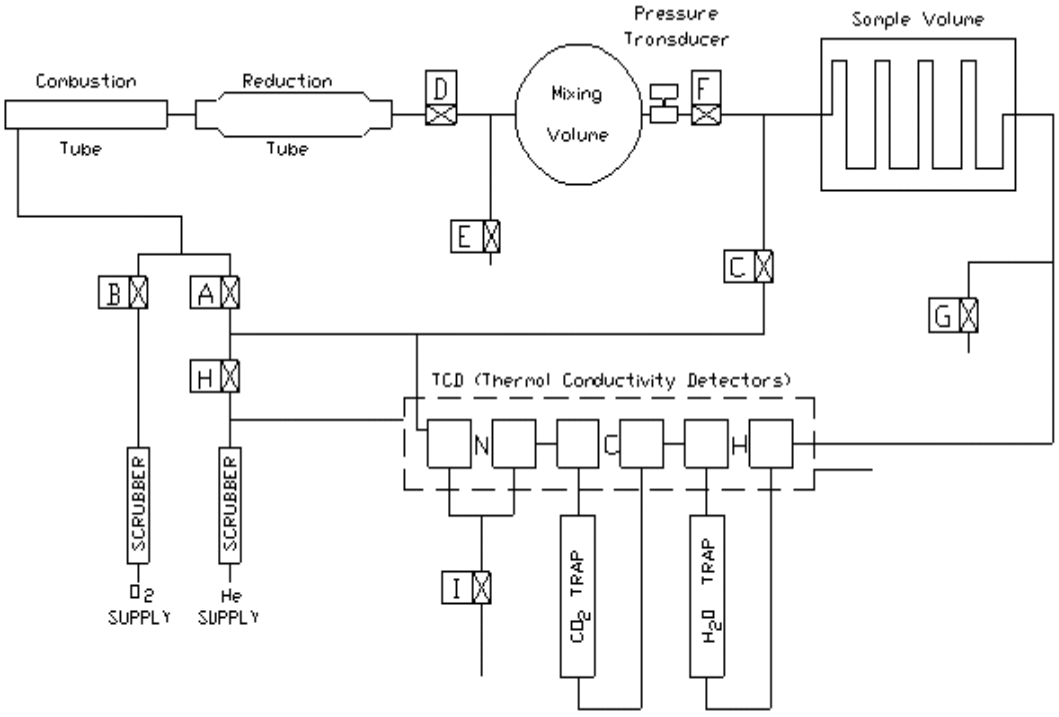

Figure 3.7: Schematic of CHN analyser

3.6.8 Surface area measurement

The BET surface area was analysed for HfC and HfB_2 powders using a gas adsorption analyser (Tristar™ 3000, Micromeritics Instrument Corporation, Norcross, USA). The samples were placed in a round bottomed long neck glass flask and were degassed in a nitrogen atmosphere at 150^{o}C for 60 minutes before testing. During the test, the samples were evacuated to <20 µm Hg vacuum, cooled down to 77 K by immersing into a liquid nitrogen container and exposed to high purity nitrogen (>99.99% pure). This process of degassing, evacuating, lowering the sample into liquid nitrogen bath and then exposing the sample to high purity N_2 was carried out automatically by the instrument as predefined by the user using the Tristar 3000 software. 40 adsorption and desorption points were collected with p/po, (the ratio of relative pressure, p, to the saturation vapour pressure, p_o, at a constant temperature of adsorption), values in the range 0.05 to 0.99. The Tristar™ 3000 had a resolution within 0.05 mm Hg and an accuracy of 0.5% of full scale.

3.6.9 Malvern Mastersizer

The particle size distribution of HfB_2 powders synthesised at Loughborough and those obtained commercially was analysed using a Mastersizer 2000 (Malvern, Worchestershire, UK), using prop-3-ol, (99%, Fisher Scientific, Loughborough, UK), as solvent. The equipment works on the principle of the laser diffraction technique, where the particles passing through the laser beam scatter light at an angle that is directly related to their size, i.e. large particles scatter at low angles and small particles scatter at higher angles. The powders were dispersed in prop-3-ol, ultrasonicated for a few minutes to break the soft agglomerates and then circulated into the cell. Five measurements were taken for each sample.

3.6.10 X-ray photoelectron spectroscopy (XPS)

XPS is one of the most widely used surface characterisation methods. It is also known as electron spectroscopy for chemical analysis (ESCA). XPS can identify all the elements (except H and He) present at concentrations >0.1 atomic % to a depth of 10 nm. This was exploited to analyse the impurities present and any surface oxidation in the powder samples.

XPS spectra for HfC and HfB_2 powders were recorded on a K α surface analyser (Thermo Scientific, West Sussex, UK) operating with an un-monochromatized Al Kα X-ray source (1486.6 eV). The samples were placed in a vacuum environment and then irradiated with photons in the X-ray energy range. As a consequence of the direct energy transfer from the irradiated photons to the electrons at the core level of the sample, photoelectrons were emitted. The energy of the emitted photoelectrons is a characteristic of the atomic and molecular environment from which they originated, and the number of photoelectrons is directly proportional to the quantity of the emitting atom.

3.6.11 Secondary ion mass spectroscopy (SIMS)

To study the chemical composition of the HfB_2 powder samples and to identify the impurity content, SIMS (Atomika 6500 UHV-SIMS fitted with FLIG gas ion gun) was used. Unlike XPS, SIMS uses charged ions to bombard the surface of the sample and to sputter atoms and molecules from it, characteristic of the top surface of the sample. By controlling the primary ion dose, damage to the sample can be prevented. A positive and negative secondary ion mass spectrometer detector covered the entire periodic table. The technique had a sub-nano-metre resolution and parts per million sensitivity.

3.6.12 Rheology

The rheological characterization of the pre-ceramic sols was carried out at a constant sheer rate of 10 s^{-1} using a Rheolab QC rheometer (Anton Paar Ltd, Garz, Austria). The rotational rheometer was equipped with a RheolabQC plus temperature control system for exact control of the measuring cup and the sample with a water bath thermostat and Rheoplus software for data analysis. The measurement could be carried out at any temperature between -20^oC to 150^oC.

The sols used for infiltration were synthesized to a viscosity of 0.6 Pa s by altering the time for which they were stirred after removing the reflux, this meant that the pre-ceramic sols for the SiC and HfB_2 were stirred for 30 min whilst the HfC sol was stirred for 10 min. The viscosity of both the HfB_2-phenolic-acetone slurries prepared from fine HfB_2 powder obtained when using powder phenolic resin as the carbon source and the commercial HfB_2 powder was measured using Rheolab QC rheometer.

3.6.13 Contact angle measurement

In order to quantify the wettability of the C and SiC fibre tows by the pre-ceramic sols, contact angle measurement was carried out using an OCA 20 contact angle measuring device (DataPhysics, Filderstadt, Germany) at

ambient temperature. The pre-ceramic sol was dispensed onto the surface of the substrate, i.e. C and/or SiC fibre tows using the sample dispenser fitted with the equipment and the profile of the drop was recorded using a CCD camera featuring 6x optical zoom and 4.5x magnification.

The contact angle was calculated using Young's equation, Equation 3.10 by measuring the angle formed between the solid and the drop profile with the vertex at the three-phase line, as shown in Figure 3.8.

$$\gamma^{sv} = \gamma^{sl} + \gamma^{lv} \cos\theta \tag{3.10}$$

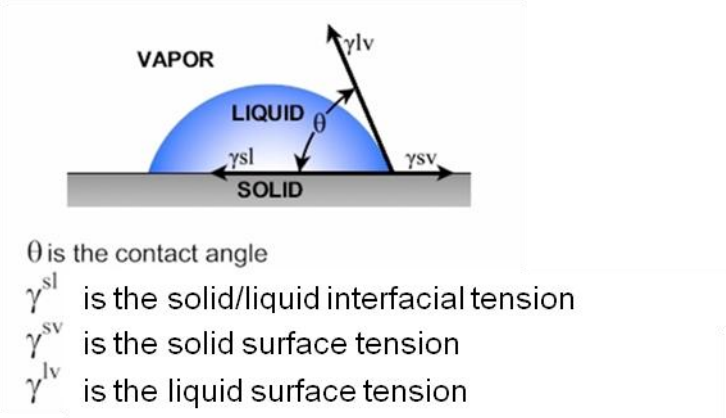

Figure 3.8: Contact angle measurement [234]

3.6.14 X-Ray Micro Computer Tomography (Micro CT)

Micro CT uses X-rays to create a 3D image of the sample that can later be re-constructed virtually without destroying the original sample. The samples are placed on a rotating stage and scanned using X-rays to obtain tomograms which are then stacked to provide a 3D structure. The schematic of the principle of a micro CT is shown in Figure 3.9 [235].

HfB_2-Cf composites were analysed using Micro-CT (Metris X-Tek 160Xi, Metris, Hertfordshire, UK) to determine depth of powder impregnation and distribution and after oxyacetylene torch testing to determine the erosion

depth. The larger the sample, the lower the resolution and since the sample size was 30x20 mm it restricted the resolution to around 5 µm.

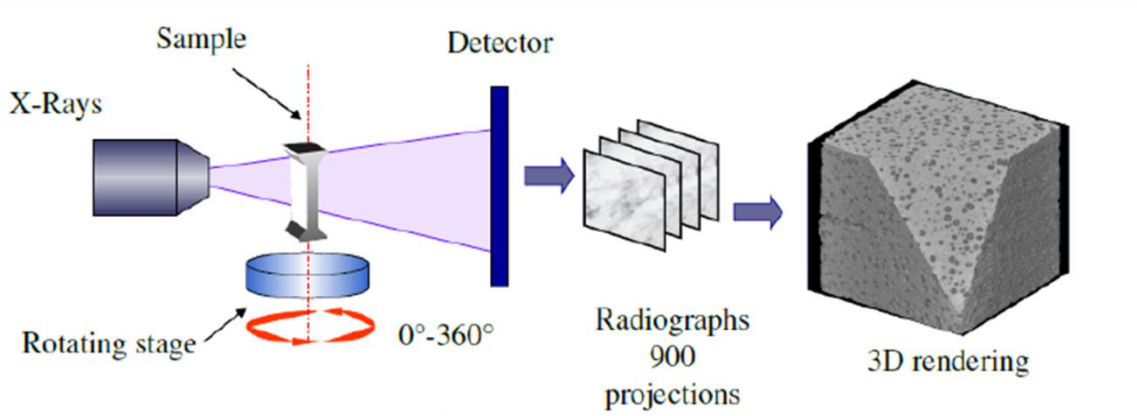

Figure 3.9: X-Ray Micro Tomography [235]

3.6.15 Microstructural analysis

3.6.15.1 Field emission gun scanning electron microscopy

The agglomerate morphology, shape and primary particle size of the various HTC, and UHTC powders, with their respective precursor powders, were analysed using a field emission gun scanning electron microscope (FEGSEM, Leo 1530VP, LEO Elektronenskopie GmbH, Oberkochen, Germany) at different magnifications, viz.1kx, 5kx, 10kx and 15kx. Each powder was sprinkled using a spatula on a conducting carbon film (Agar Scientific, UK) mounted an aluminium stub. The microstructure of the sintered specimens was also observed by FEGSEM on surfaces polished to a 1 µm surface finish. The impregnated performs and mini-composites after the boro/carbothermal reduction reaction, were cut, and FEGSEM images were recorded across the cross section to find the depth of impregnation and matrix infiltration respectively. All the powders and samples were sputter coated with gold using a Polaron Emitech SC7640 sputter coater (Quorum Technologies Ltd, UK) prior to analysis, to make them conductive and to prevent charging. The secondary detector was used to record the images at 5 kV accelerating voltage and 30 µm aperture. The different phases present in the UHTC

powders was analysed using EDS mapping (EDAX, EDAX Inc., NJ, USA). Besides the employment of high current, EDS requires a high accelerating voltage of 15 kV and large aperture size of 120 µm to enable detection of low molecular weight atoms, especially B.

3.6.15.2 Focused ion beam (FIB)

A Dual Beam Nanolab 600 FEI FIB, which combines a focused ion beam microscope and FEGSEM, was used for preparing TEM specimens from HfB_2 powder samples to identify the chemical structure using electron diffraction.

To prepare a TEM sample from a ceramic powder, a thin layer of Pt was deposited on the surface to protect the sample area. Then a gallium ion beam was used to remove material from both sides of the sample area and a micromanipulator was used to remove and attach the sample to a TEM grid using Pt as an adhesive. Then the final thinning was carried out to achieve the desired thickness, in this case it was 120 nm. Rod shaped particles found in HfB_2 powder obtained by heat treating the precursor powder with a Hf:B:C stoichiometry of 1:3:5 at 1300^{o}C for, 25 h, those with a stoichiometry of 1:8:5 and heat treated at 1600^{o}C for 2 h and also the faceted B_4C particles present in the HfB_2 powder prepared from the precursor with Hf:B:C stoichiometry of 1:8:10 and heat treated at 1600^{o}C for 2 h were all examined. The green body of former two powder samples were also polished using the FIB in order to achieve the good surface finish required for EBSD analysis, (refer to section 3.6.14.4). The grain and grain boundaries of the sintered HfB_2 samples were also lifted out using FIB to analyse their chemical composition and orientation using TEM.

3.6.15.3 Transmission electron microscopy (TEM)

Transmission electron microscopy (TEM, A JEOL JEM 2000FX JEOL Ltd. Tokyo, Japan) was used to measure the particle sizes of the HfB_2, HfC and SiC powders. The TEM also gave an indication of the shapes of the particles and the nature of any agglomerates and their sizes. The samples were

prepared by suspending the powders in ethanol using ultra-sonication and placing a drop using a pipette onto the copper grids coated with holey carbon film. TEM was also used to observe rod-shaped particles thinned down by FIB, (refer to section 3.6.14.2). To collect electron diffraction patterns from a sample, it had to be electron transparent and for this reason thick samples had to be thinned down to 40 to 50 nm using FIB. The crystal orientation of the rod shaped HfB_2 particles that formed when the HfB_2 precursor powder with a Hf:B:C stoichiometry of 1:3:5, were subjected to certain conditions such as a 25 h dwell at 1300^{o}C, or increasing the boron content from 3 to 8. The faceted B_4C crystals found in the HfB_2 powders were thinned down by FIB and the electron diffraction patterns were collected. The d spacings were calculated from the diffraction pattern by measuring the radius of the rings in the case of a polycrystalline or amorphous sample or by measuring the linear distance between bright spots for a single crystal. Equation 3.11 gives the d spacing value:

$$d = L\lambda / R \tag{3.11}$$

Where:

L is the distance from the camera to the screen (1000 mm);

Λ is the wavelength of the electron beam (0.00255 nm);

R is the distance between two bright spots or the radius of the rings.

3.6.15.4 Electron Backscattered Secondary Detection (EBSD)

Electron backscattered diffraction (EBSD) imaging (a Hikari hi-speed camera fitted within the FIB) was used to identify the orientation of different shaped particles in the HfB_2 powder sample, which consisted of mixture of rods and particles. The high speed, high sensitivity CCD detector collected 450 indexed patterns per second. Sample preparation was carried out by dry pressing the HfB_2 powders, obtained by heat treating the precursor powders with a Hf:B:C molar ratio equal to 1:8:5 to 1600^{o}C for 2 h and that with 1:3:5 to 1300^{o}C for

25 h. The green body obtained by pressing about 1.5 g of the aforementioned powders, using a 12 mm diameter stainless steel die and a pressure of 100 MPa for a minute, was then mounted in epoxy resin (Struers, Rotherham, UK). Subsequent polishing was carried out using a linisher, (RJH Morrisflex Antelope Vertical Belt Linisher, 3ph, Aldridge, UK), to remove the resin and to expose the sample surface. EBSD requires a flat surface for analysis. However, fine polishing could not be accomplished using traditional polishing, as the samples were green bodies and hence easily smeared over the polishing discs. In order to prepare a flat surface for analysis the FIB was used (refer to section 3.6.14.2), and mapping was then carried out.

Chapter 4

4 Results & Discussions

4.1 Introduction

This chapter discusses the synthesis of HTC and UHTCs such as, SiC, HfC and HfB_2 in two forms, powders and coatings, along with their subsequent processing and testing. The mechanism of the UHTC powder formation and the effect of different carbon sources on the particle size of HfB_2 powders are discussed. The sintering conditions of HfB_2 using SPS were investigated along with the impregnation of the HfB_2 powders into carbon preforms followed by oxyacetylene torch testing. At the beginning of this study, both HfC and HfB_2 were of interest for hypersonic applications, however, a parallel study on oxyacetylene torch testing of UHTC powders-impregnated carbon preforms, carried out by Dr. Anish Paul at Loughborough University, showed that HfB_2 fared better in protecting the carbon preform compared to HfC, (refer to section 2.4.2.6). Since the ultimate aim of this study was to protect carbon preforms from oxidation at hypersonic temperatures, i.e. over 2700^{o}C, HfB_2 was the centre of focus in the later stages of this study.

4.2 Synthesis of UHTC powders

4.2.1 Characterization of the carbon sources

The carbon sources used in this study for which the carbon content was unknown, i.e. liquid phenolic resin, powder phenolic resin, pitch or sucrose, were subjected to thermogravimetric analysis up to 1000^{o}C in an argon atmosphere with a heating rate of 5^{o}C min^{-1}, to quantify the char content present. The other sources, which included graphite, MWCNT and carbon black and which did not contain any volatiles, were assumed to have a carbon content that was the same as their purity. Figure 4.1 shows that all the carbon sources tested showed an initial weight loss curve that plateaued as the temperature increased over 600^{o}C. The weight loss was highest for sucrose

and the residual carbon content was just 21.8%; pitch had the lowest weight loss with a residual mass of 65.6%. The sucrose was stable up to 200^{o}C after which there was a very significant weight loss caused by dehydration, dehydrogenation and volatilization of CO and CO_2 [236]. The pitch showed no mass loss up to 350^{o}C due to the absence of both physically and chemically bonded water, after which it slowly began to lose weight due to breaking of the aromatic chains and dehyrdrogenative cross-linking during the process of pyrolysis [237]. The liquid and powder phenolic resins both lost water until they cured at around 145^{o}C. Beyond this temperature the weight loss remained almost stable up to 400^{o}C and only CO and CO_2 degassing occurred. The degradation of the resin then started involving the release of volatile compounds like phenol, cresol and toluene [238]. The residual weight of each carbon source after pyrolysis in argon, which was the weight of the carbon present in the chemical, was obtained and used for further calculations.

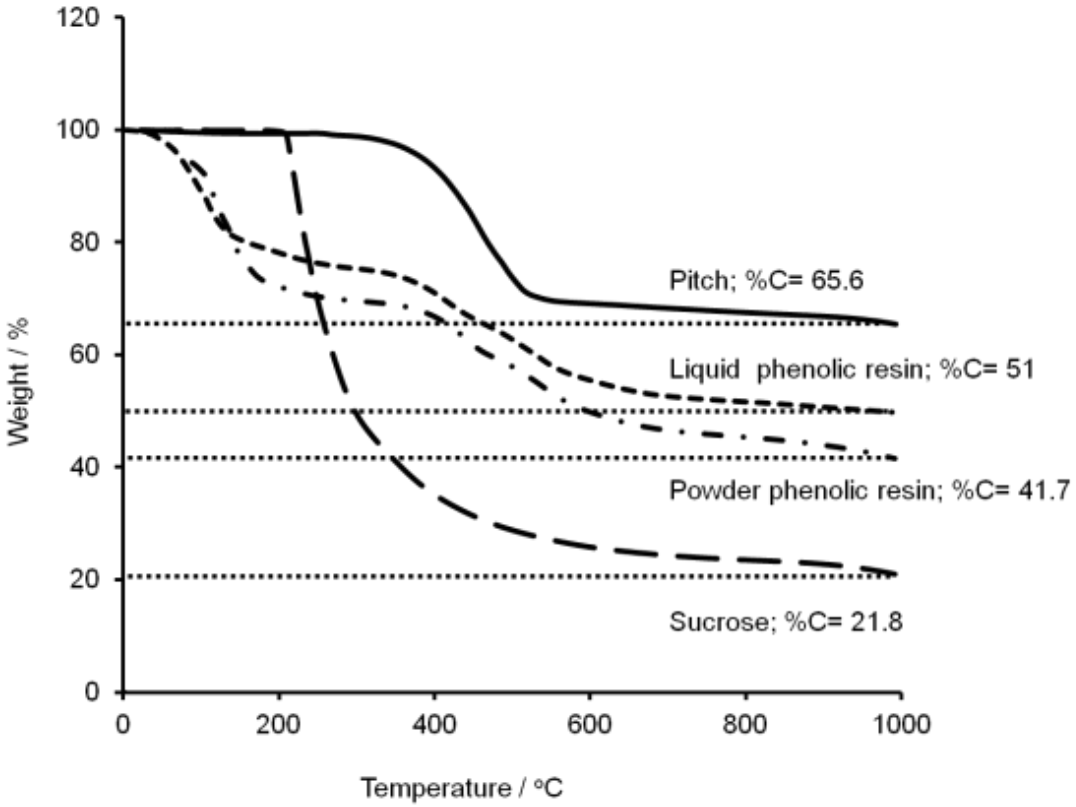

Figure 4.1: TGA of the different carbon sources

4.2.2 FTIR of the precursor powders

The FTIR absorption spectra for SiC, HfC (HC) and HfB_2 (HB_eC) precursor powders and liquid phenolic resin dried at 250^oC for 2 h, are shown in Figure 4.2 across the 4000 to 400 cm^{-1} range. The peaks in the LPR spectra were reproduced in the other precursor powders, indicating that LPR did not react with other precursors in the system.

The sol gel process involved in the carbide (SiC and HfC) and diboride (HfB_2) sols are given in equations 4.1 and 4.2 respectively.

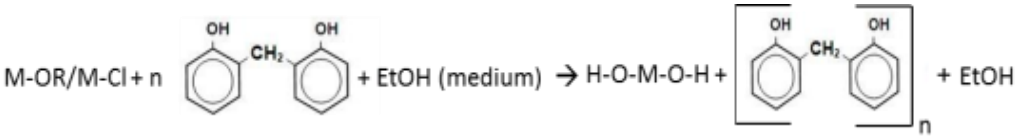

(4.1)

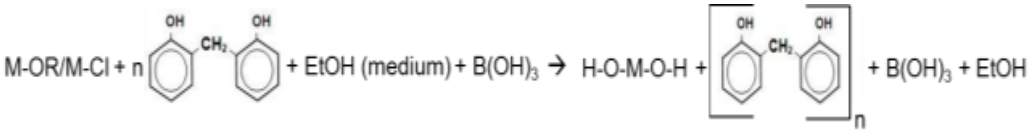

(4.2)

where M: Si/Hf

The broad peak at around 3400 cm^{-1} is attributed to the O-H stretching vibrations associated with the hydroxyl groups in the phenolic resin, boric acid and the Hf-OH stretching vibrations. The peaks at 1392, 2841 and 2914 cm^{-1} are attributed to the aliphatic C-H stretching vibrations from the phenolic resin, whilst those at 1099 and 1622 cm^{-1} represent the aromatic C-H deformation and C=C deformation from the phenolic resin. The peaks at 2330 and 2357 cm^{-1} are due to C=O stretching arising from the CO_2 and $C_3O_2^+$ groups present in the system.

The insert in Figure 4.2 reveals some characteristic peaks for the carbide and diboride sols that are not a part of phenolic resin. The peaks at 470 and 626 cm^{-1} represent the the M-$(OH)_2$ bend and M-O stretch respectively. The O-B-O stretching vibrations peaks are present at 520 cm^{-1} and this is associated with boric acid present in the system. The peaks at 642 and 748 cm^{-1} are attributed

to OHfO- asymmetric stretching [239]. The FTIR result confirms that there was no complex formation between the reactants and that at the end of the sol-gel process and subsequent drying step, the precursor powder consisted of $M(OH)_4$, aromatic and aliphatic chains resulting from the cross-linking of the phenolic resin and H_3BO_3 in the case of the diboride sol.

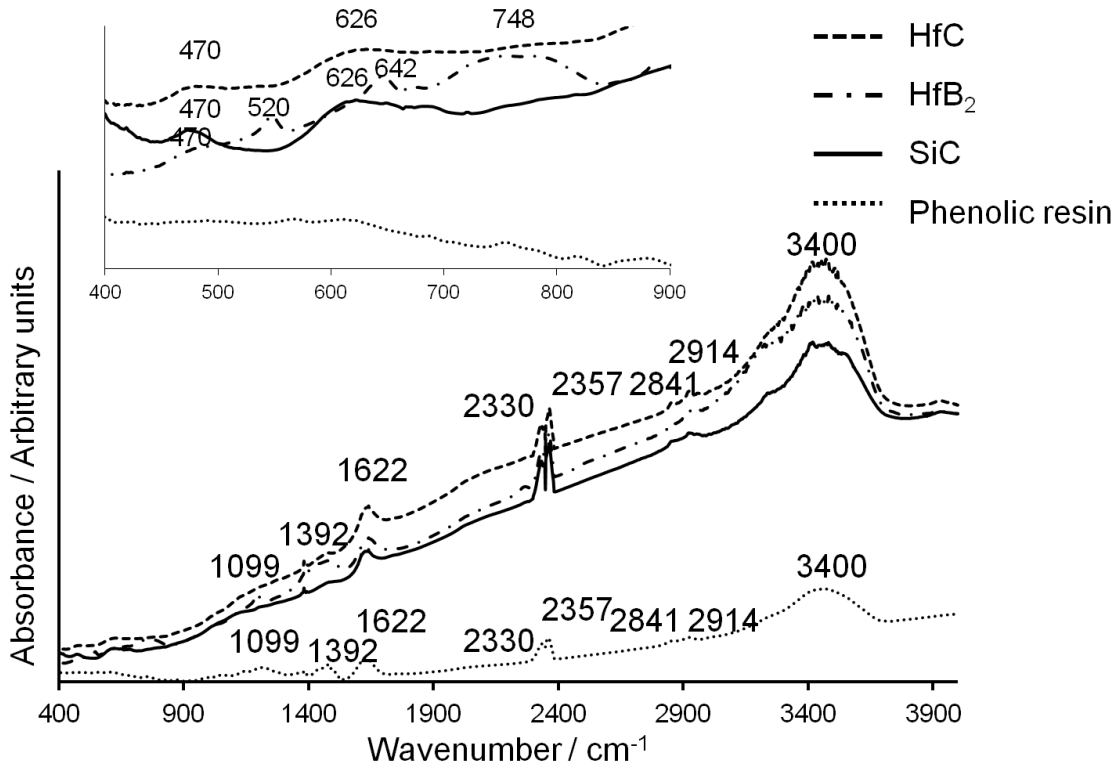

Figure 4.2: FTIR of the SiC, HfC and HfB_2 precursor powders and dried phenolic resin powder

4.2.3 Thermal analysis of the precursor powders

Figure 4.3 shows the TGA/DTA curves of the precursor powders HB_eC, HC and SC. TG analysis shows that the main weight loss occurred below 700^oC for all the three precursor powders due to the evaporation of the bound water and the decomposition of the phenolic resin and evolution of chlorides in the case of the Hf-based precursors. The maximum weight loss for HC and SC was 35%, which was less than that for HB_eC 51%. This is due to the volatile B_2O_3 formed when HB_eC precursor or any boric acid containing HfB_2 precursor powder was subjected to high temperature heat treatment.

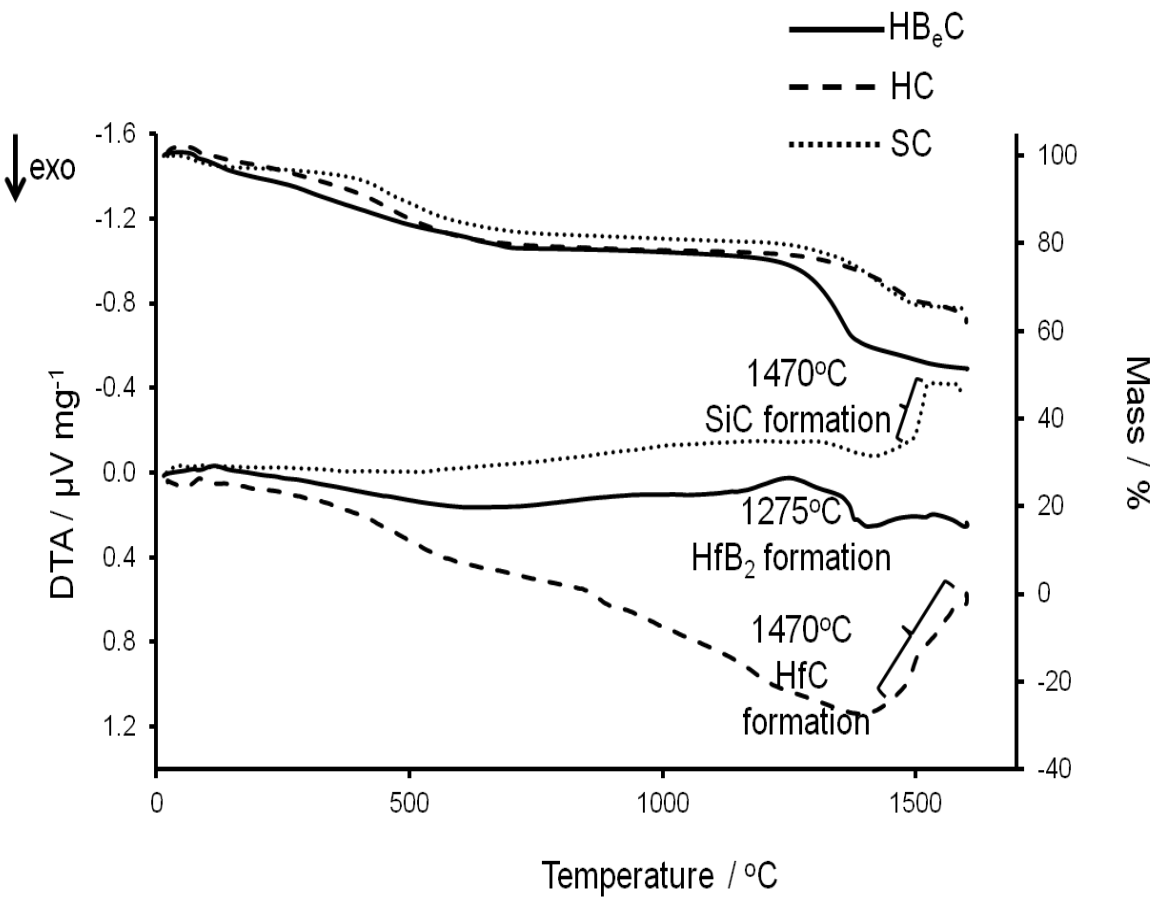

Figure 4.3: TGA/DTA of precursor powder HB_eC, HC and SC powders

For HB_eC the weight loss accelerated from 1275^{o}C and stabilized towards 1600^{o}C due to the onset of the boro/carbothermal reduction reaction, which is also indicated by the endothermic peak at 1275^{o}C in the DTA curve. For the HC and SC precursor the weight loss acceleration began at a higher temperature of 1470^{o}C and this feature in the TG curve was also accompanied by the endothermic peak in the DTA curve, indicating the carbothermal reduction reaction and the formation of HfC and SiC. This indicated that the carbide formation required a higher temperature than that required for HfB_2 formation.

4.2.4 SiC powders; Phase and microstructural analysis

Based on the TGA/DSC analysis of the SiC precursor powders, heat treatment of the SC and SC_e was carried out at 1500^{o}C for 1 h and 2 h with subsequent

XRD analysis. As seen from the XRD data, Figure 4.4, 1 h at 1500^{o}C was not sufficient to complete the carbothermal reduction reaction and peaks corresponding to SiO_2 and carbon were present. However, 2 h at 1500^{o}C gave pure SiC with 3C – cubic phase (JCPDS pattern number 29-1129) and about 3% of 6H – hexagonal phase (JCPDS pattern number 29-1128). The data for SC_e heat treated at 1500^{o}C for 2 h yielded a similar result as for SC, except for the additional expected carbon peak.

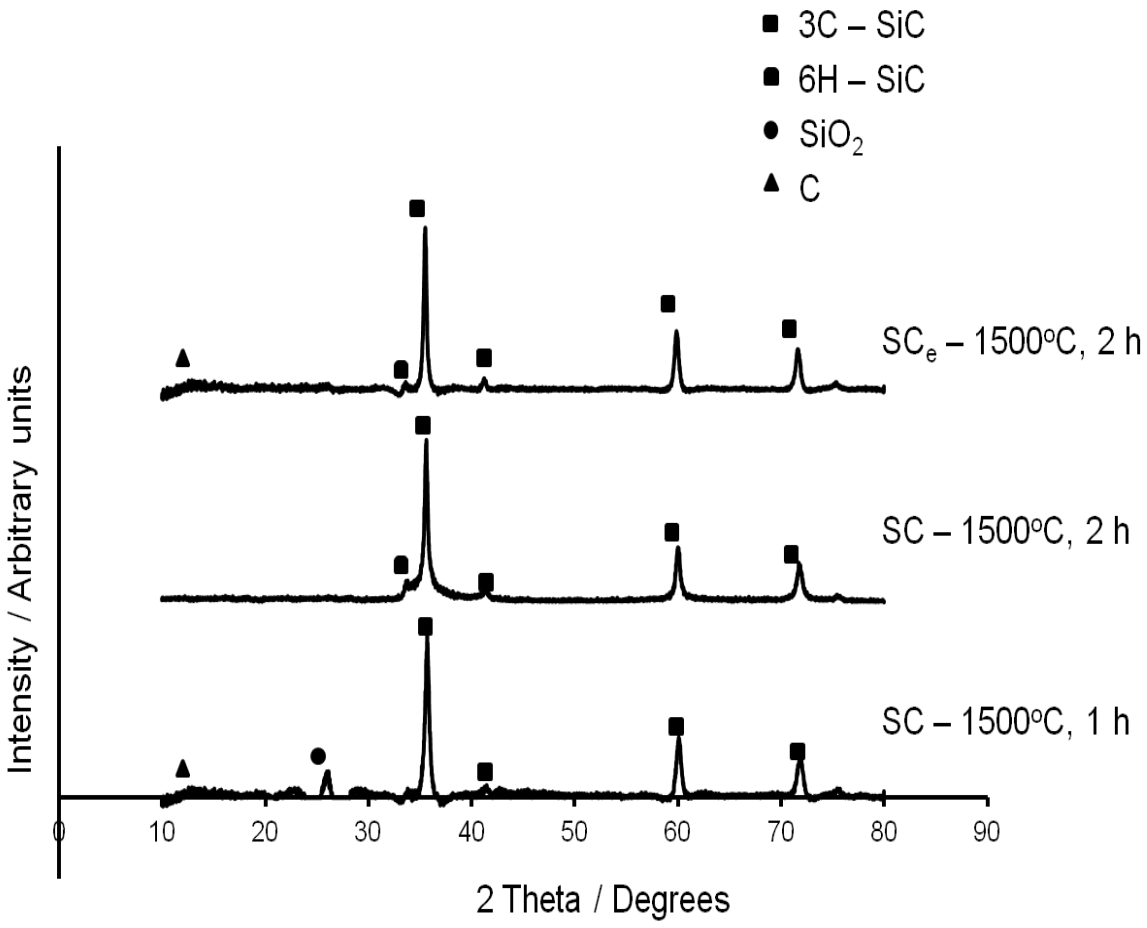

Figure 4.4: XRD data for SC and SC_e precursor powder heat treated at 1500^{o}C for 1 h and 2 h

TEM images of the SC precursor powder heat treated at 1500^{o}C for 2 h, Figure 4.5 a, show heavily agglomerated particles with a primary particle size of between 20 to 40 nm. Along with the spherical particles, which were

identified as 3C SiC using electron diffraction, there were also long rods, which were been identified as 6H SiC from their diffraction pattern.

The TEM image of SC_e precursor powder heat treated at 1500^oC for 2 h, Figure 4.5 b, reveals the SiC particles, both elongated and equiaxed, engulfed in a carbon matrix. The diffraction pattern of the same sample showed the amorphous carbon rings, (indexed on the left side), present along with the SiC rings, (indexed on the right). This image sheds some light on the structure of the precursors during heating where the phenolic resin decomposed into sheet like amorphous carbon with SiO_2 particles randomly embedded in it. Necking and agglomeration of the ceramic particles were prevented, as long as the amorphous carbon matrix remained in the system during the heat treatment. When the stoichiometric carbon was added as in the case of SC precursor powder, the absence of the excess carbon matrix in the later stages of the heat treatment caused the particles to agglomerate. This phenomenon was also observed in HfC and HfB_2 synthesis and is dealt with in detail in the following sections.

Another observation from the TEM images was the presence of two different morphologies of particles viz. rods and spherical particles. This indicates two different growth mechanisms namely, a solid-solid (Si-C) reaction resulting in spherical particles with a low stacking faults and a solid-gas (C-SiO gas) reaction yielding whisker morphology with a high stacking fault density (SFD) [240]. The low concentration of rods showed that the solid-solid mechanism is dominant.

Since SiC was synthesized mainly for coating purposes, which will be dealt in section 4.2, the work on powder synthesis was limited to phase and particle size analysis.

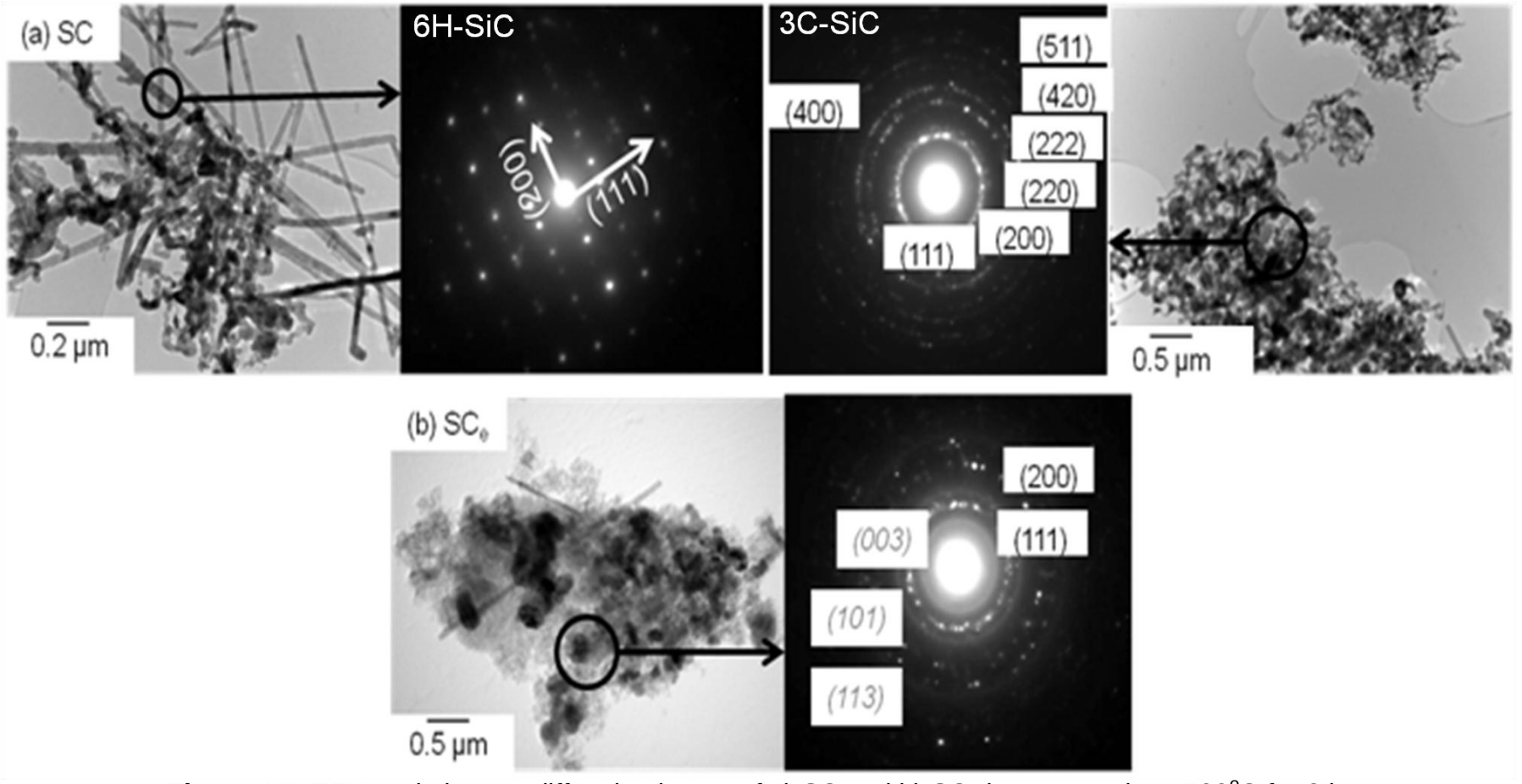

Figure 4.5: TEM and electron diffraction image of a) SC and b) SC_e heat treated at 1500^{o}C for 2 h

4.2.5 HfC powders; phase, microstructural and purity analysis

Figure 4.6 shows the XRD patterns for the HB_eC precursor powders heated from 600°C to 1500°C with a 0.1 h dwell. The results show that HfO_2 was formed at 650°C (JCPDS 00-03901491). At this temperature, the degradation of phenolic resin to carbon will also have been complete [241]. Therefore, at 650°C the powder mixture consisted of un-reacted but intimately mixed HfO_2 and C. By 1500°C HfC peaks formed (JCPDS 00-03400104), indicating the onset formation of HfC. This supports the TGA/DSC results in Figure 4.3, where the endothermic peak appeared at 1475°C.

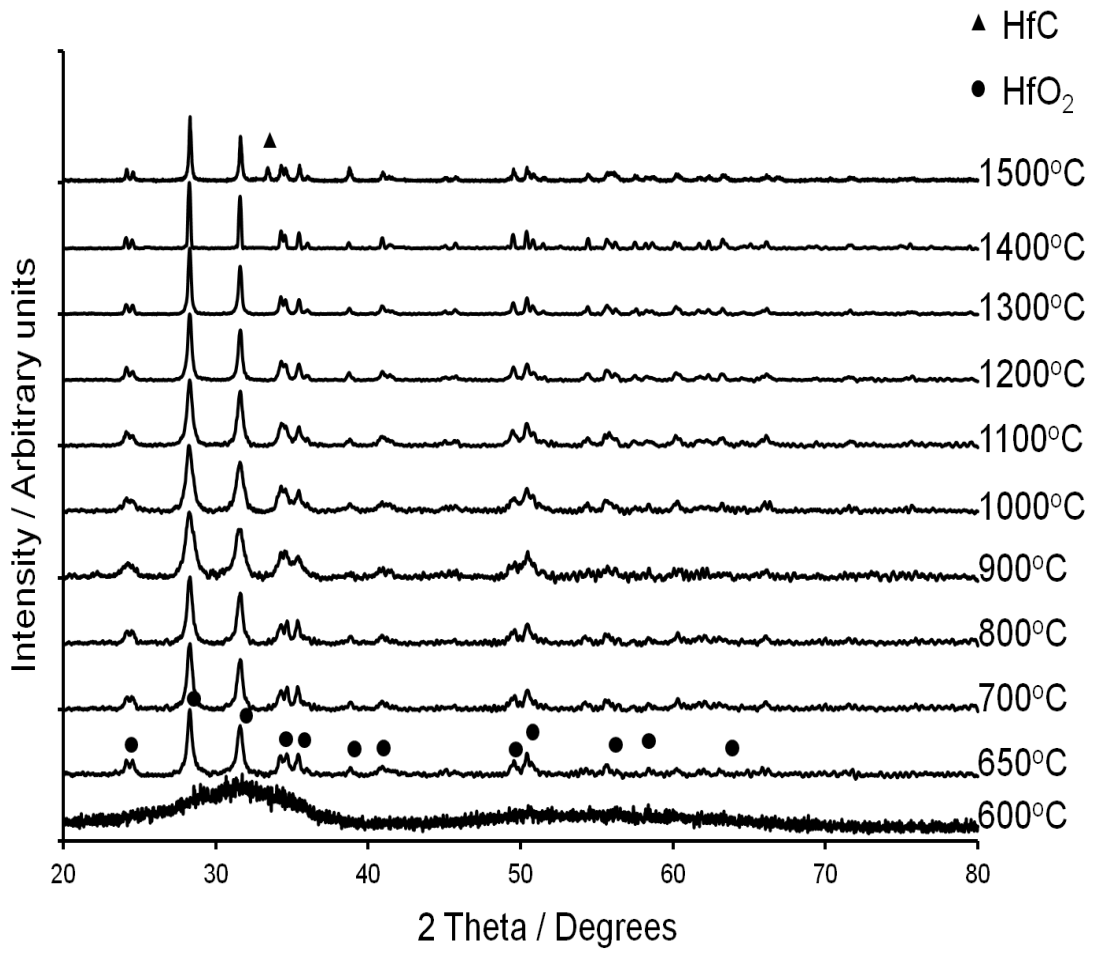

Figure 4.6: XRD patterns of the HC precursor powder heated from 600°C to 1500°C with a 0.1 h dwell

The percentages of HfO_2 present in these powders were calculated using the k value method [242], as shown in equation 4.3.

$$x_2 = \frac{1}{1 + I_1 K_1 / I_2 K_2} \tag{4.3}$$

where, x_2 is the 2nd phase's mass fraction, I_1 and I_2 are the relative intensities of 1st phase and 2nd phase's strongest diffraction peak respectively, and K_1 and K_2 are the reference spectral intensities of 1st phase and 2nd phase, respectively.

For cubic HfC and monoclinic HfO_2 the spectral intensities were K_1 16.98 and K_2 7.30 according to the JCPDS card numbers 00-039-1491 and 00-034-0104 respectively. Based on this data, HfO_2's mass fraction in HC precursor powder heat treated at 1500°C for 2 h and at 1600°C for 1 h was estimated to be 13% and 5% respectively. In order to achieve single phase face centred cubic HfC, 2 h at 1600°C was required.

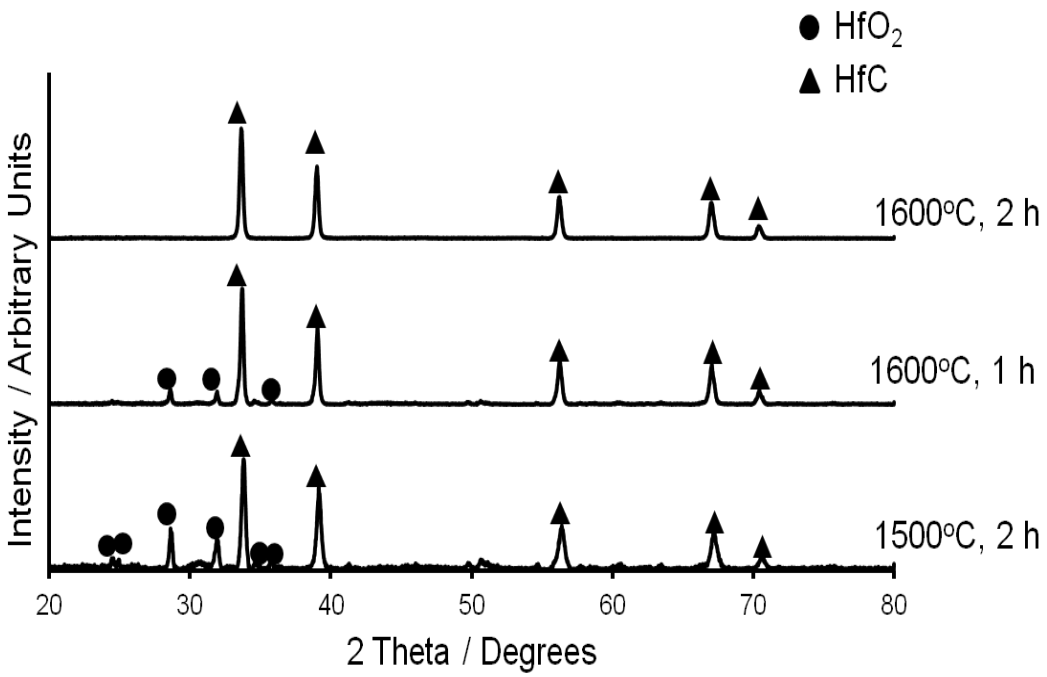

Figure 4.7: XRD of the HC precursor powder heat treated at 1500°C for 2 h and at 1600°C for 1 h and 2 h

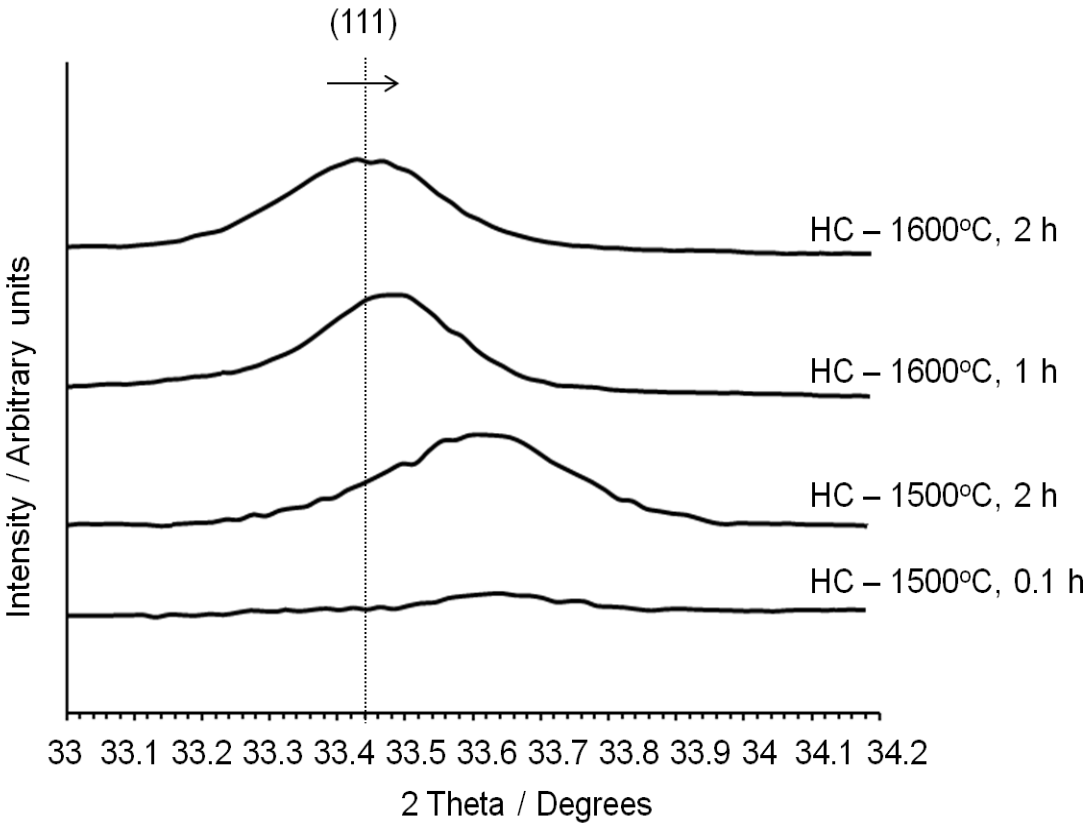

Figure 4.8: 2 Theta position of the (111) diffraction peak for HC sample heat treated at 1500^{o}C 0.1 h, 1500^{o}C 2 h, 1600^{o}C 1 h and 1600^{o}C 2 h

Figure 4.8 shows the shift in the 2 theta position of the strongest diffraction peak (111) of HfC with the heat treatment time and temperature. Increase in the temperature caused the reflection peaks to shift towards the low angle direction, with the 2 theta of the (111) peak of the sample heat treated at 1600^{o}C for 2 h positioned at 33.44 degrees. As reported in the literature [243], the peak shift was due to the change in the lattice parameter of HfC arising from the change in composition, i.e. the presence of dissolved oxygen in the HfC unit cell with high concentrations of oxygen producing larger shifts. The lattice parameter[iv] 'a' as calculated for the HfC samples synthesized at 1500^{o}C for 0.1 h, 1500^{o}C for 2 h and 1600^{o}C for 1 h were 0.4613, 0.4615, 04634 nm respectively. These values are lower than those reported for stoichiometric

[iv] λ=0.154056 nm, n =1; $d_{33.44}$ = 0.26773, $a_{33.44}$ =0.46372; $d_{33.46}$= 0.26758, $a_{33.46}$=0.4634; $d_{33.6}$=0.26649 $a_{33.6}$= 0.4615; $d_{33.62}$=0.26634, $a_{33.62}$=0.4613.

HfC by Gusev et.al. [244] (0.46408 nm) and JCPDS card number 00-039-1491 (0.4637 nm). However, the lattice parameter 'a' for the sample heat treated at 1600^{o}C for 2 h matched the JCPDS value of 0.46372 nm and was believed to have the stoichiometric Hf:C ratio whilst the other samples had a small amount of dissolved oxygen in them giving rise to an HfC_xO_y (y=1-x) intermediate compound. Thus the carbothermal reduction of HfO_2 has an intermediate reaction stage indicating the slow displacement of oxygen and the formation of intermediate hafnium oxy-carbide. This data explains the slow and steady weight loss occurring from 1400^{o}C to 1600^{o}C in the TGA thermogram for the HC precursor, (refer to Figure 4.3).

Figure 4.9 shows the FEGSEM image for HC and HC_e precursor powders heat treated at 1600^{o}C for 2 h. HC precursor powder after heat treatment has a particle size of 1 to 2 µm and there were no other visible impurities. However, the HC_e precursor powder, which had a greater stoichiometric amount of carbon initially, comprised of nanometer sized HfC particles and free carbon, as confirmed by EDX analysis. The excess carbon when present in the system acted as a separator and prevented the particles from agglomeration and growth.

Figure 4.10 shows the TEM images of different stages of HfC formation from HC precursor powder. As seen in the image, the dark HfO_2 particles were engulfed in the grey carbon matrix in a similar manner to the SiC. At carbothermal reduction temperatures carbon slowly reduces HfO_2 to HfC and leaves the system as CO.

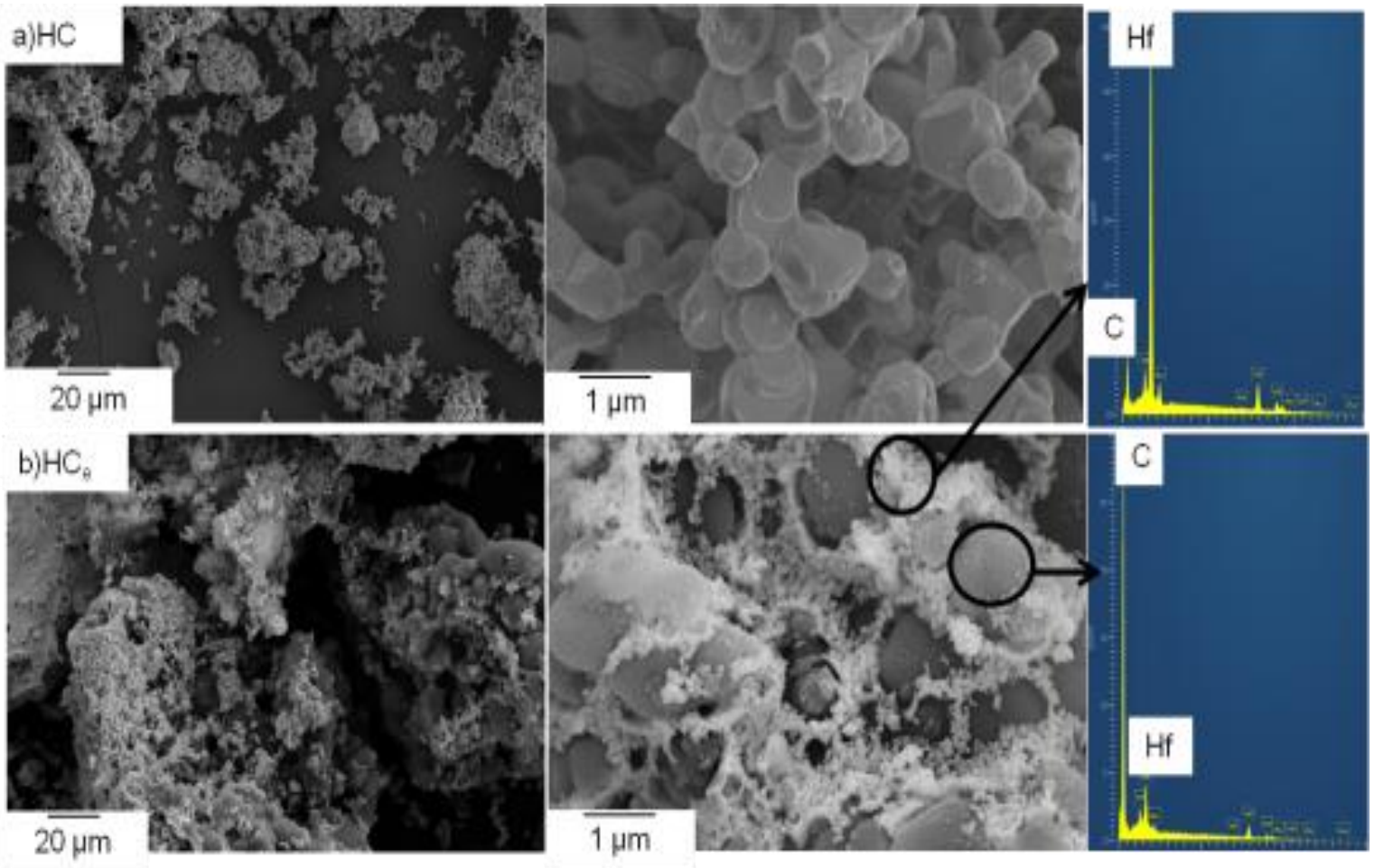

Figure 4.9: FEGSEM images of a) HC and b) HC_e precursor powders heat treated at 1600^{o}C for 2 h

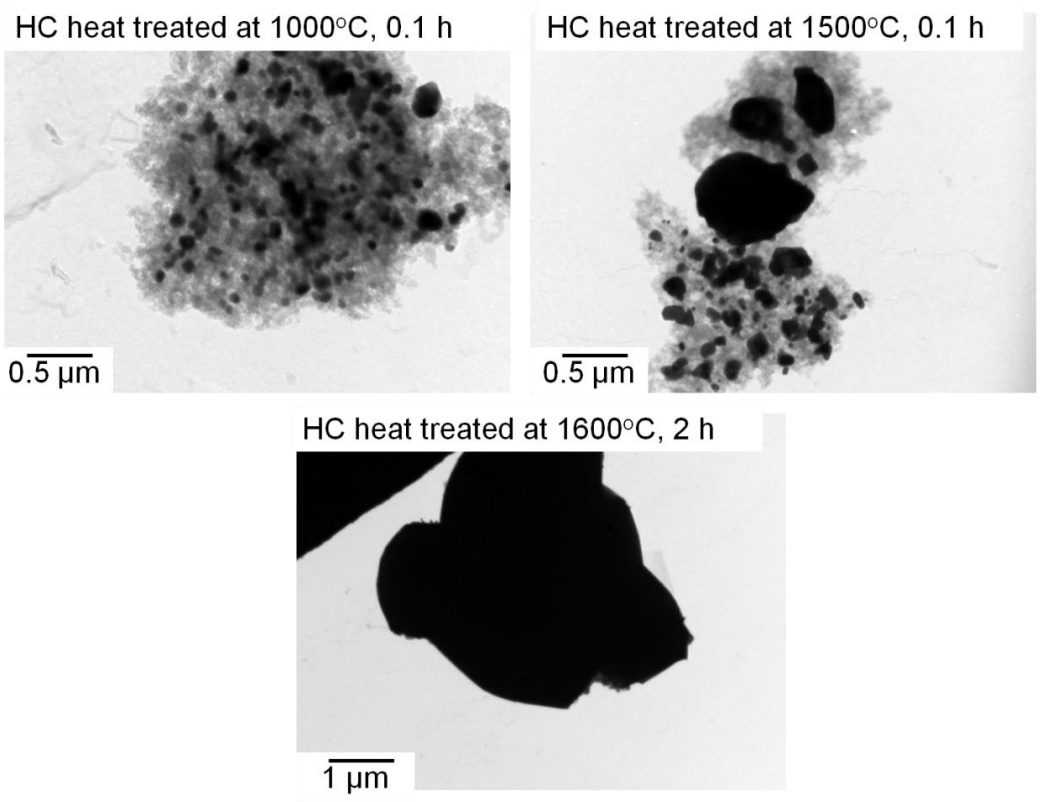

Figure 4.10: TEM images of HC precursor powder heat treated at a) 1000°C and b) 1500°C for 0.1 h and at c) 1600°C for 2 h

The formation mechanism of HfC is a simple substitution reaction and can be explained by Figure 4.11. The oxygen in HfO_2 was slowly displaced and substituted by carbon, which led to the formation of an oxy-carbide and carbon mono-oxide gas. Subsequent displacement and substitution resulted in depletion of the free carbon and formation of stoichiometric HfC. Upon complete depletion of free carbon, which was responsible for prevention of agglomeration, the particles began to coalesce and grow/agglomerate, for as long as the required thermal energy was available.

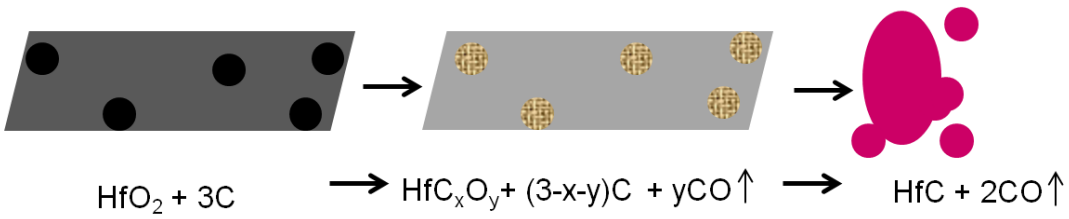

Figure 4.11: The schematic process for the HfC formation mechanism

Figure 4.12a shows the TEM image of HC_e precursor powder heat treated at 1600^oC for 2 h, yielding a particle size of 60 to 80 nm. The HfC particles and the excess carbon were mapped with the help of electron diffraction. Since the presence of excess carbon was required to produce nanometer sized particles and the absence of it lead to agglomeration and growth, resulting in micrometer sized particles, HfC was first synthesized using excess carbon precursor and was later subjected to a heat treatment at 550^oC in air for 16 h to remove the excess carbon. The TEM image of the resulting HfC particles is shown in Figure 4.12b. Although the heat treatment retained the particle size in the nanometer scale, surface oxidation of the high surface energy nano-particles was suspected.

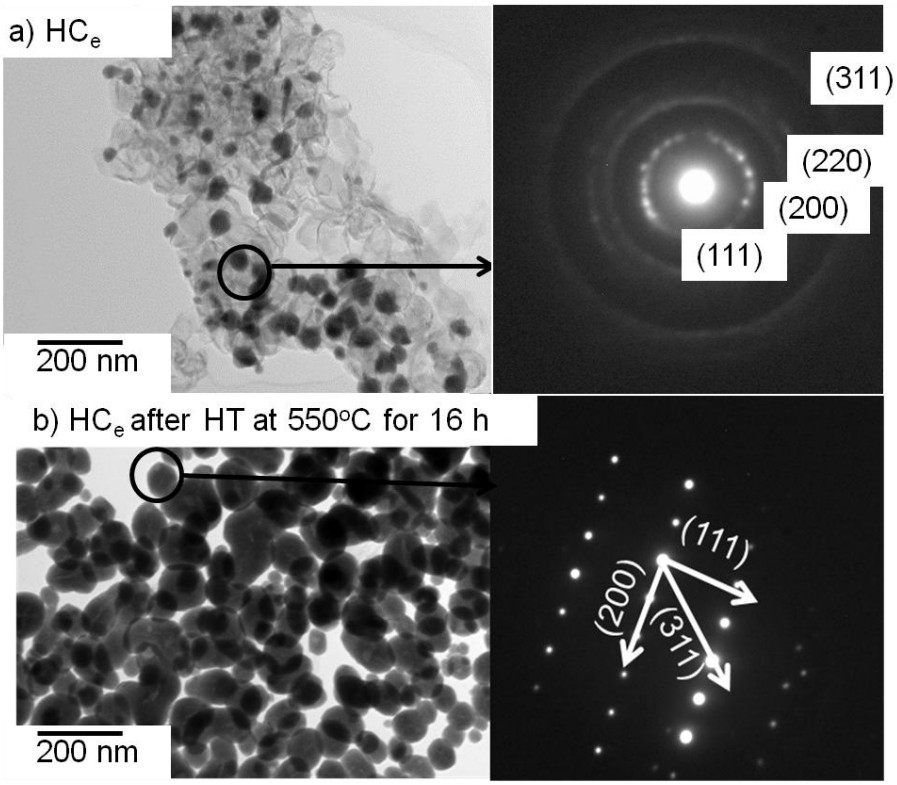

Figure 4.12: TEM image and electron diffraction pattern of HC_e precursor powder heat treated at 1600^oC, 2 h a) before carbon removal, b) after carbon removal at 550^oC for 16 h in air

X-Ray photoelectron spectroscopy analysis was carried out on the HfC powders synthesized from HC_e precursor powders, before and after carbon

removal, to check for surface oxidation. Whilst the intensity of the carbon peak decreased after the carbon removal step, a peak corresponding to 1s shell of oxygen had appeared, as shown in Figure 4.13a. The peak corresponding to the 4f orbital of Hf was present at 17.7 eV before the carbon removal step indicating an Hf-B bond whilst after the carbon removal an additional peak at 16.7 eV corresponding to an Hf-O bond appeared, Figure 4.13b.

Although the additional heat treatment step following the carbothermal reduction at 1600^{o}C, 2 h for HC_e precursor powder helped to retain the nanometer particles, the surface of the particles underwent undesired oxidation.

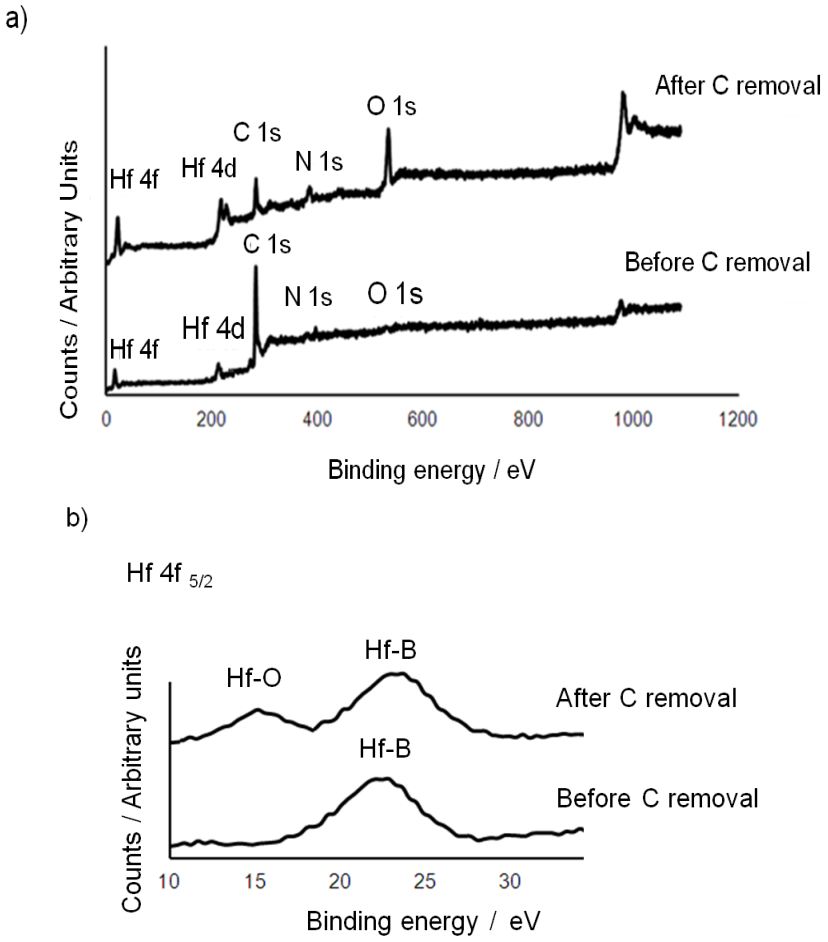

Figure 4.13: a) XPS spectra of HC_e precursor powder heat treated at 1600^{o}C, 2 h before and after carbon removal, b) peaks corresponding to Hf $4f_{5/2}$ orbital before and after carbon removal

At this stage of the research program, it was decided to focus entirely on HfB_2 processing, as it was proved to be the best candidate for protecting carbon from oxidative ablation by Dr. Anish Paul as mentioned earlier, (section 2.4.2.6).

4.2.6 HfB_2 powders; phase, microstructural and purity analysis

4.2.6.1 Synthesis: time and temperature effect

Figure 4.14 shows the XRD patterns for the HB_eC precursor powders heated from 600^{o}C to 1500^{o}C with a 0.1 h dwell. The results show that HfO_2 was formed at 650^{o}C. At this temperature, the degradation of phenolic resin to carbon and dehydration of boric acid to boron trioxide will also have been complete [241]. Therefore at 650^{o}C, the powder mixture consisted of un-reacted but intimately mixed B_2O_3, HfO_2 and C. At 1300^{o}C HfB_2 peaks formed, indicating the onset formation of HfB_2 which is in support of the TGA/DTA results in Figure 4.3, where an endothermic peak appeared at 1275^{o}C.

Figure 4.15 shows the indexed XRD patterns of HBC and HB_eC calcined at 1600^{o}C for 2 h. The patterns were indexed according to the JCPDS cards 00-039-1491 and 00-038-1398 for HfC and HfB_2 respectively. It can be seen that the pattern corresponding to the HBC precursor, which was made using the stoichiometric mix of the 3 elements, includes significant amounts of HfC impurity, whilst the HB_eC XRD pattern shows only HfB_2 peaks. This confirms the need to include excess B in the initial mix to allow for B_2O_3 losses by vaporization, as observed by Ni et.al.[6]. The boron loss depended on various random factors like Cl^- ions trapped in the system during sol-gel processing (Cl^- ions can react with B_2O_3 at 550^{o}C to form volatile BCl_3, thus depleting the boron concentration), extent of reaction between H_3BO_3 and ethanol to form volatile ethyl borate, flow rate of the inert gases, and the substrate used. For this reason the ratio of B:Hf was kept between 3:1 and 3.8:1 instead of 2:1 for subsequent compositions.

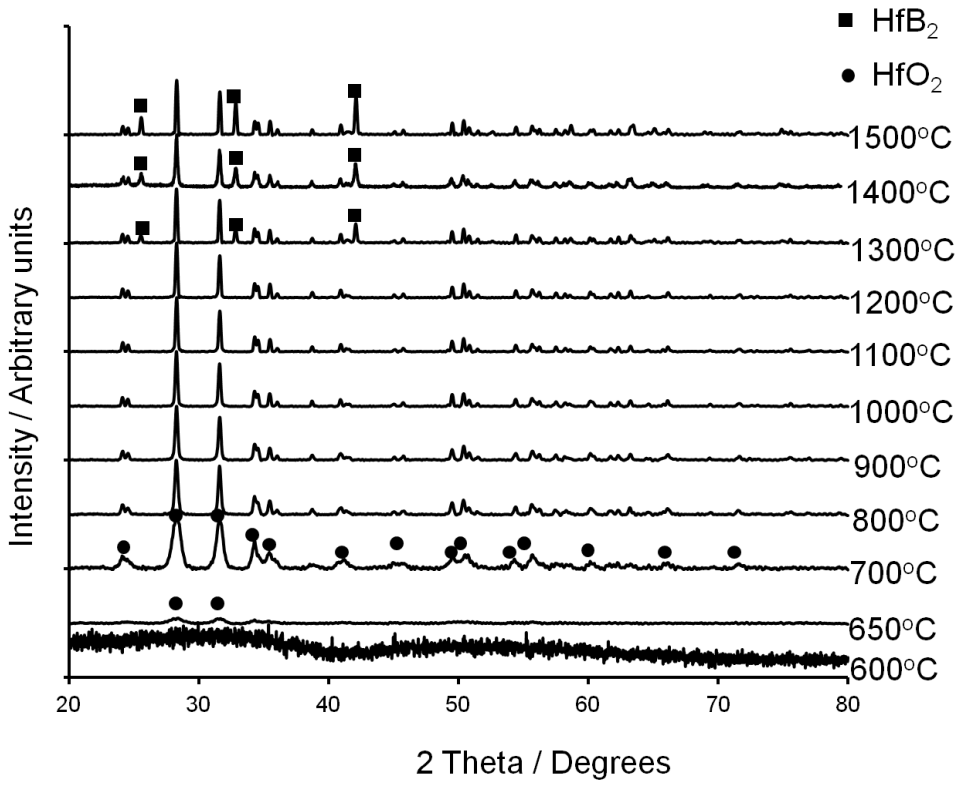

Figure 4.14: XRD patterns of the HB_eC precursor powder heated from 600°C to 1500°C with a 0.1 h dwell

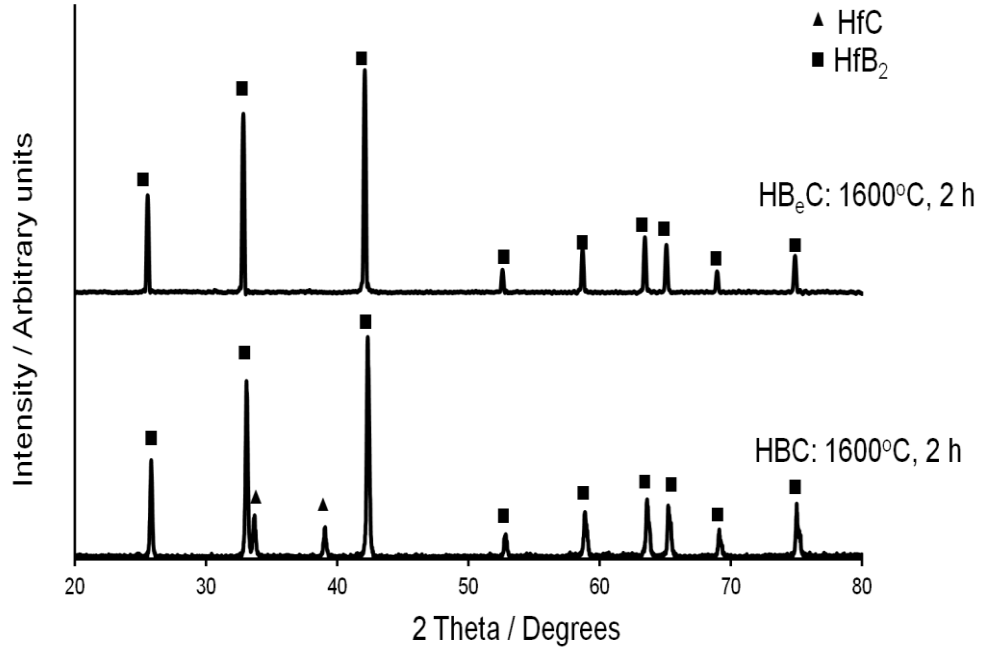

Figure 4.15: XRD patterns of the HBC and HB_eC precursor powders calcined at 1600°C for 2 h

Both isothermal TGA, Figure 4.16, and subsequent heat treatment in the tube furnace, revealed that 25 h was needed at 1300^{o}C to complete the boro/carbothermal reaction and achieve hexagonal HfB_2 with no secondary phases, (refer to Figure 4.17); only 2 h was required at 1600^{o}C. This bit of work was done at Wright Patterson Airforce Research Laboratories (WPAFB), Dayton, Ohio, following which second trials were carried out at Loughborough.

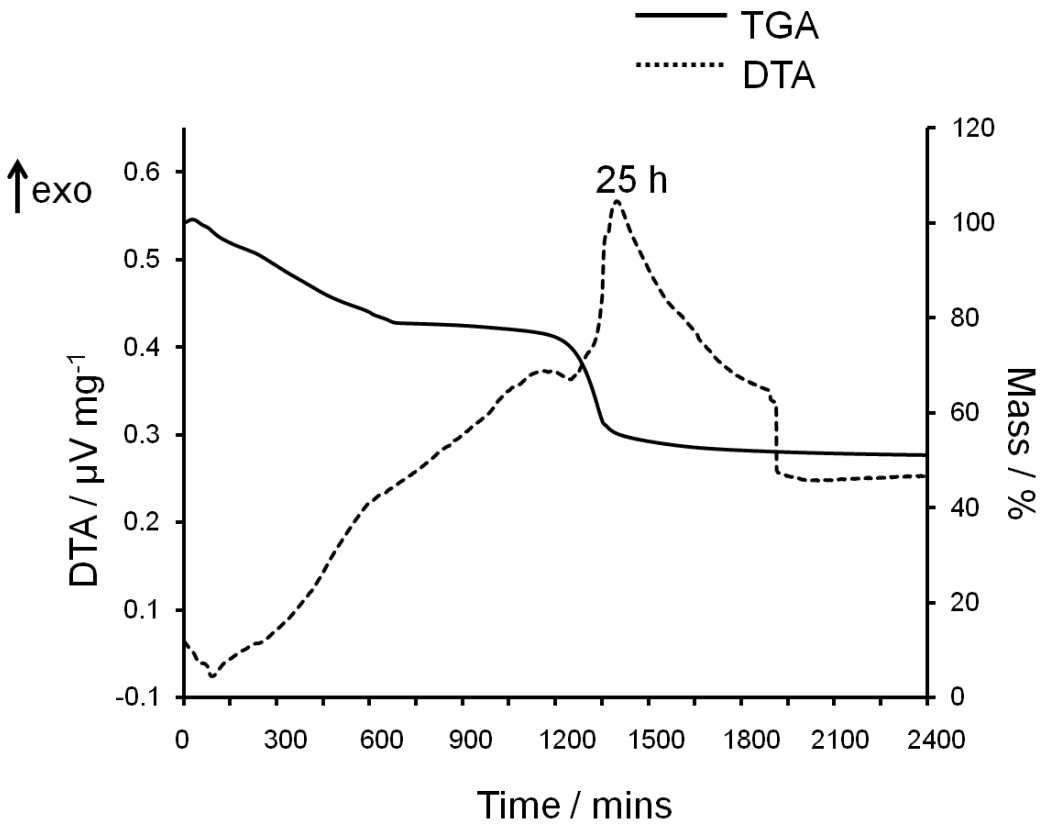

Figure 4.16: Isothermal TGA/DTA of HB_eC precursor powders at 1300^{o}C

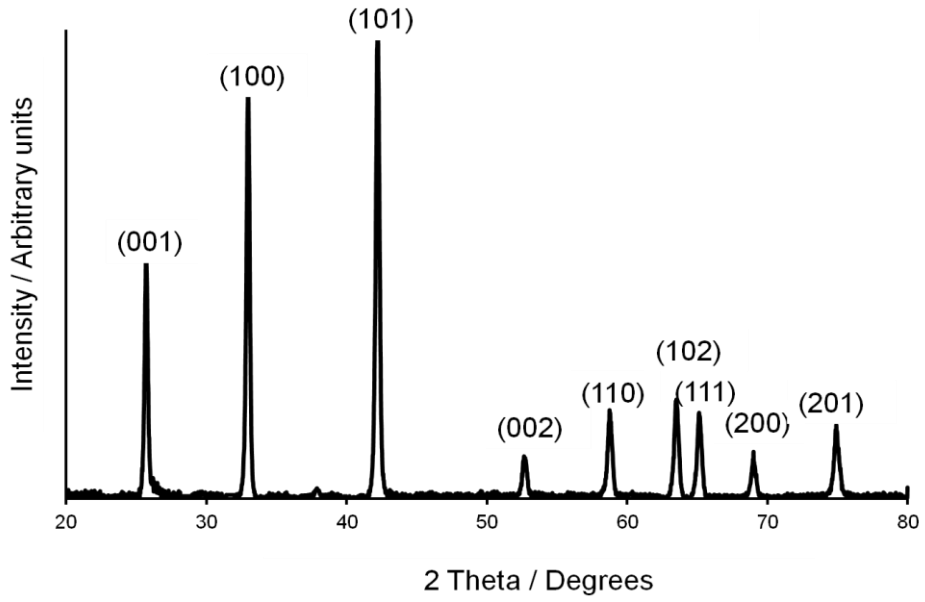

Figure 4.17: XRD of HB_eC precursor powder calcined at 1300^oC for 25 h

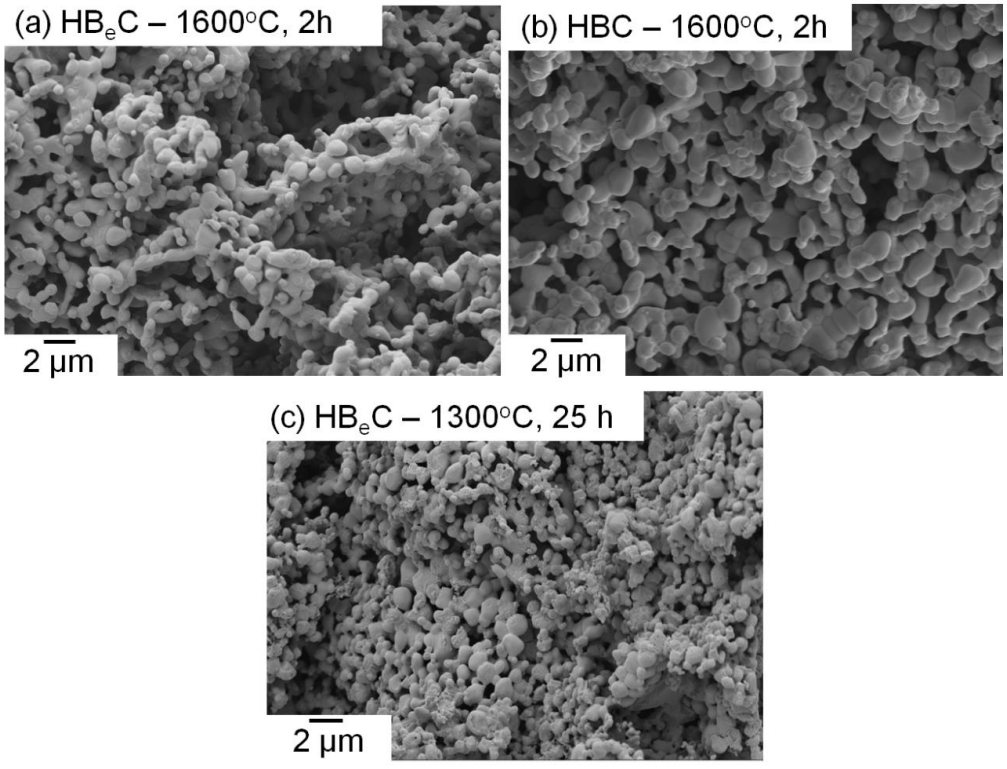

Figure 4.18: FEGSEM micrographs showing the particle morphology for (a) HB_eC, (b) HBC, calcined at 1600^oC for 2 h (c) HB_eC calcined at 1300^oC for 25 h

As seen from Figure 4.18, the products from HB_eC and HBC have a very similar particle size of about 1 to 2 µm indicating that an increase in boron oxide content does not have any effect on the particle size of the end product. On the other hand, lowering the synthesis temperature from 1600^oC to 1300^oC and increasing the dwell time from 2 to 25 h, resulted in a slight decrease in particle size, the size of the particles obtained from HB_eC ranged from 0.25 to 2 µm, but also yielded a high proportion of rod shaped particles, (refer to Figure 4.19a). It is believed that the particles grow into rods due to the long heating time involved, with the growth occurring along the c-axis, Figure 4.19b. The mechanism of this growth is dealt with in section 4.1.6.4. Similar structures were reported by Begin et al. [245] when they synthesized HfB_2 through mechanical activation. As determined by elemental CHN analysis, the percentage of carbon in this powder was around 0.19%.

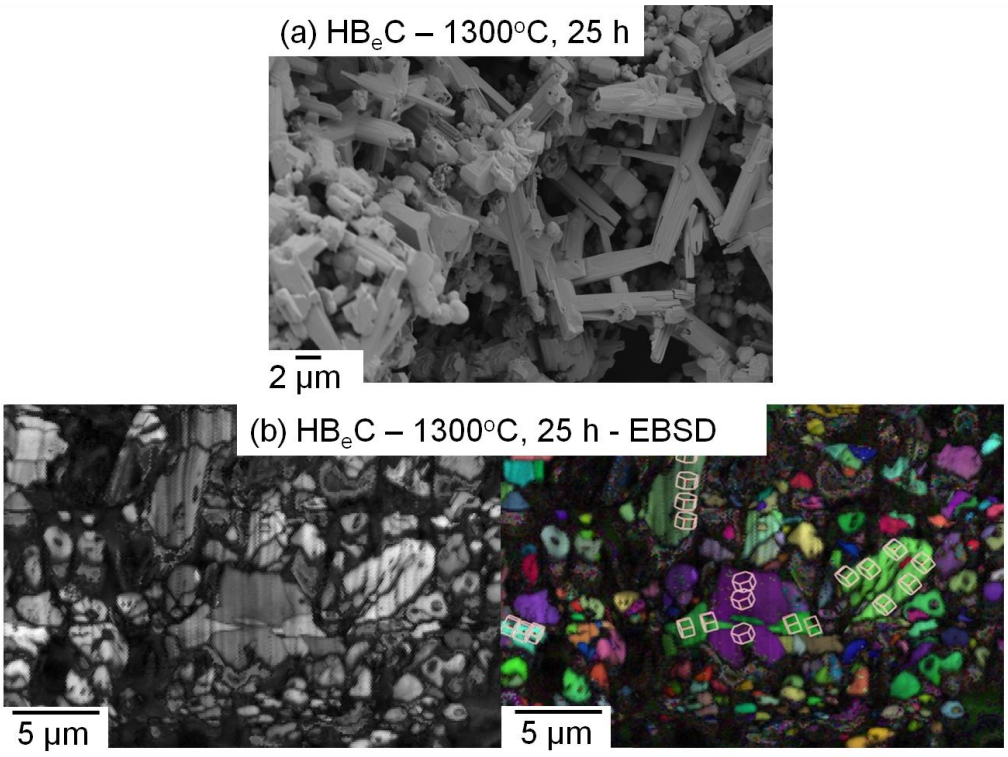

Figure 4.19: a) FEGSEM of HB_eC calcined at 1300^oC for 25 h showing rod shaped particles, b) FIB and EBSD image of 'a'

Figure 4.20 shows the FIB-cut rod and its electron diffraction pattern confirming the structure of the rod as hexagonal HfB_2.

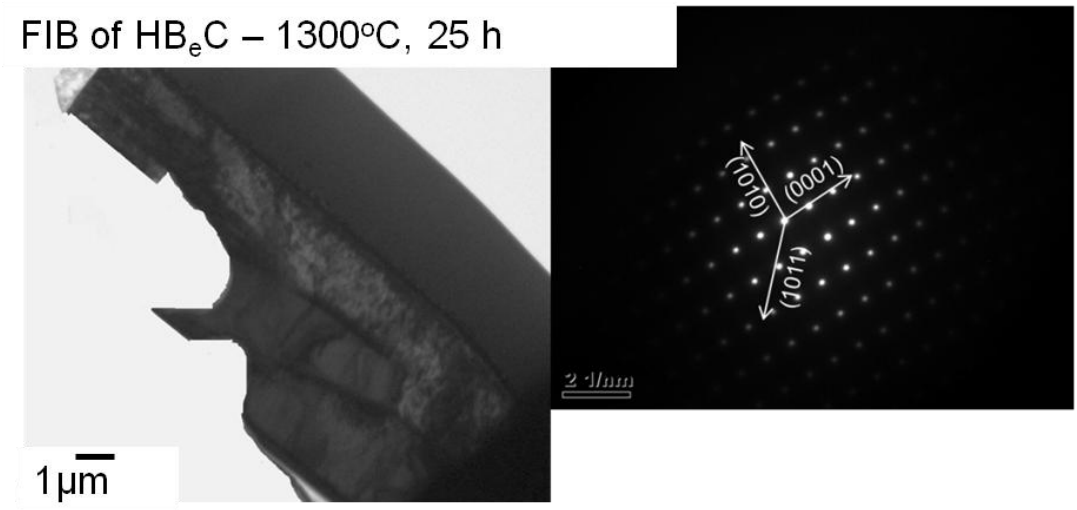

Figure 4.20: FIB machined HfB_2 rod and the corresponding electron diffraction pattern

4.2.6.2 Effect of varying the Hf:B and Hf:C molar ratio

No HfB_2 formation was observed after heat treating HB at 1600°C for 5 h; the end product consisted of HfO_2 rod like particles and B_2O_3 melt, see Figure 4.21; as identified by EDX. This confirms, that without carbon, no reduction reaction occurs in the system, i.e. carbon plays an important role in creating the reducing conditions required for HfB_2 formation.

In the presence of excess carbon, HB_eC_e, the end product contained both HfB_2 and ~25% free carbon, as determined by elemental CHN analysis, Figure 4.22a. Interestingly, the size of the HfB_2 particles was only 20 to 30 nm. The presence of the free carbon in the HB_eC_e system again appears to act as a barrier, preventing particle growth and yielding much finer HfB_2 compared to the other powders synthesised. Without free carbon, the particles are free to grow in size during calcination. Similar results were reported by Krishnarao et. al. [246] during TiB_2 synthesis and were also observed in this work on HfC and SiC powders. Reaction 4.4 represents the excess C respectively:

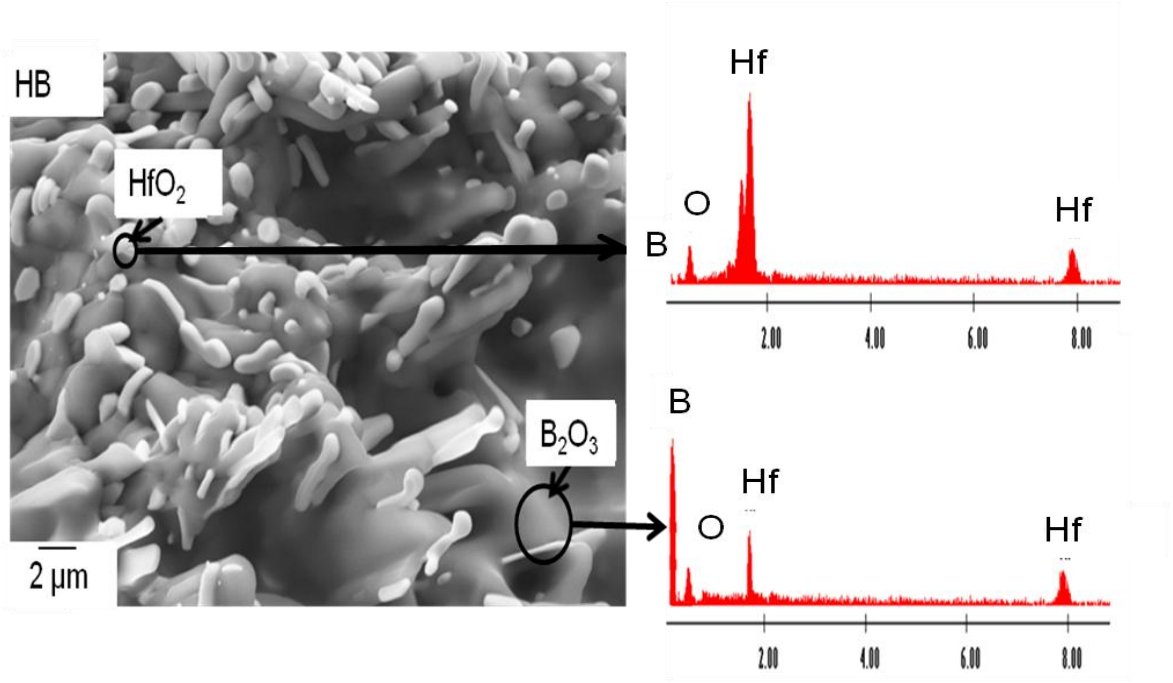

Figure 4.21: HB precursor powder heat treated at 1600°C for 2 h, showing HfO_2 and B_2O_3 phases

With excess carbon

$$HfO_2 + B_2O_3 + (5+x)C \rightarrow HfO_2 + 2B + (2+x)C + 3CO\uparrow \rightarrow HfB_2 + xC + 2CO\uparrow \quad (4.4)$$

Similar to the HfC work, the attempt to retain the nanometer sized HfB_2 particles, was carried out by first carbothermally reducing HB_eC_e precursor at 1600°C for 2 h, with a subsequent carbon removal step at 550°C for 16 h. 20 to 30 nm sized particles free from carbon was obtained after this step as shown in Figure 4.22b.

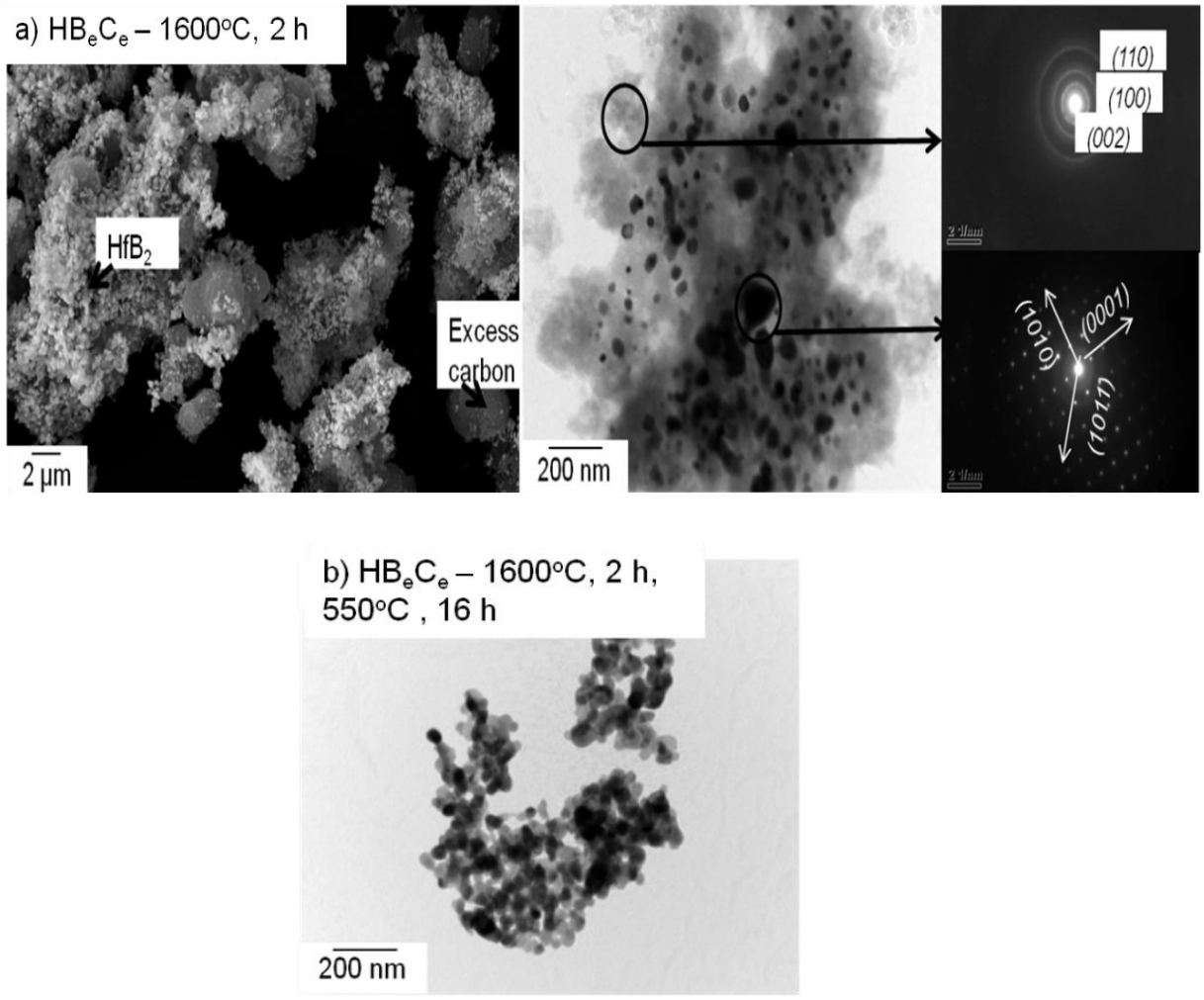

Figure 4.22: TEM image of HB_eC_e precursor powder heat treated at 1600°C for 2 h, a) before C removal showing HfB_2 and C phases along with the electron diffraction patterns and FEGSEM image, b) after C removal

Raman analysis, which has high sensitivity for carbon, was carried out on the powders before and after carbon removal to check for decrease in carbon content, see Figure 4.23. A significant decrease in carbon was observed.

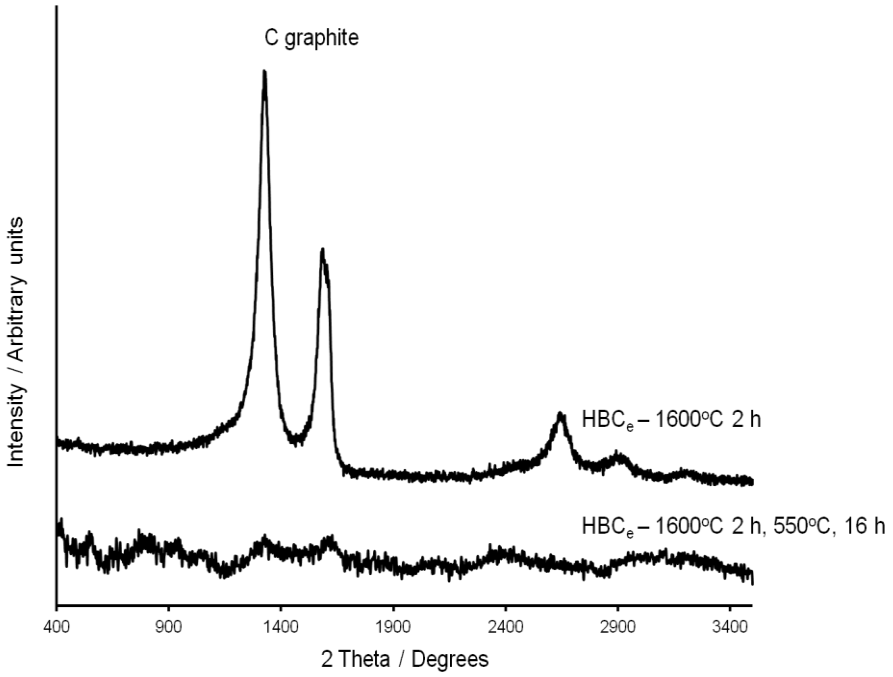

Figure 4.23: Raman analysis on HB_eC_e powders calcined at 1600°C for 2 h before and after C removal

However, surface oxidation of the nano-particles with high surface energy was suspected and the same was confirmed through surface analysis using XPS, see Figure 4.24.

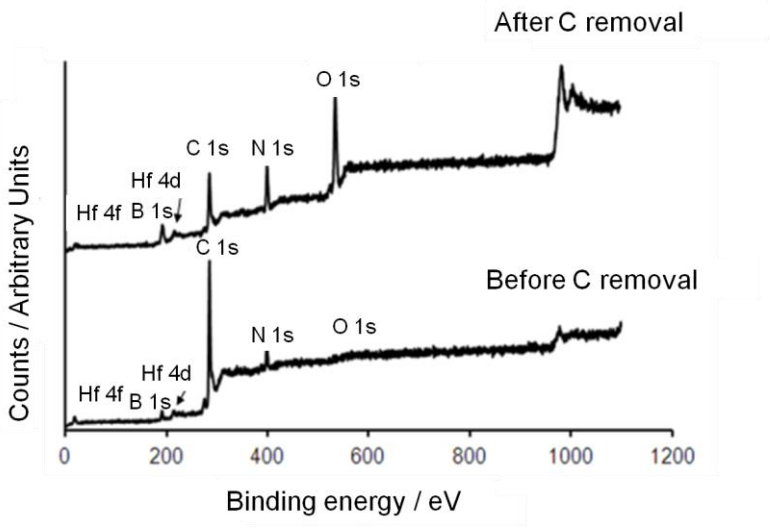

Figure 4.24: XPS spectra of HB_eC_e precursor powder heat treated at 1600°C, 2 h before and after carbon removal

On the other hand, if both excess boron and carbon were used, $HB_{e1}C_e$, then boron carbide was formed, see Figure 4.25, and the HfB_2 particles were 1 to 2 µm in size.

With excess boron and carbon:

$$HfO_2 + zB_2O_3 + yC \rightarrow HfO_2 + 2xB + (y-3z)C + 3zCO\uparrow \rightarrow \quad (4.5)$$

$$HfB_2 + z/13(12B(B\text{-}C\text{-}B)) + 2CO\uparrow$$

(y= 5+x; z= 3+x and x is the extra amount needed)

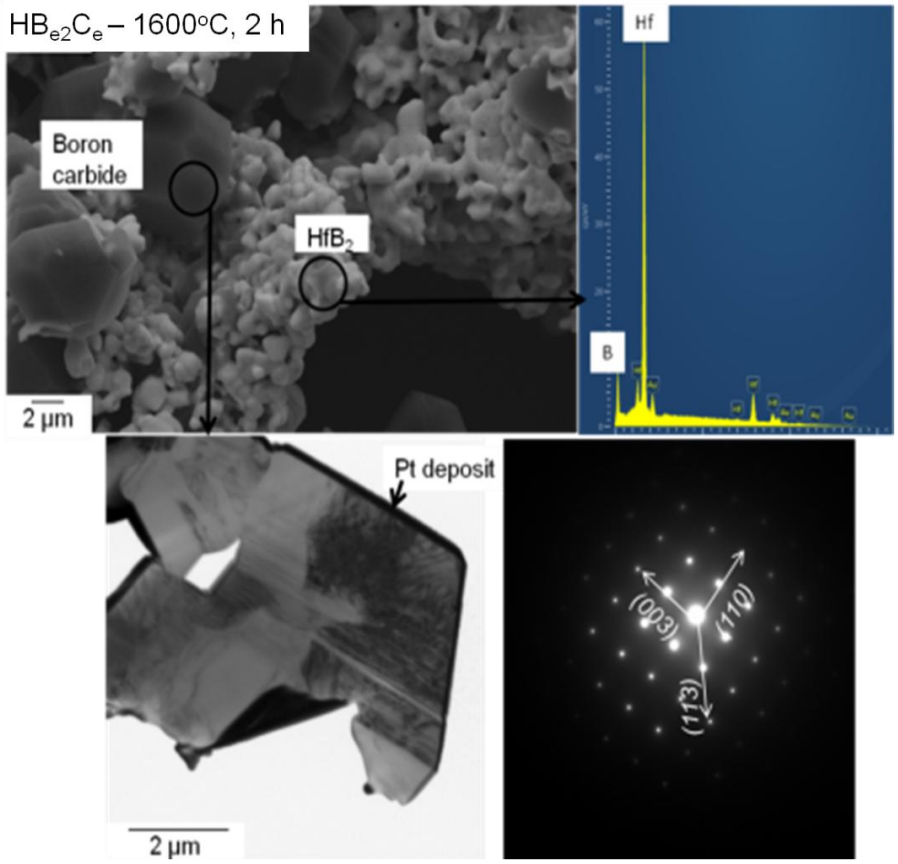

Figure 4.25: $HB_{e2}C_e$ precursor powders, calcined at 1600°C for 2 h showing EDS spectrum of HfB_2 particles and FIB'ed section of faceted boron carbide and its electron diffraction pattern.

The faceted boron carbide structure was $B_{13}C_2$ with icosahedron B_{12} and a B/C ratio of 6.5. The formation of this phase of boron carbide is only possible if active boron vapours were present in the system, i.e. B_2O_3 was reduced by carbon to form B* [247]. This was an important observation that was later used to explain the reaction mechanism of HfB_2, in the following section. A similar structure of boron carbide, was also observed by Zhang et.al.[247] after carbothermal reduction of B_2O_3.

4.2.6.3 Reaction Mechanism

For any reaction to be thermodynamically favourable and spontaneous the Gibbs free energy (ΔG) of the reaction should be negative. For reaction 4.6,

$$HfO_2 + B_2O_3 + 5C \rightarrow HfB_2 + 5CO\uparrow \quad (4.6)$$

ΔG is negative only at >1523^{o}C, as calculated using Factsage 6.1. However, it has been shown that HfB_2 forms at a temperature as low as 1300^{o}C. In order to explain this difference, the mechanism by which HfO_2, B_2O_3 and C react to form HfB_2 was studied in detail.

There are three possible routes by which these three reactants could form HfB_2; they are indicated below as reactions 4.7, 4.8 and 4.9. Note that the latter has some variations within it.

$$HfO_2 + B_2O_3 + 5C \rightarrow HfC + B_2O_3 + 3C + 2CO\uparrow \rightarrow HfB_2 + 3CO\uparrow \quad (4.7)$$

$$HfO_2 + B_2O_3 + 5C \rightarrow HfO_2 + \tfrac{1}{2}B_4C + 1.5C + 3CO\uparrow \rightarrow HfB_2 + 2CO\uparrow \quad (4.8)$$

$$HfO_2 + B_2O_3 + 5C \rightarrow HfO_2 + 2B \text{ or } B_2O_2 + 2C \text{ or } 4C + 3CO \text{ or } CO\uparrow \rightarrow HfB_2 + 2CO \text{ or } 4CO\uparrow \quad (4.9)$$

The intermediate reactions 4.7i, 4.8i and 4.9i are given below, along with when their ΔG values are less than zero, i.e. when the reaction is thermodynamically favourable.

$$HfC + B_2O_3 + 3C \rightarrow HfB_2 + 3CO\uparrow \qquad \Delta G < 0 \text{ above } 1425^oC \qquad (4.7i)$$

$$HfO_2 + \tfrac{1}{2}B_4C + 1.5C \rightarrow HfB_2 + 2CO\uparrow \qquad \Delta G < 0 \text{ above } 1453^oC \qquad (4.8i)$$

$$HfO_2 + 2B \text{ or } B_2O_2 + 2C \text{ or } 4C \rightarrow HfB_2 + 2CO \text{ or } 4CO\uparrow \qquad \Delta G < 0 \text{ above } 1350^oC \qquad (4.9i)$$

Hence, based on thermodynamic calculations, the only reaction that has a realistic chance of leading to HfB_2 formation at ~1300^{o}C, is reaction 4.9. Note that at higher temperatures, e.g. above ~1450^{o}C, there may be more than one reaction path.

If the mechanism of formation of HfB_2 were to proceed through reaction 4.7, then HfC should form at a much lower temperature than HfB_2. From Figure 4.14 it can be seen that HfC peaks did not appear even at 1500^{o}C, though in theory this could be due to the HfC being consumed immediately as it is formed. However, even when HC precursor powder containing only Hf and C were heated from 600^{o}C to 1500^{o}C with 0.1 h dwell and subjected to XRD analysis, as shown in Figure 4.6, HfO_2 formation occurred at 650^{o}C but HfC peaks only began to appear at 1500^{o}C. Blum et al. [248] observed that there was a kinetic preference and a lower threshold temperature for the onset of the reaction of Hf with B powder compared to the reaction with C powder. The present work shows that the same also occurs for the reaction between HfO_2 and B or C. Hence it is concluded that HfC is not an intermediate product during HfB_2 synthesis, suggesting that reaction 4.7 is not the correct formation mechanism.

When the $HB_{e2}C_e$ precursor powder was calcined, there was clear evidence of HfB_2 formation at 1300°C, as for the HB_eC. However, although no boron carbide phases were detected by XRD, even after heat treatment at 1600°C for 2 h, Figure 4.26, they were detected by electron microscopy, Figure 4.25, and EDX and electron diffraction analysis revealed the presence of both boron and carbon in the faceted phase. The amount of the boron carbide phase was probably below the level for XRD detection, especially given the low X-ray density of boron carbide in comparison with hafnium-based compounds.

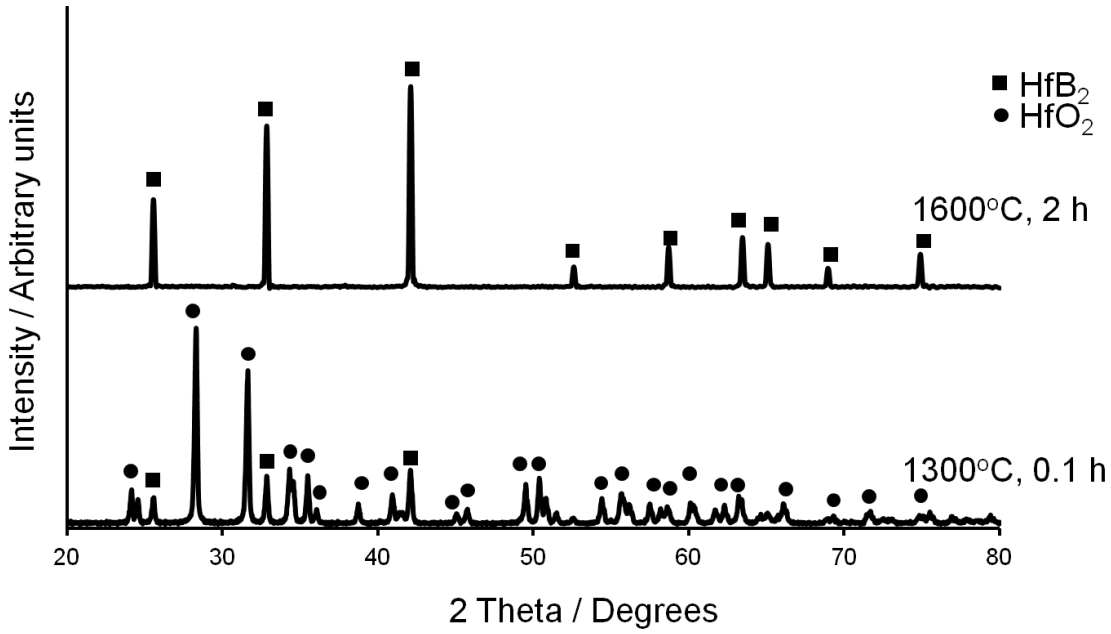

Figure 4.26: XRD of the $HB_{e2}C_e$ precursor powder calcined at 1300°C for 0.1 h and 1600°C for 2 h

Reaction 4.8 requires that carbon reacts with B_2O_3 to form B_4C as an intermediate product, which subsequently reacts with HfO_2 to form HfB_2. If this is the case then B_4C has to form below 1300°C, i.e. at a temperature lower than that required for HfB_2 formation. Since potential boron phases were not detected by XRD when they occurred in combination with a heavy metal compound, a composition containing only boron and carbon was synthesized ($B_{e2}C_e$). The carbothermic reduction sequence of B_2O_3 is presented by reactions 4.10-4.13 [249,250].

$$B_2O_3 + C \rightarrow B_2O_2 + CO\uparrow \quad (4.10)$$

$$B_2O_2 + C \rightarrow B_2O + CO\uparrow \quad (4.11)$$

$$B_2O + C \rightarrow 2B + CO\uparrow \quad (4.12)$$

$$4B + C \rightarrow B_4C \quad (4.13)$$

Figure 4.27 shows the XRD pattern of the $B_{e2}C_e$ precursor powder calcined at different temperatures in a scan range of $2\theta = 30^o$ to 40^o. It is evident that a boron carbide peak does not appear until 1450°C and hence it is very unlikely to be an intermediate product in HfB_2 formation, unless there are some very significant, and unknown, catalytic effects occurring when Hf-based compounds are present.

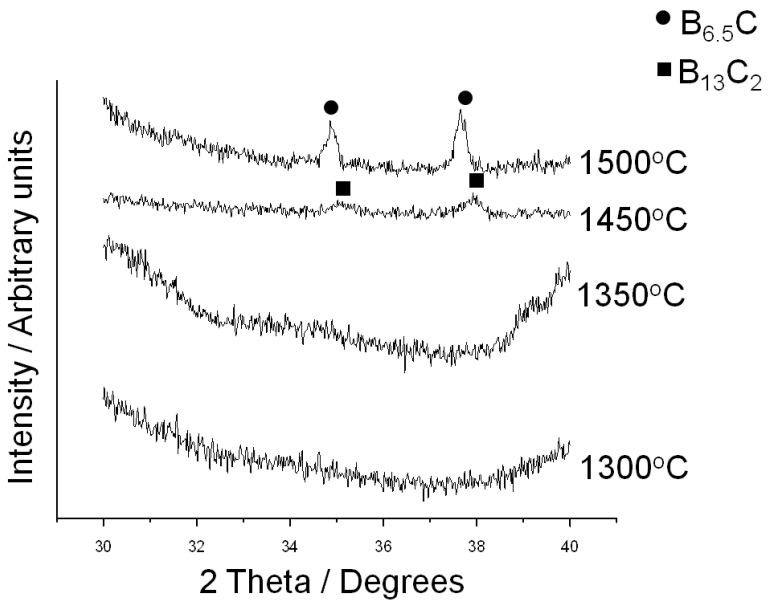

Figure 4.27: XRD patterns of the $B_{e2}C_e$ precursor calcined at different temperatures for 0.1 h

This may possibly suggest that, at the end of reactions 4.10, 4.11 and 4.12, the products react with HfO_2 to form HfB_2 before reaction 4.10 can occur. This is the basis of reaction 4.9, according to which HfB_2 is formed by the reaction between HfO_2 and boron sub oxides and/or amorphous boron.

In order to confirm the formation of boron sub-oxides or boron amorphous vapours, XPS was carried out on $B_{e2}C_e$ system, heat treated at 1300^{o}C and 1450^{o}C for 0.1 h, see Figure 4.28. Since these sub-oxides are highly volatile, no detections were made until a sample was heat treated at 1450^{o}C.

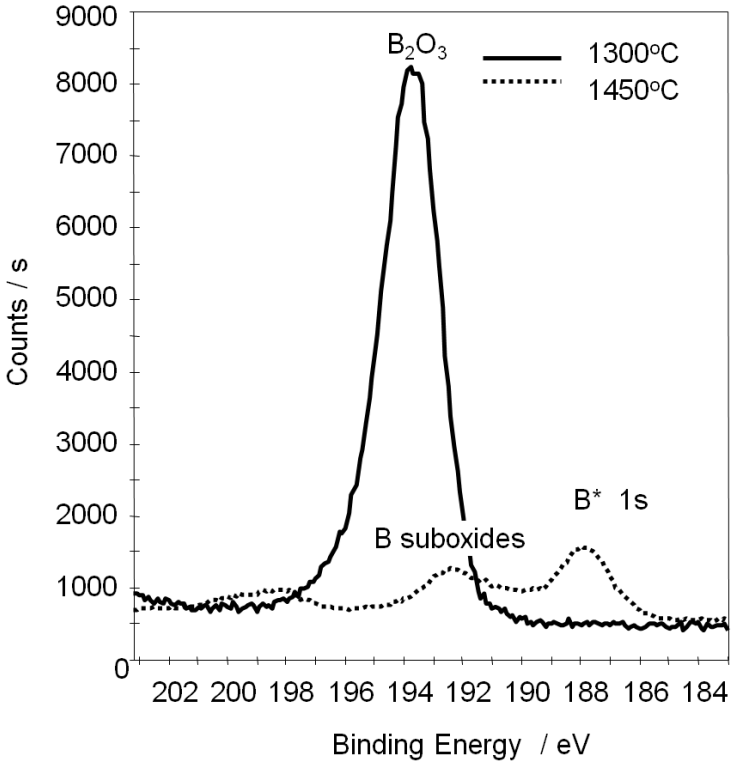

Figure 4.28: High resolution B 1s scan for $B_{e2}C_e$ heat treated at 1300^{o}C and 1450^{o}C for 0.1 h

Table 4.1 shows the XPS elemental composition of B_eC_e precursor carbothermally reduced either at 1300 or 1450^{o}C for 0.1 h. There was an 87% reduction in the atomic concentration of boron as temperature is increased by 150^{o}C. This demonstrates the volatile nature of boron oxide species and the difficulty in detecting them at the temperature at which they are formed. Due to the limitations of experimental conditions it was difficult to detect B_2O_2, B_2O or amorphous B in the intermediate reaction products as they were formed. Hence, to shed further light on this issue, the experiments were performed involving amorphous boron powder as the source of boron.

Table 4.1: XPS elemental quantification of $B_{e2}C_e$ heat treated at 1300°C and 1450°C for 0.1 h

Element	1300°C At. %	1450°C At. %
B1s	26.9	3.5
C1s	22.7	91.0
N1s	2.1	-
O1s	48.3	4.9

High temperature DTA curves for the precursors HB_eC, HB_aC and HB_{ae} showed similar trends, see Figure 4.29. The total weight loss for HB_aC was 34 wt% whilst that for HB_eC was 51 wt%, as mentioned earlier. The difference in the total weight loss may be due to the loss of B_2O_3 in the HB_eC system. The weight loss for HB_{ae} was 26% and was the lowest of the three due to the absence of both the carbon source and volatile B_2O_3, and hence any weight loss with the degradation of phenolic resin or the volatility of B_2O_3 is absent. The weight loss for the HB_{ae} and HB_aC system occurred up to 500°C due to the loss of physisorbed and chemisorbed water, and then the degradation of the phenolic resin in the latter, whilst that for HB_eC occurred up to 700°C due to the presence of B_2O_3 and excess resin. The weight remained stable up to 1275°C in all cases and then rapidly decreased, to stabilise at approching 1600°C.

The endothermic peaks depicting the boro/carbothermal reduction reactions at 1275°C and 1470°C, are identical for all the precursor powders, indicating that the reaction paths were similar for the three. This could only mean that either the B_2O_3 had dissociated into B during the course of the HfB_2 formation in the HB_eC precursor powder, or the amorphous B in the HB_aC and HB_{ae} precursor had oxidised into B_2O_3. Since the reaction was carried out in a reducing atmosphere in the presence of carbon, the likelihood for the latter was extremely small.

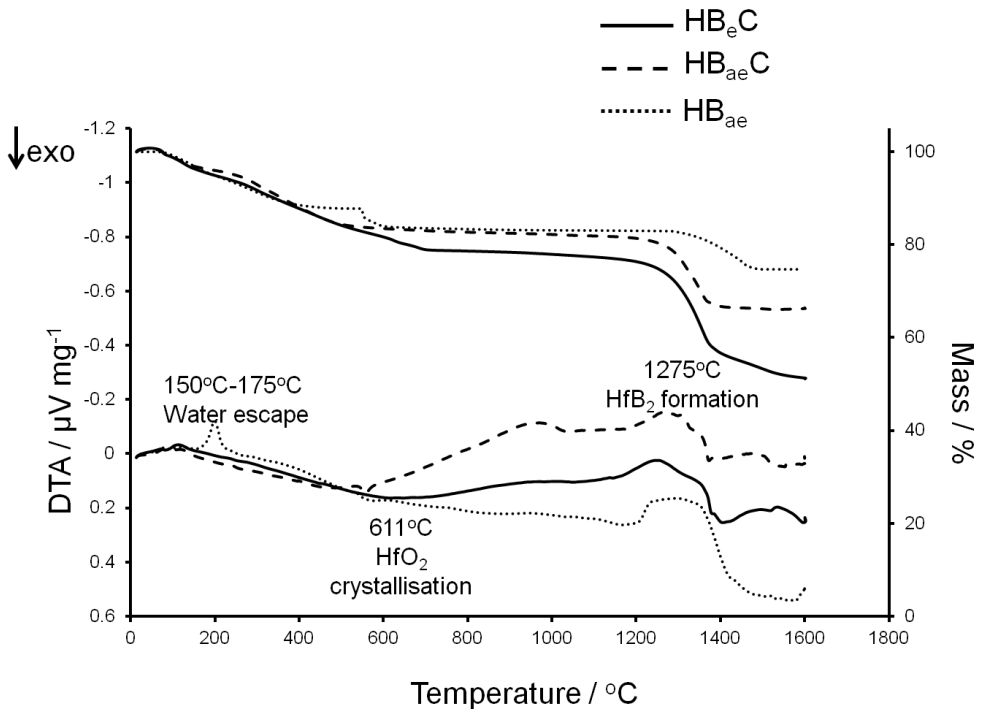

Figure 4.29: TGA/DTA of HB_eC, $HB_{ae}C$ and HB_{ae} precursor powders

This result, combined with the Gibbs free energy value, and the XPS data of $B_{e2}C_e$ indicates that the formation of HfB_2 at 1300°C was most likely to occur through the formation of amorphous boron or boron sub oxides as the intermediate product (Reaction 4.9), though, as indicated earlier, at higher temperatures there could be more than one reaction mechanism occurring simultaneously.

Figure 4.30 gives the schematic of the HfB_2 formation mechanism at 1300°C. From HT-XRD and TGA/DTA analyses it was clear that at 650°C, the precursor to HfB_2 consisted of HfO_2, B_2O_3 and C. From Figure 4.21 and Figure 4.22 the structure can be visualised as HfO_2 particles embedded in a solid C matrix and surrounded by B_2O_3 melt[v] [251].

[v] Since the melting point of B_2O_3 is 450°C, it must have been in the liquid phase.

The first step in HfB_2 formation involved carbothermal reduction of B_2O_3 to form active boron species[vi]. The lighter active boron species diffused towards HfO_2 displacing oxygen and resulting in HfB_2 formation at 1300^oC. With an increase in the energy input, i.e. by increasing the dwell time at 1300^oC or by increasing the temperature, other mechanisms stated in equations 4.7 and 4.8 may initiate. All these reactions are simple substitution reactions, however, to explain the formation of rod-shaped HfB_2 particles (see Figure 4.19), another possible mechanism which could take place over 1400^oC, is proposed in this study. Around 1400^oC any mono-borides that may have formed during the aforementioned process, would dissolve carbon into its lattice leading to the formation of an unstable solid solution held in the B_2O_3 melt, which would continuously precipitate out as HfB_2 upon cooling. The evidence for the presence of a solid solution between Hf-B-C has not been observed in this study. However, Rudy et.al. [252] studied the phase diagram of Hf-B-C and found that at 1400^oC about 2.5 at% of B dissolved interstitially in HfC_{1-x} and 14 at% C dissolved interstitially in HfB both resulting in precipitation of HfB_2 upon cooling, and this precipitation cannot be prevented unless cooled at a rate faster than 100^oC s^{-1} [253]. If this were true, any boron deficiency would yield hafnium carbide in the end product; and this has been observed in this study, (refer to Figure 4.15).

When amorphous boron was used instead of B_2O_3 as the boron source, the mechanism could be explained by eliminating only the first step in the above process.

If carbon was absent in the system i.e. during borothermal reduction of HfO_2 with amorphous boron, HfB_2 will be formed through a direct displacement/substation reaction and no complicated anisotropic growth of HfB_2 will be observed, unlike during the boro/carbothermal reduction. This is explained in detail in the following section.

[vi] Active boron species are highly reactive amorphous boron and/or boron sub-oxides.

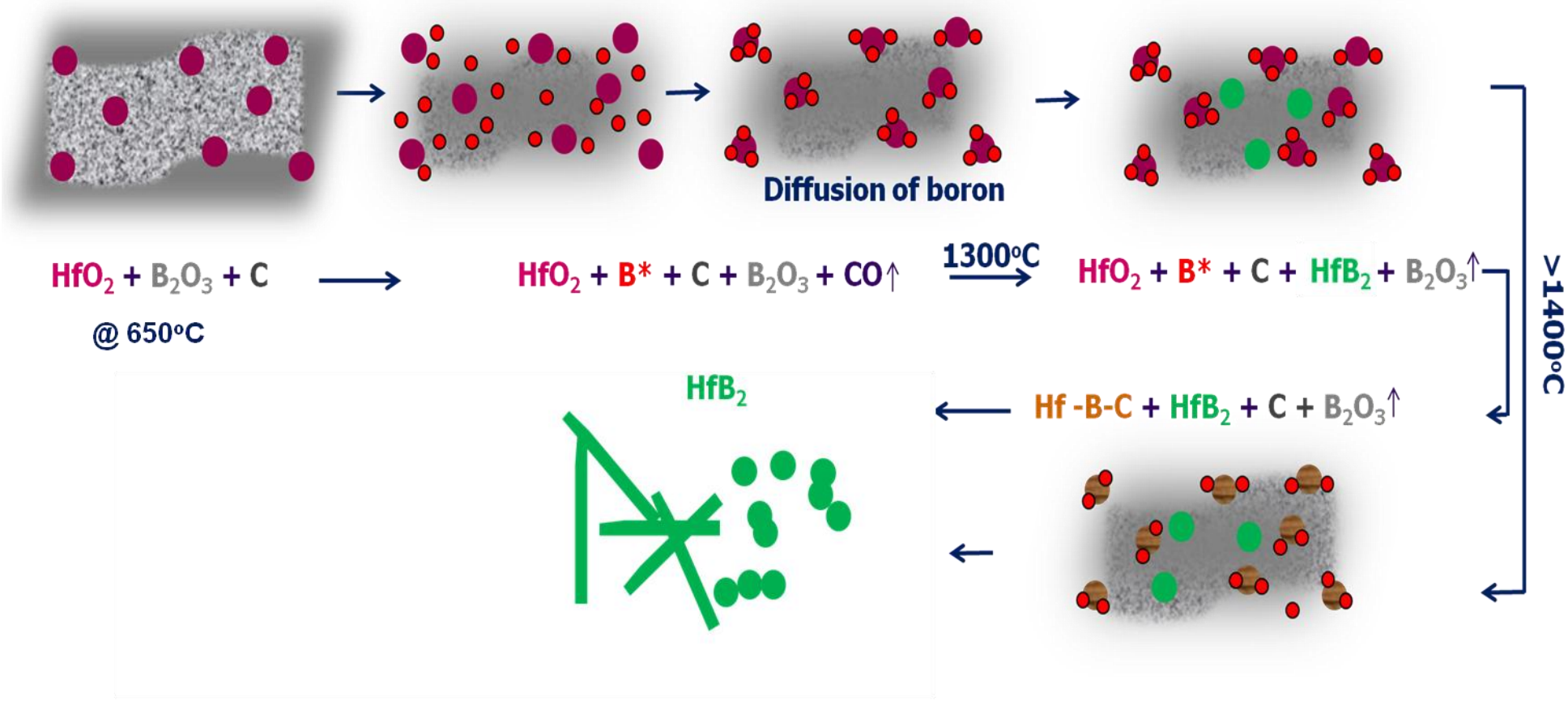

Figure 4.30: The schematic process of HfB_2 formation mechanism

4.2.6.4 Growth Mechanism

The main focus of this section is to explain the growth mechanism of rods, as shown in Figure 4.19. Crystal nucleation is usually heterogeneous and occurs under supersaturation conditions. As explained in the previous section, boron is carbothermally reduced to active boron species, which then reduces HfO_2 to Hf. This Hf and B in the presence of C form Hf $(B, C)_{1-x}$ solid solution which was precipitated as HfB_2 upon cooling. The precipitation under high supersaturation conditions resulted in the formation of islands of HfB_2 particles with axial screw dislocations at the top surface, as shown in Figure 4.31. The reason for these dislocations was understood to be due to the presence of elastic strain in the first few continuous layers of atoms precipitated, introduced by mismatch in the lattice (in this case, alumina crucible was the lattice) between the substrate and the crystal. It should be noted that strain energy will have increased with the size of the precipitated crystal. The strain energy could be either accommodated by straining both crystal and substrate, if the lattice mismatch was small, or relaxed by formation of dislocations if the mismatch was large. In the present scenario, the strain energy relaxation led to the formation of screw dislocations in the HfB_2 crystals.

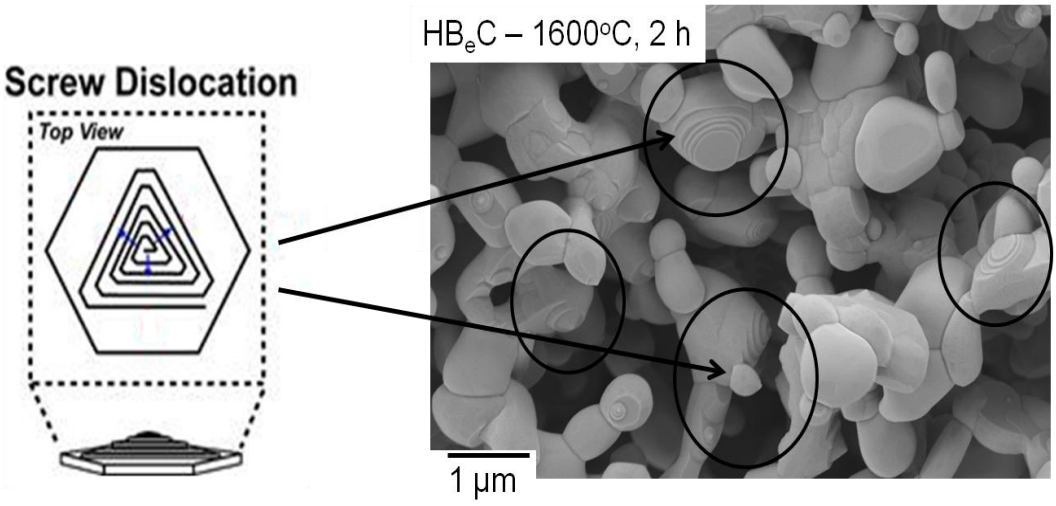

Figure 4.31: FEGSEM image of HB_eC precursor heat treated at 1600°C for 2 h showing axial screw dislocations

Growth of these islands to rods or tubes could not be explained through a vapour-liquid-solid (VLS) mechanism, as there was no evidence of any metal catalyst at the tip of the rods/tubes, which is the signature of the VLS mechanism. Moreover, the presence of screw dislocations on the particles clearly indicated that the anisotropic growth was driven by a dislocation growth mechanism. Dislocation-driven anisotropic one dimensional (1D) crystal growth is believed to be due to the preferred growth at the self-perpetuating spirals of axial screw dislocations under low supersaturations. According to KVS (Kossel Stranski Volmer) [254], BCF [255] (Burton Cabrera Frank) and PBC [256] (periodic bond chain) theory, the growth of crystal takes place along the stepped or kinked surfaces rather than flat surfaces. Under low supersaturation conditions, layer-by-layer (LBL) growth of HfB_2 is prohibited, due to the energy penalty for creating a new surface layer and growth occurs only at the dislocation spiral causing highly anisotropic one-dimensional (1D) growth. Low supersaturations were assumed to be caused by slightly higher concentration of B_2O_3 melt than the stoichiometric amount and the concentration of the melt not being uniform in the bulk, due to the convective diffusion that is generally operative and the following factors;

1. different densities of the solvent (B_2O_3), solute (Hf, B and C) and the growing refractory compound (HfB_2);

2. different viscosities for various regions of the solution due to a temperature gradient;

3. viscosity variations during the crystallization process due to up and down diffusion flows; with high viscosity of the bulk giving rise to thicker anisotropic structures and vice versa [257].

When the HB_eC precursor was heat treated at 1300^oC for 25 h, this relatively low temperature could have prevented the rapid evaporation of B_2O_3, unlike when it was heat treated at a faster rate to a higher temperature (1600^oC). This could have led to certain areas rich in melt, creating low supersaturation conditions i.e. the higher the concentration of solvent, the lower the

supersaturation of the solute, leading to the formation of anisotropic hexagonal HfB_2 crystals with growth along the common c-axis, Figure 4.32.

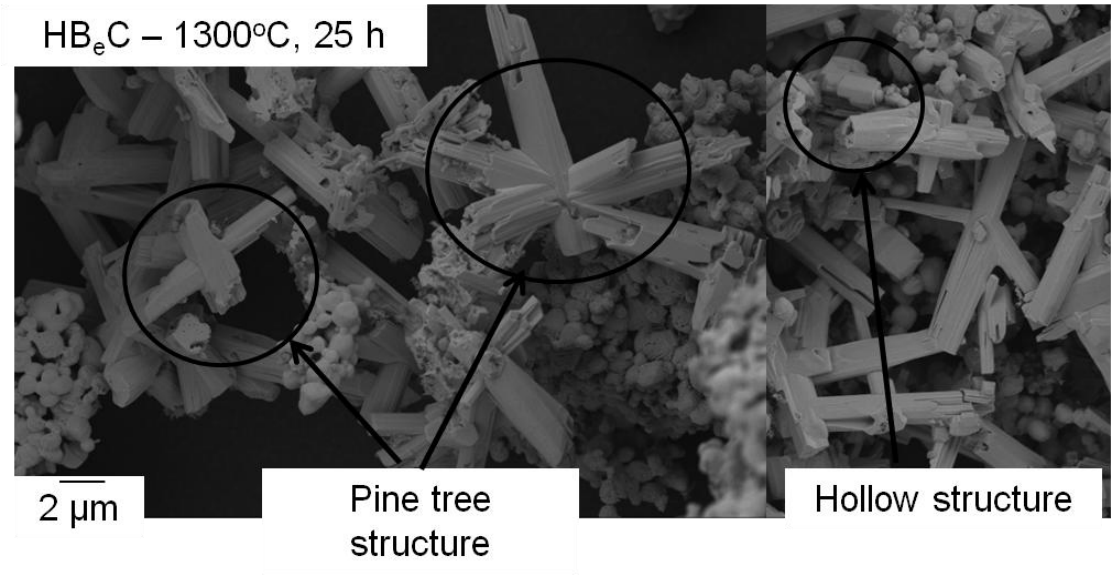

Figure 4.32: FEGSEM image of HB_eC precursor heat treated at 1300°C for 25 h showing pine tree and hollow structures of the anisotropic HfB_2 crystals.

The anisotropic crystals exhibited several different morphologies such as 'pine tree' and hollow tube-like forms. Nearly all the crystals formed were voided or hollow. Axial screw dislocations contained within solid rods not only drive anisotropic growth but also cause the spontaneous formation of tubes due to the dislocation strain energy [257].

The formation of the structures shown in Figure 4.33 were the result of the disruption of the perfect periodicity within the crystal lattice, i.e. screw dislocations give rise to strain energy per unit length (E), that is quadratically dependent on the magnitude of the Burgers vector (b), see equation 4.14:

$$E = \frac{b^2 \mu}{4\pi} \ln \frac{R}{r} \tag{4.14}$$

where µ is the shear modulus, and R and r are the outer and inner tube radii, respectively. This strain could be alleviated by:

i) by hollowing out of the dislocation core to create a tube,;

ii) or, by a torque around the crystals, known as the Eshelby twist (α) [258] as given in equation 4.15.

$$\alpha = b / \pi(R^2+r^2) \quad (4.15)$$

Where b is the Burger's vector[vii] and R and r are the outer and inner radius of the anisotropic hollow crystal;

iii) through the combination of i) and ii).

As the strain energy given in equation 4.14 equals or becomes higher than the surface energy of the crystal, dislocation cores become hollow, see Figure 4.33. When the Burgers vector was sufficiently large, the equilibrium morphology of the anisotropic crystals, whose growth was driven by screw dislocations, should be hollow. However, there exists an intermediate case which is on threshold and oscillates between the solid and hollow conditions due to small fluctuations in growth environment arising from HfB_2 anisotropic crystal thickness that subtly change the energy balance, due to which the tubes initially formed could partially close up after synthesis and vice versa [259].

An Eshelby twist is the rotation of a crystal lattice around a screw dislocation, as the consequence of its associated stress. Smaller diameter crystals show large twists and vice versa. If two different known zone axes perpendicular to the growth direction can be observed at different locations of the same rod, the distance between the two collection points and the angle between the two zone axes, can be used to calculate the twist. As shown in Figure 4.34, isolating a single rod was difficult and collection of the SAED pattern without any interference from the surrounding rods was close to impossible. However, Stephen et.al. [259] observed similar twist in their attempts to deliberately

[vii] Burger vector represents the magnitude and direction of the lattice distortion of the dislocation in a crystal lattice.

grow ZnO nanowires and were able to isolate a single anisotropic crystal and calculate the twist.

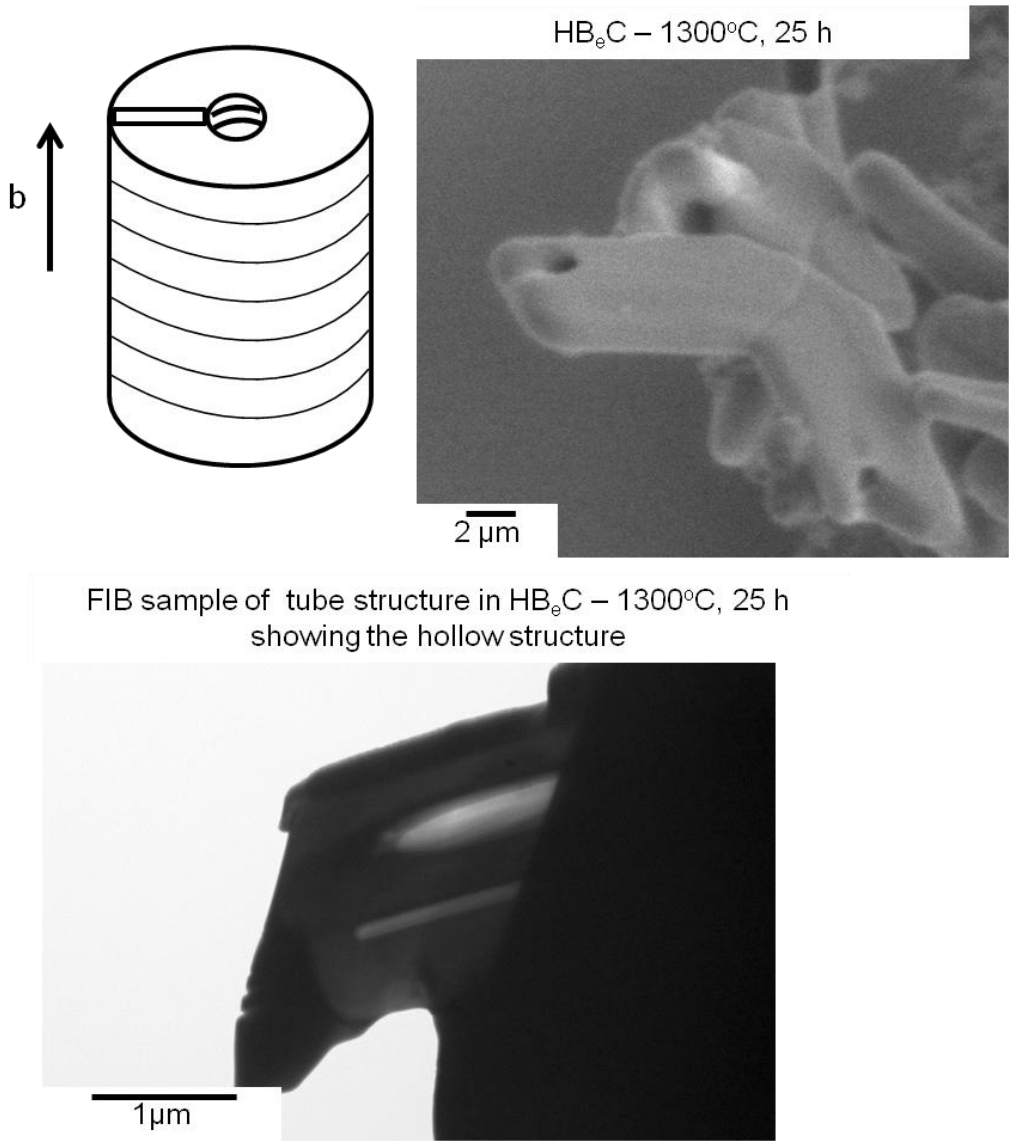

Figure 4.33: SEM and TEM of HB_eC precursor heat treated at 1300^{o}C for 25 h showing hollow structures

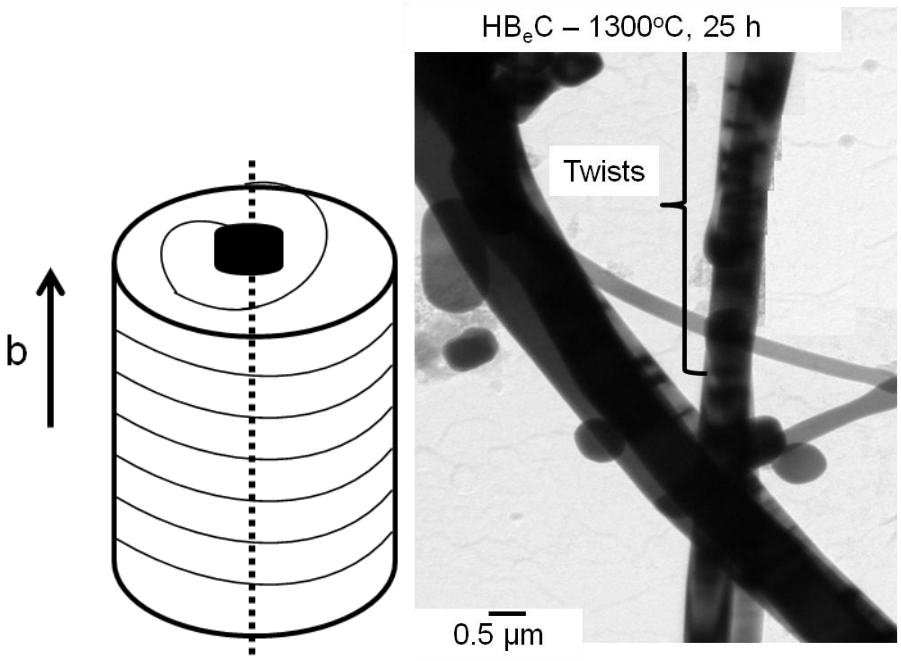

Figure 4.34: TEM image of HB_eC precursor heat treated at 1300°C for 25 h showing Eshelby twists

Certain parameters that influence the rod formation are discussed below.

i. Effect of dwell time

With the increase in dwell time at 1300°C, there could be a possibility for the solute to diffuse from high concentration areas to low concentration areas, resulting in homogeneous concentration throughout the bulk. The higher the dwell time, the longer the solute ($Hf(C,B)_{1-x}$) will have to diffuse through the solvent (B_2O_3), giving rise to more anisotropic growth. This was confirmed by heating the precursor powder at 1300°C for 40 or 50 h, where it was found that the rods increased with the time, see Figure 4.35.

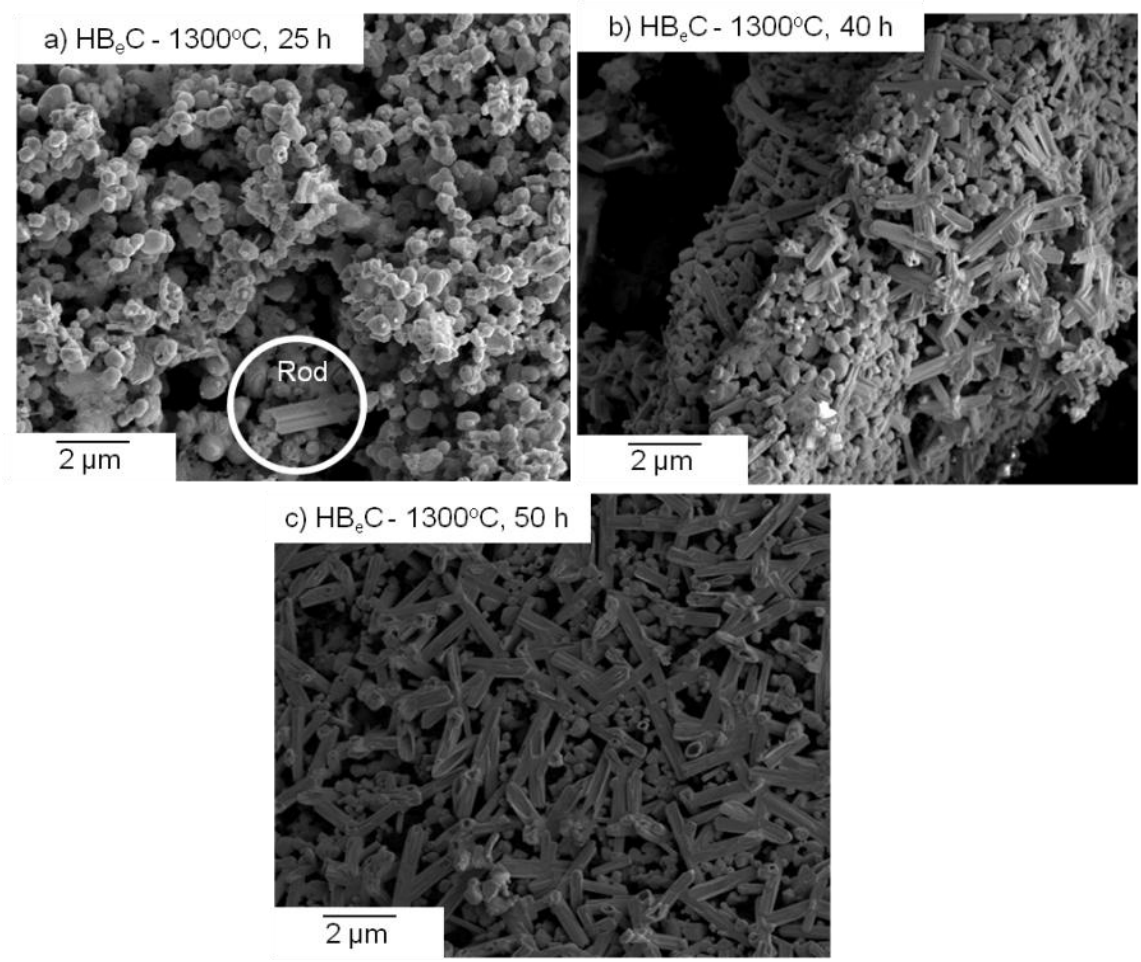

Figure 4.35: FEGSEM of HB_eC calcined at 1300°C for a) 25, b) 40 and c) 50 h showing increase in rod shaped particles

ii. Effect of variation of ratio of boron

Increasing the concentration of B_2O_3 increased the concentration of melt, which in turn decreased the degree of supersaturation resulting in anisotropic crystal growth. Figure 4.36 shows the FEGSEM images of HfB_2 made from two different Hf:B ratios, 6 and 8. The increase not only favoured the anisotropic growth but the liquid melt also wetted and bonded the crystals together, leading to coalescence.

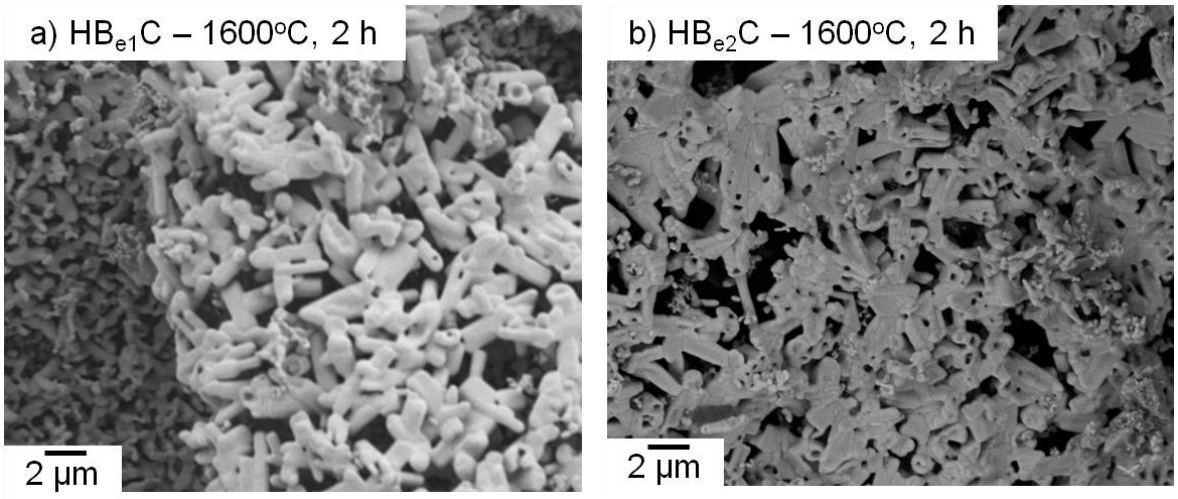

Figure 4.36: FEGSEM of a) $HB_{e1}C$ and b) $HB_{e2}C$ precursor powder heated to 1600°C for 2 h

When amorphous boron was used as the boron source, increasing the ratio of boron, as in $HB_{ae1}C$, resulted in a few rod shaped crystals. This could be due to the presence of B_2O_3 impurity in the 95% pure amorphous boron powder used, see Figure 4.37a. However, when the boron ratio was increased in HB_a precursor powder, i.e. HB_{ae}, there was no anisotropic crystal growth. This supports the earlier claim that the presence of carbon is essential for the solid solution between Hf, B and C to exist and, in the absence of C, HfB_2 was formed through a normal substitution mechanism, i.e. oxygen in HfO_2 is substituted by B, see Figure 4.37b. Popov et.al [260] crystallized MO_2B_5 and W_2B_5 from the respective precursors (solute) contained in Al melt (solvent) and found that increasing the initial content of the transition metal, compared to the stoichiometric ratio (for Mo by 1.25 times, for W by 1.4 times), increased the amount of isometric crystals in the final product. On the other hand increasing the initial content of B (for Mo_2B_5 from 1.6 to 4.8 times, for W_2B_5 from 1.6 to 2 times) resulted in an increase in the amount of plates and tubular crystals. However, while precipitating TiC and TaC from their precursors held in Al melt, a three-fold excess of metal compared with the stoichiometric ratio and a two-fold excess of carbon, did not result in any variation of the shape of the grown crystals. These results were consistent with those achieved in this study.

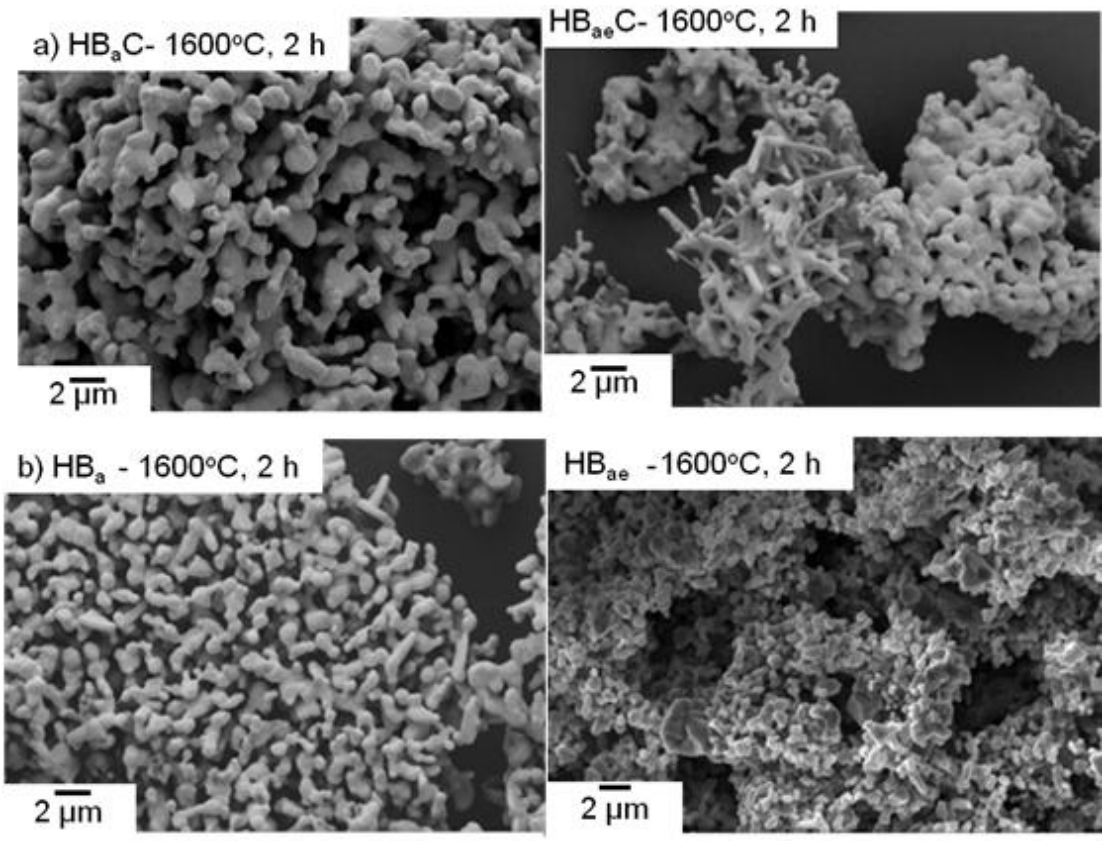

Figure 4.37: FEGSEM of a) HB_aC and $HB_{ae}C$ and b) HB_a and HB_{ae} heat treated at 1600^oC for 2 h

4.2.6.5 HfB_2 structures resulting from different carbon sources

All the compositions dealt with in this section are HB_eC but derived from different carbon sources. Figure 4.38 shows TEM micrographs (on the left) of the various carbon sources after pyrolysis and FEGSEM micrographs (on the right) of the corresponding HfB_2 powders synthesized from the sources. Since the only difference between the different precursor powders was the carbon source, the resultant differences in the size and/or structure of the particles in the final powders can be attributed directly to the specific carbon source used. The carbon from pitch is spherical and very uniform and so was the final HfB_2 powder resulting from this source, see Figure 4.38a; the particle size was approximately 1.5 µm. Sucrose and graphite both form sheet-like carbon and the HfB_2 particle size obtained from them were around 1 µm and 3 µm, respectively, see Figure 4.38b and c. The effect of carbon being in the form of sheets will be discussed below.

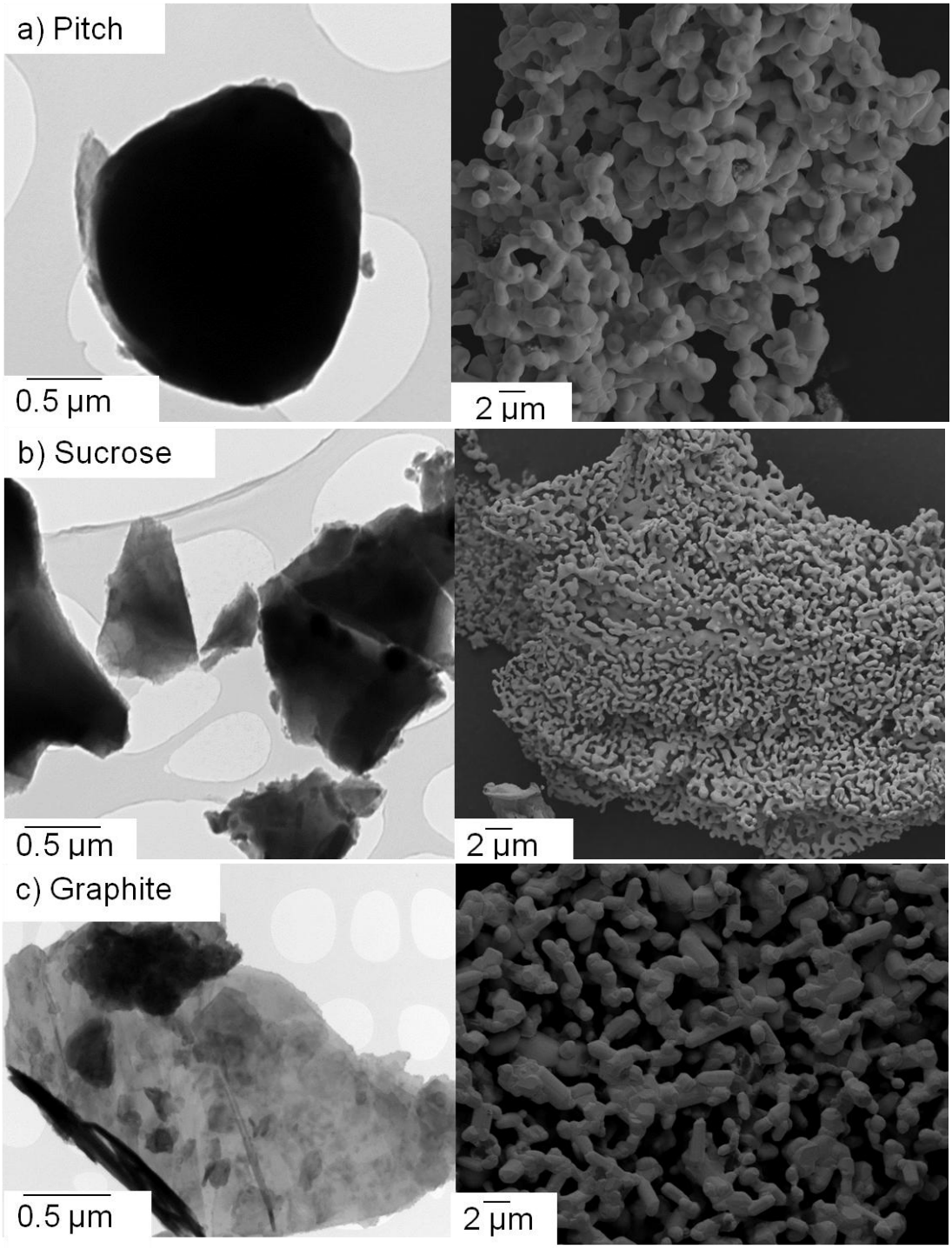
a) Pitch
0.5 µm
2 µm
b) Sucrose
0.5 µm
2 µm
c) Graphite
0.5 µm
2 µm

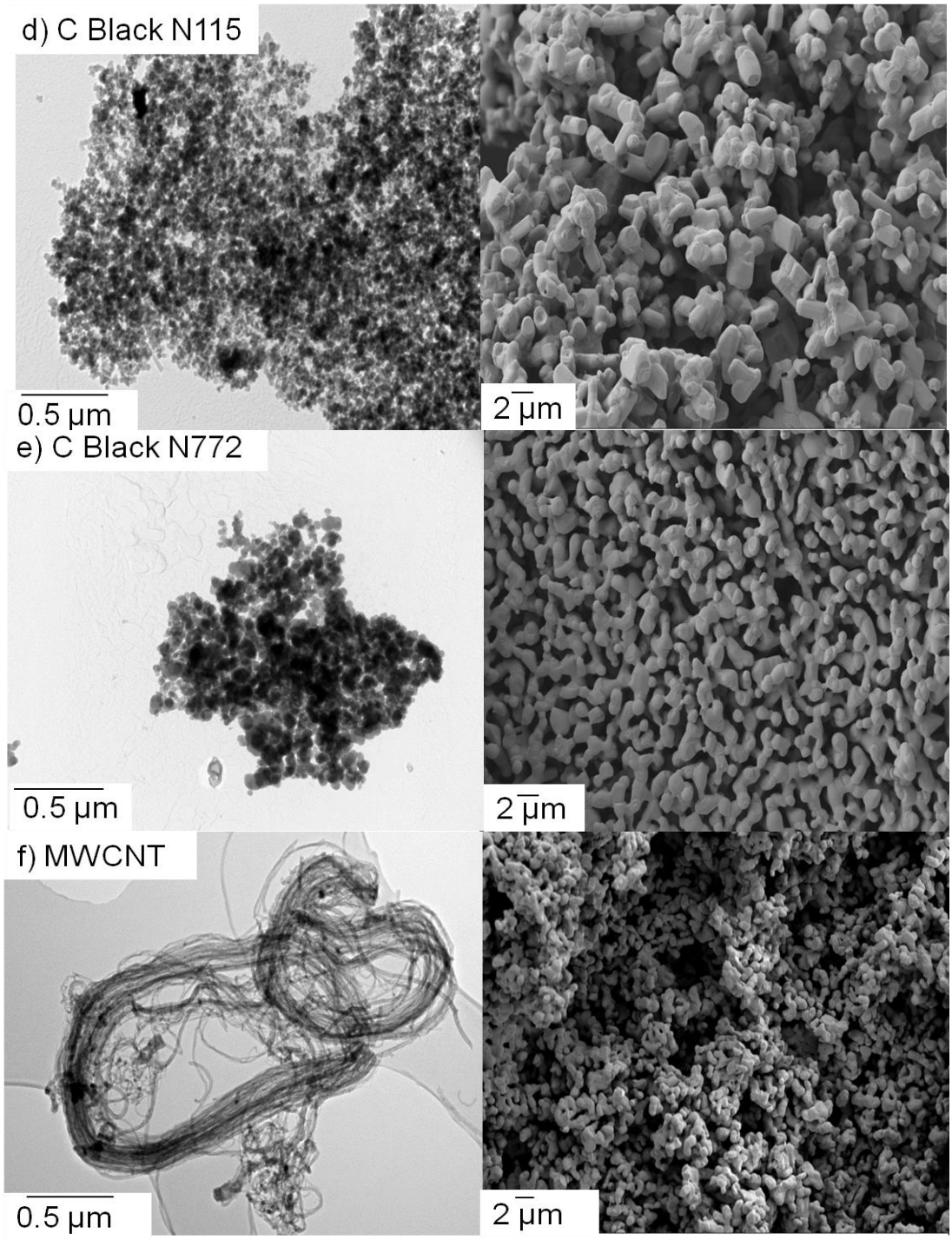

Figure 4.38: TEM images of the carbon structure (left) resulting from the pyrolysis of different carbon sources at 1000^{o}C for 0.1 h and the corresponding FEGSEM images of the resultant HfB_2 powders after heat treatment at 1600^{o}C for 2 h using a) pitch, b) sucrose, c) graphite, d) C-Black N115, e) C-Black N772 and f) MWCNT

For HfB_2 powders resulting from the carbon black and multi-walled carbon nano tubes, i.e. Figures 4.38d – f, the final particle size was influenced by the level of agglomeration of the pyrolysed carbon sources. For instance, carbon black N115 had much finer particles at ~20 nm than carbon black N772 at ~150 nm, but the structure factor was higher for the former, meaning that it was more heavily agglomerated. This led to the resultant HfB_2 particles actually being coarser if made from N115. The average particle size of HfB_2 powders obtained from these sources was between 1 to 3 µm. Similarly, although the diameter of the MWCNT was only 10 to 20 nm, the tubes were heavily entangled and the resulting HfB_2 particles were 0.8 to 1 µm in size.

Figure 4.39 shows the electron micrographs of the carbon structures that resulted from heat treating the liquid phenolic resin (LPR) to 1000^{o}C for 0.1 h and the resulting HfB_2 powder. The carbon resulting from LPR was in the form of a sheet, as for the sucrose and graphite, and the size and the level of agglomeration of the sheets directly influenced the size of the HfB_2 particles in the final product formed, as illustrated in Figure 4.40.

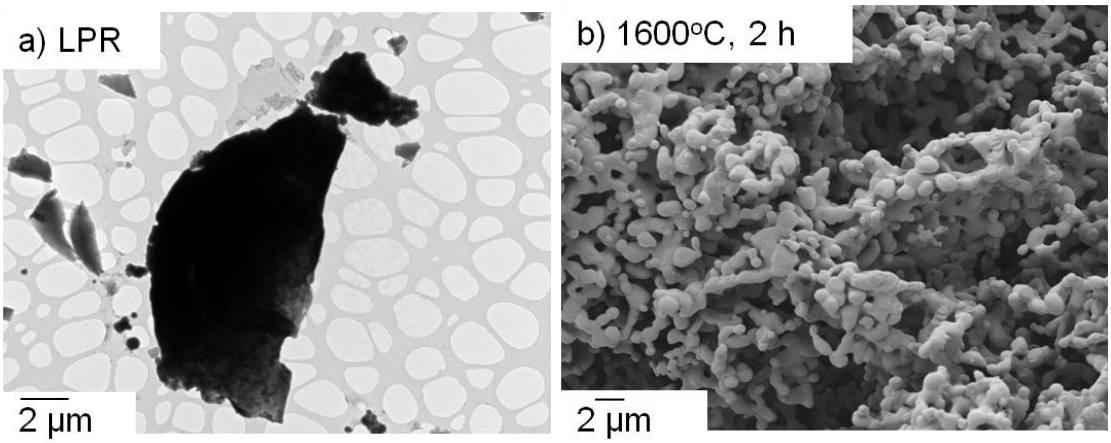

Figure 4.39: a) TEM image of the carbon structure resulting from pyrolysis at 1000^{o}C for 0.1 h and b) a FEGSEM image of the resultant HfB_2 powder

It is believed that the sheet like carbon resulting from the LPR acted like a matrix with the Hf and B precursors embedded in it. Figure 4.40a, shows the structure after heating to 1000^{o}C for 0.1 h; several islands of the carbon sheets may be seen with the embedded ceramic particles appearing clearly

within them. The different situations are illustrated in Figure 4.40b, c, d and e, one with excess carbon and one with the stoichiometric carbon content. If excess carbon was present then the carbon matrix will have prevented the ceramic particles from coalescing and growing larger resulting in fine HfB_2 particles of 20 to 80 nm, Figure 4.40b, but retaining a significant carbon impurity. On the other hand, if a stoichiometric amount of carbon was present then the matrix was consumed in the process of HfB_2 formation and the ceramic particles tended to coalesce, yielding coarser HfB_2 of 1 to 3 µm in size, see Figure 4.40c. It is believed that this explanation is also valid for the other carbon sources, sucrose and graphite, where pyrolysis yielded sheet-like carbon.

The finest HfB_2 synthesized was obtained when using the powder phenolic resin (PPR) as the carbon source. The latter yielded nanometer sized, well dispersed platelets of carbon on pyrolysis, see Figure 4.41a, and consequently the resultant HfB_2 particles were 30 to 150 nm in size. Figure 4.41c shows the formation of the HfB_2 particles as a resultant of different calcination temperatures.

At 700^{o}C the ceramic particles and the carbon from the PPR, were well dispersed and intermixed, with the carbon formed surrounding the ceramic particles. As the calcination temperature increased, the carbon appeared to prevent significant growth of the ceramic particles in a similar manner to the LPR but on a finer scale. After heat treatment at 1600^{o}C for 2 h, the carbon was found to be consumed and the ceramic particle grew at the expense of each other, yielding HfB_2 particles of the approximate shape and size of the carbon island in which it was contained.

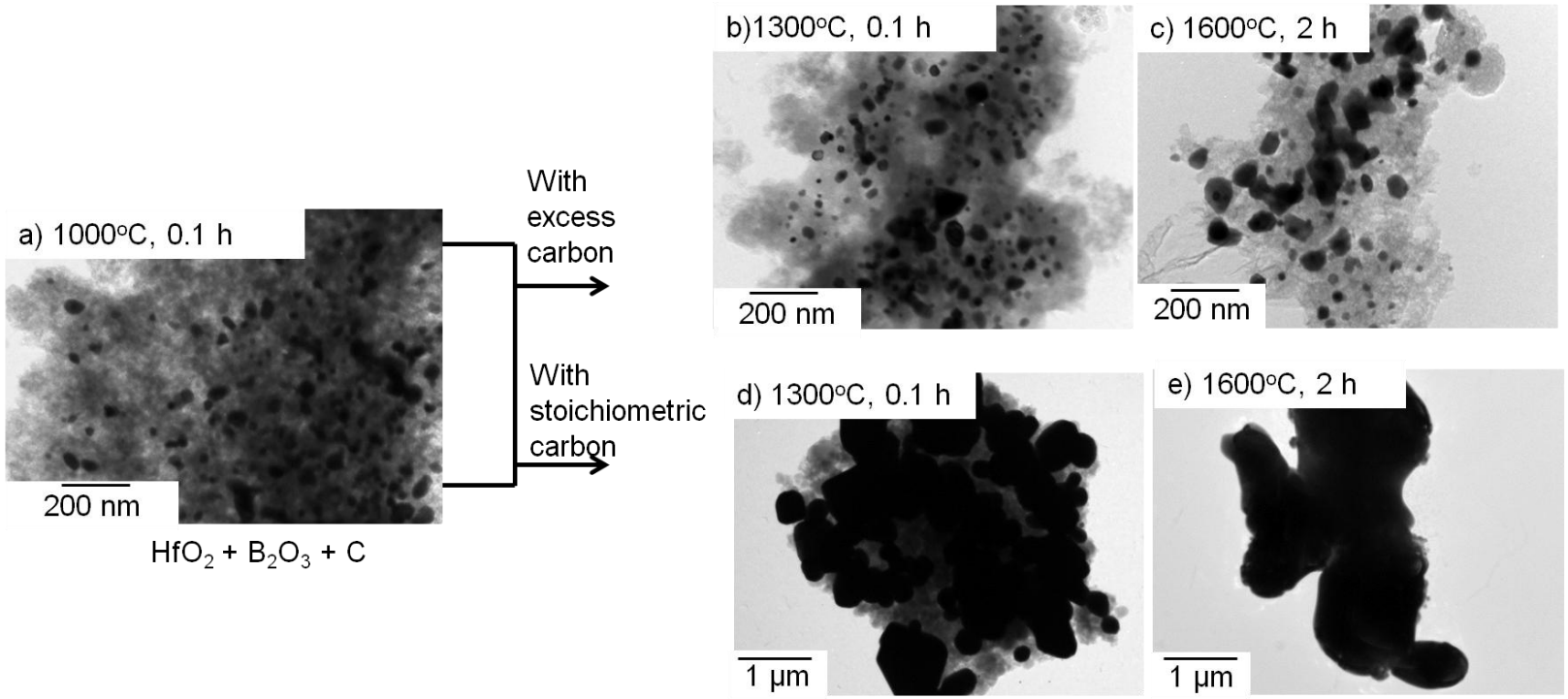

Figure 4.40: Method of formation of HfB_2 powder with LPR as the carbon source

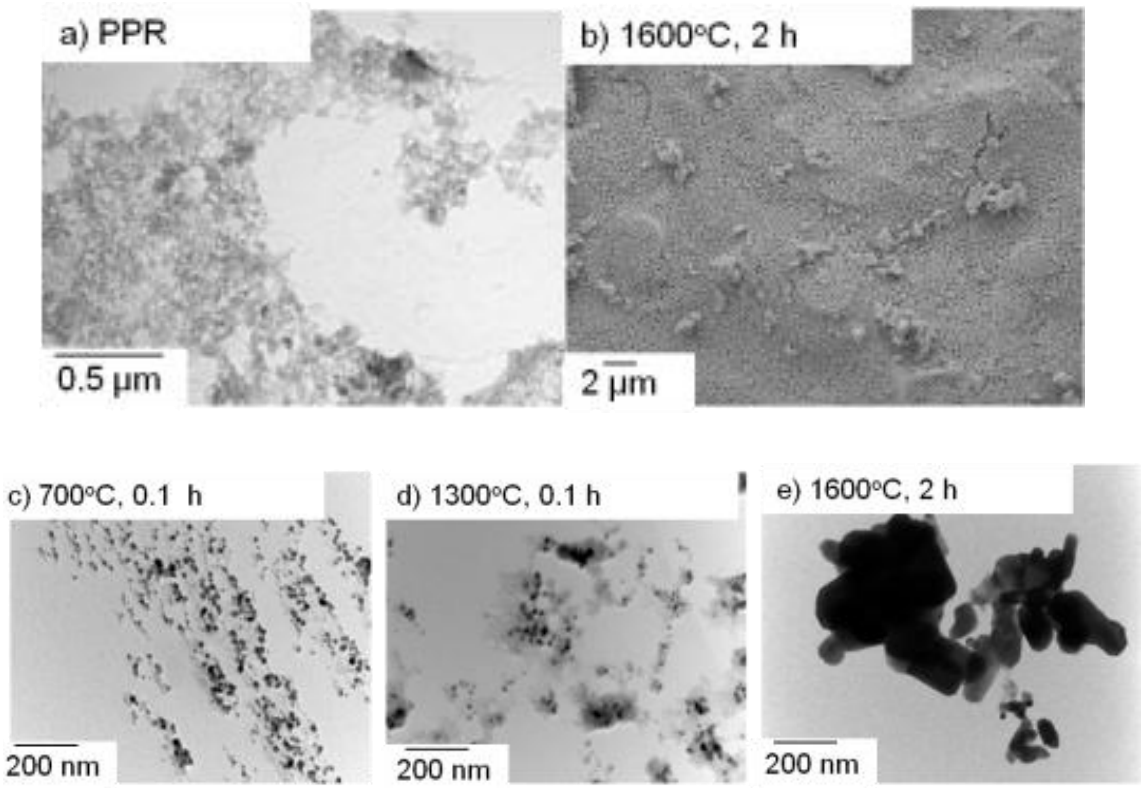

Figure 4.41: a) TEM image of carbon structure resulting from heat treating PPR to 1000^{o}C for 0.1 h, b) FEGSEM picture of HfB_2 powders made using PPR and c, d, e) formation of HfB_2 powder from PPR

Figure 4.42 shows the particle size analysis of the HfB_2 powder formed from the PPR carbon source, as measured using Malvern Mastersizer. The d10, d50 and d90 number % values were 30, 70 and 130 nm respectively, whilst the values for volume % were 90, 200 and 2331 nm respectively. The BET surface area was 21.8 m^2 g^{-1}; this yields a particle size of ~26 nm when calculated using equation 4.16.

$$D = 6 / (A\rho) \qquad (4.16)$$

Where D: particle size in metres

A: BET surface area (m^2 g^{-1})

ρ: density of HfB_2 (105 x 10^5 g m^{-3})

The fine powders obtained from the PPR carbon source were also characterized for their purity using SIMS. Figures 4.43b and c show the positive and negative SIMS data respectively acquired on the area of the HfB_2 particle island shown in Figure 4.43a. The positive mass spectrograph showed peaks corresponding to boron isotopes, hafnium isotopes and traces of potassium. The hafnium peaks corresponding to hafnium oxide at 191-194 AMU were not found indicating its absence. The negative mass spectrograph showed that only traces of impurity atoms like chlorine and oxygen were present in the HfB_2 powder [261].

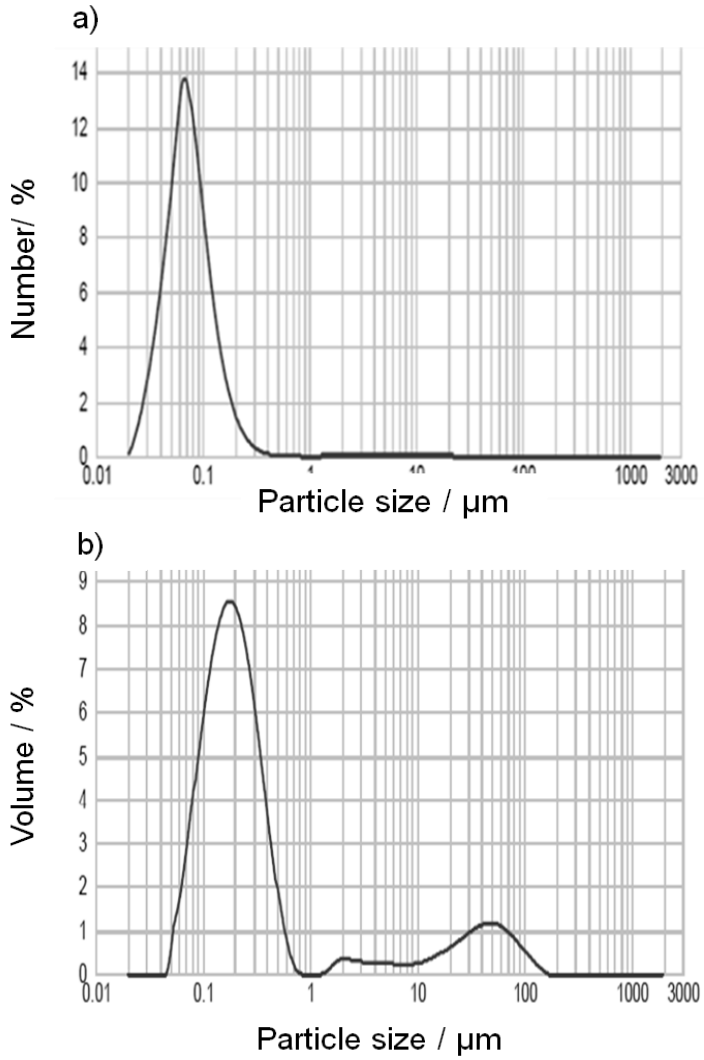

Figure 4.42: Particle size analysis for the HfB_2 powder synthesized using PPR as the carbon source and calcined at 1600^{o}C for 2 h as a) number %, b) volume %

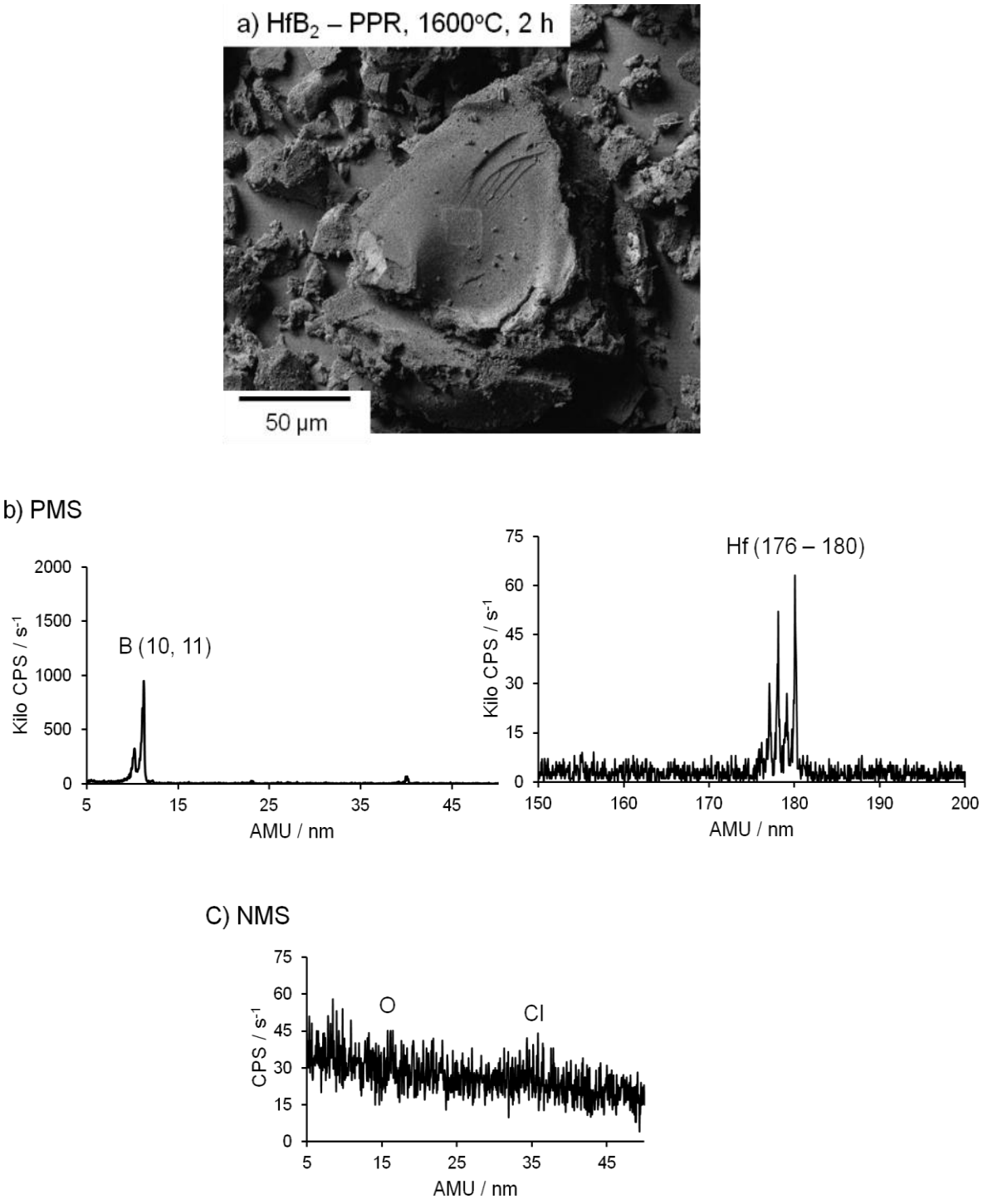

Figure 4.43: a) FEGSEM of HfB_2 obtained from PPR, b) positive mass spectrograph and c) negative mass spectrograph of a)

4.2.6.6 Spark plasma sintering of HfB_2 powders obtained using PPR

The fine HfB_2 powder obtained when using PPR as the carbon source and the commercial powders obtained from Treibacher, Germany (fine grade) were sintered at different temperatures using spark plasma sintering. A load of 16 kN was used for all the runs. The time-temperature and force profiles of different runs used is given are Figure 4.43. The run at 2100^{o}C was conducted first and a fast cooling rate was employed by reducing the pressure rapidly and by turning off the DC power, with the intention of reducing grain growth. Subsequent mounting and polishing of the samples showed cracks, which, at first were assumed to be due to fast cooling. Hence subsequent runs were subjected to slow cooling of 50^{o}C min^{-1} and slow release of pressure. It was later discovered that the isostatic pressure applied to the sample whilst mounting, had infact caused the cracks. The latter also resulted in pull out during polishing. Since the density measurements were done before mounting and polishing these were more accurate, as the cracks due to mounting did not influence them.

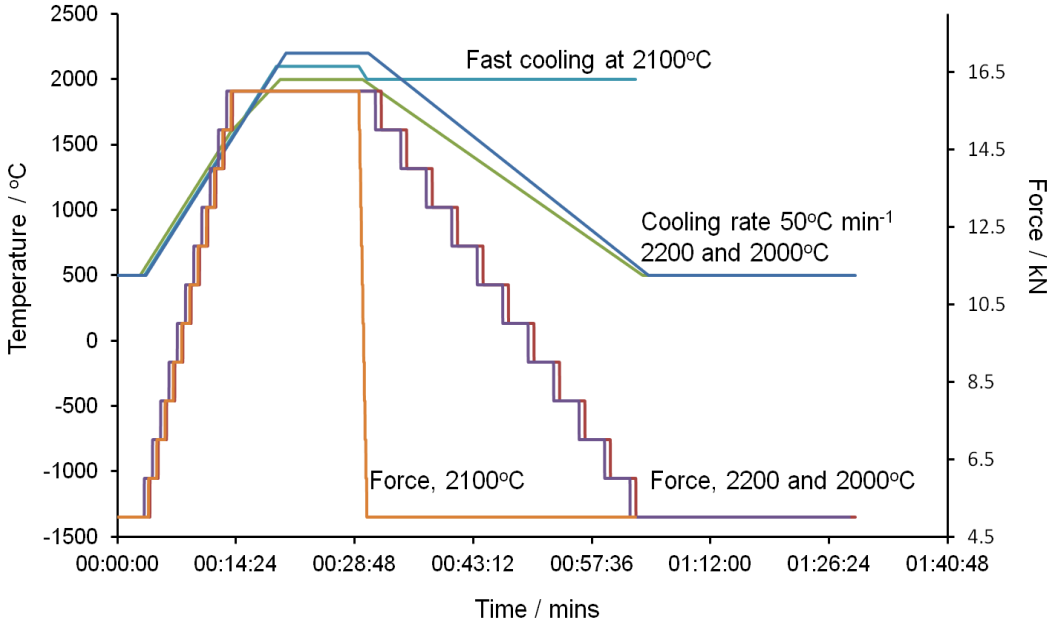

Figure 4.44: Time temperature force profile used for SPS of the fine HfB_2 powders

Figure 4.45a-c shows the FEGSEM images of the Treibacher powders (left) and Loughborough (LU) synthesized fine powders, (right), sintered at 2000^{o}C, 2100^{o}C and 2200^{o}C for 10 mins, along with their theoretical density values. As seen from the photographs, the LU HfB_2 powders showed a higher percentage theoretical density which was indicative of the fine size of the starting powder with a high surface energy. HfB_2 with covalent bonding and low self-diffusion coefficient is difficult to sinter without any addition of sintering aids, however the nanometer sized powder sintered to 99% of its theoretical density at 2200^{o}C. There was a linear increase in density for the samples with every 100^{o}C increase in temperature. The grain size of the fully sintered sample was between 5 to 10 µm, this will be discussed below.

The fracture surface of the sintered sample obtained from LU powders shown in Figure 4.45c right, revealed many pore like structure although the density was measured to be 99% of the theoretical. On close observation these pores were found to be triple points at the grain boundaries. Figure 4.46a shows the polished surface of the LU powders sintered at 2200^{o}C. An electron diffraction pattern on a FIB lift out of the grain boundary, showed the chemical composition of the triple point to be a boron rich oxide (B_7O), whilst the electron diffraction on the grains confirmed the composition to be HfB_2, Figure 4.46b.

Oxygen impurities are known to limit the maximum attainable densities of diborides due to the evaporation/condensation kinetics [262]. The boron oxide melt impurities will trigger the initial densification of HfB_2 by causing localized particle rearrangement, which would in turn lead to coarsening [263]. However, the final densification itself would be hindered due to the rapid collapse of the open pore structures, during SPS, which would result in trapping of B_2O_3 gas generated within the closed pores. In order to eliminate these pores high temperature and pressure will be required, which in turn will lead to grain growth. Hence the presence of B_2O_3 is suspected to be responsible for the grain growth to about 5 to 10 µm although the starting particle size was only between 30 to 150 nm.

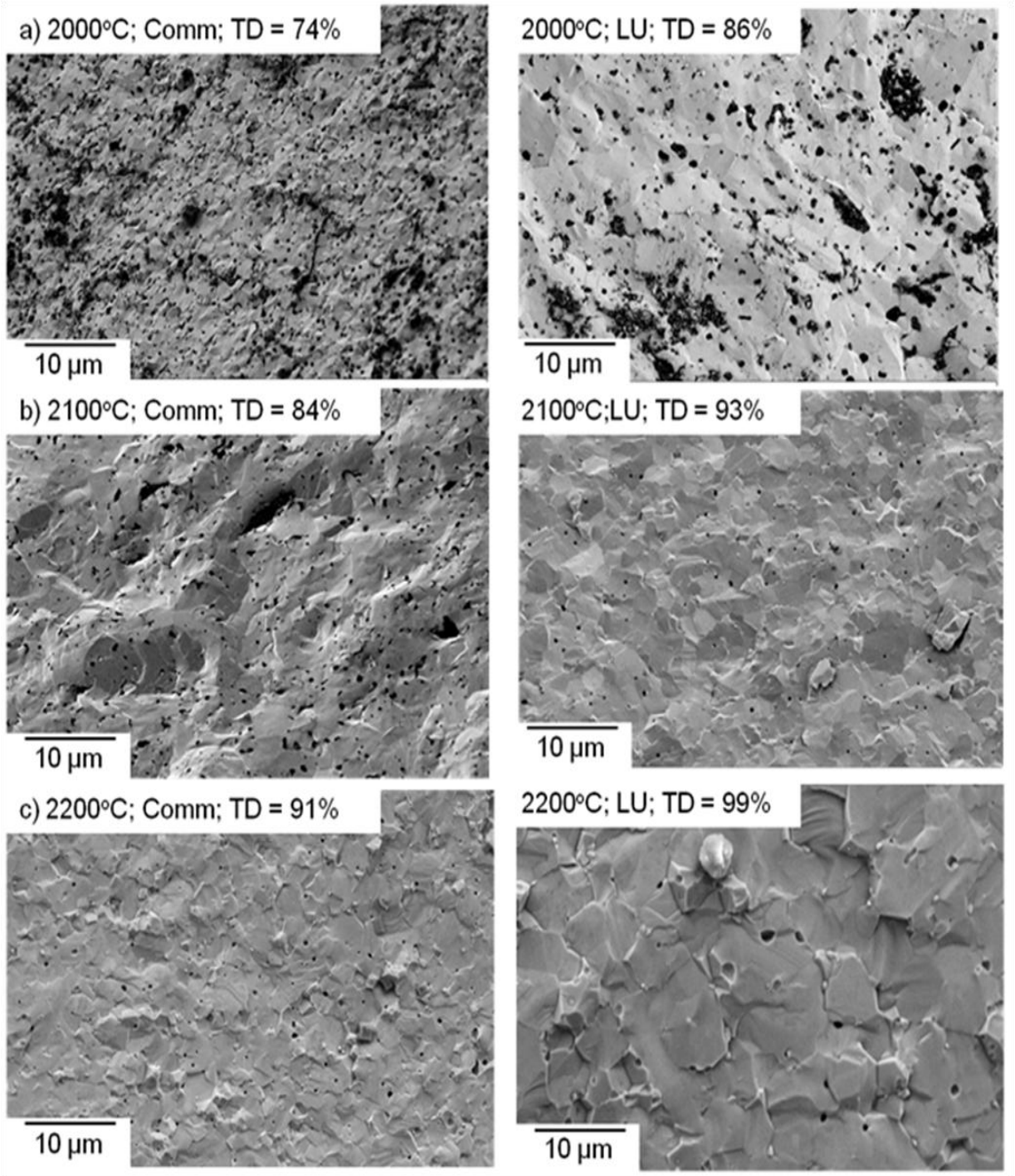

Figure 4.45: FEGSEM images of the fracture surface of commercial (left) and LU fine (right) HfB_2 powders spark plasma sintered at a) 2000^{o}C, b) 2100^{o}C and c) 2200^{o}C for 10 min under 16 kN pressure

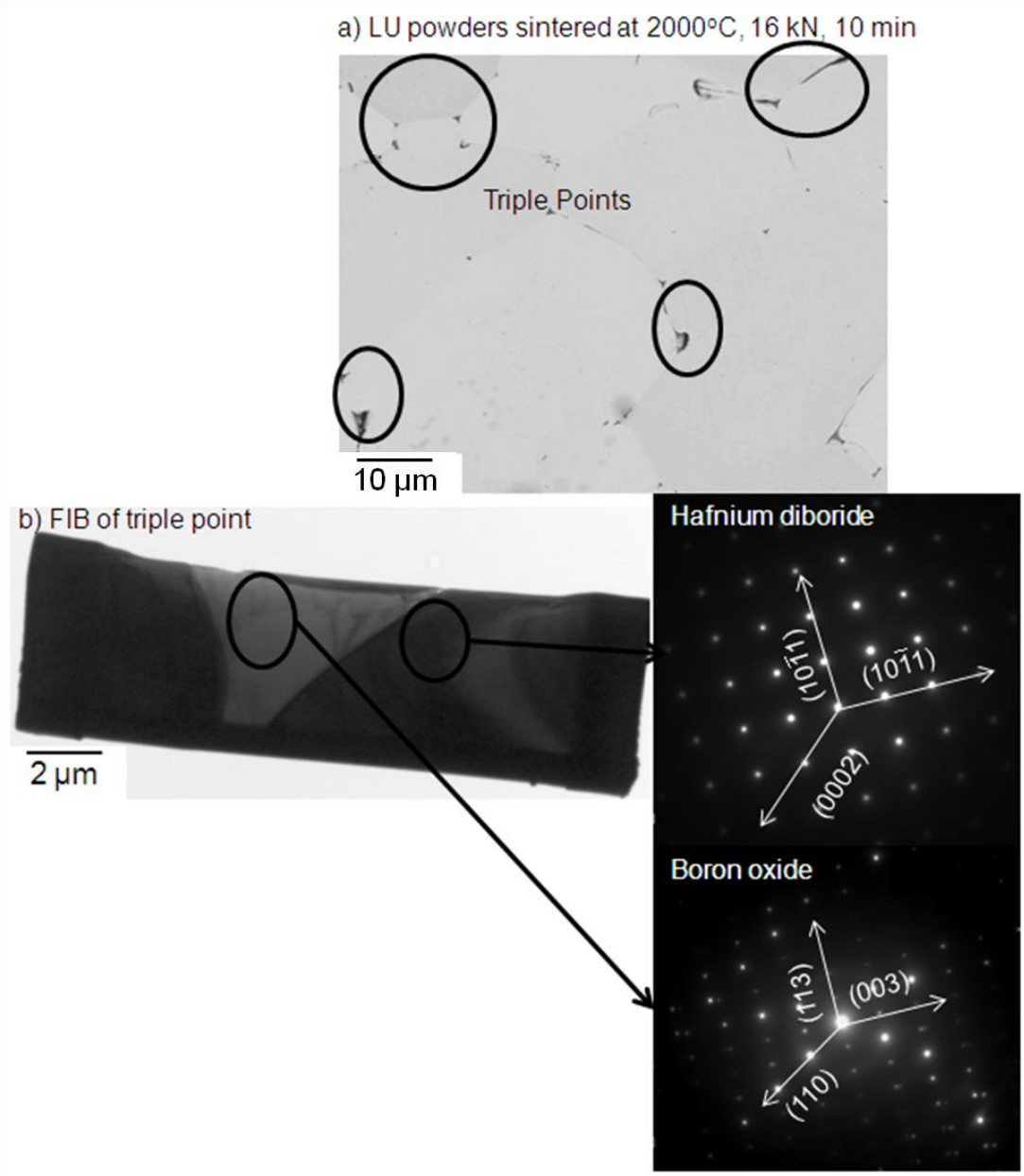

Figure 4.46: Investigation of triple points along the grain boundaries of sintered LU HfB_2 powders

The boron oxide might be present as an impurity buried within the islands of the LU synthesized HfB_2 powders and hence was not detectable by SIMS which provides only surface analysis. This was also not detected by TEM analysis as TEM sample preparation involves sonication of the powder in ethanol, which may have separated the boron oxide if any were present along with the particles. Leaching of B_2O_3 from the fine sized HfB_2 particles, which are prone to and affected by surface oxidation, is another possible and more

probable scenario. Under SPS conditions of high pressure and high temperature, B_2O_3 is known to form B_7O or other boron sub-oxides [264]. More work is required to investigate the location of the boron oxide impurities in the powders, albeit, using the fine LU HfB_2 powder, full density can be achieved using SPS at 2200^oC and 16 kN for 10 mins. Any removal of the boron oxide impurity will only aid the sintering process by preventing an initial coarsening.

4.3 HTC and UHTC coatings and infiltration/impregnation

4.3.1 Viscosity and contact angle measurements of the pre-ceramic sols

The viscosity of the SiC, HfC (HC) and HfB_2 (HB_eC_e) pre-ceramic sols were measured using a Rheolab QC rheometer (Anton Paar Ltd, Garz, Austria). The evolution of viscosities of the sols after removing the reflux was also measured and the results discussed.

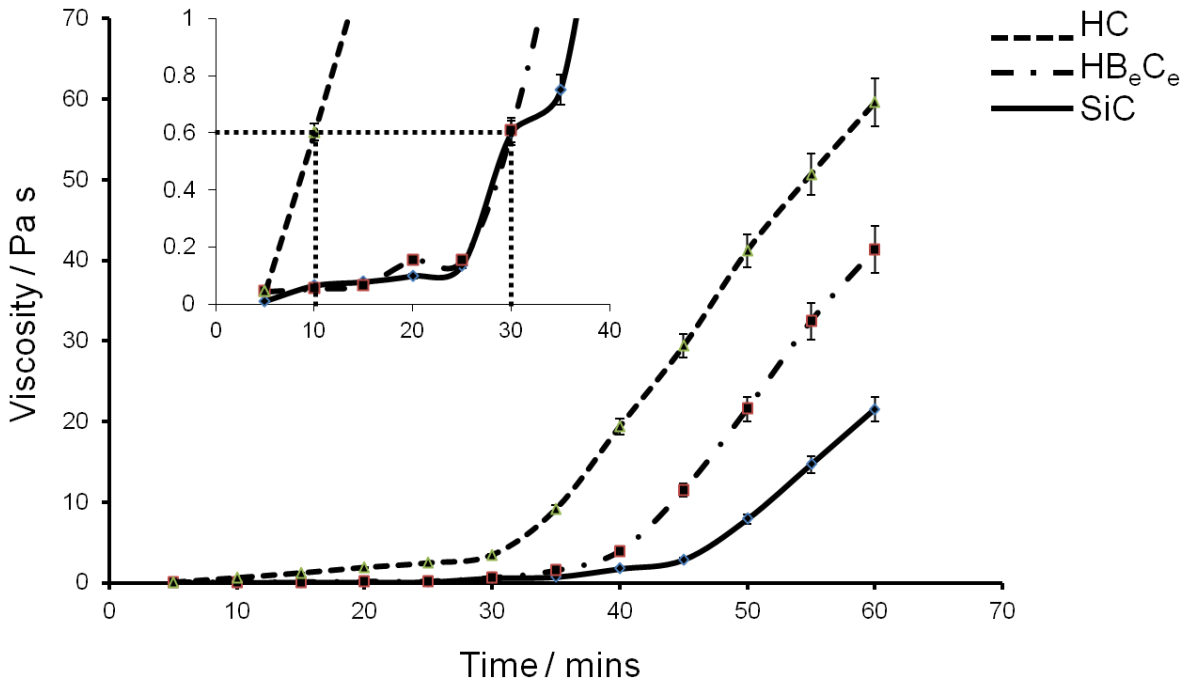

Figure 4.47: Viscosity of SiC, HfC and HfB_2 pre-ceramic sols at 5 min interval

The viscosity depends on various factors including the pH, temperature, pressure, solvent and concentration of the M-OH (metal-hydroxides) present in the sol. Figure 4.47 shows the viscosity versus reaction time curves for the

pre-ceramic sols. Such behaviour would be observed if the volume fraction of the solid in the suspension increased, either by the evaporation of the solvent or by the formation and growth of the sol particles, or a combination of the both. For the sake of consistency in the experiments, the viscosity of all sols were maintained at 0.6 Pa s by varying the time at which they were stirred after removing the reflux. As shown in the Figure 4.46, HfC required 10 min to attain 0.6 Pa s whilst HfB_2 and SiC required 30 min. Since the evolution of the sols was interrupted, the difference in the time required to attain 0.6 Pa s for the different sols was therefore attributed to the solvent concentration. The solvent evaporation rate and any contribution from the nucleation and growth of the sol particles was considered insignificant.

The compatibility and suitability of the SC_e, HC and HB_eC_e sols on C and SiC fibres were tested by measuring the contact angle of the sols on the fibre surfaces. The contact angle of all the pre-ceramic sols on both the fibre surfaces was less than 90^o, as shown in Table 4.2, Figure 4.48, and were believed to have relatively strong solid-liquid interactions. Since all the sols used were of the same viscosity, the wettability of the sols was purely based on the adherence between the materials involved.

Table 4.2: Contact angle of the pre-ceramic sols with C and SiC fibre surface

Sol	Contact Angle / ^{o}	
	On Carbon Fibres	On SiC Fibres
HC_e	62	8
HB_eC_e	63	17
SC_e	36	-

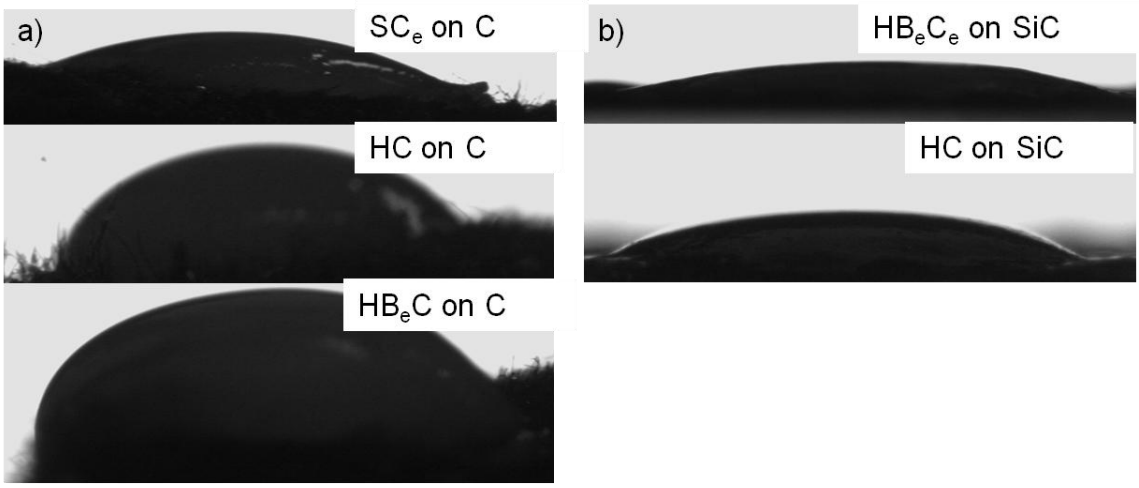

Figure 4.48: Profile of drop of pre-ceramic sols on C and SiC fibre surface

4.3.2 UHTC coatings on SiC and C fibres

Since the CTE values of HfC and HfB_2 are closer to that of SiC than to C, Table 4.3, the HfC and HfB_2 pre-ceramic sols were first coated on SiC fibres using a manual dip coating method to test their ability to spread. The coated fibres were dried and were subjected to carbothermal and boro/carbothermal reduction at 1600^oC for 2 h. The coatings showed no cracking, Figure 4.49, they were porous, due to the low yield of 65 and 49% from the sol-gel derived HfC and HfB_2 precursors respectively.

Table 4.3: CTE of C, SiC, HfC and HfB_2

Elements	CTE from room temperature to 2700°C / °C
Carbon fibre[viii]	0.7×10^{-6}
SiC	$4.0 \pm 0.2 \times 10^{-6}$
HfB_2	$5.7 \pm 0.2 \times 10^{-6}$
HfC	$7.3 \pm 0.2 \times 10^{-6}$

[viii] Derived from polyacrylonitrile (PAN) based in longitudinal direction

Figure 4.50, shows HfB_2 and HfC coatings on carbon fibre tows, produced by manual dip coating. The coatings showed cracking due to the large CTE mismatch between carbon and UHTC materials, resulting in compressive and tensile stresses. In order to bridge the difference in CTE values between 0.7 to 5.7 and 7.3, SiC was used as an intermediate coating. The resultant structure was also found to be cracked and SiC also acted as a weak link in the system during oxidation testing. Subsequent experiments were focused on producing crack-free coatings of HfB_2 and HfC directly on to carbon fibres.

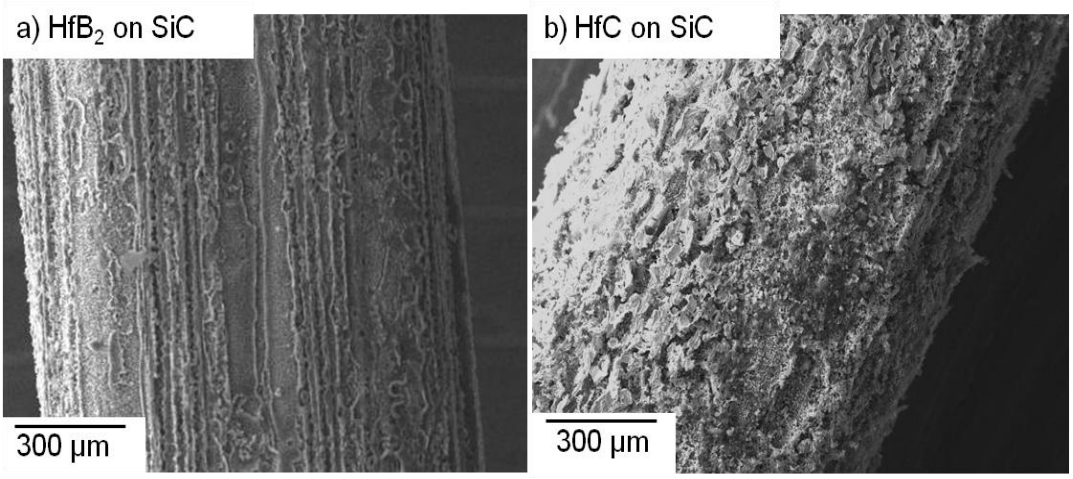

Figure 4.49: FEGSEM image of a) HfB_2 and b) HfC coating on a SiC fibre tow obtained using manual dip coating

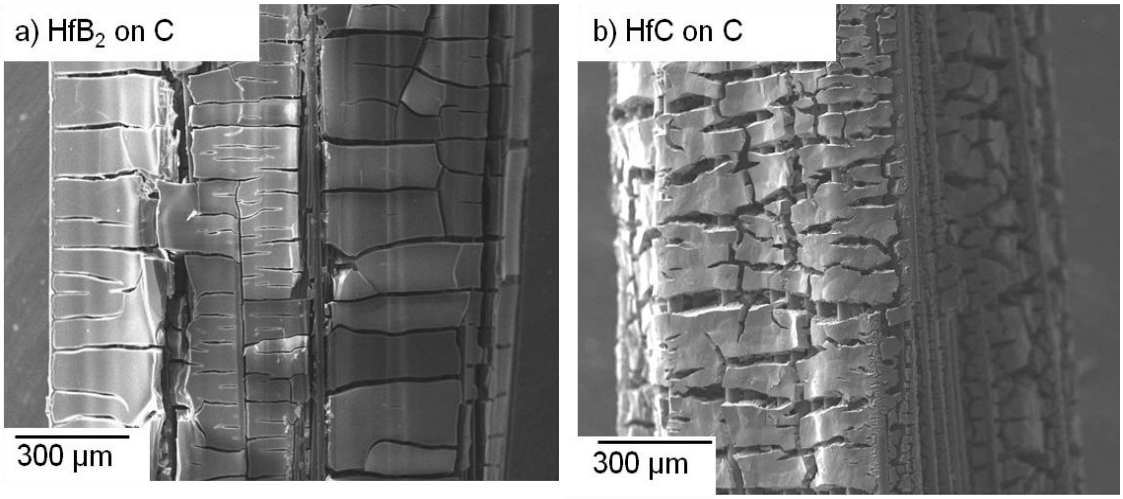

Figure 4.50: FEGSEM image of a) HfB_2 and b) HfC coating on C fibre tow obtained using manual dip coating

The cracking could be prevented by reducing the thickness of the coating, since the stress due to the CTE mismatch is inversely proportional to coating thickness, from equation 4.17.

$$\sigma = -\frac{E}{(1-\vartheta)}\frac{h^2}{6Rt} \tag{4.17}$$

where, E/(1-ϑ) is the biaxial modulus of the substrate, (in this case it is carbon), h is the diameter of the carbon fibre, which was 7 µm, t is the thickness of the coating and R is the radius of curvature of the carbon fibres.

Precise control of the coating thickness was not achievable using manual dip coating and hence an automatic dip coater (DC 100, Mega Electronics, Cambridge, UK) was used to produce uniform thin coatings of around 2 µm. There was found to be a linear relationship between the withdrawal speed set up for the automatic dip coater and the thickness of the resultant coating after boro/carbothermal reduction, as expected, see Figure 4.51. The slowest achievable speed in the equipment was 20 mm min^{-1} and was used to produce thin HfB_2 coatings on carbon fibres.

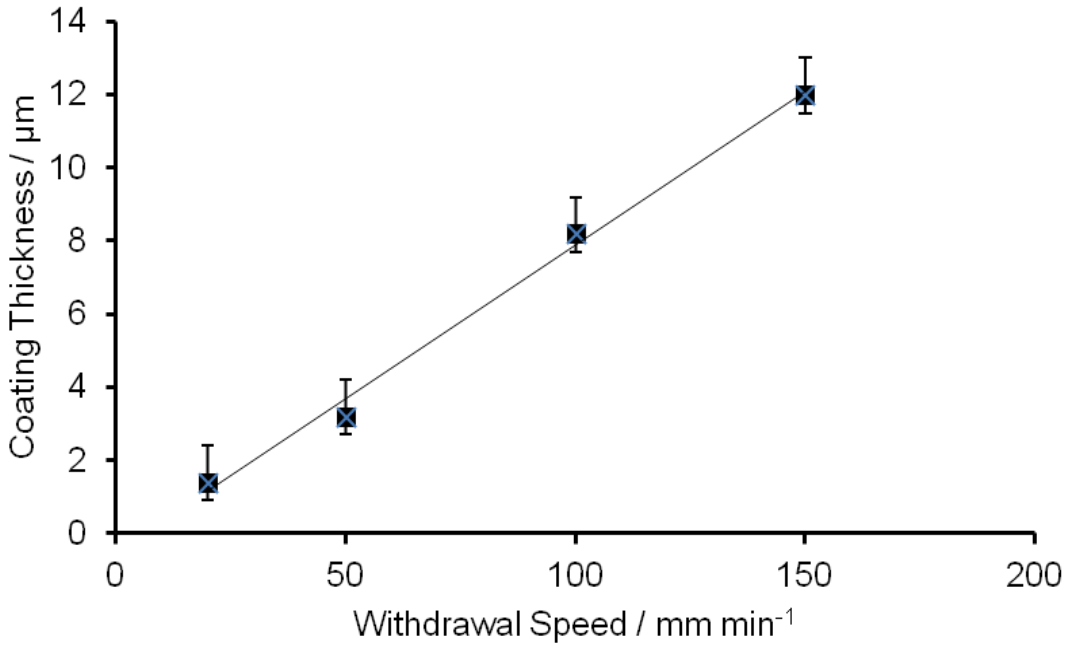

Figure 4.51: Coating thickness vs. Withdrawal speed in an automatic dip coater

Further coating studies were focussed on HfB_2, as HfC was found to be associated with the problem of yielding a HfO_2 layer that delaminated on oxidation. More details about this study are given in section 4.2.3. Using the automatic dip coater a very thin and crack-free coating of HfB_2 was obtained on carbon fibre tows. Cross-section and surface area analysis of the coated tows showed poor infiltration and discontinuity between the tows, see Figure 4.52. This was explained by the effect of trapped air bubbles during drying and subsequent heat treatment process.

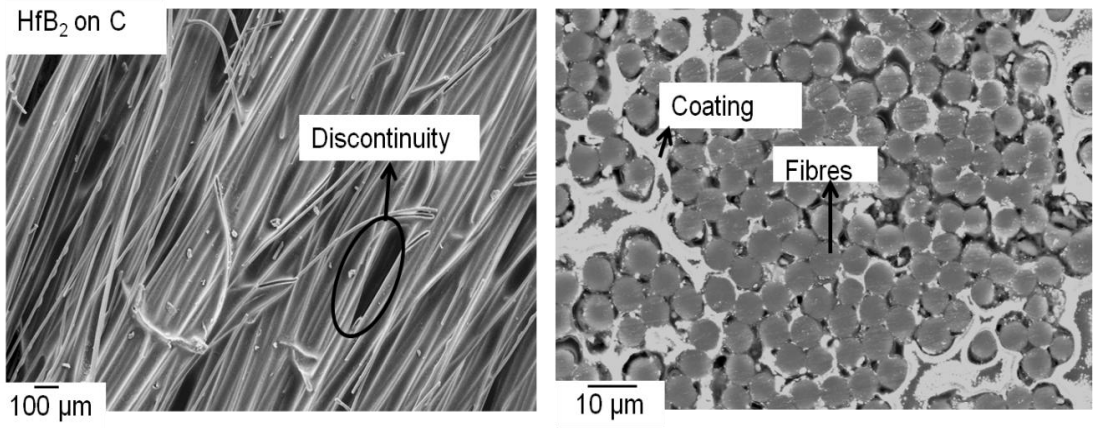

Figure 4.52: FEGSEM of HfB_2 coating on C obtained using automatic dip coating

All the pre-ceramic sols used for coatings had greater than stoichiometric carbon content and the resultant coatings included free carbon along with UHTC particles, (refer to Figure 4.53 b). When HfB_2 pre-ceramic sol containing the exact stoichiometry of carbon i.e. HB_eC, the surface analysis used, following the boro/carbothermal reduction reaction revealed a highly discontinuous coating and in some areas damage to the carbon fibre surfaces due to chemical attack arising from the reaction process, see Figure 4.53.

The free carbon thus helped to protect the carbon fibres surfaces, and also improve the adhesion of HfB_2 particles on the fibre surfaces.

It was therefore concluded that the presence of free carbon was important to achieve an acceptable quantity of coating without any fibre damage. An attempt to eliminate discontinuities in the coatings was carried out by using a

squeeze tube method; refer to section 3.4. The resulting coatings were crack-free and uniform, see Figure 4.54a. The free carbon containing the HfB_2 nano particles is shown in a FEGSEM backscattered photograph in Figure 4.54b.

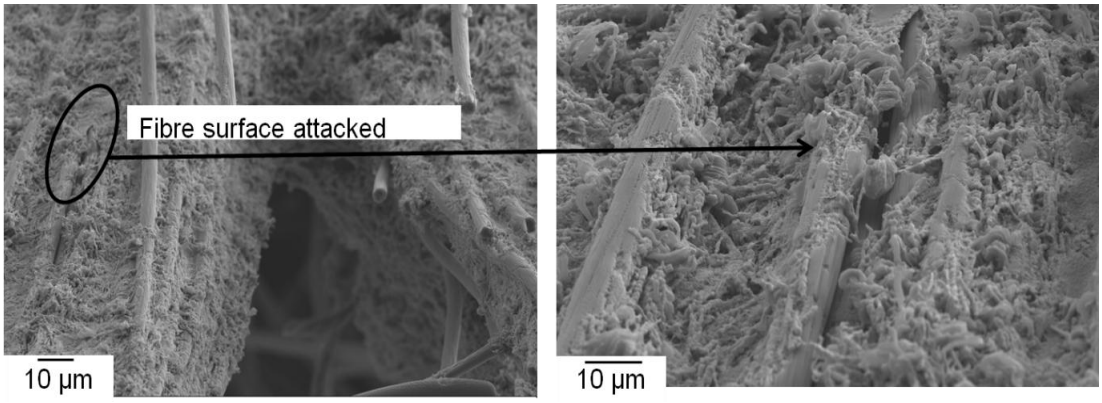

Figure 4.53: FEGSEM image of HfB_2 coating from HB_eC pre-ceramic sol on C fibres automatic dip coating

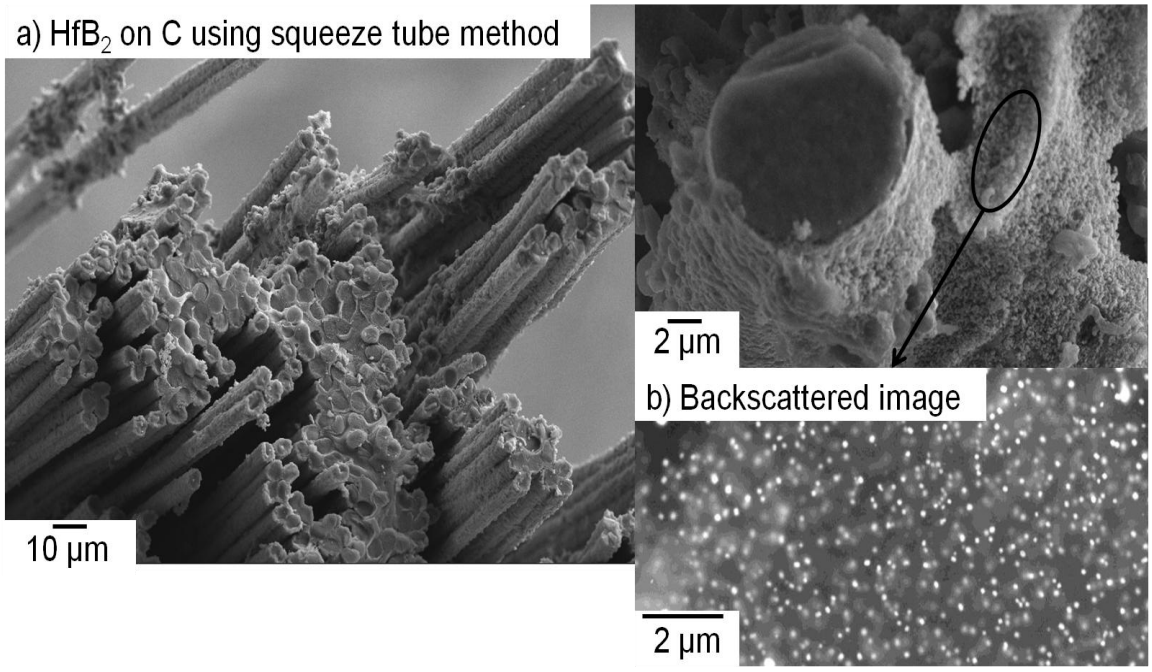

Figure 4.54: a) Secondary electron image and b) Back scattered electron image HfB_2 coating on C obtained from squeeze tube method

4.3.3 HTC impregnation in to C fibres

Following the success of the squeeze tube method in obtaining crack free and uniform coatings, an attempt was made to impregnate the carbon fibre tows using the LU synthesized HfB_2 powders; refer to section 3.5. Figure 4.55 shows the resultant crack-free surface area and well infiltrated intra-fibre pores.

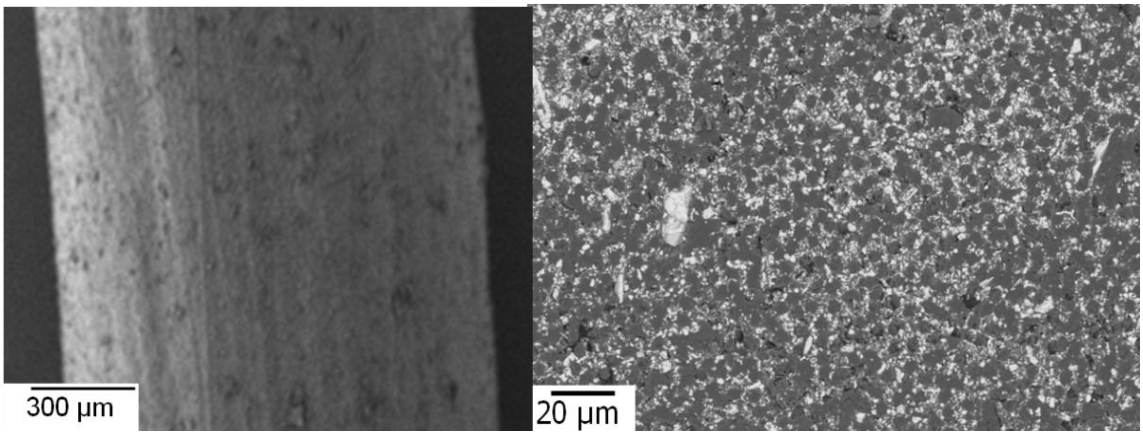

Figure 4.55: FEGSEM image of C fibres infiltrated with HfB_2 powder

The strength of the mini-composites obtained by infiltration of the HfB_2 slurry, was compared against those coated with pre-ceramic sol to check the influence of the heat treatment temperature on these mini-composites.

4.3.3.1 Tensile testing of mini-composites

The tensile strength of plain carbon fibre tows, and C fibre tows heat treated at 800^{o}C for 30 mins and at 1600^{o}C for 2 h, were tested along with those impregnated using the slurry and the pre-ceramic sol.

As seen from Figure 4.56, the maximum load a 5-fold carbon fibre tow can withstand a decrease from 230 MPa to 170 MPa, after heat treatment at 800^{o}C for 30 min. The heat treatment at 1600^{o}C further decreased the ultimate tensile load to 40 MPa. Any effect caused by the impregnation or infiltration is negligible, compared to the effect caused by the heat treatment. Figure 4.57

shows the fracture surface of the mini-composite prepared from slurry sol infiltration.

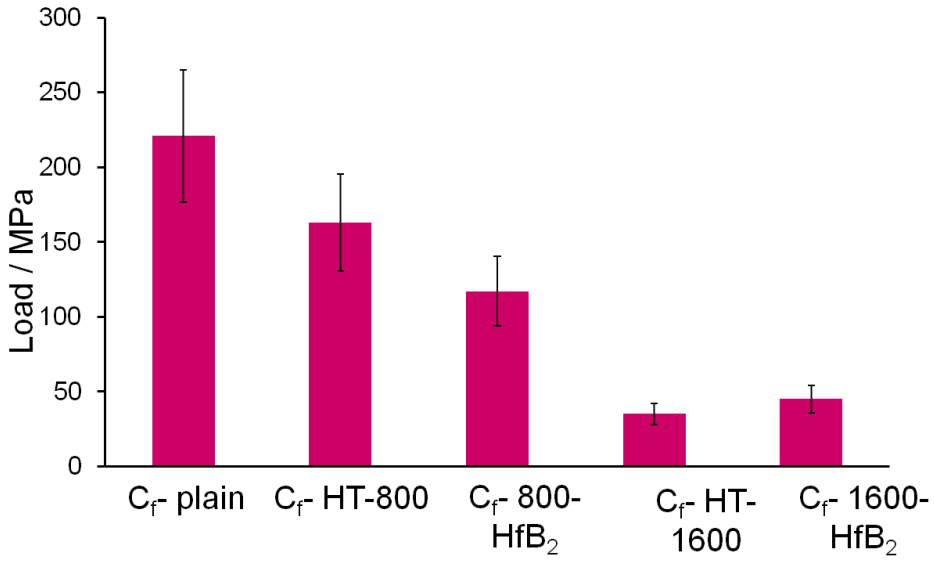

Figure 4.56: Tensile strength of carbon fibres impregnated with HfB_2 slurry and infiltrated with HB_eC_e pre-ceramic sol

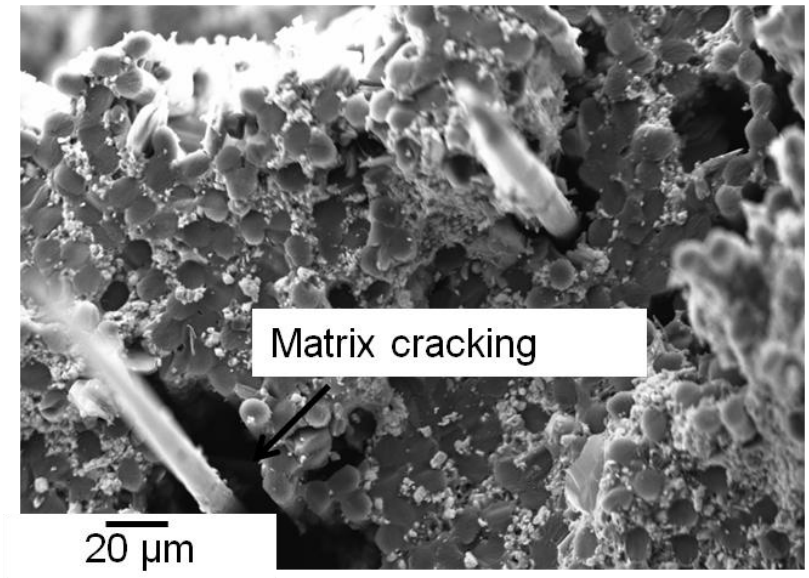

Figure 4.57: Fracture surface of a HfB_2 slurry impregnated C fibre mini-composite

The fracture was mainly due to matrix cracking, as expected. The strength of the carbon fibre being higher than that of HfB_2, the addition of the latter was

only to improve the oxidation resistance and not the overall strength. However, it was necessary to identity a processing method that did not decrease the strength of the carbon fibres drastically. Using this data, it was concluded that slurry impregnation using squeeze tube method, was a better technique to obtain crack free and non-porous coatings on carbon fibre tows, compared to pre-ceramic sol infiltration processed using the same method.

4.3.4 UHTC impregnation into C fibre preforms

Following the success of squeeze impregnation for both mini-composites and Cf-UHTC composites, an attempt to increase the percentage of solid-loading into the carbon preform was carried out using vacuum impregnation. These trials were carried out using commercially procured HfB_2 powders. A comparison of the weight increase after squeeze and vacuum impregnation is given in Table 4.4.

Table 4.4: Comparison of weight increase after squeeze and vacuum impregnation

Composite	Cf-HfB_2 Squeeze Impregnation	Cf-HfB_2 Vacuum Impregnation	Cf-HfC Squeeze Impregnation	Cf-HfC Vacuum Impregnation
weight increase / %	250	540	370	620

The vacuum impregnated Cf-HfC and Cf-HfB_2 composites were tested for their oxidation resistance, each for 140 and 180 s using an oxyacetylene torch. The time-temperature data during the test is given in Figure 4.58. The heating rate and peak temperatures were similar to those achieved in our previous work and the temperature data along with weight loss and erosion depth data are summarised in Table 4.5. Figure 4.59 shows images of the sample after the test.

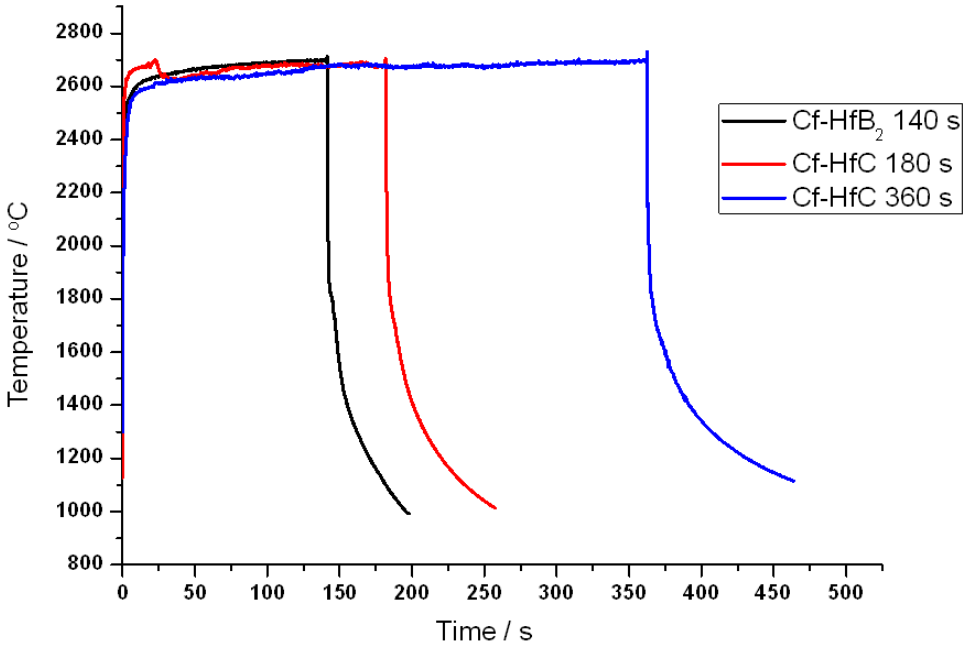

Figure 4.58: Time-temperature data during the long duration oxyacetylene testing of vacuum impregnated UHTC composites

Comparing the erosion depth from Table 4.5 and Figure 4.59, it can be seen that Cf-HfB2 offered superior oxidation protection compared to Cf-HfC. The erosion depth of the HfC-based composites may be limited by the length of the inner cone of the oxyacetylene flame. No erosion was observed if the inner flame was not touching the sample and the total length of the hottest flame was ~16 mm.

Table 4.5: Summary of the results after long duration oxyacetylene testing of vacuum impregnated UHTC composites

Sample	Test Duration / s	Peak Temperature / °C		Weight loss / g	Erosion Depth / mm
		Front face	Back face		
Cf-HfB_2	140	2712	786	1.5	<2.0
Cf-HfC	180	2706	635	2.0	9.0
Cf-HfC	360	2730	776	3.1	10.5

There was considerable erosion during the 360 s torch test and a series of photographs taken during and immediately after the test indicated that the HfO_2 formed was bonded immediately after the test, but fell off as the temperature dropped further, see Figure 4.60.

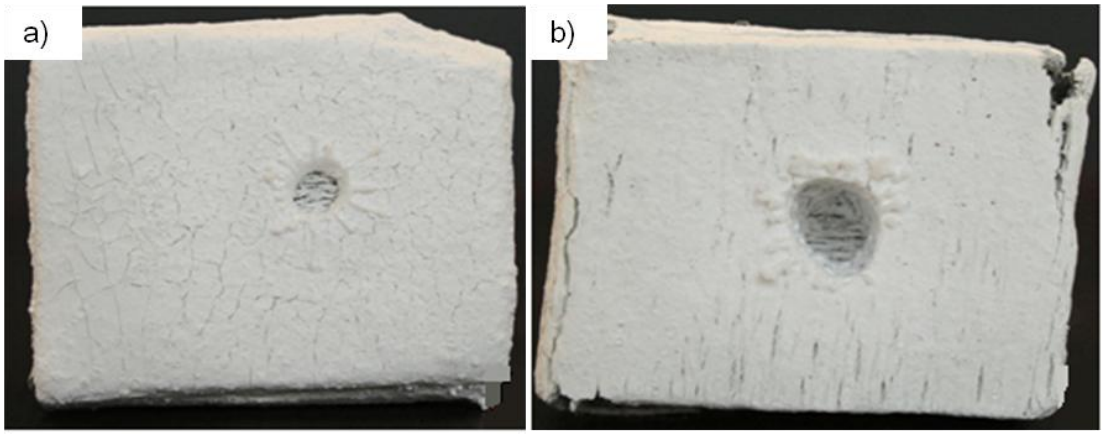

Figure 4.59: Vacuum impregnated UHTC composites after oxyacetylene torch testing a) Cf-HfB_2 composite after 140 s test and b) Cf-HfC composite after 180 s test

Figure 4.60: Series of images taken during and immediately after oxyacetylene testing showing spallation of the oxide layer for Cf-HfC composite

These results helped to narrow the focus to HfB_2-based composites as they produced the best results of all the compositions studied.

An attempt to vacuum impregnate the carbon fibre preforms using fine LU powders, showed poor solid loading, (<50%), compared to the commercial powder, although the initial solid content (55%) of the slurries were same and the two were prepared in the same manner. To investigate this, the rheology of the slurries containing the fine LU powders and the commercial HfB_2 powders was examined. As shown in Figure 4.61, the viscosity of the slurry containing the LU fine HfB_2 powder (100 mPas) was ten times higher than that prepared from the commercial HfB_2 (10 mPas). This is not unexpected given the differences in particle sizes. The former also showed a shear thinning behaviour, whilst the latter showed slight shear thickening. This difference is clearly indicative of the fine sized LU HfB_2 powders forming an emulsion as opposed to a micrometre sized commercial HfB_2 powder. Maintaining a constant mass of particles in the slurry whilst reducing the particle size, will lead to an increase in the number of particles. A higher number of fine particles will potentially result in more particle-particle interactions compared to lower number of larger particles and hence produce an increased resistance to flow. Increasing the shear rate will probably weaken this interaction, causing them to break down with further increase in the shear rate, resulting in shear thinning behaviour. The increased number of particle-particle interactions whilst using fine particles, is also the reason for higher viscosity of LU-based HfB_2 slurry compared to the commercial slurry. Similar effects of the particle size on the rheology of a fluid, have been reported by several [265, 266, 267] in other systems.

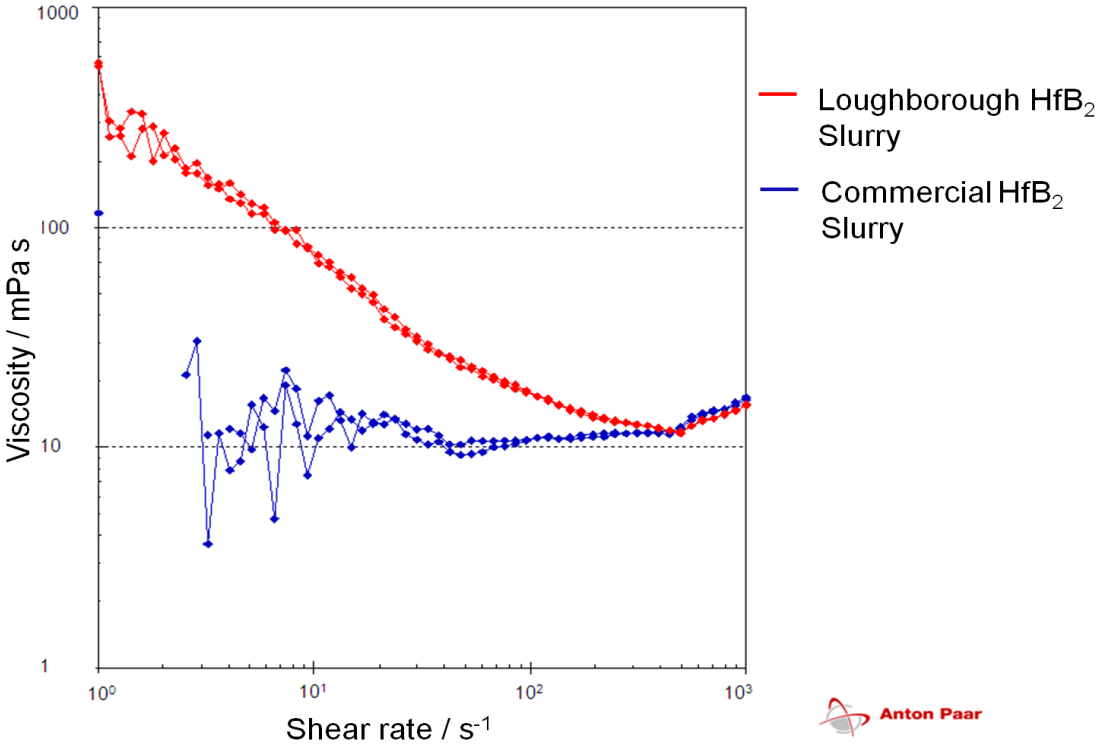

Figure 4.61: Rheology of HfB_2-phenolic slurry prepared from LU HfB_2 and commercial HfB_2 powders

The high viscosity of the LU HfB_2 slurry explains the poor solid loading. In order to compare the performance of Cf-LU HfB_2 composite and Cf-Comm. HfB_2, they have to contain the same mass of HfB_2. For this reason a latter with the same solid loading as the former was prepared and was subjected to oxyacetylene torch test. The heating rate and the peak front face temperatures, shown in Figure 4.62 revealed a heating rate of over $100^oC\ s^{-1}$ and temperatures generated as high as 2600^oC.

Comparing the erosion depth and weight loss values from Table 4.6 and Figures 4.63 and 4.64, it can be seen that the Cf-LU HfB_2 composite had a larger erosion volume, which was indicative of the poor ablation resistance of finer HfB_2 particles present. Both composites did not perform as well as those seen in the previous work done at Loughborough, due to poor solid loading [208].

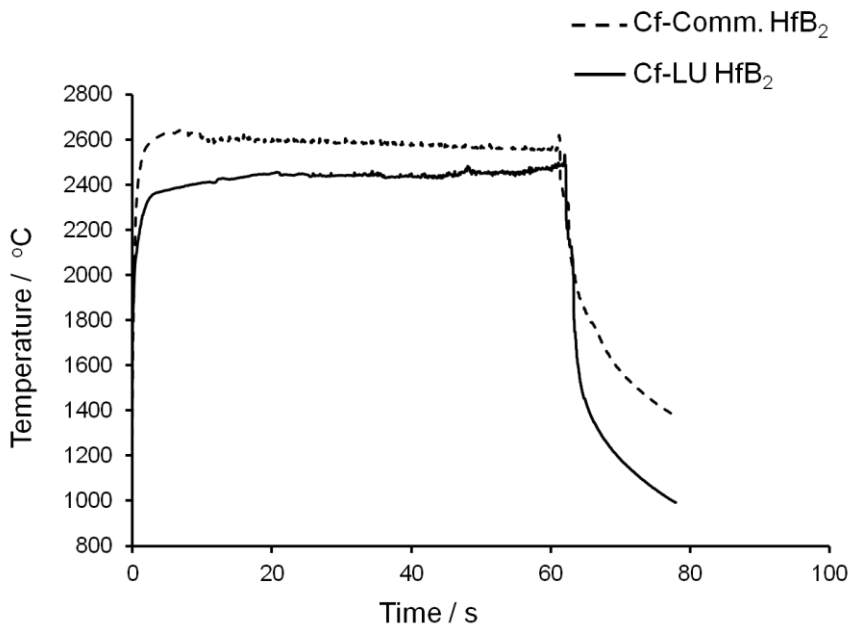

Figure 4.62: Time-temperature data during 60 s oxyacetylene testing of vacuum impregnated composites

Table 4.6: Summary of the results after 60 s oxyacetylene testing of vacuum impregnated composites

Composite	Bulk density before testing / g cm^{-3}	Test duration / s	Peak temperature / ^oC		Weight loss / g	Erosion Depth / mm
			Front (±150^oC)	Back (±10^oC)		
Cf-Comm. HfB_2	1.12	60	2620	150	0.972	11
Cf-LU HfB_2	1.02	60	2450	140	1.45	10

Figure 4.64 clearly shows that finer powders have penetrated deeper into the composite whilst the coarser powders were concentrated on the top 4 to 5 mm i.e. the bright grey areas indicate the presence of powders whilst the dark grey indicate carbon fibres within the preform.

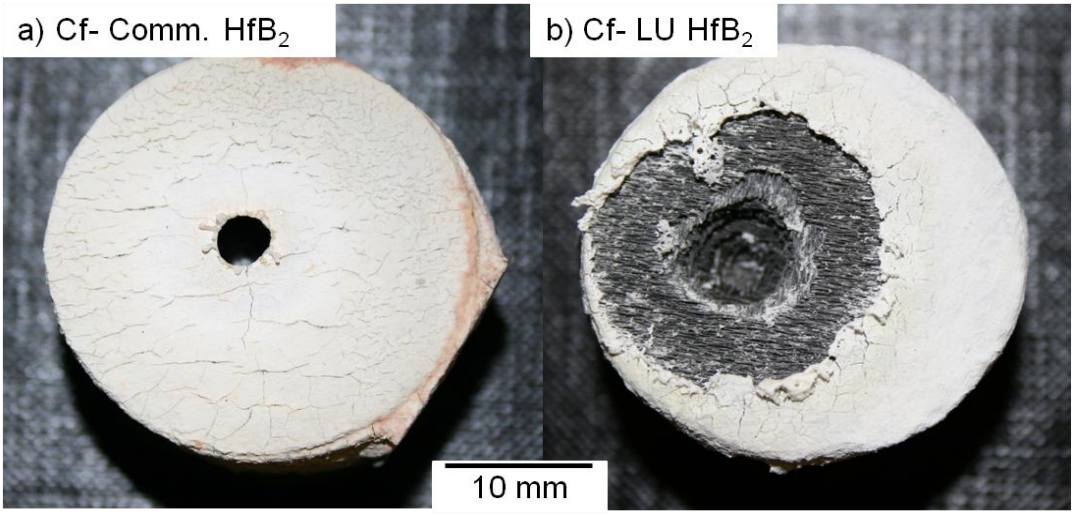

Figure 4.63: Vacuum impregnated UHTC composites after 60 s oxyacetylene torch testing a) Cf- Comm. HfB_2 and b) Cf- LU HfB_2 composite

Once the flame penetrated the top protective layer in the Cf-Comm HfB_2, it caused larger erosion, damaging the unprotected carbon fibres. This is evident from the micro CT image 4.64 a, where the hole gets wider after the UHTC protected surface is penetrated. On the other hand although the Loughborough HfB_2 showed better penetration into the Cf preform, the lack of powder concentration on the top surface, coupled with the fact that fine powders begin to oxidise at much lower temperature of around 400^{o}C (Figure 4.65) due to high surface area and ablate faster, when compared to coarser powder – which begins to oxidise around 600^{o}C (Figure 4.65), resulted in large surface erosion and poor performance.

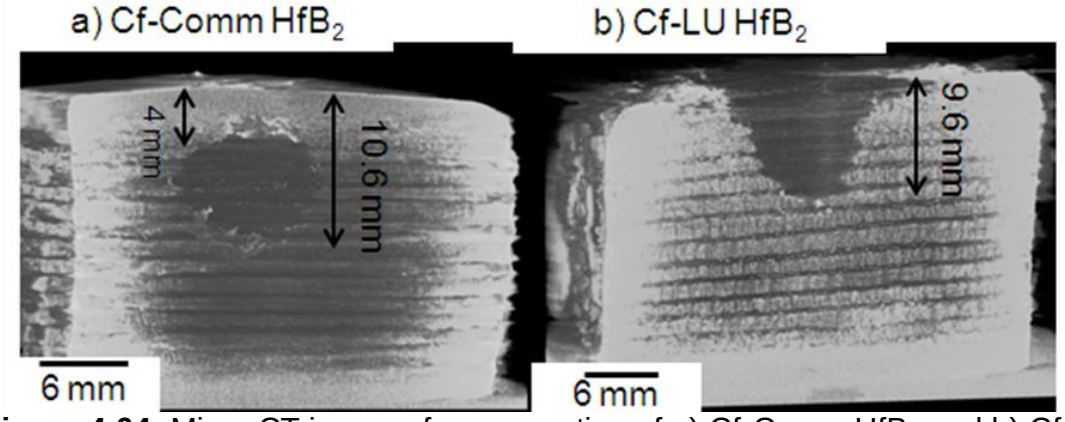

Figure 4.64: Micro CT image of cross section of a) Cf-Comm HfB_2 and b) Cf-LU HfB_2 after oxyacetylene torch testing

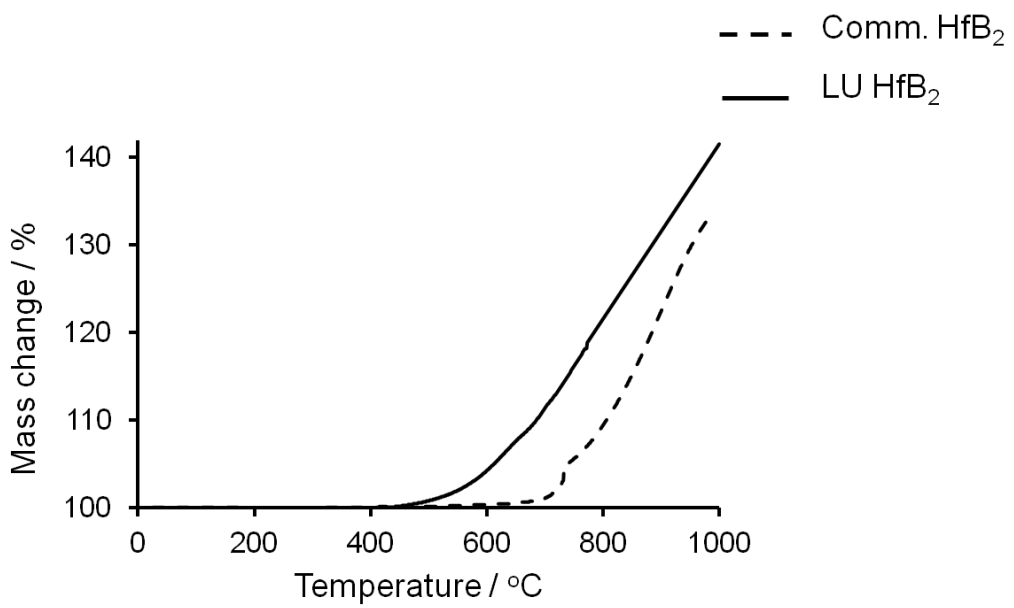

Figure 4.65: TGA of commercial and LU HfB_2 powder

If HfB_2 oxidises completely to HfO_2 and B_2O_3 as shown in equation 4.18,

$$1 \text{ mol } HfB_2 \rightarrow 1 \text{ mol } HfO_2 + 1 \text{ mol } B_2O_3 \quad (4.18\text{ a})$$

$$\text{i.e. } 200.1 \text{ g } HfB_2 \rightarrow 210.5 \text{ g } HfO_2 + 69.6 \text{ g } B_2O_3 \quad (4.18\text{ b})$$

then there should be 40% increase in weight assuming there was no evaporation of B_2O_3. As seen from Figure 4.65, the LU fine powder shows a weight increase of around 40% and since the B_2O_3 evaporation is not known to take place below 1100^{o}C it still exists in the system in liquid phase at this temperature 1000^{o}C.

The microstructures formed after the oxyacetylene testing of Cf-Comm. HfB_2 composites, Figure 4.66, revealed that the oxide of the UHTC particles melted and sintered on the surface and the degree of sintering decreased towards the edge of the composite. This was because the temperatures experienced by the edge (see Figure 4.66 a) were relatively low compared to the flame tip region. Closer to the flame tip (3 to 4 mm from the tip, see Figure 4.66 b) there was good contact between the particles indicated by signs of necking. This area was porous and many cracks were also visible. At the flame tip boundary, see Figure 4.66 c, liquid phases were formed as expected [268]. Figure 4.66 d

is a higher magnification image of one of the droplets formed after the test. This also shows signs of sintering between the particles.

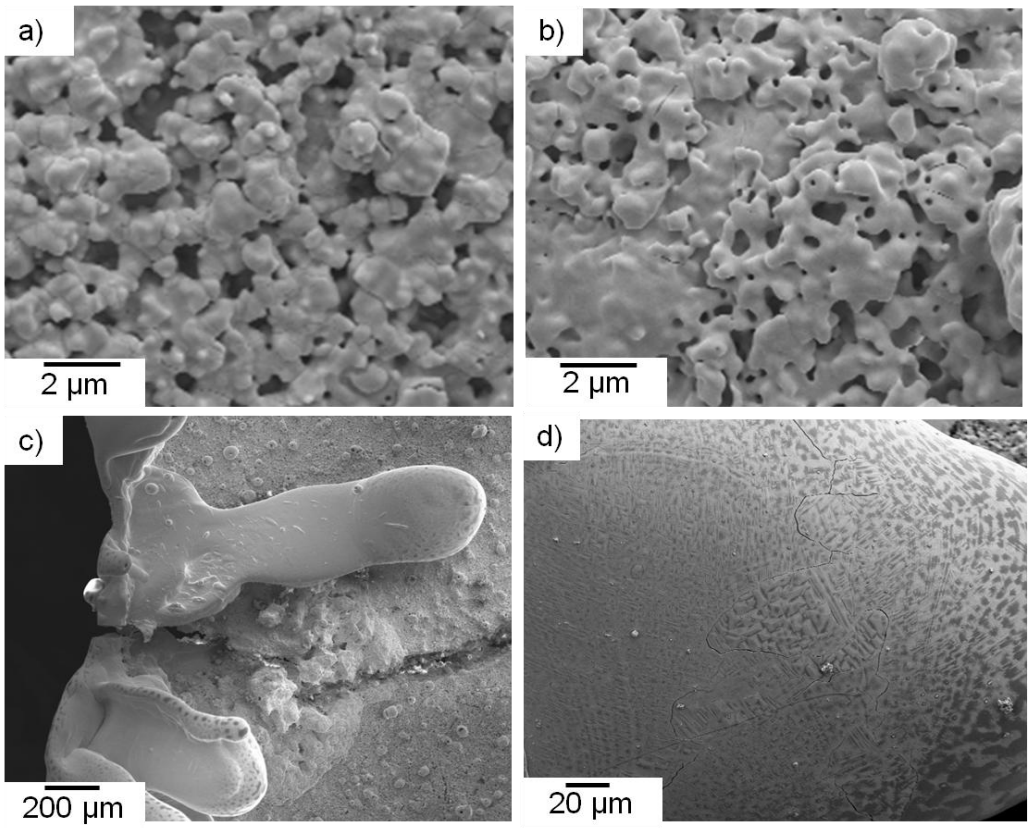

Figure 4.66: Microstructures after 60 s oxyacetylene testing of Cf-Comm. HfB_2 composite a) near the edge b) 3 to 4 mm from flame tip c) molten structure and d) high magnification on one of the molten droplets.

On the other hand the microstructures after 60 s oxyacetylene testing of Cf-LU HfB_2 composite, showed that the carbon fibres suffered severe degradation, which led to the formation of pointed fibres, see Figure 4.67 a, b. The surfaces of the fibres were also oxidised leading to pitting. This type of fibre degradation has been reported for carbon fibre composites at elevated temperatures [269]. Investigation of the HfO_2 particles within the eroded pit, showed the presence of B_2O_3 melt surrounding the particles, Figure 4.67 c. Further, the melt appeared to dissolve some of the HfO_2 particles to provide a liquid phase sintering mechanism, to achieve structures as seen in Figure 4.67 d.

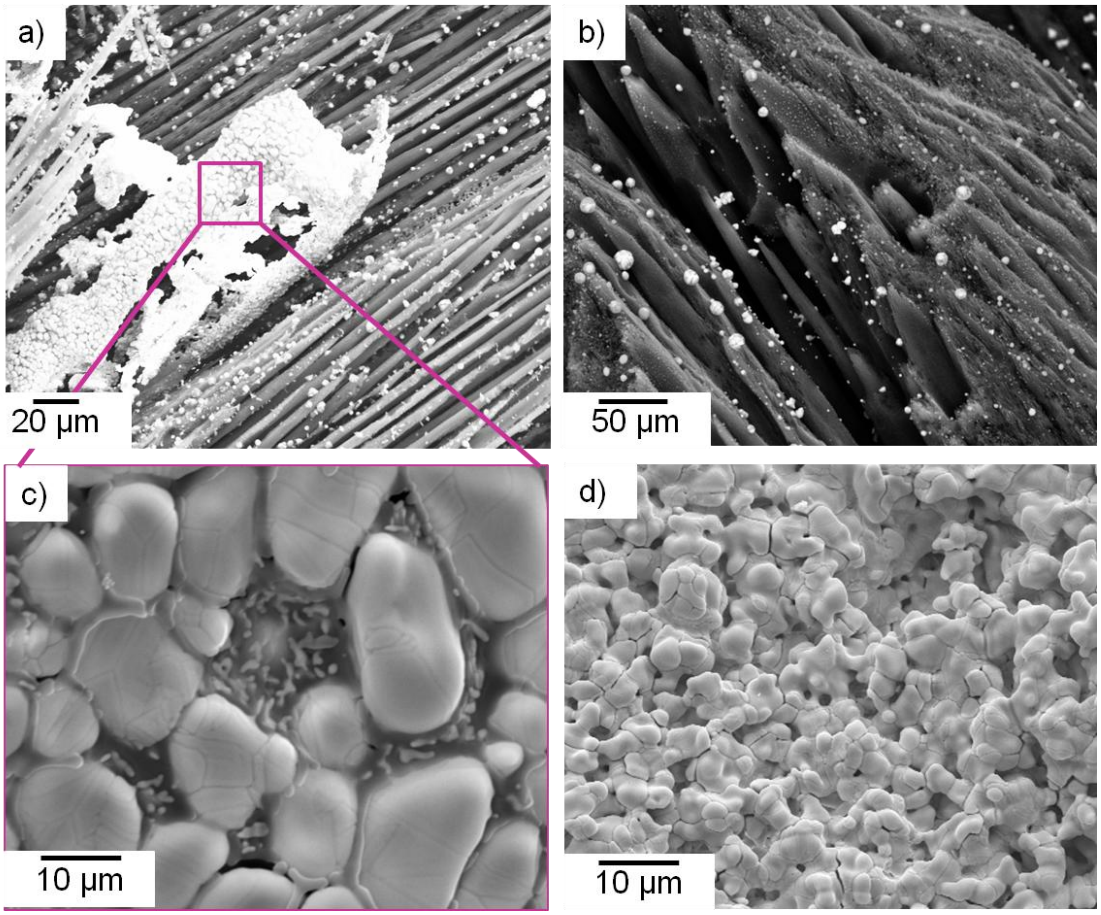

Figure 4.67: Microstructures after 60 s oxyacetylene testing of Cf-LU HfB_2 composite a) eroded area b) high magnification on the damaged C fibres from the eroded area c) deep within the eroded area and d) near the edge of the composite.

Ablation and oxidation resistance are extensive properties and depend on the mass and size of the particles used. Whilst there is no doubt that increasing the solid loading will improve the performance of the Cf-UHTC composites, finer particles will always have poor ablation and oxidation resistance compared to the coarser particles. To put the fine size of the particles to best use, a mixture of fine and coarse powders could be impregnated into the carbon preforms, where the fine powders could penetrate into the porous Cf preform that the coarse particles could not penetrate, (refer to Figure 2.26 [208])

Chapter 5

5 Conclusions

SiC, HfC and HfB_2 powders were prepared using a simple sol-gel approach. After the synthesis conditions were optimised, the powders were found to be XRD phase pure. The effect of changing the stoichiometry of the precursors on the purity of the final powders was studied. It was observed that if the carbon source was present in excess it acted as a capping agent for the ceramic particles and lead to a much finer final particle size. However, attempts to remove the free carbon and to retain the particle size and chemistry were unsuccessful and resulted in surface oxidation of the powders. For the HfB_2 powder synthesis, if both boron (Hf:B $\geq$ 6) and carbon source were in excess, then the final product consisted of boron carbide in addition to the HfB_2 particles. The carbothermal and boro/carbothermal reduction reaction mechanisms were studied for both HfC and HfB_2. HfC formation occurred through the formation of an intermediate HfC_xO_y phase and required a minimum of 1500^{o}C; it was complete after 2 h at 1600^{o}C. Phase pure HfC was obtained when the elemental stoichiometric ratio of Hf:C was kept at 3 and the resulting particle size was 1 to 2 µm.

HfB_2 could be formed at temperatures as low as 1300^{o}C by a boro/carbothermal reduction reaction. However, it required 25 h at this temperature to become phase pure. This long dwell time gave rise to a significant fraction of rod shaped particles, with growth occurring along the c-axis. The formation of HfB_2 did not proceed through the formation of either HfC or B_4C. The former was obtained at calcination temperatures lower than the latter, viz. 1300^{o}C for HfB_2 compared to 1500 and 1450^{o}C for HfC and B_4C respectively. The TGA/DTA results of the HfB_2 precursor powders made from B_2O_3 and amorphous B, however, showed identical peaks for the boro/carbothermal reduction reactions. Hence it is believed that the only thermodynamically favourable path for HfO_2, B_2O_3 and C to react and form

HfB_2 at 1300^oC is through the intermediate formation of amorphous B or boron sub oxides, although at higher temperatures more than one reaction mechanism could be active.

Rod formation was observed only during the boro/carbothermal reduction reactions and under conditions such as longer dwell times or under high concentrations of B_2O_3. No rods were formed as a result of a borothermal reduction reaction, where carbon was absent. This gives an insight into the role of carbon and B_2O_3 for anisotropic growth. Thus was found to be due to the formation of a Hf-B-C solid solution [252], which was contained in a B_2O_3 melt with the former instantly precipitating out of the latter, as HfB_2.

The effect of different carbon sources on the final particle size of the HfB_2 was also studied and it was found that the structure and the level of agglomeration of the carbon source had a direct influence on the particle size of HfB_2 powder. Liquid phenolic resin (LPR), sucrose, graphite and powder phenolic resin (PPR) resulted in a sheet like carbon that engulfed the ceramic particles on pyrolysis. The size of the sheets formed dictated the size and agglomeration of the HfB_2 particles. Tiny and well dispersed sheets resulted in finer and agglomeration-free HfB_2 particles. When carbon black and carbon nanotubes were used as the carbon source, the size of the resultant HfB_2 particles was directly dependent on the level of agglomeration of the source. The finest sub-micron sized HfB_2 powder was obtained when using PPR, the particle size was between 30 to 150 nm and the surface area was 21.8 m^2g^{-1}. SPS sintering of the sub-micron sized HfB_2 powders obtained using PPR as the carbon source at 2200^oC and 16 kN, resulted in 99% dense body, whilst under the same sintering conditions commercial powders reached only 91% of theoretical density.

Sol-gel coatings onto and slurry infiltration of the HfB_2 powder into carbon fibre tows was successfully carried out using a ‘squeeze tube’ method. The conclusions drawn from this study, was that excess carbon was required to help in the adhesion of the coating to the fibre and also to prevent the fibre surface being attacked during the boro/carbothermal reduction reaction.

Tensile testing results on both the slurry infiltrated and sol-gel coated samples showed that the strength of the carbon fibre mini-composite depended on the heat treatment temperature it was subjected to and deteriorated with higher heat treatment temperatures, as expected.

The assessment of the ablation resistance of Cf-UHTC composites has also been carried out by preparing composites utilizing a slurry impregnation route. Based on previous oxyacetylene torch testing, it was concluded that impregnation of Cf preforms with UHTC powders significantly improved the high temperature oxidation resistance of the composites compared to plain carbon preforms. A comparison of the oxidation and ablation resistance of the Cf-HfB_2 composites prepared with both commercial micron sized HfB_2 powder and with Loughborough sub-micron sized HfB_2 powder, each with a similar level of solid loading, showed that the ablation and oxidation resistance of latter was poor compared to the former. Since the properties under study viz: oxidation and ablation are dependent on the size of the particles increasing the solid loading of the composites may not improve the performance of Cf-Lu HfB_2 composite over Cf-Comm. HfB_2 composite. Hence the only possible way to improve the oxidation resistance of the Cf-HfB_2 composite will be to use a mixture of fine and coarse HfB_2 powders with the former filling those pores in the carbon preform that the latter cannot penetrate whilst the latter is expected to be concentrated on the surface of the preform thus giving the best possible protection through this route. More work is required to prove this hypothesis.

Chapter 6

6 Future Work

a. Although sol-gel synthesis of sub-micron sized HfB_2 was successful in small batches of 5 to 10 grams, larger batch synthesis of >15 grams lead to problems of inhomogeneous mixing amongst the precursors and single phase HfB_2 could not be obtained. In order to make sure the same level of mixing is obtained for larger batch synthesis, mixing equipment other than magnetic stirring, such as use of a shear mixer and sonicator, need to be investigated.

b. The source of the B_2O_3 impurity, which was undetectable using SIMS but surfaced during sintering leading to triple point formation, needs to identified and if it just residue from synthesis process, it has to be thoroughly removed by washing the fine HfB_2 powders with inorganic solvents in order to prevent the surface oxidation of the latter.

c. More work on the rheological charecterisation of the Loughborough HfB_2-phenolic slurry needs to be undertaken to acheive the maximum solid loading of the powder in the carbon preform.

d. Investigation of the oxidation and ablation performace of carbon fibre preforms impregnated with a mixture of Loughborough-synthesised fine HfB_2 and commercially available coarse powders needs to be carried out. The fine powders are expected to increase the percentage of solid loading in the preform, whilst the coarser powders are expected to fill the first few layers of the preform and provide the composite good ablation and oxidation resistance.

e. Oxidation testing of carbon fibre-HfB_2 composites showed a cracked HfO_2 layer on the surface, which would enable easy permeation of oxygen. Although formation of monoclinic HfO_2 with oxidation of Cf-HfB_2 is inevitable, the cracks forming due to phase transformation of HfO_2 from

monoclinic to tetragonal or cubic, should be prevented by stabilizing HfO_2 in the one of the two phases. This can be done with the help of dopants such as Y_2O_3, MgO, and Ta_2O_5 that can be mixed with HfB_2 so that, on oxidation, they dissolve into the HfO_2 lattice and stabilise the latter in the required high temperature phase. This work is now underway via a PhD studentship at Loughborough University.

f. The oxidation and ablation resistance of Cf-UHTC compostes can be further improved by developing layered UHTC coatings such as HfC and HfB_2 on the cabon fibre using chemical vapour infiltration, (CVI).

7 References

[1] Hicks, JW, Flight testing of airbreathing hypersonic vehicles, NASA technical memorandum, 4524.

[2] http://solarsystem.nasa.gov/missions/profile.cfm?Print=1&Sort=Alpha&Alias=Bumper%20WAC&Letter=B&Display=ReadMore&FIELDNAMES=

[3] Upadhya, K.; Yang, J.-M.; Hoffman, W. P., Materials for ultra-high temperature structural applications. *Am. Ceram. Soc. Bull.* **1997,** 76, (12), 51-56.

[4] Berton, B.; Bacos, M. P.; Demange, D.; Lahaye, J., High-temperature oxidation of silicon carbide in simulated atmospheric re-entry conditions. *J. Mater. Sci.* **1992,** 27, 3206-3210.

[5] Scott, H. G., Phase relationships in the zirconia-yttria system. *J. Mater. Sci.* **1975,** 10, 1527-1535.

[6] Wuchina, E.; Opila, E.; Fahrenholtz, W. G.; Talmy, I. G., UHTCs: Ultra-high temperature ceramic materials for extreme environment applications. *Interface* **2007**.

[7] Monteverde, F.; Bellosi, A.; Scatteia, L., Processing and properties of ultra-high temperature ceramics for space applications. *Mater. Sci. and Eng. A-Structural Materials Properties Microstructure and Processing* **2008,** 485, (1-2), 415-421.

[8] Fahrenholtz, W. G.; Hilmas, G. E.; Talmy, I. G.; Zaykoski, J. A., Refractory diborides of zirconium and hafnium. *J. Am. Ceram. Soc.* **2007,** 90, (5), 1347-1364.

[9] Monti, R.; Pezzella, G.; Savino, R.; Paterna, D.; Esposito, A., Aerothermodynamic study of an advanced thermal protection system. *4th European Workshop on Hot Structures and Thermal Protection Systems for Space Vehicles* **2003,** 521, 275-285.

[10] Russo, G.; Marino, G., The USV program & UHTC development. *4th European Workshop on Hot Structures and Thermal Protection Systems for Space Vehicles* **2003,** 521, 29-38.

[11] Tului, M.; Marino, G.; Valente, T., High temperature characterization of an UHTC candidate materials for RLV's. *4th European Workshop on Hot Structures and Thermal Protection Systems for Space Vehicles* **2003,** 521, 161-165.

[12] Monti, R.; Pezzella, G., Design criteria for low risk re-entry vehicles. *Proceedings of the Fifth European Symposium on Aerothermodynamics for Space Vehicles* **2004,** 563, 197-204.

[13] Opeka, M. M.; Talmy, I. G.; Zaykoski, J. A., Oxidation-based materials selection for 2000 degrees C plus hypersonic aerosurfaces: Theoretical considerations and historical experience. *J. Mat. Sci.* **2004,** 39, (19), 5887-5904.

[14] Chamberlain, A. L.; Fahrenholtz, W. G.; Hilmas, G. E.; Ellerby, D. T., Characterization of zirconium diboride for thermal protection systems. *Euro Ceramics Viii, Pts 1-3* **2004,** 264-268, 493-496.

[15] Savino, R.; Fumo, M. D.; Paterna, D.; Serpico, M., Aerothermodynamic study of UHTC-based thermal protection systems. *Aerospace Science and Technology* **2005,** 9, (2), 151-160.

[16] Levine, S. R.; Opila, E. J.; Halbig, M. C.; Kiser, J. D.; Singh, M.; Salem, J. A., Evaluation of ultra-high temperature ceramics for aeropropulsion use. *J. Euro. Ceram. Soc.* **2002,** 22, (14-15), 2757-2767.

[17] Candane, S. R.; Balaji, C.; Venkateshan, S. P., Ablation and aero-thermodynamic studies on thermal protection systems of sharp-nosed re-entry vehicles. *Journal of Heat Transfer-Transactions of the Asme* **2007,** 129, (7), 912-916.

[18] Bartuli, C.; Valente, T.; Tului, M., Plasma spray deposition and high temperature characterization of ZrB_2-SiC protective coatings. *Surface & Coatings Technology* **2002,** 155, (2-3), 260-273.

[19] Fahrenholtz, W. G.; Hilmas, G. E. *NSF-AFOSR joint work-shop on future ultra high temperature materials* **2004.**

[20] Akin, I.; Hotta, M.; Sahin, F. C.; Yucel, O.; Goller, G.; Goto, T., Microstructure and densification of ZrB_2-SiC composites prepared by spark plasma sintering. *J. Euro. Ceram. Soc.* **2009,** 29, (11), 2379-2385.

[21] Balbo, A.; Sciti, D., Spark plasma sintering and hot pressing of ZrB_2-$MoSi_2$ ultra-high-temperature ceramics. *Materials Science and Engineering a-Structural Materials Properties Microstructure and Processing* **2008,** 475, (1-2), 108-112.

[22] Cao, J. L.; Xu, Q.; Zhu, S. Z.; Zhao, J. F.; Wang, F. C., Microstructure of ZrB_2-SiC composite fabricated by spark plasma sintering. *High-Performance Ceramics V, Pts 1 and 2* **2008,** 368-372, 1743-1745.

[23] Chamberlain, A. L.; Fahrenholtz, W. G.; Hilmas, G. E., Low-temperature densification of zirconium diboride ceramics by reactive hot pressing. *J. Am. Ceram. Soc.* **2006,** 89, 3638-3645.

[24] Chen, D. J.; Xu, L.; Zhang, X. H.; Ma, B. X.; Hu, P., Preparation of ZrB_2 based hybrid composites reinforced with SiC whiskers and SiC particles by hot-pressing. *International Journal of Refractory Metals & Hard Materials* **2009,** 27, (4), 792-795.

[25] Guo, W. M.; Vleugels, J.; Zhang, G. J.; Wang, P. L.; Van der Biest, O., Effects of Re_2O_3 (Re=La, Nd, Y and Yb) addition in hot-pressed ZrB_2-SiC ceramics. *J. Europ. Ceram. Soc.* **2009,** 29, (14), 3063-3068.

[26] Ramirez-Rico, J.; Bautista, M. A.; Martinez-Fernandez, J.; Singh, M., Compressive Strength Degredation in ZrB_2-SiC and ZrB_2-SiC-C Ultra High Temperature Composites. In *Mechanical Properties and Performance of*

Engineering Ceramics and Composites IV, Singh, D.; Kriven, W. M., Eds. **2010;** Vol. 30, pp 127-136.

[27] Guo, S. Q., Densification of ZrB_2-based composites and their mechanical and physical properties: A review. *J. Euro. Ceram. Soc.* **2009,** 29, (6), 995-1011.

[28] Tang, S. F.; Deng, J. Y.; Wang, S. J.; Liu, W. C., Fabrication and characterization of an ultra-high-temperature carbon fiber-reinforced ZrB_2-SiC matrix composite. *J. Am. Ceram. Soc.* **2007,** 90, 3320-3322.

[29] Tang, S. F.; Deng, J. Y.; Wang, S. J.; Liu, W. C.; Yang, K., Ablation behaviors of ultra-high temperature ceramic composites. *Materials Science and Engineering: A* **2007,** 465, 1-7.

[30] http://ceramics.org/ceramictechtoday/2011/08/12/hafnium-and-zirconium-diboride-composites-for-leading-edges-of-hypersonic-vehicles/

[31] http://www.nasa.gov/centers/dryden/history/pastprojects/HyperX/index.html

[32] Squire, T. H.; Marschall, J., Material property requirements for analysis and design of UHTC components in hypersonic applications, *J. Eur. Ceram. Soc.* **2010,** 30, (11), 2239–2251.

[33] Borrelli, R.; Riccio, A.; Tescione, D.; Gardi, R.; Marino, G., Thermo-structural behavior of an UHTC made nose cap of a reentry vehicle. *Acta Astronautica* **2009,** 65, 442-456

[34] Savino, R.; Fumo, M. D. S.; Paterna, D.; Serpico, M., Aerothermodynamic study of UHTC-based thermal protection systems. *Aerospace Science and Technology* **2005,** 9, 151-160

[35] Uahakov, S. V.; Navrotsky, A., Experimental approaches to thermodynamics above 1500 degrees C. *J. Am. Ceram. Soc.* **2012,** 102, (5), 1551-2916.

[36] Fahrenholtz, W. G.; Hilmas G. E., Refractory diborides of zirconium and hafnium, *J. Am. Ceram. Soc.* **2007,** 90, (5), 1347-1364.

[37] Upadhya, K.; Yang, J. M.; Hoffman, W., Advanced materials for ultra-high temperature structural applications above 2000 degrees C, AFRL-PR-ED-TP-1998-007

[38] Bronson, A. B.; Ma, Y. T.; Musto, R. R., Compatibility of refractory metal boride/oxide composites at ultra-high temperatures, *J. Electrochem. Soc.* **1992,** 139, (11), 3183-3196.

[39] Lawson, J. W.; Daw, M. S., and Bauschlicher, C. W. Jr. , Lattice thermal conductivity of ultra high temperature ceramics ZrB_2 and HfB_2 from atomistic simulations, *J. Appl. Phys.* **2011**, 110, 083507.

[40] Sacks, M. D.; Wang, C. A.; Yang, Z. H.; Jain A., Carbothermal reduction synthesis of nanocrystalline zirconium carbide and hafnium carbide powders using solution-derived precursors. *J. Mater. Sci.* **2004,** 39, 6057- 6066.

[41] Liu, J. X.; Kan, Y. M.; Zhang, G. J., Synthesis of ultra-fine hafnium carbide powder and its pressureless sintering. *J. Am. Ceram. Soc.* **2010,** 93, (4), 980-986.

[42] Shimada, S.; Inagaki, M., Oxidation kinetics of hafnium carbide in the temperature range of 480 to 600 degrees C, *J. Am. Ceram. Soc.* **1992,** 75, (10), 2671-2678.

[43] Shimada, S., A thermoanalytical study on the oxidation of ZrC and HfC powders with formation of carbon. *Solid State Ionics* **2002,** 149, 319-326

[44] Barraud, E.; Begin-Colin, S.; Le Caer, G.; Barres, O.; Villieras, F., Mechanically activated solid-state synthesis of hafnium carbide and hafnium nitride nanoparticles. *Journal of Alloys and Compounds* **2008,** 456, 224-233.

[45] Opeka, M. M.; Talmy, I. G.; Wuchina, E. J.; Zaykoski, J. A.; Causey, S. J., Mechanical, thermal, and oxidation properties of refractory hafnium and

zirconium compounds. *Journal of the European Ceramic Society* **1999,** 19, 2405-2414.

[46] Upadhya, K.; Yang, J. M.; Hoffman, W. P., Materials for ultra-high temperature structural applications. *American Ceramic Society Bulletin* **1997,** 76, (12), 51-56.

[47] Bacciochini, A.; Glandut, N.; Lefort, P., Surface densification of porous ZrC by a laser process. *Journal of the European Ceramic Society* **2009,** 29, 1507-1511.

[48] Bargeron, C. B.; Benson, R. C.; Jette, A. N.; Phillips, T. E., Oxidation of hafnium carbide in the temperature range 1400 degrees C to 2060 degrees C, *J. Am. Ceram. Soc.* **1993,** 76, (4), 1040-1046.

[49] Opeka, M. M.; Talmy, I. G.; Zaykoski, J. A., Oxidation-based materials selection for 2000 degrees C + hypersonic aerosurfaces: Theoretical considerations and historical experience. *J. Mater. Sci.* **2004,** 39, 5887-5904.

[50] Shimada, S.; Nakajima, K.; Inagaki, M., Oxidation of single crystals hafnium carbide in a temperature range of 600 to 900 degrees C, *J. Am. Ceram. Soc*. **1997,** 80, (7), 1749-1756.

[51] Rao, R; Venugopal, V., Kinetics and mechanism of the oxidation of ZrC. *Journal of Alloys and Compounds* **1994,** 206, 237-242.

[52] Voitovich, R. F.; Pugach, E. A., High-temperature oxidation of ZrC and HfC. *Institute of Materials Science, Academy of Science of the Ukrainian SSR, translated from Poroshkovaya Metallurigiya* **1973,** 131, (11), 67-74.

[53] Wuchina, E. J.; Opeka, M. M., The oxidation behavior of HfC, HfN, and HfB_2. *High temperature corrosion and materials chemistry III, The Electrochemical Society, Inc.: New Jersey,* **2001,** 136-140.

[54] Holeomb, G. R.; St. Pierre, G. R., Application of a counter-current gaseous diffusion model to the oxidation of hafnium carbide at 1200 to 1530 degrees C. *Oxidation of Metals* **1993,** 40, 109-118.

[55] Li, G. D.; Xiong, X.; Huang, B. Y.; Zeng, Y. L., Oxidized characteristic and oxidized mechanism of TaC coating. *The Chinese Journal of Nonferrous Metals* **2007,** 17, (3), 360-367.

[56] McClaine, L. A., Thermodynamic and kinetic studies for a refractory materials program, ASD-TDR-62-204.

[57] Fahrenholtz, W. G.; Hilmas, G. E., Refractory diborides of zirconium and hafnium. *J. Am. Ceram. Soc.* **2007,** 90, (5), 1347-1364.

[58] Kufman, L.; Clougherty, E.V., Investigation of boride compounds for very high temperature applications, AFML-TR-68-190.

[59] Chen, L.; Gu, Y.; Shi, L.; Yang, Z.; Ma, J.; Qian, Y., Synthesis and oxidation of nanocrystalline HfB_2. *J. Alloys Compd.* **2004,** 368, (2), 353–356.

[60] Yan, Y. J.; Huang, Z. R.; Dong, S. M.; Jiang, D. L., New route to synthesize ultra-fine zirconium diboride powders using inorganic–organic hybrid precursors, *J. Am. Ceram. Soc.* **2006,** 89, (11), 3585-3588.

[61] Mishra, S. K.; Das, S.; Das, S. K.; Ramachandrarao, P. Sintering studies on ultrafine ZrB_2 powder produced by a self-propagating high-temperature synthesis process. *J. Mater. Res.* **2000,** 15, (11), 2499-2504.

[62] Khanra, A. K.; Pathak, L. C.; Godkhindi, M. M., Double SHS of ZrB_2 powder. *Journal of Materials Processing Technology* **2008,** 202, 386-390.

[63] Camurlu, H. E.; Maglia, F., Preparation of nano-size ZrB_2 powder by self-propagating high-temperature synthesis. *Journal of the European Ceramic Society* **2009,** 29, 1501-1506.

[64] Munir, Z. A., Reaction synthesis processes: mechanisms and characteristics, *Metall. Mater. Trans.* **1992,** A23, (1), 7–13.

[65] Blum, Y. D.; Marschall, J.; Hui, D.; Adair, B.; Vestel, M., Hafnium reactivity with boron and carbon sources under non-self-propagating high-temperature synthesis conditions. *J. Am. Ceram. Soc.* **2008,** 91, (5), 1481–1488.

[66] Fahrenholtz, W. G.; Hilmas, G. E., Refractory diborides of zirconium and hafnium. *J. Am. Ceram. Soc.* **2007,** 90, (5), 1347-1364.

[67] Ni, D. W.; Synthesis of monodispersed fine hafnium diboride powders using carbo/borothermal reduction of hafnium dioxide, *J. Am. Ceram. Soc.* **2008,** 91, (8), 2709-2712.

[68] Zhang, G. J.; Guo, W. M.; Ni, D. W.; Kan, Y. M., Ultra-high temperature ceramics (UHTCs) based on ZrB_2 and HfB_2 systems: powder synthesis, densification and mechanical properties. *16th International Symposium on Boron, Borides and Related Materials, Journal of Physics: Conference Series* **2009***,* 176.

[69] Guo, W. M.; Yang, Z. G.; Zhang, G. J., Synthesis of submicrometer HfB_2 powder and its densification. *Materials Letters* **2012,** 83, 52–55.

[70] Blum, Y. D.; Kleebe, H. J.; Chemical reactivities of hafnium and its derived boride, carbide and nitride compounds at relatively mild temperature. *J. Mater. Sci.* **2004,** 39, 6023 – 6042.

[71] Rhodes, W. H.; Kalish, D.; Clougher.Ev, High temperature mechanical properties of ZrB_2 and ZrB_2+SiC. *American Ceramic Society Bulletin* **1970,** 49, (4), 382.

[72] Meeson, G. A.; Gorbunow, A. F., Activated sintering of zirconium boride. *Inorg. Mater.* **1968,** 4, 267-270.

[73] Guo, S. Q., Densification of ZrB_2-based composites and their mechanical and physical properties: A review. *J. Euro. Ceram. Soc.* **2009,** 29, (6), 995-1011.

[74] Guo, S. Q.; Yang, J. M.; Tanaka, H.; Kagawa, Y., Effect of thermal exposure on strength of ZrB_2-based composites with nano-sized SiC particles. *Comp. Sci. and Tech.* **2008,** 68, (14), 3033-3040.

[75] Kalish, D. Z.; Clougher, E. V., Densification mechanisms in high-pressure hot-pressing of HfB_2. *J. Am. Ceram. Soc.* **1969,** 52, (1), 26-30.

[76] Kalish, D. Z.; Clougher, E. V.; Kreder, K., Strength, fracture mode, and thermal stress resistance of HfB_2 and ZrB_2. *J. Am. Ceram. Soc.* **1969,** 52, (1), 30-36.

[77] Venkateswaran, T.; Basu, B.; Raju, G. B.; Kim, D.-Y., Densification and properties of transition metal borides-based ceramics via spark plasma sintering. *J. Europ. Ceram. Soc.* **2006,** 26, 2431-2440.

[78] Anselmi-Tamburini, U.; Kodera, Y.; Gasch, M.; Unuvar, C.; Munir, Z. A.; Ohyanagi, M.; Johnson, S. M., Synthesis and characterization of dense ultra-high temperature thermal protection materials produced by field activation through spark plasma sintering (SPS): I. Hafnium Diboride. *J. Mater. Sci.* **2006,** 41, (10), 3097-3104.

[79] Rhodes, W. H.; Clougherty, E. V.; Kalish, D., Research and development of oxidation resistant diborides: Mechanical properties, AFML-T-68-190 Part II, Vol IV

[80] Clougherty, E.V.; Wilkes, K. E.; Tye, R. P., Research and development of oxidation-resistant diborides: Thermal, Physical, Electrical, and Optical Properties. AFML-TR-68-190 Part II, Vol V.

[81] http://thermophysical.tainstruments.com/PDF/technotes/TPN-67%20Principal%20Methods%20of%20Thermal%20Conductivity%20Measurement.pdf

[82] Tye, Clougherty, The Thermal and Electrical Conductivities of Some Electrically. Conducting Compounds. *Proceeding of the fifth symposium of thermophysical properties*, **1970,** 396-401.

[83] Branscomb, Hunter, Improved Thermal Diffusivity Method Applied to TiB_2, ZrB_2 and HfB_2 from 200°-1300°C, *J. App. Phy.* **971,** 42, 2309-2315.

[84] Zhang, L; Pejaković, D. A; Marschall, J; Gasch, M, Thermal and Electrical Transport Properties of Spark Plasma-Sintered HfB_2 and ZrB_2 Ceramics, *J. Am. Ceram. Soc.* **2011,** 94, 2562-2570.

[85] Fridlender, B. A; Ordan'yan, S. S; Neshpor, V. S; and Savel'ev, G. A., Thermal conductivity and thermal diffusivity of materials of the TiC-TiB_2 system at high temperatures, Teplofiz. Vys. Temp.,18, No. 5, 1002–1006 (1980).

[86] Andrievskii, et al., Effect of zirconium carbide and carbon additions on some physicomechanical properties of zirconium diboride, *Soviet Powder Metallurgy and Metal Ceramics, Vol 19(2)* **1980,** 27-29.

[87] Zimmermann, J. W; Hilmas, G; Fahrenholtz, W; Dinwiddie, Porter, Wang, Thermophysical Properties of ZrB_2 and ZrB_2–SiC Ceramics, *J. Am. Ceram. Soc.* **2008***,* 91, 1405-1411.

[88] Thompson, M. J; Fahrenholtz, W; Hilmas, G, Elevated Temperature Thermal Properties of ZrB_2 with Carbon Additions, *J. Am. Ceram. Soc.,* **2012,** 95, 1077-1085.

[89] Bronson, A. B; Ma, Y. T; Musto, R R; Compatibility of refractory metal boride/oxide composites at ultrahigh temperatures. *J. Electrochem. Soc.* **1992,** 139, (11), 3183-3196.

[90] Chen, L. Y.; Gu, Y. L.; Shi, L.; Yang, Z. H.; Ma, J. H.; Qian, Y. T., Synthesis and oxidation of nanocrystalline HfB_2. *J. of Alloys and Cmpds***,** 368, 353-356.

[91] Parthasarathy, T. A.; Rapp, R. A.; Opeka, M.; Kerans, R. J., Effects of phase change and oxygen permeability in oxide scales on oxidation kinetics of ZrB_2 and HfB_2. *J. Am. Ceram. Soc.* **2009,** 92, (5), 1079-1086.

[92] Parthasarathy, T. A.; Rapp, R. A.; Opeka, M.; Kerans, R. J., A model for the oxidation of ZrB_2, HfB_2 and TiB_2. *Acta Materials* **2007,** 55, 5999-6010.

[93] Kaufman, L.; Clougherty, E. V., Investigation of boride compounds for high temperature applications, *AFRL technical documentary report no. RTD-TDR-63-4096, Part II* **1965.**

[94] Tripp, W. C.; Graham, H. C., Thermogravimetric study of the oxidation of ZrB_2 in the temperature range of 800^{o}C to 1500^{o}C, *J. Electrochem. Soc.: solid state science* **1971,** 118, (7), 1195-1199.

[95] Kuriakose, A. K.; Margrave, J. L., The oxidation kinetics of zirconium diboride and zirconium carbide at high temperatures, *J. Electrochem. Soc.* **1964,** 111, (7), 827-831.

[96] Wang, Y.; Liang, J.; Han, W.; Zhang, X. H., Mechanical properties and thermal shock behavior of hot-pressed ZrB_2-SiC-AlN composites. *Journal of Alloys and Compounds* **2009,** 475, (1-2), 762-765.

[97] Monteverde, F., Hot pressing of hafnium diboride aided by different sinter additives. *J. Mater. Sci.* **2008,** 43, (3), 1002-1007.

[98] Klein, R.; Desmaison-Brut, M.; Desmaison, J.; Mazerolles, L.; Trichet, M. F., High-temperature oxidation behaviour of a hot isostatically-pressed Si_3N_4-HfB_2 ceramic composite. *High Temperature Corrosion and Protection of Materials 6, Prt 1 and 2, Proceedings* **2004,** 461-464, 849-856.

[99] Chamberlain, A. L.; Fahrenholtz, W. G.; Hilmas, G. E.; Ellerby, D. T., High-strength zirconium diboride-based ceramics. *J. Am. Ceram. Soc. 2004,* 87, (6), 1170-1172.

[100] Zhou, X. J.; Zhang, G. J.; Li, Y. G.; Kan, Y. M.; Wang, P. L., Hot pressed ZrB2-SiC-C ultra high temperature ceramics with polycarbosilane as a precursor. *Materials Letters* **2007,** 61, (4-5), 960-963.

[101] Kinoshita, M.; Kose, S.; Hamano, Y., Hot-pressing of zirconium diboride-molybdenum disilicide mixtures. *Yogyo-Kyokai-Shi 1970,* 78, (2), 32-41.

[102] Hwang, S.; Vasiliev, AL.; Padture, NP., Improved processing, and oxidation-resistance of ZrB_2 ultra-high temperature ceramics containing SiC nanodispersoids. *Materials Science and Engineering a-Structural Materials Properties Microstructure and Processing* **2007,** 464, (1-2), 216-224.

[103] Guo, S. Q.; Nishimura, T.; Mizuguchi, T.; Kagawa, Y., Mechanical properties of hot-pressed ZrB2-MoSi2-SiC composites. *J. Europ. Ceram. Soc.* **2008,** 28, (9), 1891-1898.

[104] Zhang, H.; Yan, Y. J.; Huang, Z. R.; Liu, X. J.; Jiang, D. L., Pressureless sintering of ZrB2-SiC ceramics: the effect of B4C content. *Scripta Materialia* **2009,** 60, (7), 559-562.

[105] Zou, J.; Zhang, G. J.; Kan, Y. M.; Wang, P. L., Pressureless densification of ZrB2-Sic composites with vanadium carbide. *Scripta Materialia* **2008,** 59, (3), 309-312.

[106] Zhu, M. A.; Wang, Y. G., Pressureless sintering ZrB2-SiC ceramics at low temperatures. *Materials Letters* **2009,** 63, (23), 2035-2037.

[107] Wang, X. G.; Liu, J. X.; Kan, Y. M.; Zhang, G. J.; Wang, P. L., Slip casting and pressureless sintering of ZrB_2-SiC ceramics. *Journal of Inorganic Materials* **2009,** 24, (4), 831-835.

[108] Wang, X. G.; Guo, W. M.; Zhang, G. J., Pressureless sintering mechanism and microstructure of ZrB_2-SiC ceramics doped with boron. *Scripta Materialia* **2009,** 61, (2), 177-180.

[109] Zou, J.; Zou, J., Pressureless sintering mechanisms and mechanical properties of hafnium diboride ceramics with pre-sintering heat treatment. *Scripta Materialia* **2009,** 62, (3), 159.

[110] Zhang, S. C.; Hilmas, G. E.; Fahrenholtz, W. G., Pressureless sintering of ZrB2-SiC ceramics. *J. Am. Ceram. Soc.* **2008,** 91, (1), 26-32.

[111] Cheng, Z. Q.; Zhou, C. L.; Tian, T. Y.; Sun, C. G.; Shi, Z. H.; Fan, J., Pressureless sintering of ultra-high temperature ZrB_2-SiC ceramics. *High-Performance Ceramics V, Pts 1 and 2* **2008,** 368-372, 1746-1749.

[112] Guo, S. Q.; Kagawa, Y.; Nishimura, T.; Tanaka, H., Pressureless-sintering and physical properties of ZrB_2-based composites with $ZrSi_2$ additive. *Scripta Materialia* **2008,** 58, (7), 579-582.

[113] Silvestroni, L.; Sciti, D., Effects of $MoSi_2$ additions on the properties of Hf- and Zr- B_2 composites produced by pressureless sintering. Scripta Materialia **2007,** 57, (2), 165-168.

[114] Zhang, S. C.; Hilmas, G. E.; Fahrenholtz, W. G., Pressureless densification of zirconium diboride with boron carbide additions. *J. Am. Ceram. Soc.* **2006,** 89, (5), 1544-1550.

[115] Chamberlain, A.; Fahrenholtz, W. G.; Hilmas, G. E., Pressureless sintering of zirconium diboride. *J. Am. Ceram. Soc.* **2006,** 89, (2), 450-456.

[116] Akin, I.; Hotta, M.; Sahin, F. C.; Yucel, O.; Goller, G.; Goto, T., Microstructure and densification of ZrB_2-SiC composites prepared by spark plasma sintering. *J. Euro. Ceram. Soc.* **2009,** 29, (11), 2379-2385.

[117] Balbo, A.; Sciti, D., Spark plasma sintering and hot pressing of ZrB_2-$MoSi_2$ ultra-high-temperature ceramics. *Materials Science and Engineering a-Structural Materials Properties Microstructure and Processing* **2008,** 475, (1-2), 108-112.

[118] Guo, S. Q.; Kagawa, Y.; Nishimura, T.; Chung, D.; Yang, J. M., Mechanical and physical behavior of spark plasma sintered ZrC-ZrB_2-SiC composites. *J. Europ. Ceram. Soc.* **2008,** 28, (6), 1279-1285.

[119] Carney, C. M.; Mogilvesky, P.; Parthasarathy, T. A., Oxidation behavior of zirconium diboride silicon carbide produced by the spark plasma sintering Method. *J. Am. Ceram. Soc.* **2009,** 92, (9), 2046-2052.

[120] Licheri, R.; Orru, R.; Musa, C.; Cao, G., Fabrication of fully dense ZrB_2- and HfB_2-based Ultra High Temperature Ceramics by combining Self-propagating High-temperature Synthesis and Spark Plasma Sintering. *cheap-9: 9th International Conference on Chemical and Process Engineering, Pts 1-3* **2009,** 17, 1705-1710.

[121] Zhu, S. Z.; Xu, Q.; Feng, C.; Zhao, J. F.; Cao, J. L.; Wang, F. C., Effect of glass phase on the thermal shock resistance of ZrB_2-SiC ultra high

temperature ceramic. *High-Performance Ceramics V, Pts 1 and 2* **2008,** 368-372, 1727-1729.

[122] Camurlu, H. E.; Maglia, F., Self-propagating high-temperature synthesis of ZrB_2 or TiB_2 reinforced Ni-Al composite powder. *Journal of Alloys and Compounds* **2009,** 478, (1-2), 721-725.

[123] Qu, Q.; Han, J. C.; Han, W. B.; Zhang, X. H.; Hong, C. Q., In situ synthesis mechanism and characterization of ZrB_2-ZrC-SiC ultra high-temperature ceramics. *Materials Chemistry and Physics* **2008,** 110, (2-3), 216-221.

[124] Licheri, R.; Orru, R.; Locci, A. M.; Cao, G., Efficient synthesis/sintering routes to obtain fully dense ZrB_2-SiCUHTC materials. *High-Performance Ceramics V, Pts 1 and 2* **2008,** 368-372, 1733-1736.

[125] Mishra, S. K.; Das, S. K.; Sherbacov, V., Fabrication of Al_2O_3-ZrB_2 in situ composite by SHS dynamic compaction: A novel approach. *Composites Science and Technology* **2007,** 67, (11-12), 2447-2453.

[126] Yu, Z. Q.; Yang, Z. G., ZrB_2, Al_2O_3 composite powders prepared by self-propagating high-temperature synthesis. *Transactions of Nonferrous Metals Society of China* **2005,** 15, (4), 851-854.

[127] Tsuchida, T.; Yamamoto, S., MA-SHS and SPS of ZrB_2-ZrC composites. *Solid State Ionics* **2004,** 172, (1-4), 215-216.

[128] Rangaraj, L.; Divakar, C.; Jayaram, V., Reactive hot pressing of ZrB_2-ZrCx ultra-high temperature ceramic composites with the addition of SiC particulate. *J. Euro. Ceram. Soc.* **2010,** 30, (15), 3263-3266.

[129] Lee, S.; Lee, S. J. U. N, Reactive hot pressing and oxidation behavior of Hf-based ultra-high- temperature ceramics. *Surface Review and Letters* **2010,** 17, (2), 215.

[130] Rangaraj, L.; Divakar, C.; Jayaram, V., Fabrication and mechanisms of densification of ZrB_2-based ultra high temperature ceramics by reactive hot pressing. *J. Euro. Ceram. Soc.* **2010,** 30, (1), 129-138.

[131] Chamberlain, A. L.; Fahrenholtz, W. G.; Hilmas, G. E., Reactive hot pressing of zirconium diboride. *J. Euro. Ceram. Soc.* **2009,** 29, (16), 3401-3408.

[132] Wu, W. W.; Zhang, G. J.; Kan, Y. M.; Wang, P. L., Reactive synthesis and mechanical properties of ZrB_2-SiC-ZrC composites. *High-Performance Ceramics V, Pts 1 and 2* **2008,** 368-372, 1758-1760.

[133] Qu, Q.; Zhang, X. H.; Meng, S. H.; Han, W. B.; Hong, C. Q.; Han, H. C., Reactive hot pressing and sintering characterization of ZrB_2-SiC-ZrC composites. *Materials Science and Engineering a-Structural Materials Properties Microstructure and Processing* **2008,** 491, (1-2), 117-123.

[134] Zhang, X. H.; Qu, Q.; Han, J. C.; Han, W. B.; Hong, C. Q., Microstructural features and mechanical properties of ZrB_2-SiC-ZrC composites fabricated by hot pressing and reactive hot pressing. *Scripta Materialia* **2008,** 59, (7), 753-756.

[135] Wu, W. W.; Zhang, G. J.; Kan, Y. M.; Wang, P. L.; Vanmeensel, K.; Vleugels, J.; Van der Biest, O., Synthesis and microstructural features of ZrB_2-SiC-based composites by reactive spark plasma sintering and reactive hot pressing. *Scripta Materialia* **2007,** 57, (4), 317-320.

[136] Wu, W. W.; Zhang, G. J.; Kan, Y. M.; Wang, P. L., Reactive hot pressing of ZrB_2-SiC-ZrC ultra high-temperature ceramics at 1800 degrees C. *J. Am. Ceram. Soc.* **2006,** 89, (9), 2967-2969.

[137] Monteverde, F., Beneficial effects of an ultra-fine alpha-SiC incorporation on the sinterability and mechanical properties of ZrB_2. *Applied Physics a-Materials Science & Processing* **2006,** 82, (2), 329-337.

[138] Hwang, S., Improved processing, and oxidation-resistance of ZrB_2 ultra-high temperature ceramics containing SiC nanodispersoids. *Materials science & engineering A, Structural materials* **2007,** 464, (1-2), 216-224.

[139] Baik, S.; Becher, P. F., Effect of oxygen contamination on densification of TiB_2. *J. Am. Ceram. Soc.* **1987,** 70, (8), 527-530.

[140] Monteverde, F.; Bellosi, A., Effect of the addition of silicon nitride on sintering behaviour and microstructure of zirconium diboride. *Scripta Mat.* **2002,** 46, 223-228.

[141] Weng, L.; Zhang, X. H.; Han, J. C.; Han, W. B., The Effect of Si_3N_4 on Microstructure, Mechanical Properties and Oxidation Resistance of HfB_2-based Composite. *Journal of Composite Materials* **2009,** 43, (2), 113-123.

[142] Sciti, D.; Monteverde, F.; Guicciardi, S.; Pezzotti, G.; Bellosi, A., Microstructure and mechanical properties of ZrB_2-$MoSi_2$ ceramic composites produced by different sintering techniques. *Mater. Sci. and Eng. A-Structural Materials Properties Microstructure and Processing* **2006,** 434, (1-2), 303-309.

[143] Bellosi, A.; Monteverde, F. D.; Sciti, D., Fast densification of ultra-high-temperature ceramics by spark plasma sintering. *Inter. J. Appl. Ceram. Tech.* **2006,** 3, (1), 32-40.

[144] Guo, S. Q.; Kagawa, Y.; Nishimura, T., Mechanical behaviour of two-step hot-pressed ZrB_2-based composites with $ZrSi_2$. *J. Europ. Ceram. Soc.* **2009,** 2009, (4), 787-794.

[145] Cech, B.; Oliverius, P.; Sejbal, J., Sintering of zirconium boride with activating additions. *Powder Metall.* **1965,** 8, (15), 142-151.

[146] Kislui, P. S.; Kuzenkova, M. A., Regularities of sintering of zirconium diboride-molybdenum alloys. *Soviet Powder Metallurgy and Metal Ceramics* **1966,** 5, 360-365.

[147] Einarsrud, M. A.; Hagen, E.; Pettersen, G.; Grande, T., Pressureless sintering of titanium diboride with nickel, nickel boride, and iron additives. *J. Am. Ceram. Soc.* **1997,** 80, (12), 3013-3020.

[148] Sciti, D.; Brach, M.; Bellosi, A., Oxidation behavior of a pressureless sintered ZrB_2-$MoSi_2$ ceramic composite. *J. Mater. Res.* **2005,** 20, (4), 922-930.

[149] Yan, Y. J.; Zhang, H.; Huang, Z. G.; Liu, J. X.; Jiang, D. L., In situ synthesis of ultrafine ZrB_2-SiC composite powders and the pressureless sintering behaviors. *J. Am. Ceram. Soc.* **2008,** 91, (4), 1372-1376.

[150] Sciti, D.; Balbo, A.; Bellosi, A., Oxidation behaviour of a pressureless sintered HfB_2-$MoSi_2$ composite. *J. Europ. Ceram. Soc.* **2009,** 29, (9), 1809-1815.

[151] Silvestroni, L.; Sciti, D.; Bellosi, A., Microstructure and properties of pressureless sintered HfB2-based composites with additions of ZrB_2 or HfC. *Adv. Eng. Mater.* **2007,** 9, 915-920.

[152] Cao, J. L.; Xu, Q.; Zhu, S. Z.; Zhao, J. F.; Wang, F. C., Microstructure of ZrB_2-SiC composite fabricated by spark plasma sintering. *High-Performance Ceramics V, Pts 1 and 2* **2008,** 368-372, 1743-1745.

[153] Zhu, S.; Fahrenholtz, W. G.; Hilmas, G. E.; Zhang, S. C., Pressureless sintering of zirconium diboride using boron carbide and carbon additions. *J. Am. Ceram. Soc.* **2007,** 90, 3660-3663.

[154] Zhang, X. H.; Wang, Z.; Sun, X.; Han, W. B.; Hong, C. Q., Effect of graphite flake on the mechanical properties of hot pressed ZrB_2-SiC ceramics. *Materials Letters* **2008,** 62, (28), 4360-4362.

[155] Fahrenholtz, W. G.; Hilmas, G. E.; Zhang, S. C.; Zhu, S., Pressureless sintering of zirconium diboride: Particle size and additive effects. *J. Am. Ceram. Soc.* **2008,** 91, (5), 1398-1404.

[156] Fahrenholtz, W. G.; Hilmas, G. E.; Zhang, S. C.; Zhu, S., Pressureless sintering of zirconium diboride: Particle size and additive effects. *J. Am. Ceram. Soc.* **2008,** 91, (5), 1398-1404.

[157] Chamberlain, A. L.; Fahrenholtz, W. G.; Hilmas, G. E., Low-temperature densification of zirconium diboride ceramics by reactive hot pressing. *J. Am. Ceram. Soc.* **2006,** 89, 3638-3645.

[158] Wu, W. W.; Zhang, G. J.; Kan, Y. M.; Wang, P. L., Reactive hot pressing of ZrB_2-SiC-ZrC composites at 1600 degrees C. *J. Am. Ceram. Soc.* **2008,** 91, (8), 2501-2508.

[159] Qu, Q.; Han, W. B.; Meng, S. H.; Zhang, X. H.; Han, J. C., Microstructure and mechanical properties of ZrB_2-based UHTC via reactive hot pressing. *High-Performance Ceramics V, Pts 1 and 2* **2008,** 368-372, 1737-1739.

[160] Rangaraj, L.; Suresha, S. J.; Divakar, C.; Jayaram, V., Low-temperature processing of ZrB_2-ZrC composites by reactive hot pressing. *Metallurgical and Materials Transactions a-Physical Metallurgy and Materials Science* **2008,** 39A, (7), 1496-1505.

[161] Zimmermann, J. W.; Hilmas, G. E.; Fahrenholtz, W. G.; Monteverde, F.; Bellosi, A., Fabrication and properties of reactively hot pressed ZrB_2-SiC ceramics. *J. Europ. Ceram. Soc.* **2007,** 27, (7), 2729-2736.

[162] Guo, S. Q.; Nishimura, T.; Kagawa, Y.; Yang, J. M., Spark plasma sintering of zirconium diborides. *J. Am. Ceram. Soc.* **2008,** 91, (9), 2848-2855.

[163] Sciti, D.; Nygren, M., Spark plasma sintering of ultra refractory compounds. *J. Mater. Sci.* **2008,** 43, (19), 6414-6421.

[164] Zhao, Y. A.; Wang, L. J.; Zhang, G. J.; Chen, L. D.; Jiang, W., Rapid fabrication and reaction process of ZrB_2-SiC composites by spark plasma sintering process. *Rare Metal Materials and Engineering* **2007,** 36, 819-822.

[165] Carney, C. M.; Mah, T. I., Current isolation in spark plasma sintering of conductive and nonconductive ceramics. *J. Am. Ceram. Soc.* **2008,** 91, (10), 3448-3450.

[166] Jayaseelan, D. D.; Ueno, S.; Ohji, T.; Kanzaki, S., Differential sintering by improper selection of sintering parameters during pulse electric current sintering. *J. Am. Ceram. Soc.* **2004,** 87, (1), 159-161.

[167] Khor, K. A.; Cheng, K. H.; Yu, L. G.; Boey, F., Thermal conductivity and dielectric constant of spark plasma sintered aluminium nitride. *Mater. Sci. and Eng. A-Structural Materials Properties Microstructure and Processing* **2003,** A347, 300-305.

[168] Guillard, F.; Allemand, A.; Luetic, J. D.; Galy, J., Densification of SiC by SPS- effects of times, temperature and pressure. *J. Europ. Ceram. Soc.* **2007,** 2725-2728.

[169] Medri, V.; Monteverde, F.; Balbo, A.; Bellosi, A., Comparison of ZrB_2-ZrC-SiC composites fabricated by spark plasma sintering and hot-pressing. *Adv. Eng. Mater.* **2005,** 7, (3), 159-163.

[170] Guo, S. Q.; Kagawa, Y.; Nishimura, T.; Tanaka, H., Elastic properties of spark plasma sintered (SPSed) ZrB_2-ZrC-SiC composites. *Ceram. Inter.* **2008,** 34, (8), 1811-1817.

[171] Monteverde, F.; Melandri, C.; Guicciardi, S., Microstructure and mechanical properties of an HfB_2+30 vol.% SiC composite consolidated by spark plasma sintering. *Materials Chemistry and Physics* **2006,** 100, (2-3), 513-519.

[172] Kaga, H.; Heian, E. M.; Munir, Z. A.; Schmalzried, C.; Telle, R., Synthesis of hard materials by field activation: the synthesis of solid solutions and composites in the TiB_2-WB_2-CrB_2 system. *J. Am. Ceram. Soc.* **2001,** 84, (12), 2764-2770.

[173] Sciti, D.; Silvestroni, L.; Bellosi, A., Fabrication and properties of HfB_2-$MoSi_2$ composites produced by hot pressing and spark plasma sintering. *J. Mater. Res.* **2006,** 21, (6), 1460-1466.

[174] Sciti, D.; Silvestroni, L.; Nygren, M., Spark plasma sintering of Zr- and Hf-borides with decreasing amounts of $MoSi_2$ as sintering aid. *J. Euro. Ceram. Soc.* **2008,** 28, (6), 1287-1296.

[175] Sciti, D.; Guicciardi, S.; Nygren, M., Densification and mechanical behavior of HfC and HfB_2 fabricated by spark plasma sintering. *J. Am. Ceram. Soc.* **2008,** 91, (5), 1433-1440.

[176] Silvestroni, L.; Sciti, D.; Melandri, C.; Guicciardi, S., Toughened ZrB_2-based ceramics through SiC whisker or SiC chopped fiber additions. *J. Europ. Ceram. Soc.* **2010,** 30.

[177] Sarin, P.; Driemeyer, P. E.; Haggerty, R. P.; Kim, D. K.; Bell, J. L.; Apostolov, Z. D.; Kriven, W. M., In situ studies of oxidation of ZrB_2 and ZrB_2-SiC composites at high temperatures. *J. Euro. Ceram. Soc.* **2010,** 30, (11), 2375-2386.

[178] Zou, J.; Zou, J., Hot-pressed ZrB_2-SiC ceramics with VC addition: chemical reactions, microstructures, and mechanical properties. *J. Am. Ceram. Soc.* **2009,** 92, (12), 2838.

[179] Licheri, R.; Orru, R.; Musa, C.; Locci, A. M.; Cao, G., Consolidation via spark plasma sintering of HfB_2/SiC and HfB_2/HfC/SiC composite powders obtained by self-propagating high-temperature synthesis. *Journal of Alloys and Compounds* **2009,** 478, (1-2), 572-578.

[180] Li, W. J.; Zhang, X. H.; Hong, C. Q.; Han, W. B.; Han, J. C., Microstructure and mechanical properties of zirconia-toughened ZrB_2-$MoSi_2$ composites prepared by hot-pressing. *Scripta Materialia* **2009,** 60, (2), 100-103.

[181] Tripp, W. C.; Davis, H. H.; Graham, H. C., Effect of an SiC addition on oxidation of ZrB_2. *American Ceramic Society Bulletin* **1973,** 52, (8), 612-616.

[182] Sciti, D.; Sciti, D., Oxidation behavior of HfB_2-15 vol.% $TaSi_2$ at low, intermediate and high temperatures. *Scripta Materialia* **2010,** 63, (6), 601-604.

[183] Zhang, H.; Yan, Y. J.; Huang, Z. R.; Liu, X. J.; Jiang, D. L., Properties of ZrB_2-SiC ceramics by pressureless sintering. *J. Am. Ceram. Soc.* **2009,** 92, (7), 1599-1602.

[184] Varshal, B. G., A structure model for immiscibility in silicate glass-forming melts. *Glass Phys. Chem.* **1993,** 19, (2), 218-225.

[185] Talmy, I. G.; Zaykoski, J. A.; Opeka, M. M., High-temperature chemistry and oxidation of ZrB_2 ceramics containing SiC, Si_3N_4, Ta_5Si_3, and $TaSi_2$. *J. Am. Ceram. Soc.* **2008,** 91, (7), 2250-2257.

[186] Opila, E.; Levine, S.; Lorincz, J., Oxidation of ZrB_2 and HfB_2 based ultra-high temperature ceramics: Effect of Ta additions. *J. Mater. Sci.* **2004,** 39, (19), 5969-5977.

[187] Talmy, I. G.; Zaykoski, J. A., Oxidation resistance of Si_3N_4 ceramics modified with boron and transition metal diborides. *High Temperature Corrosion and Materials Chemistry* **2003,** 2003, (16), 361-376.

[188] Zhang, S. C.; Hilmas, G. E.; Fahrenholtz, W. G., Improved oxidation resistance of zirconium diboride by tungsten carbide additions. *J. Am. Ceram. Soc.* **2008,** 91, (11), 3530-3535.

[189] Levine, S. R.; Opila, E. J.; Halbig, M. C; Kiser, J. D.; Singh, M.; Salema, J. A., Evaluation of ultra-high temperature ceramics for aero propulsion use, *Journal of the European Ceramic Society* **2002,** 22, 2757–2767.

[190] Courtright, E. L.; Prater, J. T.; Holcomb, G. R.; St. Pierre, G. R.; Papp, R. A., Oxidation of hafnium carbide and hafnium carbide with additions of tantalum and praseodymium, *Oxidation of Metals* **1991,** 36, 423-437.

[191] Zimmermann, J. W.; Hilmas, G. E.; Fahrenholtz, W. G., Thermal shock resistance and fracture behavior of ZrB_2–Based Fibrous Monolith Ceramics, *J. Am. Ceram. Soc.* **2009,** 92, (1), 161-166.

[192] Sayir, A., Carbon fiber reinforced hafnium carbide composite, *J. Mater. Sci.* **2004,** 39, 5995-6003.

[193] Windhorst, T.; Blount, G.; Carbon-carbon composites, a summary of recent developments and applications, *Mater Des* **1997,** 18, (1), 11-15.

[194] Strife, J. S.; Sheehan, J. E., Ceramic Coating for carbon/carbon Composites, *Ceramic Bulletin* **1988,** 67, (2), 369.

[195] Xuetao, S.; Kezhi, L.; Hejun, L.; Hongying, D.; Weifeng, C.; Fengtao, L., Microstructure and ablation properties of zirconium carbide doped Carbon/carbon composites, *Carbon* **2010,** 48, 344-351.

[196] Wunder, V.; Popovska, N.; Emig, G., Chemical vapour deposition of hafnium carbide on carbon substrates, *Electrochemical society proceedings* **1997,** 25, 608.

[197] Corral, E. L.; Loehman, R. E., Ultra-high-temperature ceramic coatings for oxidation protection of carbon–carbon composites. *J. Am. Ceram. Soc.* **2008,** 91, (5), 1495-1502.

[198] Wormer, O. G., Chemical gas phase reactions of hafnium carbide and hafnium nitride, *Dissertation, TH Karlsruhe,* **1995.**

[199] Wang, Y. Q., Zhou, B. L.; Wang, Z. M., Oxidation protection of Carbon fibres by coatings. *Carbon* **1995,** 33, (4), 427-433.

[200] Nordell, N.; Nishino, S.; Yang, J. -W.; Jacob, C.; Pirouz, P., Influence of H2 addition and growth temperature on CVD of SiC using hexamethyldisilane and Ar, *J. Electrochem. Soc.* **1995,** 2, 142.

[201] Ohyanagi, M.; Koizumi, M. J.; Miyaji, Y.; Izawa, H.; Inumaru, N., SiC coating on carbon block by the self-propagating high-temperature synthesis method, *Journal of Materials Science Letters* **1993,** 12, 513-515.

[202] Jaglin, D.; Binner, J. G. P., Prentice, C.; Shatwell, R.; Timms, L.; Westby, W., SiCf/SiC fabrication via vacuum bagging, electrophoretic infiltration and microwave enhanced CVI, *J. Am. Ceram. Soc.* **2006,** 89, (9), 2710-2719.

[203] Novak, S.; Radea, K.; König, K.; Boccaccini, A. R., Electrophoretic deposition in the production of SiC/SiC composites for fusion reactor applications, *Journal of the European Ceramic Society,* **2008,** 28, 2801–2807.

[204] Hara et.al, Method of making surface coated cemented carbide articles, *United States Patent* **1976,** 3, 932, 231.

[205] Huang J.F.; Liu M.; Wang B.; Cao L.-Y.; Xia C.-K.; Wu J.-P., SiCn/SiC oxidation protective coating for carbon/carbon composites, *Carbon* **2009,** 47, 1189-1206.

[206] Tang, S. T.; Deng, J. Y.; Liu, W. C.; Yang, K.; Mechanical and ablation properties of 2D-carbon/carbon composites pre-infiltrated with a SiC filler, *Carbon* **2006,** 44, 2877-2882.

[207] Newman, R. W., Oxidation-resistant high temperature materials", *Johns Hopkins APL Technical Digest* **1993,** 14, (1), 24.

[208] Patterson, M. C. L.; He, S.; Fehrenbacher, L. L.; Hanigofsky, J.; Reed, B. D., Advanced HfC-TaC oxidation resistant composite rocket thruster. *Materials and Manufacturing processes* **1996,** 11, (3), 367-379.

[209] Paul, A.; Venugopal, S.; Binner, J. G. P.; Vaidhyanathan, B.; Heaton, A. C. J., P.M. Brown, UHTC–carbon fibre composites: Preparation, oxyacetylene torch testing and characterisation, *Journal of the European Ceramic Society* **2013,** 33, 423–432.

[210] Yang, F.; Zhang, X.; Han, J.; Du, S., Mechanical properties of short carbon fibre reinforced ZrB_2–SiC ceramic matrix composites, *Materials Letters* **2008,** 62, 2925–2927.

[211] Dong, S. M; Wang Z.; Ding, Y. S.; Zhang, X. Y.; He, P.; Gao, L., Fabrication of carbon fibre reinforced ceramic matrix composites potential for

ultra high temperature applications, *Mechanical properties and performance of engineering ceramic composites IV* **2009,** 30, 2.

[212] Levine, S. R.; Opila, E. J.; Halbig, M. C.; Kiser, J. D.; Singh, M.; Salem, J. A., Evaluation of ultra-high temperature ceramics for aeropropulsion use, *Journal of the European Ceramic Society* **2002,** 22, 2757–2767.

[213] Levine, S. R.; Opila, E. J.; Robinson, R. C.; Lorincz, J.A., Characterization of an ultra-high temperature ceramic composite. *NASA TM-2004-213085* **2004,** 1-26.

[214] Jackson, H. F.; Jayaseelan, D. D.; Lee, W. E.; Reece, M. J.; Inam, F.; Manara, D.; Casoni, C. P.; Bruycker, F.; Boboridis, K., Laser melting of spark plasma sintered zirconium carbide: Thermophysical properties of a generation IV very high temperature reactor material. *Inter. J. Appl. Ceram. Tech.* **2009,** 7, (3), 316-326.

[215] Jackson, H. F.; Jayaseelan, D. D.; Manara, D.; Casoni, C. P.; Lee, W. E., Laser melting of zirconium carbide: Determination of phase transitions in refractory ceramic systems. *J. Am. Ceram. Soc.* **2011,** 94, (10), 3461-3469.

[216] Manara, D.; Pflieger, R.; Sheindlin, M., Advances in the experimental determination of the uranium-oxygen phase diagram at high temperature. *Int. J. Thermophys* **2005,** 26, (4), 1193-1206.

[217] Jayaseelan, D. D.; Jackson, H. F.; Eakins, E.; Brown, P.; Lee, W. E., Laser modified microstructures in ZrB_2, ZrB_2/SiC and ZrC. *J. Euro. Ceram. Soc.* **2010,** 30, 2279-2288.

[218] Manara, D.; Sheindlin, M.; Heinz, W.; Ronchi, C., New technique for high-temperature melting measurements in volatile refractory materials via laser surface heating. *Rev. Sci. Instrum.* **2008,** 79, (11), 113901-113911.

[219] Bansal, N. P., Handbook of ceramic composites, Science, Springer, **2005**, 554

[220] Monteverde, F.; Savino, R.; Fumo, M.; Maso, A., Plasma wind tunnel testing of ultra-high temperature ZrB_2-SiC composites under hypersonic re-entry conditions*. J. Euro. Ceram. Soc.* **2010,** 30, (11), 23113-2321.

[221] www.astm.org, ASTM Standard E 285- 08, Standard test method for oxyacetylene ablation testing of thermal insulation materials, *ASTM International, West Conshohocken, PA* **2008.**

[222] Mark, P., Oxidation resistant HfC-TaC rocket thruster for high performance propellants, *NASA report NAS3-27272* **1999,** 1-24.

[223] Song, G. M.; Wang, Y. J.; Zhou Y., Elevated temperature ablation resistance and thermophysical properties of tungsten matrix composites reinforced with ZrC particles. *J. Mater. Sci.* **2001,** 36, 4625-31.

[224] Song, G.; Zhou, Y.; Wang, Y., Effect of carbide particles on the ablation properties of tungsten composites, *Mater Charact* **2003,** 50, 293-303.

[225] Zhang, X.; Hu, P.; Han, J.; Xu, L.; Meng, S., The addition of lanthanum hexaboride to zirconium diboride for improved oxidation resistance, *Scr. Mater.* **2007,** 57, 1036-9.

[226] Han, J.; Hu, P.; Zhang, X.; Meng, S; Han, W., Oxidation-resistant ZrB2–SiC composites at 2200°C, *Composites Sci. Technol.* **2008,** 68, 799-806.

[227] Chen, Z.; Yan, B., Morphology and microstructure of three-dimensional orthogonal C/SiC composites ablated by an oxyacetylene flame at 2900 degrees C, *International Journal of Applied Ceramic Technology* **2009,** 6, 164-70.

[228] Chen, Z.; Fang, D.; Miao, Y.; Yan, B., Comparison of morphology and microstructure of ablation centre of C/SiC composites by oxy-acetylene torch at 2900 and 3550 degrees C, *Corros. Sci.* **2008,** 50, 3378-81.

[229] Marra, F.; Pulci, G.; Tiril, J.; Bartuli, C.; Valente, T., Numerical simulation of oxy-acetylene testing procedure of ablative materials for re-entry space

vehicles, *Proceedings of the Institution of Mechanical Engineers, Part L: Journal of Materials: Design and Applications* **2011,** 225, 32-40.

[230] http://ceramics.org/ceramictechtoday/2011/06/02/video-of-the-week-ash-sand-resistant-thermal-barrier-coatings-and-novel-test-rig/

[231] Wunder, V. K.; Popovska, N., Emig, G., Study of hafnium from in-situ chlorinated hafnium. *Electrochem. Soc.* **1999,** 98–23, 263–267.

[232] Information at http://www.reade.com/western-region-(usa)/10454

[233] Brinker, C. J.; Hurd, A. J., Fundamentals of sol-gel dip-coating, *J. Phys.III* **1994,** 4, 1231-1242.

[234] http://www.ramehart.com/contactangle.htm

[235] Henry Proudhon, Centre des Mat´eriaux, MINES ParisTech, UMR CNRS 7633.
http://mms2.ensmp.fr/tribo_paris/lectures/wemesurf_tomo_seminar_handouts.pdf

[236] Kumaresan, R.; Moorthy Babu, S., Crystal growth and characterization of sucrose single crystals, *Mater. Chem. Phy.* **1997,** 49, 83-86.

[237] Mashau, S. N., The preparation of pitches from antracene oil, *Master of Science Thesis, University of Pretoria,* **2007.**

[238] Lum, R.; Wilkins, C. W.; Robbins, M.; Lyons, A. M.; Jones, R. P., Thermal analysis of graphite and carbon-phenolic composites by pyrolysis-mass spectrometry, *Carbon* **1983,** 21, 111-116.

[239] www.webbook.nist.gov

[240] Seo, W. S.; Koumoto, K., Stacking faults in β-SiC formed during carbothermal reduction of SiO_2, *Journal of the American Ceramic Society* **2005,** 79, (7), 1777-1782.

[241] Parsons, J., Milberg ME. *J. Am. Ceram. Soc.* **1960,** 43, (6), 326–30.

[242] Liu, Y. H.; Liu, P. A., X-Ray Diffraction analysis theoretics and application. *Chemical Industry Press, China* **2003,** 127-34.

[243] Liu, J. X.; Kan, Y. M.; Zhang, G. J., Synthesis of Ultra-Fine Hafnium Carbide Powder and its Pressureless Sintering, *J. Am. Ceram. Soc.* **2010,** 93, (4), 980–986.

[244] Gusev, A. I.; Zyryanova, A. N., Ordering and Magnetic Susceptibility of Non-Stoichiometric Hafnium Carbide, *Phys. Status Solidi A* **2000,** 177, 419–37.

[245] Bégin-Colin, S.; Le Caër, G.; Barraud, E.; Humbert, O. J., *Mater. Sci.* **2004**, 39, (16–17), 5081-9.

[246] Krishnarao, R. V.; Subrahmanyam, *J. Mater. Sci. Eng A* **2003,** 362, 145-51.

[247] Zhang, L; Gu, Y.; Wang, W; Wang, J; Zhao, G; Qian, Q; Zhang, Z; Zhang, F. A fast-pyrolysis self-propagating high temperature synthesis route to single phase of boron carbide ultrafine powders, *Journal of the Ceramic Society of Japan* **2011,** 119, (8), 631-634.

[248] Blum, Y. D.; Marschall, J.; Hui, D.; Adair, B.; Vestel, M., *J. Am. Ceram. Soc*. **2008,** 91, 1481-8.

[249] Bigdeloo, J. A.; Hadian, A. M., *Int. J. Recent Trends Eng* **2009,** 1, (5), 176-80.

[250] Dacic, B. Z.; Jokanovic, V.; Jokanovic, B.; Dramicanin, M. D., *J. Alloys Compd*. **2006,** 413, 198–205.

[251] Wuchina, E.; Opila, E.; Fergus, J.; Maruyama, T.; Shifle, D. High Temperature Corrosion and Materials Chemistry 7, The Electrochemical Society,

[252] Rudy, E; and St. Windisch,, Phase diagrams of the systems Ti-B-C. Zr-B-C, and Hf-B-C, Ternary phase equilibria in transition metal-boron-carbon-

silicon systems, Part II. Ternary Systems, *Technical report no. AFML-TR-65-Z*, Part II, Volume XIII, April **1966**.

[253] Rogl, P, and Bittermann, H., On the Ternary System Hafnium-Boron-Carbon, *J. Solid State Chem.*, **2000**, 154, 257-262.

[254] Vere, A.W., Crystal Growth: Principles and Progress, Plenum, New York, **1987**.

[255] Burton, W; Cabrera, N; and Frank, F.C., Philos. Trans. R. Soc., **1951**, 243, 299..

[256] Cao, G.; and Wang. Y. Chemical Vapour Deposition of Ceramics, Processing of Specialty Ceramics, Section V, *Chemical Processing of Ceramics, Second Edition*

[257] Gurin, VN; and Derkachenko, LI., Growth habit of crystals of refractory compounds prepared from high temperature solutions, *Prog. Crys Growth and Charac*. **1993**, 27, 163-199.

[258] Morin, S. A., et al., Mechanism and Kinetics of Spontaneous Nanotube Growth Driven by screw dislocations. *Science* **2010,** 328, 476.

[259] Morin, S. A.; Jin, S., Screw Dislocation-Driven Epitaxial Solution Growth of ZnO Nanowires Seeded by Dislocations in GaN Substrates, *Nano Lett.* **2010,** 10, 3459-3463

[260] Popov, V. E.; Vil'k, Ju. N.; Gurin, V. N.; Tchekrygina, T. M., *Poroshkovaya metallurgia* **1981,** 8, 76.

[261] http://physics.nist.gov/cgi-bin/ASD/lines1.pl

[262] Freiman, S.; Cook, R.; ed.al., Global roadmap for ceramics and glass technology, Wiley-Interscience, **2007**.

[263] Rangaraj, L.; Divakar, C.; and Jayaram, V.; Processing of Refractory metal Borides, Carbides and Nitrides. *Key Engineering Materials*, **2009,** 395, 69-88.

[264] Andrews, A.; Mclachlan, D.; Sigalas, I.; Mathias Herrmann, M.; Boron Suboxide Composite Materials, Patent application number: 20100300004, **2010**.

[265] G. Tari, G.; Ferreira, J.; Fonsecaa, A.; and. Lyckfeld, Influence of particle size distribution on colloidal processing of alumina. *J. Eur. Ceram Soc.,* **1998**, 18, 249-253.

[266] Pal, R., Effect of droplet size on the rheology of emulsions. *J. AIChE*., 42: 3181–3190.

[267] Araki, J.; Wada, M.; Kuga, S.; Okano, T.; Flow properties of microcrystalline cellulose suspension prepared by acid treatment of native cellulose. Colloids and Surfaces A: Physicochemical and Engineering Aspects, **1998**, 142, 75-82.

[268] Jayaseelan, D. D.; Jackson, H. F.; Eakins, E.; Brown, P.; Lee, W. E., Laser modified microstructures in ZrB_2, ZrB_2/SiC and ZrC. *J. Europ. Ceram. Soc.* **2010,** 30, 2279-2288.

[269] Han, J. C.; Hu, P.; Zhang, X. H.; Meng, S. H.; Han, W. B., Oxidation-resistant ZrB_2-SiC composites at 2200^{o}C. *Composites Science and Technology* **2008,** 68, (3-4), 799-806.